Charles University Prague, Faculty of Mathematics and Physics,
Department of Condensed Matter Physics

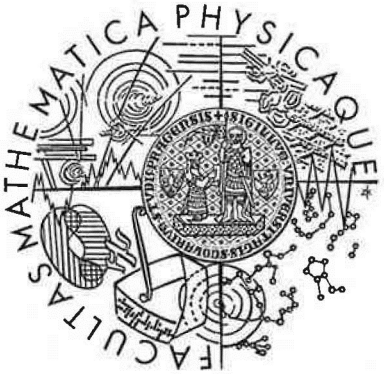

Impurities in rare earth metallic systems:
from super-purified metals to heavy fermion superconductors

RNDr. Jana Poltierová Vejpravová

PhD. Thesis

supervisor: Prof. RNDr. Vladimír Sechovský, DrSc.

Prague, July 2007

Na tomto místě bych ráda vyjádřila upřímné díky všem, bez jejichž vydatné podpory, profesní i osobní, by tato práce zřejmě nevznikla.

Školitel, konzultanti, vedoucí pracoviště: Prof. RNDr. Vladimír Sechovský, DrSc., Doc. RNDr. Martin Diviš, CSc., Doc. RNDr. Pavel Svoboda, CSc., Doc. RNDr. Radomír Kužel, CSc.
Kolegové z KFKL, kteří se podíleli na četných experimentech v rámci disertace: RNDr. Jan Prokleška, RNDr. Stanislav Daniš, PhD., Jan Matlák
Další kolegové z KFKL: Mgr. Zdeněk Matěj, Mgr. Jiří Pospíšil, Mgr. Klára Uhlířová, Mgr. Karel Carva, PhD., Mgr. Khrystina Miliyanchuk, PhD., Mgr. Alexandra Rudájevová, CSc., RNDr. Ján Rusz, PhD., RNDr. Jiří Prchal, PhD., Dr. Olexander Kolomiyets, PhD., Doc. Mgr. Pavel Javorský, Dr., Doc. RNDr. Ladislav Havela, CSc., Doc. RNDr. Ilja Turek, DrSc., Mgr. Kateřina Mikšová, Štěpán Sechovský, DiS.
Kolegové ze SLMS, kteří se podíleli na měřeních na PPMS: Ing. Eva Šantavá, CSc., Ing. Josef Šebek, PhD.
Kolegové z PřF UK, AV ČR a VUK, kteří realizovali měření Mössbauerovy spektroskopie a SEM: RNDr. Daniel Nižňanský, PhD., Bc. Václav Tyrpekl, Ing. Karel Jurek, Mgr. Jaroslav Uhlíř
Vysokopolní experimenty: Nadjezda Kozlova, PhD.
Růst monokrystalů a metoda SSE: Prof. Takemi Komatsubara, Prof. Kunihiko Maezawa
Metoda splat-cooling: Antonio Goncalves, PhD.
Jazykové korekce: Prof. Dr. Frank de Boer

Rodina a přátelé: Ing. Michal Poltier, Mgr. Jana Vejpravová, Marcel Šup, Daniel Šup, Mgr. Jiří Vejprava, Olga Vejpravová, Mgr. Zoja Seyčková, MUDr. Jana Linhartová, MUDr. Markéta Vališová, RNDr. Jaroslav Cihelka, RNDr. Irena Matulková, PhD., Mgr. Dana Provazníková, RNDr. Michal Šála

Děkuji všem.

Prohlašuji, že jsem dizertační práci vypracovala samostatně a pouze s využitím uvedené literatury. Souhlasím se zapůjčováním práce.

V Praze, 16.7.2006

RNDr. Jana Poltierová Vejpravová

Contents

List of Figures

List of Tables

Chapter 1

Introduction - Impurity concept

In general, impurities are substances inside a confined amount of solid (liquid, gas), which differ from the chemical composition of the material or compound. They are either naturally occurring or added during synthesis of a desired (chemical or commercial) product. During production, impurities may be purposely, accidentally, inevitably, or incidentally added into the substance. The concentration level of impurities in a material is generally defined in relative terms. Standards have been established by various organizations that attempt to define the permitted levels of various impurities in a manufactured product.

The impurity content covers a large scale; from several ppm to tenths of a percent of the impurity agent in the host medium. Of course, the concentration of impurities influences the electronic structure of the material and hence, its physical properties. A typical scale diagram is depicted in Figure 1.1.

Impurities can be destructive when they obstruct the working nature of the material. Contrary, they can add constructive properties to a material. The resulting combination has desirable properties not found in the constituent materials. Steel, for example, is made by introducing a controlled amount (less than 2%) of carbon into pure iron. In the manufacturing of solar cells, pure silicon is mixed with a very small portion of impurities (0.001% to 0.01%) in the form of phosphorus and boron atoms in order to generate electricity. This is known as doping of silicon and is constructive, although the phosphorus and boron could be called impurities.

Impurities are able to serve as initiation points for phase transitions because the energetic cost of creating a finite-size domain of a new phase is lower at a point defect. The nucleus of a new phase becomes stable only after it reaches a critical size. This threshold size is often lower at an impurity site. In other words, when an impure liquid is cooled to its melting point, the liquid, undergoing a phase transition, crystallizes around the impurities and becomes a crystalline solid. If there are no impurities then the liquid is said to be pure and can be supercooled below its solidification point without becoming a solid. This occurs because the liquid has nothing to condense around so the solid cannot form a natural crystalline solid. The solid is eventually formed when a dynamic arrest or glass transition occurs, but it forms into an amorphous solid - a glass, instead, as there is no long-range order in the structure.

Impurities in metals present a great challenge to condensed- matter physicists, for which a strong starting point has long been the early insight of Kondo into the resistance medium.

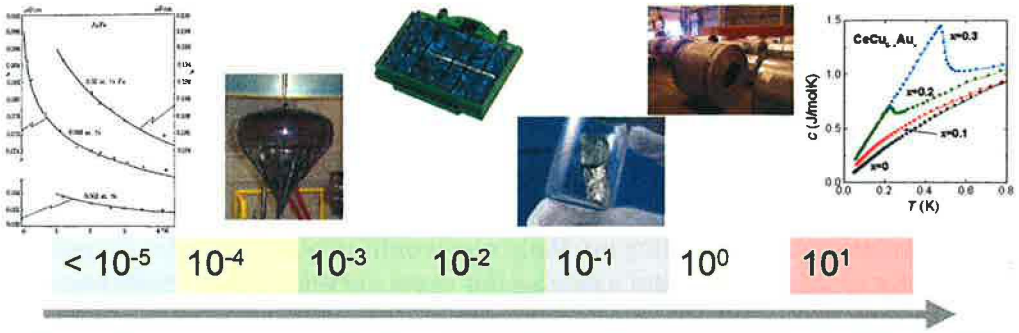

Example system	*Impurity*	
Trace impurities in high purity gases	$< 10^{-5}$	Nobel gases
Kondo effect in Cu	$< 10^{-5}$	Several ppm of Fe in Cu or Au
6N semiconductors (Ge, Si)	10^{-4}	O_2
Silicon doping	10^{-3} - 10^{-2}	B, As
Commercial 3N RE metals	10^{-1}	various elements (Ca, other RE...)
Steel	10^{0}	~ 2 % C in Fe
Raw iron	10^{0}	~ 3 – 5 % C in Fe
Ce Kondo lattices	10^{1}	4 % of Ce in ($CeCu_6$)

Figure 1.1: Scaling of the impurity concentration.

The presence of foreign elements may have important effects on the mechanical, transport and magnetic properties of metals and alloys. Magnetic impurities in superconductors can serve as generation sites for vortex defects. Iron atoms in copper cause the famous Kondo effect where the conduction- electron spins form a magnetic bound state with the impurity atom. Point defects can nucleate reversed domains in ferromagnets and dramatically affect their coercivity and so on. As a special case, constituting atoms of one kind in a stoichiometric substance may act as magnetic impurities, like cerium in many intermetallic compounds, resulting in the mentioned Kondo-like behavior.

The aim of the present thesis is to investigate and discuss the impurity phenomenon in the context of metallic systems from different points of view:

- *Impurity as an alien medium in metals - effect on electronic properties*: The impurity effect on electronic properties in pure transition metals is described together with the most effective method for transition- metals purification - solid- state electrotransport (SSE). The set of results obtained using the SSE apparatus, recently installed in the Department of Condensed Matter Physics (Faculty of Mathematics and Physics, Charles University, Prague) is presented.

- *Single-electron impurity - Ce strongly correlated electron systems*: The single electron

of the Ce ion is treated as a bound impurity within the context of the Kondo scenario and electronic correlations leading to exotic ground states like heavy-fermion superconductivity coexisting with long-range magnetic ordering. A series of Ce compounds related to the heavy-fermion superconductor $CePt_3Si$ was investigated and the comprehensive results are presented.

- *Ce superconductors under doping - role of injected impurities and disorder*: As the Ce intermetallic compounds are in fact fundamental impurity systems, additional effects of substitution and disorder on their electronic properties were investigated. Furthermore, the crucial role of the aggregation state (crystalline material vs. amorphous and nanogranular metal) is presented. The investigations were performed on two groups of compounds related to the $CePt_3Si$ and $CeRu_2$ superconductors.

The thesis comprises nine chapters except the introductory part (Chapter 1).

Chapter 2 is focused on the main features of the electronic structure and magnetism in of transition metals and their compounds. The accent is given put on the impurity phenomenon - Kondo effect and related problems together with the role of disorder in metals.

Chapter 3 describes the experimental methods used for preparation, characterization and investigation of the studied materials.

Chapters 4 - to 6 summarize the up-to-date knowledge of the investigated groups of materials: selected transition metals, $CePt_3Si$ and its isotypes, and $CeRu_2$ and derived compounds., respectively.

Chapters 7 - to 9 present and discuss the obtained results with respect to the listed groups of materials.

Finally, Chapter 10 gives a summary and conclusions.

In addition, references to the related literature and supplementary appendices containing relevant overviews regarding technology, theory, experiment and electronic properties of the studied compounds are included. The appendices also contain additional results on disordered systems (CeNi-CeCu and $La(Fe,Mn)_2Si_2$) and isostructural compounds related to $CePt_3Si$ ($LaPt_3Si$, $PrPt_3Si$).

Chapter 2

Electrons in transition metal systems

The chapter was composed using mainly the following references: [1]-[9].

2.1 Introduction - mobile electrons in solids

Solids are characterized by a regular (almost fixed) arrangement of a macroscopically large number of atoms (about 10^{22} per cm^3). The latter consist of the core and an appropriate number of electrons which are strongly bounded. Only a small number of them are mobile. Usually, these mobile electrons are primarily responsible for the thermal -, electric - and magnetic properties of a solid.

Beside the negative charge, the spin of the electrons determines the magnetic properties of the solid to a substantial extent. While, however, a macroscopic system, like a piece of permanent magnetic material may follow continuously external fields, the spin of the electrons has just two directions: spin up and spin down, i.e., parallel or antiparallel to the external field. This quantization is typical for the physics valid on an atomic scale.

Charged particles are subjected to mutual interactions due to the Coulomb force which can be both repulsive and attractive, depending on the charge. Moreover, there are also forces between magnetic moments, however much smaller if compared to the Coulomb interaction. The particles are therefore exposed to complicated many-body interactions, which can be treated exactly only in terms of quantum mechanics. The later is valid, in particular, for mobile electrons moving across the solid.

Each electron is then described by its position (radius) vector and spin. The inter-electron interaction in a solid results not only from the Coulomb force and magnetic interaction but also from the Pauli principle: for a given system, two electrons may not agree in all physical properties (= quantum numbers). For the above discussed case, two electrons may approach each other only, if they are distinguished at least in their magnetic properties, i.e., in their spin direction (spin up or spin down). This infers that the Coulomb charge interaction, which initially is independent on the spins, is eventually - due to the Pauli principle - responsible for the orientation of magnetic moments.

Interactions between microscopically small particles, arranged in a solid, may yield to fascinating physical phenomena like magnetism, metal-insulator transition, superconductivity or heavy electron behavior. These appearances are usually termed as co-operative phenom-

ena, since a macroscopic number of particles act together. In fact, the exchange interaction is simply the quantum mechanical effect of increasing or decreasing the energy of two or more fermions when their wave functions overlap. This energy change is the result of an effect due to the identity of particles and exchange symmetry.[1]

In absence of an external magnetic field, the magnetic moments of the electrons in a solid are disordered. The electrons with spin up or spin down are statistically distributed and on an average scale there are as much spin up electrons like spin down electrons. A solid is then non-magnetic. However, it is well known that there exist various alloys and compounds being magnetic. This means that the magnetic moments of the electrons are ordered in the material over a substantial distance. The sum of the ordered moments yields then the macroscopically deduced total magnetization. Beside such a ferromagnetic state there exists antiferromagnetism with alternating arrangements of the spins or much more complex structures of the spins in the ordered state.

These co-operative phenomena with respect to magnetism are known since more than 2800 years and many attempts have been made in order to describe them reasonably. The ordering temperature corresponds roughly to the energy of the Coulomb interaction between electrons and thus, with the Pauli principle, causes the alignment of the electron spins. With respect to elements like Fe, Co or Ni, these electrons are not fixed to a certain lattice site rather they are mobile. This makes the quantum theoretical many-body problem extremely complicated; no systematic theoretical solutions exist up to now. The use of models with a couple of simplifications may be sufficient in many cases to account for such observations.

If electronic effects are of interest, the ions of the solid can be considered as a positive charged background for the negatively charged, mutual repulsive electrons. In the most simplest approach we assume that an electron does not interact separately with all other electrons, but the electron is exposed to an effective interaction, resulting from an average due to the presence of all other electrons. Each electron is then in an averaged field; real interactions with e.g., exchange of energy, do not happen anymore. This simplification is known as the theory of averaged fields or molecular field theory.

Such a model yields frequently valuable findings, however in many cases the particular interaction is necessary in order to obtain sufficient results. These interactions are then called correlations. They cannot be understood in terms of simple averaged field models. Some well known examples for correlated electron systems are transition metals and their oxides, cerium, ytterbium and uranium systems with heavy fermion behavior due to the Kondo interaction as well as the new class of high-temperature superconductors.

[1] As a mathematical consequence, fermions exhibit strong repulsion when their wave functions overlap, but bosons do not. This repulsion is what the exchange interaction models. Fermi repulsion results in "stiffness" of fermions. That is why atomic matter, is "stiff" or "rigid" to touch. Where wave functions of electrons overlap, Pauli repulsion takes place. The same is true for protons and neutrons where due to their larger mass, the rigidity of baryons is much larger than that of electrons.

2.2 Electrons in simple metals

Everyone knows what a metal is and can describe many of its characteristics. It is safe to say, however, that few people would define a metal as 'a solid with a Fermi surface'. This may nevertheless be the most meaningful definition of a metal that one can give today; it represents a profound advance in the understanding of why metals behave as they do. The concept of Fermi surface, developed by quantum physics, provides a precise explanation of the main physical properties of metals: their conduction of electricity and heat, their hardness and ductility, their lustrous appearance and so on.

A. R. Mackintosh (1963)

Specific character of metallic bond in metals and intermetallic compounds originates variety of their characteristic physical behavior. The typical properties of metallic systems such as the Pauli paramagnetism caused by the conducting (free) electrons or the high cohesive energy can be sufficiently explained within the concept of free electron gas in metals.

2.2.1 Nature of metallic bond

Electron gas

When we put together two atoms of any metal, they will interact with each other to form some kind of molecule. If we pack more and more metallic atoms together - as in a solid- each neighboring pair would like to form a 'molecule' and share electrons. But each atom has a defined number of neighbors (coordination number) in a solid state, but the same number of electrons to share as the others. Then, since this is only one cell of a complete crystal lattice, other electron comes from other further cells and so on.

In general terms, this idea is quite enough to explain many characteristics of metals, most of which stem from the fact that metals are good conductors of electricity.

On the face of it, this model seems to be wildly unrealistic. The basic question is how to apply the Pauli's exclusion principle on the free electron gas.

One obvious way is to erect impenetrable walls about each electron, confining each to its own cell. But such localization costs energy (as in the covalent bond). If the width of a cell is a this represents the maximum uncertainty of the position of the electron in one dimension. Correspondingly, the momentum of the particle in this direction will have a minimum uncertainty $< p_x >$, such that

$$a < p_x > \sim \pi\hbar. \tag{2.1}$$

Adding the same components in the other two dimensions the mean total kinetic energy of the electron $< \delta >$ can be written as:

$$< \delta >= \frac{1}{2m}\{< p_x > + < p_y > + < p_z >\} \sim \frac{3\hbar^2\pi^2}{2ma^2} \tag{2.2}$$

This is a large energy - several electronvolts. To drop the barriers in the proposed model and let the electrons move freely releases a lot of energy. So, instead to keep the electronic states distinct in space, we allow them to overlap freely - the electron wave functions cover the whole cell in which the gas is confined.

As in an atomic state, the convenient wave functions must be constructed in the same region of space, then occupied with two electrons, both spins for each state. To solve the problem of 'counting states' the basic theory of the elastic and optical vibration is employed[2]

In effect, localization in co-ordinate space was replaced by localization in momentum space and the new quantization scheme does not change the energy scale.

The highest energy within the free electron gas scheme is $\frac{\pi^2\hbar^2}{ma^2}$, so the average electron energy in the gas must be lower than this by the same value. This can crudely explain a source of the high cohesive energy of metals.

This cohesion basically depends on getting the electron gas of fairly high density, not on the details of the crystal structure. The electron gas packs together more or less any arrangement of ions that is sufficiently densely packed, there is no need to construct special bonds between neighboring atoms. This can explain the tendency of metallic crystals to form close-packed structures, yet not strongly preferring one close-packed structure to another.

The complexity of the phase diagrams of metallic alloys and compounds is originated by the balance of energy in favor of one structure which may be easily tipped towards another phase by a small change of temperature or composition. The same general argument explains why metals are characteristically malleable and ductile.

---

[2]The de Broglie formula defined the wavelength of an electron of momentum p:

$$\lambda = \frac{2\pi\hbar}{p}. \tag{2.3}$$

When suppose the cubical box of side La, the number s of waves across the box is exactly:

$$s\lambda = La. \tag{2.4}$$

A wave of this wavelength, reflected from the side, and back again, would repeat itself exactly, and would be an acceptable stationary of the system. If we take the normal as the x direction, the rule for the x component of momentum is:

$$p_x = 2\pi\hbar\frac{cos\theta}{\lambda} = 2\pi\hbar\frac{s_x}{La} \tag{2.5}$$

where s_x is an integer. The similar rules exist for y and z components. These states are quantized in momentum with quantum numbers s_x, s_y and s_z, which are positive or negative integers. The energy of each term with quantum numbers s_x, s_y and s_z is than given by:

$$\xi(s_x, s_y, s_z) = \frac{p^2}{2m} = \frac{4\pi^2\hbar^2}{2m^2}\frac{(s_x^2 + s_y^2 + s_z^2)}{L^2}. \tag{2.6}$$

When we consider n electrons in the box of size La, then $n = L^3$ and the n states can be constructed running each of the s_x, s_y and s_z integers from $-\frac{1}{2}L$ to $\frac{1}{2}L$. This yields exactly L^3 different combinations of quantum numbers. In that case the highest states would have the energy:

$$\varepsilon\left(\pm\frac{1}{2}L, \pm\frac{1}{2}L, \pm\frac{1}{2}L\right) = \frac{3\pi^2\hbar^2}{2ma^2} \tag{2.7}$$

Fermi energy

The Fermi energy is a kinetic energy of the order of several electronvolts, which is much more than the ordinary thermal excitation at the room temperature ($k_B T = 0.03$ eV). The free electrons in metals must be travelling with velocities about 1000× the velocity of the ions, for their mass is smaller by factor 10^4 , and their energy larger by factor of 10^2. This implies an important *adiabatic principle*, which treats the ions 'frozen' into some typical configuration whilst the electrons swarm about them.

The electronic system has always a high kinetic energy, but when we heat up the many-electron system, only those are affected in a narrow layer near the Fermi level. The same happens for any low energy excitation such as application of an electric or magnetic field, or an acoustic vibration. The formal theory of the statistical mechanics of a system of fermions (particles obeying the Fermi-Dirac statistics) gives the rule for the average occupation number of a state of the energy E:

$$f(E) = \frac{1}{\exp[(E - E_F)/k_B T] + 1}. \tag{2.8}$$

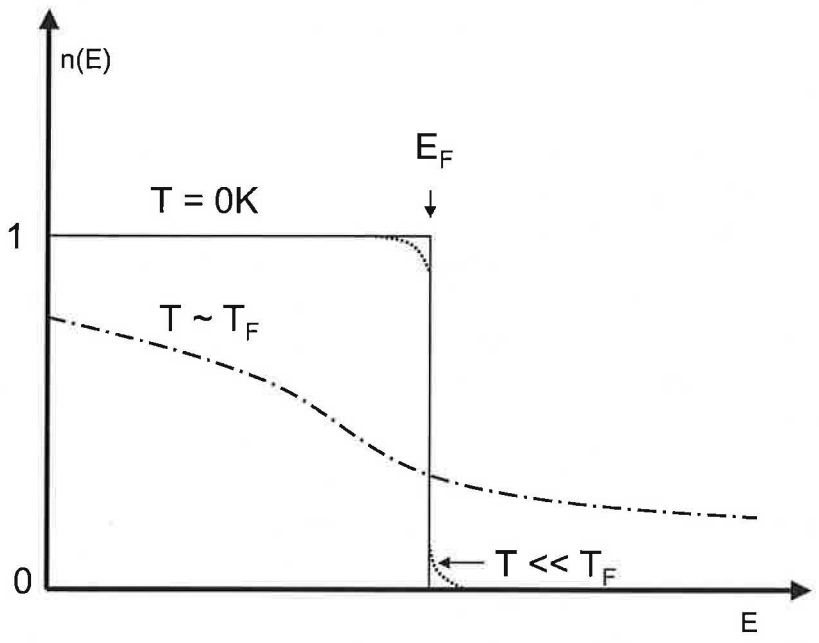

Figure 2.1: Fermi-Dirac distribution function.

The only region where $f(E)$ is appreciably different from 1 or 0 is near the E_F over a width depending on the multiple of $k_B T$. The involvement of Fermi-Dirac distribution (see Figure 2.1) results in a degenerated Fermi gas (because of $E_F \gg k_B T$).

2.2.2 Origin of bands and Fermi surfaces

Bragg reflection of electron waves

A gas of free electrons is an excellent model for the electrical properties of metals. But there are the experimental anomalies such as the positive Hall coefficient or positive thermo-electric power, which can not be explained with the free-electron model.

When the electrons move in the crystalline lattice, they are scattered by the ions and the electrons are then quantum-mechanically represented by the simple plane waves. The scattered waves from different ions will tend to interfere with one another in a systematic way, so that there may be coherence in the total diffracted wave (like in the X-ray or fast-electron diffraction on the crystal) corresponding to the Bragg reflection:

$$n\lambda = 2a\cos\theta. \tag{2.9}$$

The scattering condition can be written in form:

$$pa\cos\theta = n\pi\hbar. \tag{2.10}$$

Any electron travelling in the direction θ relative to the lattice planes, with momentum p satisfying this condition, will be coherently reflected by the crystal lattice and then the simple plane wave cannot be a good representation of the wave function of the stationary state.

To simplify discussion let us consider the case where an electron is travelling normal to a set of lattice planes. To simulate the obstacle presented by each lattice plane to the path of the electron, the actual potential function - a set of square wells will be assumed. Since the scattering is symmetrical, the effect of scattering is simply to interchange the two travelling waves in the sum or difference (a standing wave from the quantum mechanically point of view). A standing wave state means, that the electron wave is bound to the lattice and is unable to travel as a wave packet throughout the crystal.

The total energy of the final state is obtained as the minimum of sum of the kinetic and potential energy:

$$\epsilon_k = \frac{1}{2}(\epsilon_k^0 + \epsilon_{k-g}^0) - \frac{1}{2}\sqrt{[(\epsilon_k^0 - \epsilon_{k-g}^0) + 4|V_g|^2]}. \tag{2.11}$$

This state has lower energy than the free wave and is therefore acceptable wave function for the electron in lattice.

It was shown that there in a regular periodic lattice exist many solutions of the Schroedinger equation which are uniformly propagated without scattering or attenuation, and which can therefore carry an electric current without showing electrical resistance. To that extent, the conducting electrons do not 'see' the regular lattice. Close to the Fermi level, there are free electronic states. As the energy increases the wave function comes more and more distorted, until $k = \frac{1}{2}g$, where reaches just the standing wave state.

Then there is no solution of the Schroedinger equation for a whole range of energy. The next value above the first level, where the solution exists (ψ_+), corresponds in fact to the ψ_-. This is also a standing wave, not exactly out of phase with the lattice and therefore with energy $+|V_g|$ above the electron free parabola. When repeat again and again, by ever-increasing value of k, energy ranges from the free-electron parabola and back nearly to the free electron wave function.

The effect of the Bragg diffraction then simply yields not continuous relation between the energy and the momentum and originated the presence of so-called forbidden bands of energy in metallic crystal - energy gaps, where are no solutions of the Schroedinger equation, see Figure 2.2.

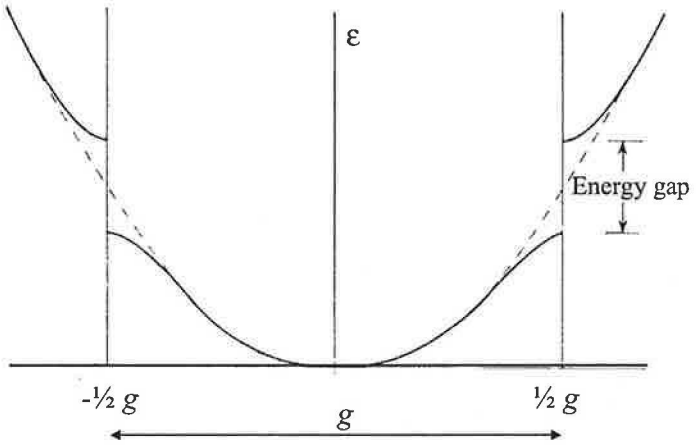

Figure 2.2: Origin of the forbidden bands.

Because of coherent diffraction of the electrons by the regular atomic planes of the crystal, some states are very strongly affected by the periodic potentials, and are very different from the free electron waves. The states which are most strongly diffracted, and whose energy is changed the most (up or down) are those whose $\overrightarrow{k}$-vectors correspond to points on a set of planes which delineate a cell in $\overrightarrow{k}$-space. The cell is a Brillouin zone.

- A Brillouin zone in momentum space contains as many allowed momentum states as there are unit cells in the lattice.

When the element fills the whole band, which is than electronically inert - like a closed shell in an atom, the element would not be a metal but semiconductor and its bands do not overlap. When the bands are not fully filled with electrons bands overlap - the lower band is not necessary quite full and the upper band not quite empty. The electrons in these bands are no longer energetically isolated under energy gaps, and can be easily made to carry electric current etc.

A good qualitative account of the properties of metals can be given from an analysis of their band structure. Furthermore, curves representing the distribution of electrons in energy in different bands can be constructed. The function representing the distribution is called density of states $N(\epsilon)d\epsilon$, define such that $N(\epsilon)d\epsilon$ is the number of electrons states in the range of energy ϵ to $\epsilon + d\epsilon$.

Fermi surface

The density of states at the Fermi level originates the electronic properties of metals. Only the states close to the Fermi level are the most important which lie on or near a surface of constant energy in $\overrightarrow{k}$-space. This specific surface, defined by the relation:

$$\epsilon \overrightarrow{k} = \epsilon_{\mathrm{F}}, \tag{2.12}$$

automatically provides all the electronic states that play the crucial role in the properties of metal or intermetallic compound. It is called Fermi surface.

From a simple mathematical point of view, $\overrightarrow{k}$-space is the natural medium for the classification of electronic states, and the construction of surfaces of constant energy is then irresistible, than instead of 'electrons at the Fermi level' is commonly used the term 'electrons on the Fermi surface'.

In a free electron gas, the Fermi surface is, of course, a sphere. But in a real system, the Fermi surface is almost sure to be different from a sphere - where are two or more electrons per atom in a unit cell; the influence of the zone boundaries is sure to be profound and thus will introduce energy gaps at every line of intersection. The properties of the electron gas will be anisotropic.

Consequently, the dynamical properties of electrons on the Fermi surface depend on their direction of motion:

- electrons are travelling in a direction where it might very easily suffer Bragg reflection by lattice, then they may seem 'slow' and 'heavy'
- in other directions electrons behave very much like a free electron gas.

This means that the shape of the Fermi surface with respect to the Brillouin zone is a guide to the basic properties of metals.

Concerning the effect of magnetic field, the simple rule is valid:

- In a magnetic field H the k-vector of an electron on the Fermi surface traces out the orbit defined by the intersection of the Fermi surface with a plane normal to H.

This elegant theorem is the key of all methods of investigating Fermi surfaces. The magnetic field itself do not change energy of an electron, but just modify its trajectory. In the momentum space the electron trajectory is described as an orbit, which is very easy to define and comprehend.

2.3 Remarks on magnetism in metals

2.3.1 Free-ion magnetism

Diamagnetism

Each solid is, at least, diamagnetic ($\chi < 0$)[3]. Diamagnetism can therefore be considered as a proof of the atomistic structure of matter, since it appears only in the case of closed or quantized electron orbits. Diamagnetism is a field induced, but temperature independent effect. It results from the attempt of the system to screen the inner parts of matter from magnetic fields (Lenz's rule).

This fundamental property is displayed from a negative magnetic susceptibility. The induced diamagnetic moments is proportional to the area of the electron orbit and therefore to the magnetic field flux through the electron orbit:

[3] χ represents the magnetic susceptibility: $\frac{\partial^2 F}{\partial H^2} = \frac{\partial M}{\partial H}|_{T=const.}$

$$\mu_{dia} = \frac{e^2 < r^2 > \overrightarrow{B}_0}{6m_e} \tag{2.13}$$

If we anticipate that the radius of the orbital is r = 0.1 nm and the magnetic field B_0 = 1 T, it follows that the induced moment is $-5 \times 10^{-6}\mu_B$, about 10^{-6} of the value of a saturated ferromagnet.

There are several metals which are diamagnets. The best known examples are copper, silver and gold. This diamagnetic behavior is explained from the always diamagnetic contribution of the valence electrons and from the orbital contribution of the conduction electrons (Landau diamagnetism), and additionally from the spin contribution of the conduction electrons (Pauli - paramagnetism).

Because of the high degeneracy temperature of metals, the spin susceptibility is small and almost temperature independent, therefore the total measured susceptibility can be negative for some metals; however, in most of the cases the susceptibility appears to be positive.

Paramagnetism

Atoms and molecules with an odd number of electrons exhibit paramagnetism ($\chi > 0$).

Four quantum numbers n, l, m_l, m_s are satisfactory to describe the state of an electron in the atom (n . . . principal quantum number, l . . . orbital angular momentum quantum number, m_l, m_s are the respective magnetic quantum numbers).

Elements of the $3d$ and the $4f$ group possess permanent magnetic moments:

How the electrons combine in an atom to produce a stable state of least energy (the ground state) is determined partly by the relative magnitudes of the energies of interaction of the following types.

The interaction of the orbital angular momentum ($\overrightarrow{l}$) with the spin ($\overrightarrow{s}$) of a given electron is called spin-orbit interaction. The orbital momentum interacts more strongly with the same-electron spin than with the spins of other electrons.

The spin-orbit coupling yields then:

$$\overrightarrow{j} = \overrightarrow{l} + \overrightarrow{s}, \tag{2.14}$$

where the corresponding quantum number $\overrightarrow{j}$ (= total angular momentum) can take the values $j = |l - s|, |l - s| + 1, ..., l + s - 1, l + s$. Of course, the magnetic quantum number m_j is also quantized; $m_j = -j, (-j + 1), ..., (j - 1), j$.

The practical calculation of the total angular momentum follows then from the Hund's rules:

- The combination of s_i that gives the lowest energy (i.e. the most stable) is that with the highest value of $(2s + 1)$.
- If when the first rule has been satisfied there are several possible l values having the same value of $(2s + 1)$, that with the largest l will be the most stable. Hund's rules have full theoretical justification only in a very limited cases, but there are very little doubts of their validity.

The argument to support them is as follows:

- Two electrons in the same orbital with opposite spins must involve large electrostatic electron-electron repulsion because of the proximity of the two electrons. Energy is lowered if dual occupations are minimized, giving as many like electrons as possible.
- Having satisfied the first condition, if the electrons orbit in the same sense electron-electron repulsive interactions are minimized because the electrons spend more of the time further apart.

The most stable configurations result from:

- $j = |l - s|$ . . .less than half filled shells
- $j = |l + s|$ . . . more than half filled shells
- $j = s$ . . . half filled shell ($l = 0$).

The corresponding magnetic moments are:

$$\mu_l = \mu_B(l(l+1))^{1/2}, \mu_s = 2\mu_B(s(s+1))^{1/2} \tag{2.15}$$

Because of the spin-orbit interaction the resultant vectors $\overrightarrow{l}$ and $\overrightarrow{s}$ are precessing about their vector sum $\overrightarrow{j}$. To account for the different weight of the spin and the orbital contribution to the total angular momentum, the Landé factor g is introduced. The total angular momentum is then:

$$\mu_l = \mu_B(l(l+1))^{1/2} \tag{2.16}$$

with

$$g = 1 + \frac{j(j+1) + s(s+1) - l(l+1)}{2j(j+1)} \tag{2.17}$$

Borderline cases are: $g = 2$ for $l = 0$ and $g = 1$ for $s = 0$. This defines the magnetic moment of a single atom/ion.

In the absence of external magnetic fields, all the atoms with equal magnetic moments have equal energy. If an external magnetic field is applied, the energy depends on the occupation of the $2j + 1$ sub-levels, all of which differ in their m_j value. The magnetic sub-levels are occupied according to the laws of statistical mechanics, the lowest energy having the largest population. The magnetic moment of an assembly of non-interacting atoms is given by the so-called Brillouin function (Figure 2.3). $B_{j,y}$.[4]

$$B_{j,y} = 1 + \frac{2j+1}{2j}\coth(\frac{2j+1}{2j}y) - \frac{1}{2j}\coth(\frac{1}{2j}y) \tag{2.18}$$

where $y = (jg\mu_B B)/(k_B T)$.

The saturation value (for large y) is 1; it means all the atomic moments are aligned in the field direction. It has been observed in strong fields and at low temperatures only in some

[4]The Brillouin function is derived supposing the relative population of a sub-level m_j defined by the partition function $Z(m_j) = \frac{exp(-E_m/k_B T)}{\sum_{m_j} Pexp(-E_m/k_B T)}$. For details, see e.g. [1].

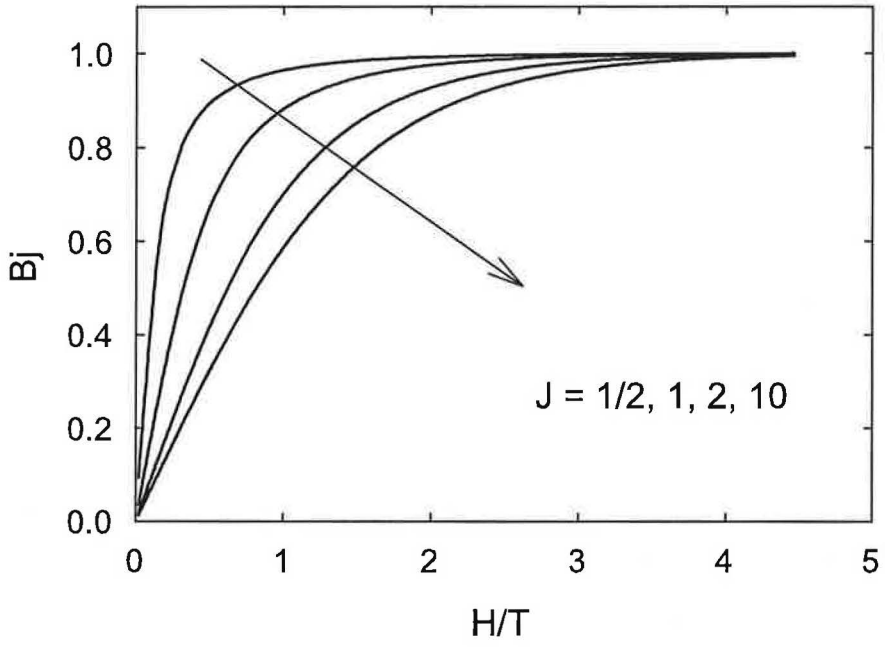

Figure 2.3: Brillouin function for several different values of j.

paramagnets. Observations are usually made under the condition of small y; that is, near the origin of the Brillouin function. The paramagnetic susceptibility is therefore related to the slope of the Brillouin curve.[5]

Finally, the molar magnetic susceptibility may be expressed as the well-known Curie law:

$$\chi_{\mathrm{m}} = \frac{C_{\mathrm{m}}}{T} = \frac{g^2 j(j+1) N \mu_{\mathrm{B}}^2}{3 k_{\mathrm{B}} T} = \mu_{\mathrm{eff}}^2 \frac{N \mu_{\mathrm{B}}^2}{3 k_{\mathrm{B}} T}, \tag{2.21}$$

where μ_{eff} is the effective magnetic moment available from common magnetic measurements.

For many materials, instead the Curie law, Curie-Weiss or modified Curie-Weiss law is valid:

$$\chi_{\mathrm{m}} = \frac{C_{\mathrm{m}}}{T - \theta_{\mathrm{P}}} \tag{2.22}$$

$$\chi_{\mathrm{m}} = \frac{C_{\mathrm{m}}}{T - \theta_{\mathrm{P}}} + \chi_0 \tag{2.23}$$

The θ_{P} value is called the paramagnetic Curie temperature and generally represents the effect of inter- or intra- lattice interaction between the magnetic ions. Depending on its sign,

[5]Using the expansion:

$$B(j,y) \approx 1/y + (y/3)(1 + 1/2j)^2 - 1/y - (y/3)(1/2j)^2 = y(j+1)/3j. \tag{2.19}$$

together with the average magnetic moment per mol:

$$N_a j g \mu_{\mathrm{B}} B(j,y) \tag{2.20}$$

either ferromagnetic ($\theta_P > 0$) or antiferromagnetic ($\theta_P < 0$) exchange dominates.[6]

The χ_0 corresponds to a temperature-independent contribution to the magnetic susceptibility. This term appears often in case of materials with strongly correlated electrons like band-metamagnets and so on. Generally, the χ_0 term signalizes certain level of electron delocalization (itinerancy) in the system. The χ_0 contribution may also occur due to Pauli paramagnetism of conduction electrons.

Pauli paramagnetism

Conduction electron ensembles exhibit also paramagnetism. The classical theory of the free electron gas does not result in a satisfactory theory of the paramagnetic susceptibility of conduction electrons. Since each electron possesses a magnetic moment of about $1\mu_B$, one should suppose that there is a Curie like behavior of the susceptibility of a metal. Pauli could show that the Fermi-Dirac distribution function yields to a temperature independent susceptibility (for derivation, please see e.g. [1]):

$$\chi_{Pauli} = \frac{\partial M}{\partial B_0} = \mu^2 N(E_F) = \frac{3N_a\mu_B^2}{2k_B T_F} \tag{2.24}$$

The equilibrium magnetization, M is given by the difference between the particularly populated spin up and spin down states, respectively.

If additionally one assumes that the applied magnetic field influences the motion of the electrons, an additional diamagnetic contribution results, which is known as Landau's diamagnetism, amounting to -1/3 of the Pauli contribution.

Measurements of the Pauli susceptibility lead immediately to information concerning the magnitude of the electronic density of states at the Fermi energy.[7]

Electrostatic interaction of the aspherical $4f$ charge density - Crystal field effect

The crystal field effect represents the electron-electron interactions in the solid due to the electrostatic interaction of the aspherical $4f$ charge density with the aspherical electrostatic field arising from the ion neighborhood. In fact it can be treated as an additional perturbation to the free-ion state besides the spin-orbit interaction.

It is an experimental fact that for the rare-earth ion, the spin-orbit interaction is much stronger than the crystal-field interaction. Owing to this fact, it is usually sufficient to consider only the lowest multiplet j, given by Hund's rules. This limitation results in a substantial simplification both in the analysis of the experimental data and theoretical calculation. [8]

[6] For single-crystals with huge uniaxial anisotropy, opposite signs of θ_P are observed for magnetic fields applied along the main principal crystallographic directions, however, the polycrystalline data of the identical material provide the θ_P value almost negligible. The reason is the comparable strength of the ferro- and antiferro- magnetic interaction in the system. UNi_2Si_2 may serve as a textbook case [10]

[7] As shown further, Kondo systems and heavy fermions are characterized be extraordinary large values of the susceptibility at low temperatures, implying that there is also an extraordinary large electronic density of states in the vicinity of the Fermi energy.

[8] Eu^{3+} and Sm^{3+} ion states require the involvement of a higher multiplet, since the higher multiplet is just 530 and 1500 K above the ground-state multiplet, respectively.

The crystal-field Hamiltonian can be written as:

$$H_{CF} = \sum_m \sum_n A_n^m \sum_i f_{nm}(r_i), \tag{2.25}$$

where f_{nm} are Tesseral harmonics describing the spatial distribution of the charge associated with the $4f$ electrons, A_{nm} describes the spatial distribution of the charge surrounding the $4f$ electrons.

Using the Stevens formalism the summation over the $4f$ electrons leads to the matrix elements of the total angular momentum. Within the ground-state multiplet the crystal-field Hamiltonian is written in the conventional form:

$$H_{CF} = \sum_m \sum_n B_n^m O_n^m(J), \tag{2.26}$$

where O_n^m are the Stevens operators(equivalents) and B_n^m are the crystal-field parameters which are usually evaluated from the analysis of the experimental data. The parameters B_n^m can be written as:

$$B_n^m = \theta_n < r_{4f}^n A_n^m >, \tag{2.27}$$

in which expression terms related to the $4f$ ion, θ_{4f}^n, and term related to the surrounding charges, $< r_{4f}^n A_n^m >$ known as the crystal field coefficients, are separated.

It is important to notice, that the crystal field scenario may be applied to the completely localized rare earth ions only. The exotic cases (like e.g. CePtSi [11]), where the crystal field perturbation competes to the Kondo effect are observed rarely. They are mostly treated by sophisticated approaches using the Coqblin-Schrieffer or Anderson model under the large-N approximation or Bethe ansatz method.[9]

Exchange interaction in $4f$ systems

The unpaired electrons in the $4f$ shell are responsible for the magnetic moment of the rare earth ion. Since the $4f$ electrons are strongly localized and their spatial distribution is much smaller than interionic distances, direct exchange of the $4f$ wave functions of different rare-earth ions is precluded. In order to account for the observed ordering temperatures, one has to resort to an indirect exchange between the rare-earth ions via the conducting electrons.[10]

This interaction is well described by the Ruderman-Kittel-Kasuya-Yosida ($RKKY$) model. A magnetic ion induces a spin polarization in the conduction electrons in its neighborhood. This spin polarization in the itinerant electrons is felt by the moments of other magnetic ions within range, leading to an indirect coupling.

[9] for further details please see e.g.

- Coqblin-Schrieffer model:[12, 13, 14]
- Anderson model:[15, 16, 17]
- large-N approximation:[18, 19]
- Bethe ansatz method:[20, 21, 22, 23]

[10] In fact other types of indirect interaction like superexchange through e.g. $4d$ ligands, and $4d$ hybridization-induced indirect exchange interaction are known.

The simplifying assumption in the *RKKY* model is that the exchange is of the *s-f* type and constant and that the Fermi surface is spherical (free electrons). The ordering temperature in this model is expected to be proportional to the deGennes factor:

$$(g-j)^2 j(j+1) \tag{2.28}$$

The exchange interaction is assumed to be of the Heisenberg type:

$$H_{ex} = -\sum_{ij} J_{ij} S_i S_j \tag{2.29}$$

where the summation (2.29) is over all magnetic ions in the lattice and J_{ij} is the exchange parameter between local spins at the i and j sites.

The *RKKY* exchange coefficient,J_{ij}, oscillates from positive to negative as the separation of the ions changes and has the damped oscillatory nature. Therefore, depending upon the separation between a pair of rare earth ions their magnetic coupling can be ferromagnetic or antiferromagnetic.

The schematic representation of the *RKKY* interaction is shown in the Figure 2.4.

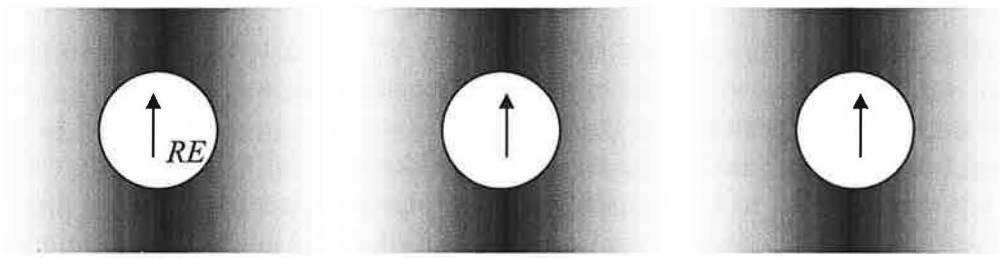

Figure 2.4: Schematic representation of the *RKKY* interaction.
The shaded area correspond to the density of the polarized conduction electrons, the localized magnetic moments of the magnetic ions are represented by the large arrows.

2.4 Transport in metals - electrical resistivity

2.4.1 Relaxation time, Matthiessen's rule

All processes where charge or heat is transported under the influence of external forces or fields are known as transport phenomena. The combination of electric or magnetic fields as well as the presence of a temperature gradient along a sample yields a variety of different transport coefficients. The theoretical understanding of the temperature dependent transport coefficients is usually accounted for in terms of the linearized Boltzmann equation. This semi quantum-mechanical theory connects a field term with a collision term and describes therefore a dynamical equilibrium between a driving force (e.g. an electrical field in case of the electrical conductivity) and scattering interactions of the charge- or conduction carriers.

A basic description of the electrical resistivity $\rho(T)$ follows from the so called *Drude* formula.

$$\rho = m/ne^2\tau, \tag{2.30}$$

where e is the electron charge and τ is the relaxation time for scattering processes. This relaxation time describes the particular scattering events which are subject to the conduction electrons. Theoretically, the relaxation time follows from the velocity of the conduction electrons $\vec{v}$, which are scattered after a certain mean free path.

The relaxation time for simple metals is mainly determined by:

- scattering processes of conduction electrons on static lattice imperfections like impurity atoms, grain boundaries, and
- scattering of the conduction electrons on thermally excited lattice vibrations (phonons).

In a first approximation both scattering processes can be considered as independent from each other (Matthiessen's rule). The temperature dependence of the electrical resistivity $\rho(T)$ of simple metals is then given by:

$$\rho = \rho_0 + \rho_{\mathrm{ph}}, \tag{2.31}$$

where ρ_0 and ρ_{ph} result from scattering processes on impurities and phonons, respectively.

Usually, the interaction of conduction electrons with lattice imperfections is temperature invariant, while the that with thermally excited lattice vibrations leads to a pronounced temperature dependence. Using a variational type calculation in the scope of the linearized Boltzmann equation results in the so called Bloch-Grnüneisen relation:

$$\rho_{\mathrm{ph}} \sim \Theta_{\mathrm{D}} \frac{T^5}{\Theta_{\mathrm{D}}^5} \int_0^{\frac{\Theta_{\mathrm{D}}}{T}} \frac{z^5 dz}{(\exp(z)-1)(1-\exp(-z))}. \tag{2.32}$$

Assuming the low- and high-temperature limit, the electrical resistivity of a simple metal is found to be proportional as follows:

- $T \longrightarrow \infty$, $z << 1 ... T >> \Theta_{\mathrm{D}}$: $\rho_{\mathrm{ph}} \sim T^5$
- $T \longrightarrow 0$, $z >> 1 ... T << \Theta_{\mathrm{D}}$: $\rho_{\mathrm{ph}} \sim T$

In magnetic systems an interaction of conduction electrons with magnetic moments takes place, a further resistivity term $\rho_{\mathrm{mag}}(T)$ has to be considered. If only local magnetic moments are considered, as it is almost perfectly the case for the $4f$ moments of the rare earth elements, a perturbation type calculation in the scope of the Heisenberg model ($H = -J.\vec{s_{4f}}.s$) yields a temperature independent expression for the paramagnetic temperature range.

In the ordered state the spins are treated independently from each other. $\rho_{\mathrm{mag}}(T)$ is determined from the so called deGennes factor:

$$(g-1)^2 j(j+1), \tag{2.33}$$

where g is the Landé - factor and j the total angular momentum of the magnetic ion. J is the coupling constant between the conduction electron spin and the spin total angular momentum of the magnetic ion.

If, e.g., a ferromagnetic spin wave dispersion relation is taken into account, one obtains $\rho_{\mathrm{mag}}(T) = AT^2$ (A represents a constant). Figure 2.5 shows the schematic temperature dependence of the electrical resistivity of all mentioned scattering processes.

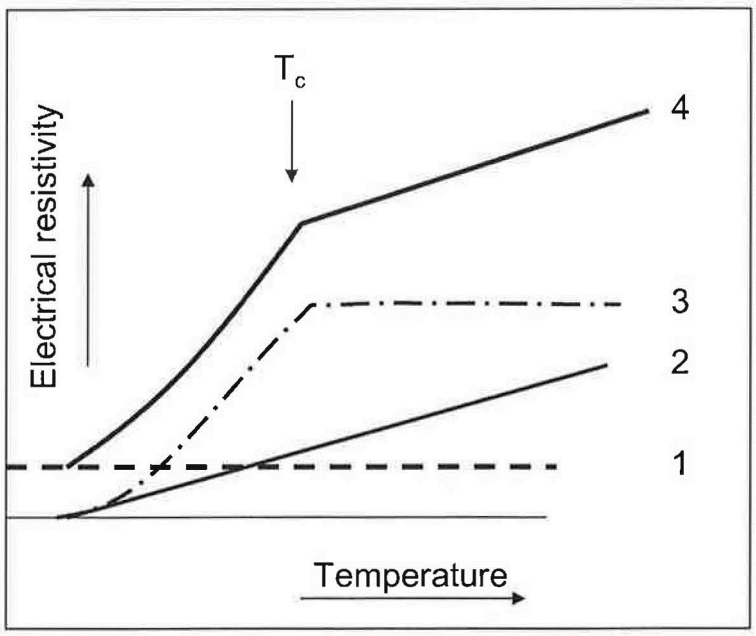

Figure 2.5: The contributions to the electrical resistivity of a metal with magnetic ordering. 1 - scattering due to impurities, 2 - phonon contribution, 3 - spin disorder scattering, 4 - total electrical resistivity.

2.4.2 Magnetoresistance in nonmagnetic metals

Magnetoresistance is the property of some materials to change the value of their electrical resistance when an external magnetic field is applied to them. The effect was first discovered by William Thomson in 1856, but he was unable to lower the electrical resistance of anything by more than 5%. This effect was later called ordinary magnetoresistance (OMR).[11]

External magnetic fields influence significantly the temperature dependence of transport coefficients. The change of the electrical resistivity parallel or perpendicular to an applied magnetic field is known as magnetoresistance. It is usually expressed as $\rho(B)/\rho(B)$. Here, $\rho(B)$ and $\rho(0)$ are the field and the zero-field resistivities reduced, by the residual resistivity, respectively.

Applying magnetic field in a particular direction, and measure the d.c. conductivity or resistivity the sections of the Fermi surface, normal to the field direction contribute dominantly.

In low magnetic field, the magnetoresistance is an average over the whole Fermi surface, regardless of whether the small areas through which electrons move before they are scattered are parts of the closed or open orbits. In high magnetic fields, there is a crucial difference between the closed and open orbits, respectively.

Inspecting the resistivity in the direction perpendicular to the applied field, it tends to

[11]Beside the OMR, the so-called giant MR, GMR occurs in magnetically inhomogeneous media containing nonaligned ferromagnetic entities on a microscopic scale. The GMR is determined by the orientations of the magnetization axes, the density, and the size of the ferromagnetic entities[24]. Recently, inter-grain tunneling magnetoresistance (TMR), reflecting high spin polarization of the carriers has been observed [25].

saturate at high magnetic fields. Contrary, the resistivity of an open orbit increases without limit, proportionally to H^2.

In experiments, the change of resistance is usually proportional to H^2 for small fields, but at high fields it can rise faster than H^2, increase linearly with H, or tend to a constant (that is, saturate), depending on the material. In most nonmagnetic solids the magnetoresistance is positive.

2.5 Specific heat in metallic systems

The total specific heat of a metallic system consists of several additive contributions:

- electronic (C_e)
- lattice (phonon)(C_ph)
- magnetic (C_mag)
- nuclear (C_n)

The nuclear part of the specific heat is related to the hyperfine interaction of the $4f$ shell with the nuclear moment of the $4f$ ion and is only significant at low temperatures for most of the $4f$ ions (the largest contribution was observed in Ho compounds [26], for RE=Y, Lu, Sm and Tm is negligible).

$$C = C_\mathrm{e} + C_\mathrm{ph} + C_\mathrm{mag} \tag{2.34}$$

It is obvious, that the experimental specific heat contains a lot of information about the system. The problem is, how to separate and classify the particular contributions. Each contribution and its origin are described in this section.

2.5.1 Electronic part

When the temperature raises to T, the energy of all electrons is not increased by the amount $k_\mathrm{B}T$, but only a fraction of the order of $k_\mathrm{B}T/E_\mathrm{F}$ is affected. Thus, the extra energy per unit volume is

$$\delta W \sim \frac{k_\mathrm{B}T}{E_\mathrm{F}} n k_\mathrm{B} T. \tag{2.35}$$

This is equivalent to a specific heat of the form

$$C_\mathrm{e} = \frac{\partial(\partial W)}{\partial T} \sim \frac{2nk_\mathrm{B}^2 T}{E_\mathrm{F}} = \gamma T. \tag{2.36}$$

The electronic contribution to the specific heat is thus

- not constant, but linear in T
- smaller by a factor like $k_\mathrm{B}T/E_\mathrm{F}$ than the classical specific heat $\frac{3}{2}nk_\mathrm{B}$.

All the electronic states are either completely full, or completely empty, except those in the range of energy of width $k_B T$ about the Fermi level. The number of states in this range is about $(k_B T/E_F)n$, where n is the number of electrons per unit volume.

More generally, we can express this number as $k_B T N(E_F)$, where $N(E_F)$ is the density of states function. Then the electronic specific heat must be proportional to:

$$C_e = \frac{\pi^2}{3} k_B^2 T N(E_F) \tag{2.37}$$

so it measures quite directly the value of the density of states at the Fermi level.

A large value of $N(E_F)$ may arise for two different reasons.

- It may be that the Fermi surface is very distorted. Where it bulges and approaches the Brillouin zone boundaries, electron velocity tends to become quite small, giving a large contribution to the integral:

$$N(E_F) \propto \int \frac{dS_F}{v} \tag{2.38}$$

  where v is the magnitude of the electron velocity on the element dS_F of Fermi surface.

- The strong many-body effects reduce the velocity at the Fermi level, even if there would be no crystal lattice.

In practice the Sommerfeld γ coefficient is determined from the experimental data fitting the linear dependence of the low temperature part in C/T vs. T^2 representation.

2.5.2 Phonon part

The amplitude of the thermal vibration, hence the amount of scattering electrons, depends on the temperature and is described with the theory of the lattice specific heat. The thermal vibrations of a crystal lattice are not simply independent oscillation of the individual atoms, as if each were isolated from its neighbors. To treat them properly, the collective vibrations of the crystal are analyzed as the travelling waves, like ordinary sound waves though of much shorter wavelengths. These waves are quantized in momentum and energy and have properties analogues to the photons of the electromagnetic field. They are called phonons.

Four different kinds of phonons can be found in a crystal and are summarized in Table 2.1. Dependence of the phonon frequency on the $\vec{k}$-vector, resp. the direction of dispersion in the $\vec{k}$-space describes the so-called dispersion law, which is characteristic for each phonon branch. The phonon dispersion is fundamentally defined with the space group of symmetry of the unit cell, all the phonon modes can be in principle derived from the knowledge of the basic symmetry of matter.
[12]

Two well-known models were proposed to describe the lattice vibrations in solids: **Einstein** and, more complicated, **Debye** model.

[12]It is important to mention that the local symmetry represented with the point group of the special site symmetry provide general relations used for prediction and possible explanation of all symmetry-driven properties of all solid-state systems, not only symmetry of phonon vibrations.

Phonon branch type	Vibration mode	No. of modes per unit cell	starting point at k-space
acoustic	longitudinal transversal	$3N$ for all acoustic	(000)
optical	longitudinal transversal	$(3n-3)N$ for all optical	given by the symmetry of the unit cell vibration

Table 2.1: Phonon modes in a general crystal lattice. n is the number of atoms per unit cell, N is the number of wave vectors valid for one Brillouin zone.

- The specific heat of the ideal crystal within the Einstein model is finally described:

$$c_{\mathrm{phE}} = 3Nk_{\mathrm{B}}\left(\frac{\Theta_{\mathrm{E}}}{T}\right)\frac{e^{-\Theta_{\mathrm{E}}/2T}}{(1-e^{-\Theta_{\mathrm{E}}/T})^2} \tag{2.39}$$

- Formula for the phonon specific heat according to the Debye model is given by:

$$C_{\mathrm{phD}}v = \frac{9NRT}{\Theta_{\mathrm{D}}}\int_0^{\Theta_{\mathrm{D}}/T}\frac{x^4e^x}{(e^x-1)^2}dx \tag{2.40}$$

The comparison of the specific heat according to both proposed models is depicted in Figure 2.6.

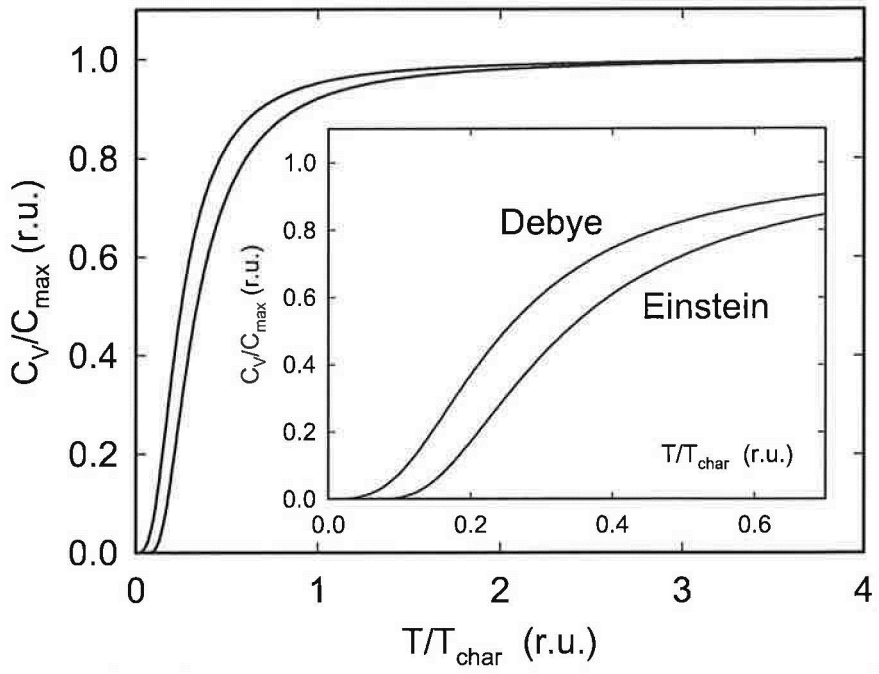

Figure 2.6: Comparison of the calculated specific heat related to the Einstein and Debye model.

Anharmonicity

Behavior of a real crystal lattice does not completely correspond to the theoretical models. First, the real crystal changes its volume with temperature, which omit the harmonic approximation grounding the ideal state. This phenomenon is called the thermal expansion and its origin is generally known as an anharmonicity.

Moreover, there are principally two types of phonon branches: low-energy acoustic phonons and optical phonons as the vibrational states populated in higher energy levels. Debye model describes the acoustic phonon branches (3 × degenerated) while the Einstein model is useful to characterize the optical phonons (3N-3 modes). Specific parameters for each phonon mode are Θ_D and Θ_E, respectively. As both models postulate the harmonic oscillators, they do not consider thermal expansion and thus describe the isochoric specific heat. In reality, the volume changes with temperature and we measure the isobaric specific heat - C_p. Therefore, the anharmonicity corrections must be involved.

The total phonon specific heat is then expressed as:

$$C_{ph} = R\left(\frac{1}{1-\alpha_D T}C_D + \sum_{i=1}^{3N-3}\frac{1}{1-\alpha_E T}C_e\right), \tag{2.41}$$

where α_D and α_E is the anharmonic term for acoustic and optical phonon branches, respectively, according to [27]. The plot of the correction to the total specific heat is shown in

Figure 2.7. [13]

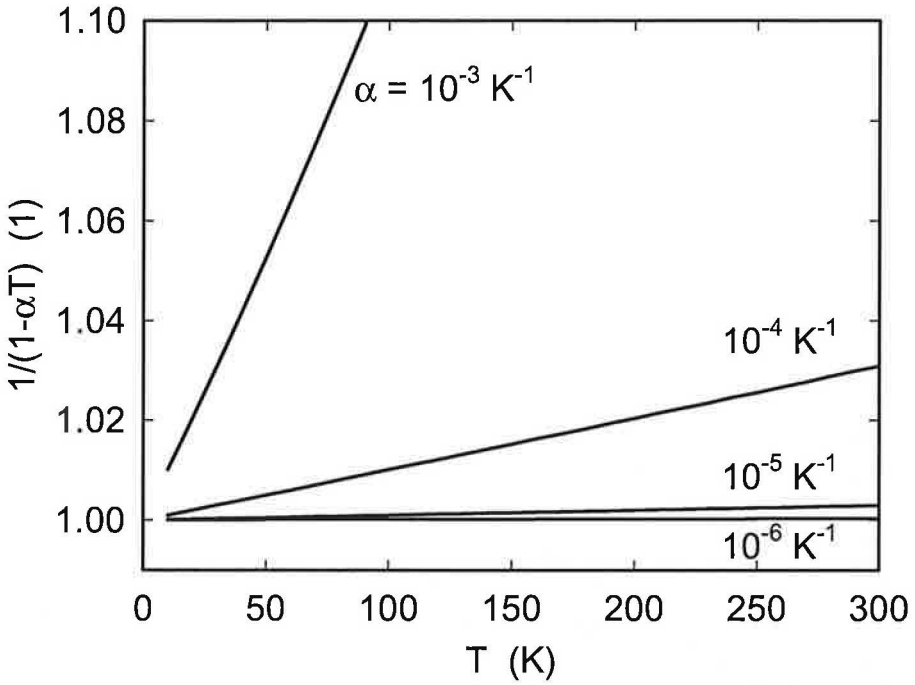

Figure 2.7: Contribution of the anharmonicity to the total specific heat. It is evident, that a significant effect is present in higher temperature region.

2.5.3 Magnetism and crystal field effect in the specific heat

A magnetic contribution to the specific heat is associated with the increasing population of the excited localized states. These localized states are caused by the crystal-field and molecular field interactions with the $4f$-ion which lift the $(2j+1)$-fold degeneracy of the ground-state multiplet.

However, it is difficult in general to separate the magnetic part from the other contributions. The so-called nonmagnetic analogues (isostructural compounds with nonmagnetic rare-earth ion) are taken as a reference for the nonmagnetic part of the specific heat (as described in previous section).

The crystal field effect, if takes place contributes to the specific heat as a n-level system, described by the Schottky formula:

$$C_{\mathrm{Sch}} = \frac{R}{T^2}\left(\frac{\sum_{i=0}^{n}\Delta_i^2 \exp[-\Delta_i/T]}{\sum_{i=0}^{n}\exp[-\Delta_i/T]} - \left(\frac{\sum_{i=0}^{n}\Delta_i \exp[-\Delta_i/T]}{\sum_{i=0}^{n}\exp[-\Delta_i/T]}\right)^2\right) \tag{2.42}$$

[13] To reduce the number of free parameters in the fitting procedure, phonon modes are grouped to the $n\times$ degenerated phonon branches described with the characteristic temperature Θ_{D} or Θ_{Ei} and anharmonicity constant α_{D} or α_{Ei}, respectively. The degeneracy is given by the space group of the crystal structure, so the most probable superpositions of phonos is preferentially tried out.

where Δ_i means the energy of crystal-field level splitting.

The crystal field removes the degeneracy of the ground state multiplet according to the Kramer's theorem:

No matter how unsymmetrical the crystal field is, an ion possessing an odd number of electrons must have a doublet as a ground state.

2.6 Electronic correlations in solids

2.6.1 Interaction energy (Hubbard model)

The simplest model to investigate correlated electrons is the Hubbard model, introduced in 1963. It describes exclusively mobile electrons. Usually one electron per atom is assumed. The ions form the lattice. There are only two items: i) the kinetic energy of the electrons and ii) a simplified type of interaction.

The kinetic energy describes the movement of the electrons: Spin up and spin down electrons are allowed to hop from one to another lattice site under the constraints of the Pauli principle. For the present subject it requires that a lattice site can be two-fold occupied only if both electrons have different spin orientations. A certain lattice site is thus: i) empty, ii) occupied either with an spin up electron or a spin down electron or iii) occupied by a spin up and a spin down electron.

As a further simplification one assumes that the repulsion between electrons decays rapidly, i.e., the repulsion is of a negligible value only if a spin up electron is on the same site like the spin down electron. The thus created interaction energy adds up to the kinetic energy and increases therefore the total energy. This interaction energy is proportional to the number of double-occupied lattice sites.

In the first view one would assume that the energy lowers if there are not any doubly occupied lattice sites - consequently with no additional interactions. However, this would cause a dramatic constraint to the movement (hoping) of electrons, in particular with respect to the twofold occupied sites. In such a case, the mobility of electrons is substantially reduced, unfavorable regarding to the energy. Hence, the kinetic - and the interaction energy have to be optimized together. For having a reasonable mobility of electrons, interactions have to be allowed at an appropriate scale. The Hubbard model is the most simplest model of correlated electron systems and studied since many years (Figure 2.8).

Although many simplifications have been made, it represents a complex problem in quantum mechanics, which exactly is not solvable. In general one has to consider additionally the temperature of the system, the electron density or the particular structure of the lattice, hence much more difficulties arise.

Ferromagnetism is not well accounted for by this model, in spite of the fact that there the interaction energy becomes exactly zero. The reason is that electrons are not allowed to hop if all the spins are aligned. Rather an antiferromagnetic arrangement of spins is better described by the Hubbard model since in such a scenario electrons may always find a possibility for a hoping process.

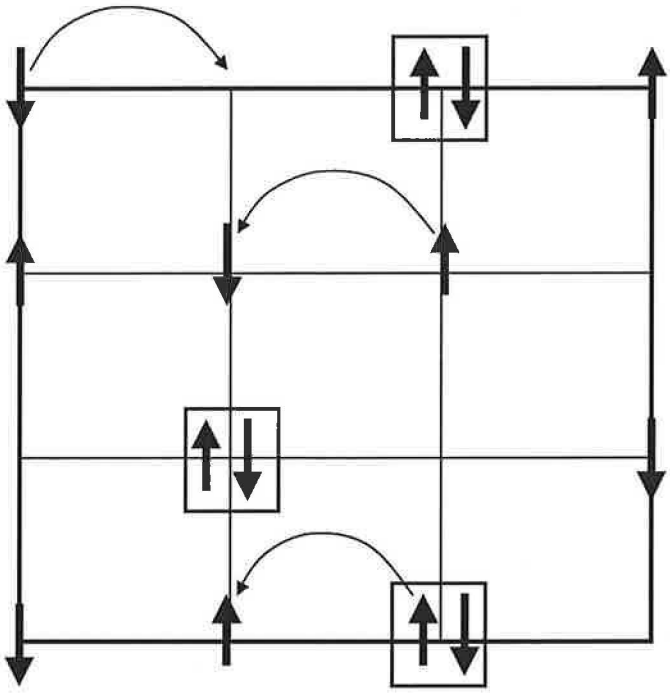

Figure 2.8: Schematic representation of electron occupation and allowed hopping in the frame of the Hubbard model.

2.6.2 Fermi liquid vs. non-Fermi liquid

In 1956 Landau introduced a phenomenological theory for the macroscopic properties of an interacting normal fermion system at low temperatures: *Fermi liquid theory.* The theory accounts also for the spin compensated state of a Kondo system at low temperatures. The eigenstates of the non-interacting electron gas and those of the interacting liquid are equalized. The interaction between the electrons leads to increase of their effective mass (the so-called mass renormalization). Many-body systems have excitations that behave like free elementary particles but are actually very complicated in their nature, which hides possibly large effects of interparticle interaction. Landau proved that at sufficiently low temperatures an interacting ensemble of Fermi particles such as electrons or ^{3}He atoms behaves as it were composed of weakly interacting free fermions, with a well defined sharp Fermi surface, and a constant mass and a spin susceptibility (not equal to the free-electron one). He introduced a quasiparticle distribution function ($n(p,\sigma)$, where p is the momentum and σ is the spin of a quasiparticle), and assumed that overall distribution function differs very little from the value for a perfectly free Fermi gas at $T \longrightarrow 0$:

$$\begin{aligned} n_0(p,\sigma) &= 1, p < p_F \\ n_0(p,\sigma) &= 0, p > p_F \end{aligned} \tag{2.43}$$

where n_0 is the occupation of the ground state and p_F is the Fermi momentum. The Fermi liquid is characterized by a discontinuity at $k = k_F$ (see Figure 2.9).

This discontinuity can be represented by the so called quasiparticle weight z according

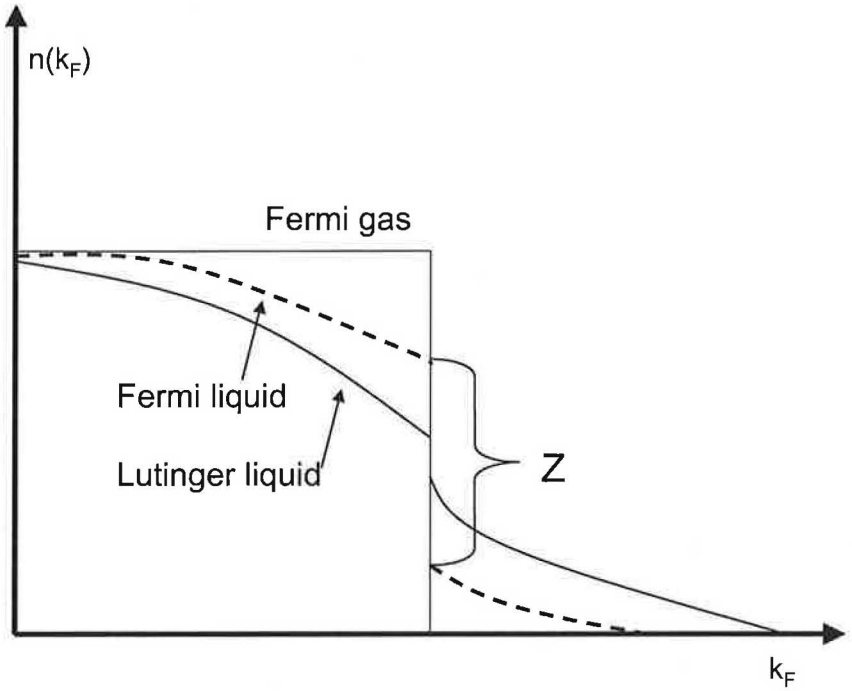

Figure 2.9: Comparison of the density of states for the Fermi gas, Fermi liquid and Lutinger liquid, respectively.

to $0 \leq z \leq 1$. As z decreases from 1 towards zero, the interaction strength within the Fermi liquid starts to grow. Accordingly the particle mobility decreases corresponding to the mass enhancement.

The concept has been generalized to many other situations, one of the most important being the BCS theory of superconductivity. By very general arguments it has been shown that the very lowest-energy excited states of any such system will usually take on the very simple form of an apparently noninteracting gas of free objects, which can be bosons, fermions or both. The expression for the specific heat and magnetic susceptibility are given within the frame of the Landau theory introducing the so-called dimensionless Landau parameters F_l^λ, where $\lambda = s(a)$ refers to the symmetric or antisymmetric parts of the interaction.

The temperature independent Pauli susceptibility of the interacting Fermi liquid is given by:

$$\chi = \widetilde{S}\chi_0 \tag{2.44}$$

where χ_0 is the Pauli susceptibility of the non-interacting system and the enhancement factor, $\widetilde{S}$ is given by:

$$\widetilde{S} = \frac{m^*/m}{1 + F_0^a} \tag{2.45}$$

The specific heat in the scope of the interacting Fermi liquid can be written as the sum of a phonon term, an enhanced linear term and a $T^3 \ln T$-term. The enhanced linear term accounts for the specific heat of the quasiparticles and the $T^3 \ln T$-term follows from a

contribution due to a small momentum transfer between the quasiparticles:

$$C = \gamma^* T + \beta_{ph} T^3 + \delta T^3 \ln(T/T^*) \tag{2.46}$$

Here, γ^* is the enhanced linear coefficient, β_{ph} is the usual phonon coefficient ($T << \Theta_D$), δ is the coefficient of the pure $T^3 \ln T$-term and $\delta \ln T^*$ is the coefficient of the spin fluctuation contribution. T* is often denoted as spin fluctuation temperature.

Numerous experimental investigations of systems near to the magnetic instability show that the low temperature behavior does not follow that power-laws in temperature which are associated with a Fermi liquid. Recently these systems have been termed as non-Fermi liquid systems. Their characteristic behavior results from the unusual features of the momentum distribution function near to the Fermi energy.

One of the well-known examples is the $CeCu_{6-x}Au_x$ [28]. The system is driven from a nonmagnetic state in the Au-free case to a magnetically ordered state for $x = 0.3$. The former case is characterized by an almost temperature independent value of $C/T \longrightarrow 0$, reflecting clearly the Fermi liquid state at low temperature. The γ value itself is three order of magnitude larger than usually observed for simple metals. On the other hand, just at the border between the nonmagnetic and the magnetic state (x = 0.1) C/T vs. T varies according to $-\ln(T/T_0)$ where T_0 is some characteristic temperature. This logarithmic dependence of the specific heat is usually considered as a typical evidence of the non-Fermi liquid behavior.

2.6.3 Scattering by an isolated magnetic impurity - the Kondo effect

Let us consider a magnetic impurity dissolved statistically in a host metal like Fe in Cu. The most important (and most simplest) way to observe the anomalous behavior of such systems is an increase of the electrical resistivity when the temperature is lowered. This phenomenon was unexplained for a long time and solved finally by J. Kondo in 1964 [29].

Kondo set out the crucial facts:

- The low temperature anomalies result from magnetic impurities.
- The depth of the minimum is proportional to the impurity concentration.
- The value of the resistivity minimum itself is also proportional to the impurity concentration; therefore $\delta\rho/\rho_{\min}$ is concentration independent.
- The temperature of the resistivity minimum is almost independent on the impurity concentration.

The listed points suggest that the phenomenon does not occur due to interactions between the impurities.

Kondo found that by considering not only the first-order but also the second-order scattering processes, the scattering of the conduction electrons by the magnetic impurity becomes temperature dependent. The second-order scattering entails a two-stage process.

In the first stage, the electron is scattered into an intermediate state by the magnetic impurity which likewise makes a transition into its intermediate state. In the second stage,

the impurity is restored to its original state and the conduction electron is scattered into its final state.

Moreover, the scattering to the intermediate state by the impurity may entail a spin flip of the conduction electron and a compensating spin change of the impurity. In going to the final state the impurity reverts to its initial state and the conduction electron reverts to its initial spin direction. It turns out that only those processes that involve these spin changes contribute a temperature dependence to the scattering.

Finally, it should be noted that of the processes involving a spin flip there are always two coherent second-order scattering processes that must be taken together. In the first, an electron is scattered by the impurity to its intermediate state and then scattered to its final state. In the second, the order of these events is reversed. An electron is scattered to its final state and then another electron is scattered into the vacant state so created. The described scattering processes are schematically described as follows[14]:

Conduction electrons	Magnetic ion
$k_{\text{up}} \longrightarrow q_{\text{down}}$	$m_s \longrightarrow m_s + 1$
$q_{\text{down}} \longrightarrow k'_{\text{up}}$	$m_s + 1 \longrightarrow m_s$
$q_{\text{down}} \longrightarrow k'_{\text{up}}$	$m_s \longrightarrow m_s - 1$
$k_{\text{up}} \longrightarrow q_{\text{down}}$	$m_s - 1 \longrightarrow m_s$

k, q, k' are the wave vectors of the initial, intermediate, and final electron state, respectively. m_s is the z-component of the impurity spin.

Taking into account all described events by means of the scattering theory, the temperature dependence of the electrical resistivity can be finally expressed as:

$$\rho_{\text{imp}} = \frac{const.J^2_{s-d/f}s(s+1)}{E_{\text{F}}}(1 - 4N(E_{\text{F}})J_{s-d/f}\ln(k_{\text{B}}T/const.)), \tag{2.47}$$

where $J_{s-d/f}$ represents the exchange coupling arising from the s-d or s-f model, respectively, and is assumed to be negative (antiferromagnetic).

Finally, the electrical resistivity of the diluted magnetic system , including the phonon contribution can be written as:

$$\rho \sim aT^5 + c_{\text{imp}}\rho_0 - const.c_{\text{imp}}\ln T, \tag{2.48}$$

where c_{imp} is the impurity concentration. The first represents the phonon scattering, the second one corresponds to the impurity term and the third one describes the magnetic scattering involving spin-flips.

This relation exhibits a minimum at finite temperatures (setting $d\rho/dT = 0$):

[14]An electron is scattered from k'_{up} to k_{up} with a spin flip in the intermediate state q. But in the first process, the z-component of the impurity spin is increased by 1, while in the second it is decreased by 1. This is the crucial point because the transition probabilities of both scattering events are different. For the first process to be possible, the intermediate state q must be empty. The probability of this is given by 1-$f_0(q)$, where f_0 is the Fermi function. For the second process the q state must be occupied. The probability of this is therefore f_0.

$$T_{\min} \sim c_{\text{imp}}^{1/5} \tag{2.49}$$

Kondo's treatment yields therefore a convincing qualitative explanation of the temperature dependent resistivity of diluted magnetic systems. However, the perturbation type calculation breaks down for $T \longrightarrow 0$, since the $\ln T$ term diverges. The disjunction between the experimental evidences and the proposed model is known as the Kondo problem.

2.6.4 Kondo problem against the experimental results

To eliminate the unphysical divergencies of various quantities for $T \longrightarrow 0$, Abrikosov suggested to sum up the logarithmic terms to higher order.[15]

$$k_{\text{B}}T_{\text{K}} \approx \exp(-1/2|J_{s-d/f}|\rho_0) \tag{2.50}$$

The finite temperature of resistivity divergence is usually called Kondo temperature T_{K}. This divergence, however, is unphysical since at $T = T_{\text{K}}$ there is no real phase transition. An expected phase transition is suppressed from very strong fluctuations. An expression with similar structure compared to equation 2.50 appears for example also in case of superconductivity.

All interaction mechanisms and microscopic parameters are summed up in a single characteristic energy or temperature. Most of the physical properties are then characterized by a scaling law. The energy gain of the order of $k_{\text{B}}T_{\text{K}}$, realized from a singlet formation, is in fact the essence of the Kondo effect. Schematically, this is depicted in the Figure 2.10 showing that the magnetic triplet state, built from the conduction electron spin and the impurity spin $s_{3d/4f} = 1/2$ is situated by $k_{\text{B}}T_{\text{K}}$ above the nonmagnetic singlet ground state.

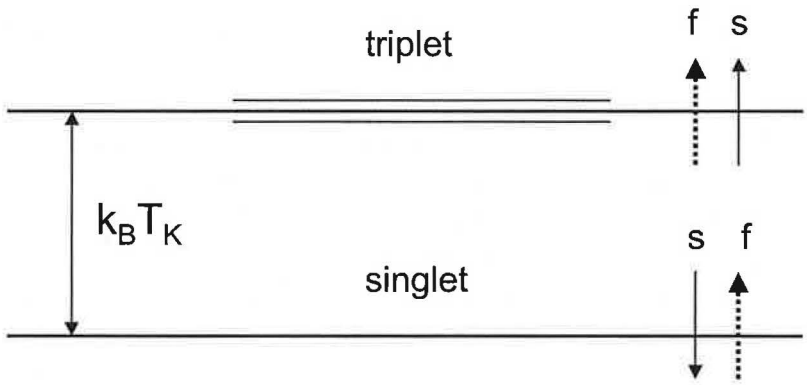

Figure 2.10: Separation of electronic states in the Kondo model.

Further sophisticated approaches yielded more realistic agreement with the experimental results. Since the impurity spin disappears for $T < T_{\text{K}}$, the specific heat, the magnetic

[15] A general n-th order perturbation theory gives $\ln T$ contributions of the form $(J_{s-d/f}\rho_0)n(\ln T)^m$ for $n > n_0$, $m \leq (n - n_0)$, where n_0 depends on the property being calculated. The leading order divergent terms for a given n corresponds to $m \leq (n - n_0)$. Since the logarithmic terms are summed up within a power series, they appear just in the denominator. For antiferromagnetic interaction the denominator diverges at finite temperatures!

susceptibility and the electrical resistivity can be calculated from a phenomenological theory for a nonmagnetic impurity with resonance scattering and interacting electrons (Fermi liquid, discussed further). The most important result is that all $\ln T$-singularities have been disappeared and the physical quantities follow a simple power law in T.

2.6.5 Heavy fermion phenomenon

Introduction

Within the last two decades various metals have been found to own heavy electrons which consequently are termed as heavy fermion systems or heavy electron systems. The carriers responsible for the electrical current (electrons or holes) are found to have masses up to several hundred times the mass of free electrons in simple metals. However, this appearance can be found only at low temperatures. At high temperatures the systems behave like normal magnetic metals.

Heavy electron systems usually contain rare earth elements like Ce or Yb or actinides like U. These materials exhibit partly filled $4f$ or $5f$ shells. Cerium and ytterbium possess the $4f$ shell which is occupied by 1 or 13 electrons, respectively, so the one electron of Ce in case of Yb a hole appears to be unstable and fluctuations of the spin and/or of the valence part into the conduction band may easily occur.

These fluctuations are considered as origin of the low temperature anomalies. They behave at high temperatures like the f-electrons are completely localized, which is already well known from stable rare earth intermetallic compounds (Nd, Gd, Tb ...). However, while the latter show in general a phase transition into a magnetically ordered ground state the former crosses over at low temperatures to a behavior known only from simple metals, like a temperature independent Pauli susceptibility or a temperature independent Sommerfeld term of the specific heat, with the exception of strongly renormalized masses (= enhanced effective masses).

Such behavior can be described phenomenologically in terms of the Fermi-liquid model. Moreover, the discovery of heavy electron superconductivity below 0.6 K in $CeCu_2Si_2$ enforced the study of unconventional ground states with anisotropic gaps in the electronic density of states and a coupling of Cooper pairs by magnetic fluctuations.

As already mentioned, the heavy electrons of these systems behave at low temperatures like the electrons of simple metals. Primarily two quantities can reflect this findings: the electronic contribution to the specific heat, γ and the magnetic susceptibility, χ below about 10 K.

Like in simple metals, this quantities are constant in the case of heavy electron systems. Moreover, the ratio γ/χ (Wilson ratio) yields again a constant in both cases of the same order of magnitude although each of the quantities is drastically different in plain and in heavy electron systems.

Diluted Kondo systems

The simplest models for heavy electron systems take into account s- and p-electrons as conduction bands and the localized f electrons have a strong repulsion for double occupancy

on the same lattice site. A transfer (fluctuations) of both charge and spin is possible between the localized f electrons and the delocalized conduction electron system. The strength of this hybridization Γ is described via Fermis golden rule (2.51).

$$\Gamma = \pi V^2 N(E_F) \tag{2.51}$$

Here, V is an average of the hybridization matrix element and $N(E_F)$ is the electronic density of states at the Fermi energy. Depending on the value of Γ in comparison to the binding energy E_0 of the unperturbed $4f$ level, different regimes can be distinguished:

- $\Gamma << E_0$ - stable $4f$ shell: the hybridization and therefore a mixing of states is negligible. The magnetic properties follow then from the classical Heisenberg exchange and in case of rare earth also from crystal field splitting. In most of the cases long range magnetic order is observable.

- $\Gamma < E_0$ - Kondo regime: a comparable stable $4f$ state in comparison to $\Gamma \geq E_0$ occurs. Just small deviations from an integer valence state can be observed.For elevated temperatures Curie-Weiss behavior is found for the magnetic susceptibility, whereas a strongly enhanced Pauli susceptibility appears at low temperatures. This regime is known in the literature as Kondo regime.

- $\Gamma \geq E_0$ - intermediate valence regime: the system is characterized from a strong mixing of local and itinerant states. The hybridization causes therefore that the $4f$ states are unstable; consequently a nonmagnetic ground state follows. The valence found for these systems deviate strongly from an integer value.

An appropriate description of such a system follows from observations made on dilute magnetic alloys. There, the spin of the conduction electron couples with the spin of the impurity magnetic moment. If this exchange interaction is of antiferromagnetic nature, i.e., both spins are antiparallel, the magnetic moment associated with the magnetic impurity is lost (when seen from a distance apart) below a characteristic temperature T_K thus a singlet ground state is formed. This nonmagnetic singlet ground state is separated by an energy $k_B T_K$ from the magnetic triplet state. The interaction process is known as the Kondo effect.

The origin of the Kondo effect is therefore an energy gain of the order of $k_B T_K$ owing to the formation of a non-magnetic ground state.

Properties of the Kondo model have been calculated already in an exact manner and are corroborated by various experimental results. This model will be one of the main subjects of this lecture. If Ce or Yb systems are considered, a periodic arrangement of the $4f$ moments occurs. However, the overlap of the $4f$ wave function is small and therefore almost negligible. At high temperatures ($T \longrightarrow T_K$) these moments are independent from each other, hence the susceptibility shows Curie-Weiss behavior. At low temperatures ($T < T_K$) the conduction electrons hybridize with the $4f$ moments, causing a strong delocalization of the latter. A description has then to be done in the scope of extended metallic states.

Hoping of such electrons rarely occurs due to the strong Coulomb repulsion (strong correlations) for two electrons on the same lattice site. However, there are many possibilities for excitations of momentum states, inferring large effective masses.

Concentrated Kondo systems

As already discussed in the previous section, the extraordinary low-temperature properties owing to magnetic impurities in a non-magnetic host metal are observed only, if the impurity concentration is small. If elements like cerium, ytterbium or uranium are dissolved in simple metals than the unusual low temperature properties like a minimum in the temperature dependent electrical resistivity can be observed even for very high concentrations of such impurities. A resistivity minimum follows again for a negative exchange coupling.[16]

One of the most important properties of $4f$ systems is the small spatial extent of the $4f$ wave function (~ 0.5 Å), which is much smaller than that of $3d$ systems and exceed the typical lattice parameter in such compounds. As a consequence $4f$ function has no direct overlap with that of the neighboring ions. Therefore a much larger number of $4f$ impurity ions can be built into a metallic host without destroying the Kondo effect. Such systems are known as concentrated Kondo systems.

Origin of the Kondo resonance

Many of the unusual physical properties at low temperatures can be related with the so called Kondo resonance, or equivalently Abrikosov-Suhl resonance, which can be attributed to the singlet formation of the $s_{4f} = 1/2$ impurity.

The almost localized $4f$ electrons carry spin and orbital angular momenta. However, owing to the hybridization, $4f$ electrons may escape into the continuum of the conduction band and may 'exchange' their orbital and spin quantum numbers with the conduction electrons. This exchange process contains an intermediate state with no or two $4f$ electrons and is accompanied by an electron-hole excitation.

This electron-hole excitation can have arbitrarily small energies and are therefore the origin of all the logarithmic divergences in the perturbation type calculations with respect to V and J. This logarithmic behavior is a precursor of the loss of the spin degrees of freedom owing to the singlet formation at low temperatures.

The spin compensation due to the Kondo effect however can not be seen only as a local effect, rather there is characteristic screening length ($v_F/k_B T_K \approx 10^3$Å). If there is a spin exchange between $4f$ electrons and the conduction electrons, then a spin relaxation of the impurity is observed. According to perturbation type calculations, the spin relaxation is proportional to the temperature (the so-called Korringa law) as a consequence of a stable spin moment with unlimited life time.

The spin compensation at low temperature requires, however a finite relaxation rate of the order of T_K for T close to zero. This fact is described in the literature as a crossover from 'asymptotic freedom' to 'infrared slavery'.[17]

[16] J. Coqblin et al. (1969) could show that a description of the properties of magnetic cerium impurities (e.g. Ce_xLa_{1-x}) can be performed in both, the s - f interaction model as well as in the non-degenerate model of the Anderson Hamiltonian (for detailed concept of the Anderson model, please see e.g. [30]). Some equivalence of both models follows from the so called Schrieffer-Wolff transformation (1966)[32].

[17] In field theories such a behavior causes a dynamically mass-production and is known for many low dimensional systems. As a consequence of the singlet formation and the continuous excitation of the Fermi gas just simple power laws in T are observed for physical properties. Similar dependencies are observed for external fields and frequencies. As long as these external energies are smaller than $k_B T_K$, all the physical

Due to the singlet formation at low temperatures, the density of states of the $4f$ electrons, as resulting from the Anderson picture, will be modified. To compensate for the loss of degrees of freedom of the spin and the orbital moment, an extra density of states peak develops in the vicinity of the Fermi energy. This peak with an extremely large value of an effective density of states is responsible for the unusual low temperature behavior of the ion ($T < T_K$) and is known as the Kondo resonance.

This resonance is strongly temperature dependent and smears out with increasing temperature or with increasing magnetic fields if the Zeeman splitting approaches $k_B T_K$.

The electronic density of states at $T = 0$ therefore consists of 3 maxima (as depicted in the Figure 2.11): (a) a broad maximum at an energy ϵ_0 in the proximity to the bottom of the conduction band resulting from transitions of $4f$ electrons into the conduction band. (b) A very narrow many body resonance in the vicinity of the Fermi energy (Kondo resonance) and (c) an additional peak at $\epsilon_0 + U$, above the Fermi energy, corresponding to transitions from the $4f^1$ to the $4f^2$ state.

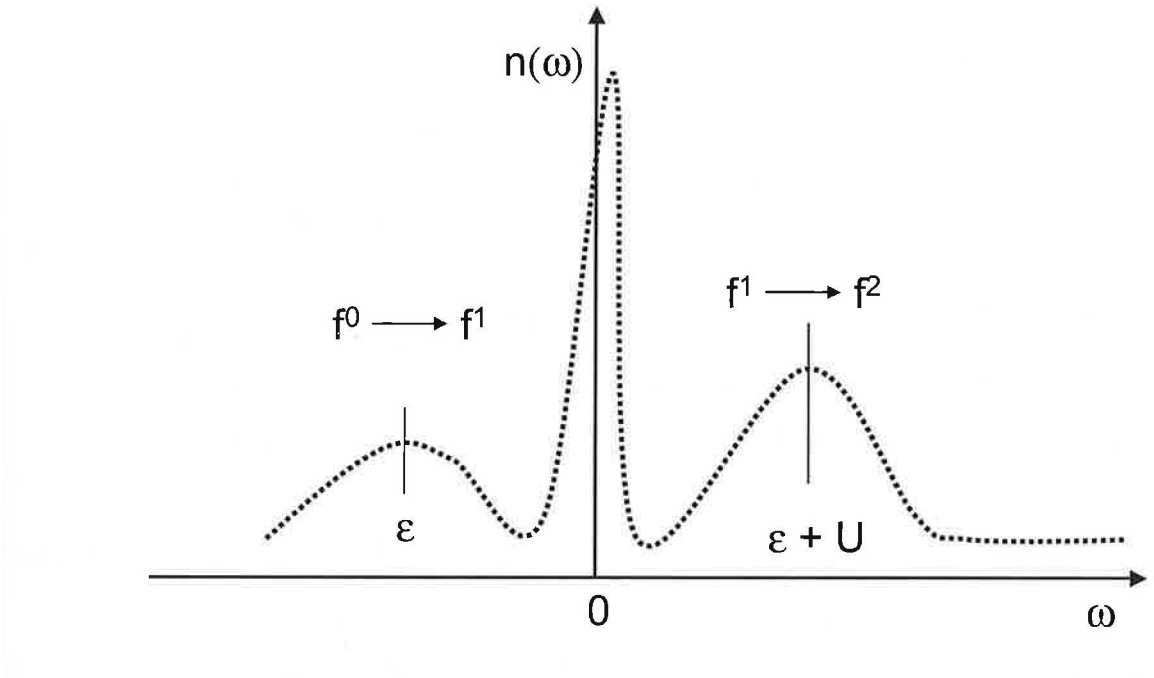

Figure 2.11: The density of states with the characteristic Kondo resonance.

Kondo lattice

Beside the important influence of the degeneracy of the ground state, which is determined by the spin-orbit coupling and by the crystalline electric field, a significant impact on the physical behavior at low temperatures is observed, if the magnetic impurities build up a regular sublattice in the crystal. Systems with this lattice periodicity are known as Kondo lattices and are described usually considering a model of Doniach [31].

properties can be accounted for in terms of the Fermi liquid model.

At high temperatures ($T > T_K$) all the physical properties are accounted for just by those models which have been developed for isolated single impurity systems. This implies that the different magnetic ions on the regular lattice site are decoupled from each other at elevated temperatures.

At low temperatures and in particular for transport properties, significant deviations from the single impurity Kondo behavior are observed. This can be seen most easily on the temperature dependence of the electrical resistivity as is depicted in the Figure 2.12.

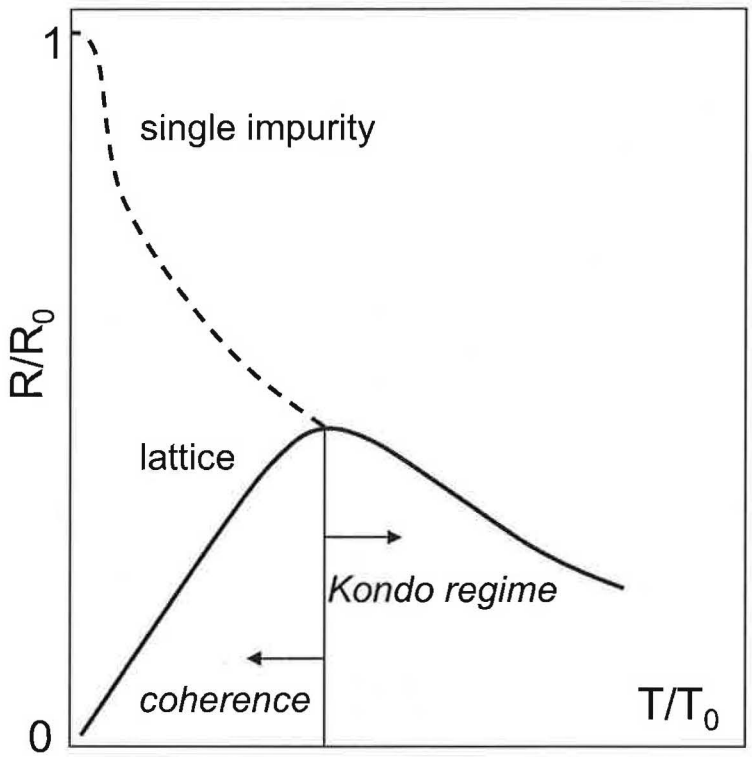

Figure 2.12: Comparison of the electrical resistivity of the single ion impurity and the Kondo lattice, respectively.

While the diluted impurity systems show the famous logarithmic increase of the resistivity towards lower temperatures, the lattice systems are characterized by a pronounced maximum below a certain characteristic temperature ($T_{\max,\rho} < T_K$) and by a strong decrease of $\rho(T)$ below this temperature.

This is explained from the strong correlations between the different scattering centers (having properties similar to that of a molecular field), causing that the conduction electrons can pass the periodic array of these centers in form of a Bloch wave. If the temperature decreases the arrangement becomes more perfect and the conditions for the Bloch waves are fulfilled; consequently the resistivity decreases further.

Due to the Fermi liquid ground state of the demagnetized system a T^2 behavior of the electrical resistivity is evident:

$$\rho = \rho_0 + AT^2 \tag{2.52}$$

The coefficient A has an unusual large magnitude and is proportional to the effective electronic density of states at the Fermi energy. Frequently, these systems are called therefore heavy fermions.

Thermodynamical quantities, however, are influenced from the lattice properties only at very low temperatures. The modifications of the physical properties due to the lattice periodicity of the Kondo scattering centers cause that a modified Hamiltonian has to be considered, which is known in the literature as periodic Anderson model (for details, please see e.g. [33, 34]).

Due to the periodicity of the Kondo lattice, a band of heavy quasi-particles is formed, with a typical band-width $\sim k_B T_K$. The related quasi-particle density of states shows a temperature dependent minimum in the Kondo resonance which increases with decreasing temperature (see Figure 2.13).

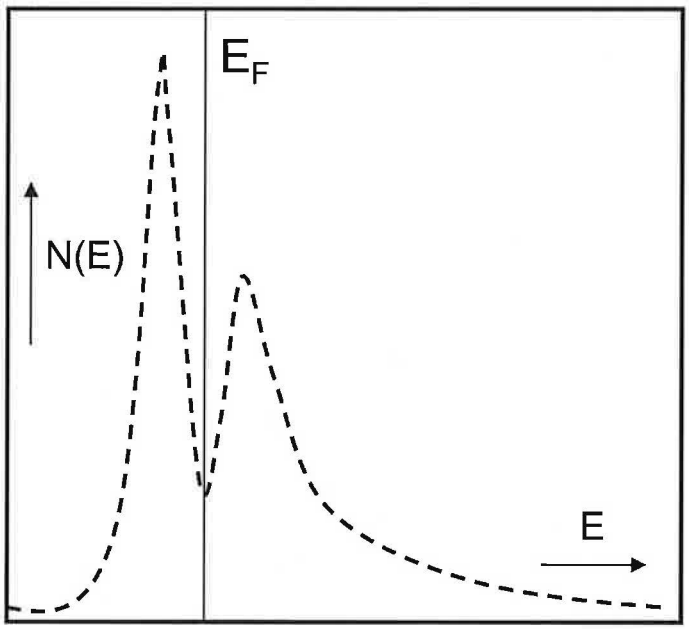

Figure 2.13: Density of states according to the Anderson model.

Magnetism in dense Kondo systems - Doniach diagram

Owing to the high concentration of magnetic moments in Kondo lattices, the interactions between the different lattice sites can no longer be neglected. Such interactions are in the case of $4f$ systems of the $RKKY$-type and are promoted by the conduction electron system. This means that the magnetic ion disturbs the wave function of the conduction electrons and a polarization of the spins of the conduction electrons happens in the proximity to the magnetic ion. This is originated from phase shifts of the Bloch waves of the conduction electrons and causes long-range oscillations. The moments of neighboring ions are influenced by this polarization and their response is an alignment of their moments.

The $RKKY$ interaction has an oscillating character, therefore shows both positive and negative values, i.e., the interaction can be of ferro - or antiferromagnetic nature. The

strength of the $RKKY$ interaction follows from:

$$T_{RKKY}/|JN(E_F)|^2 \tag{2.53}$$

while the Kondo interaction depends exponentially on $JN(E_F)$:

$$T_K \sim \exp(-1/|JN(E_F)|). \tag{2.54}$$

Doniach showed (in the scope of a molecular field approximation of the periodic Anderson model for 1-dimensional systems and for $j = 1/2$) the existence of a critical value $|JN(E_F)|_c$, which 'separates' a spin compensated state from a state with magnetic order [31]. A large value of the degeneracy of the ground state stabilizes therefore the Kondo state and spin-spin correlations are almost suppressed. The dependence of the Kondo interaction strength T_K and of the $RKKY$ interaction T_{RKKY} as functions of $|JN(E_F)|$ are depicted in the Figure 2.14.

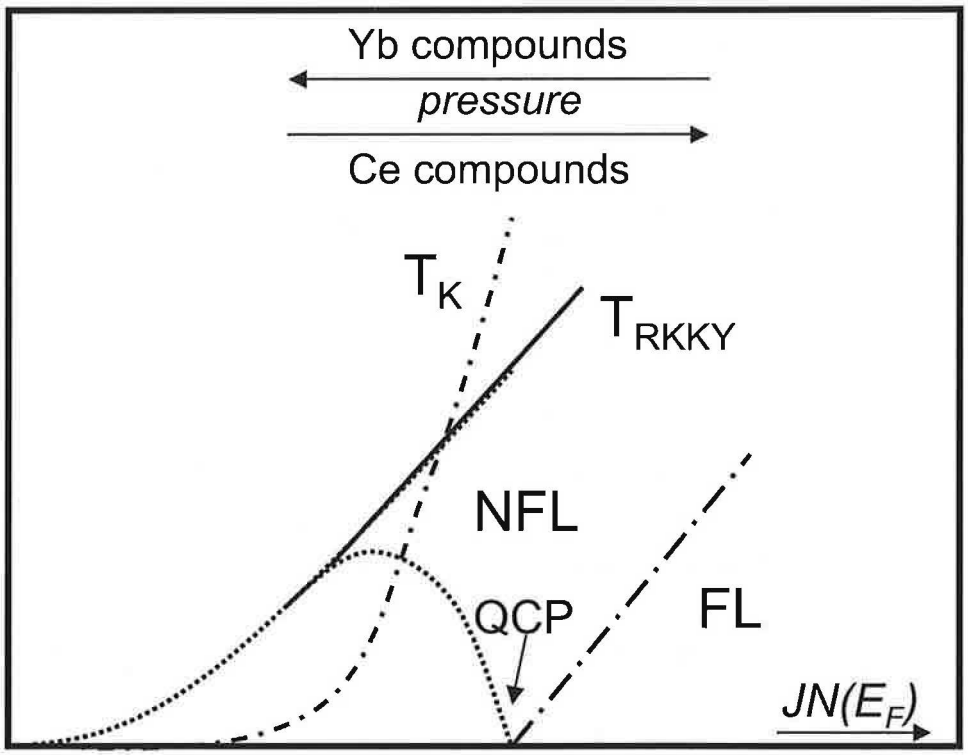

Figure 2.14: Doniach diagram.
NFL - non-Fermi liquid region, FL - Fermi liquid region, QCP - quantum critical point.

For small values of this parameter, the $RKKY$ interaction dominates. If the temperature of such systems is decreasing, the $4f$ moments order below the magnetic ordering temperature $T_{mag} \sim T_{RKKY}$. The moments are aligned and blocked and can therefore not participate in Kondo type spin-flip processes. Typical signs of the Kondo effect are not observed even at lowest temperatures.

On the contrary, if $|JN(E_F)|$ is large, then if the temperature decreases, a compensation of the magnetic moments happens roughly at temperatures $T_{mag} \sim T_K$. A singlet ground

state is formed. If the temperature further decreases, a long range magnetic order should occur at $T_{mag} \leq T_{RKKY}$. However, since all the magnetic moments are already screened, a magnetically ordered ground state becomes impossible.

The regime for intermediate values of $|JN(E_F)|$ is of major interest. Here we have $T_{RKKY} \sim T_K$ and the Kondo effect as well as long range magnetic order can set on simultaneously. The resulting magnetic structure can be very complicated and the observed ordered moments are smaller than those expected for the respective crystal field ground state.

If pressure (or chemical pressure due to substitutions) is applied to such systems, the value of $|JN(E_F)|$ is changed and the systems are 'shifted along the x-axis'. In the case of Ce-systems, hydrostatic pressure causes an increase of $|JN(E_F)|$. As a consequence, the hybridization grows and the Ce magnetic moments become more and more unstable.

In terms of Doniach phase diagram, the system shifts right (with respect to the x-axis), entering the region with a non-magnetic ground state. On passing the critical point (with a supposed magnetic instability at $T = 0$), non-Fermi-liquid behavior may occur due to extremely strong spin fluctuations.

Substitutions, on the contrary, can enlarge the crystal unit cell and 'negative pressure' may occur, therefore, a shift into the regime of a 'magnetic' ground state possibly results. It should be noted that pressure applied to ytterbium systems causes a mirror like response when compared to cerium systems.

Anderson model

Properties of $3d$ and $4f$ impurities, distributed statistically in a host metal, can generally be accounted for in the scope of the Anderson Hamiltonian. The most simplest case follows, if no orbital degeneracy is anticipated for the $3d$ or $4f$ impurities:

$$H_{Anderson} = H_{kin,k} + H_{kin,4f/3d} + H_{Coulomb} + H_{hybrid} \tag{2.55}$$

The various terms of the equation have the following meaning [18]:

- $$H_{kin,k} = \sum_{k,\sigma} \epsilon_k n_{k,\sigma} \tag{2.56}$$

  The first term describes the kinetic energy of the conduction band (e.g. that of a parabolic band for free electrons), which is filled up to the Fermi energy.

- $$H_{kin,4f/3d} = \sum_{\sigma} E_0 n_{f/d,\sigma} \tag{2.57}$$

  The second term describes a localized $3d$ or $4f$ state, resulting from an uncompensated magnetic moment of a transition element or a rare earth element. E_0 is the binding energy of this state.

[18] c^+, c represents an annihilation operators (creation operator) for conduction electrons which are described by plane waves with wave vector k and spin (up or down) and that of a localized f or d electron impurity; n's are the corresponding number operators.

- $$H_{Coulomb} = U n_{f/d-up} n_{f/d-down} \tag{2.58}$$

  The third term accounts for the Coulomb interaction (in case of non-degenerated states the exchange term is added) which is responsible for the splitting of the two spin components of the $3d$ or $4f$ impurity. With the Coulomb interaction U absent, the position of the impurity level and the occupation is the same for spin and spin electrons and the impurity is obviously non-magnetic.

- $$H_{hybrid} = \sum_{k,\sigma} V_{k,f/d} c^{+}_{k,\sigma} c_{f/d,\sigma} + V^{*}_{k,f/d} c^{+}_{f/d,\sigma} c_{k,\sigma} \tag{2.59}$$

  The fourth term describes the hybridization,V, i.e., the mixing of local impurity states and delocal conduction electron states. This yields to a broadening of the local states through the continuum of the conduction electron band.

The last term in fact causes a resonance between local and delocal states of equal energy; the bounded state is no longer exactly defined with respect to the energy. It builds up a virtual bound state. A broadening of this state is equivalent to a certain time. In a classical picture this causes a finite time for a scattering event of the conduction electrons with the impurities.

If we anticipate that the hybridization potential is spherical symmetric, then only the $l = 2$ (or $l = 3$ in the case of $4f$-impurities) components of plane waves, describing the conduction electrons, are participating on scattering processes (equivalently: on the mixing or hybridization) with the $3d$ or $4f$ electrons.

2.6.6 Consequence of strong correlation on thermal and transport properties

In $4f$ systems, based on cerium or ytterbium, crystal field effects can no longer be neglected. The thermal population of the various crystal field levels with increasing temperature changes most of the physical properties and moreover the Kondo effect itself changes.

To explain the anomalous low temperature properties of cerium compounds, the $s - f$ model has been adapted. In the scope of perturbation type calculations the Kondo effect would occur only if the exchange integral J is positive because $(g - 1)$ is negative for cerium, which is in contradiction to the Heisenberg model. To account for such a situation, the Anderson Hamiltonian for the $4f^1$ configuration has to be used instead of the classical Heisenberg model. In doing this, an effective exchange term is constructed, which considers the spin and the orbital interaction with the conduction electrons.

In the case of cerium, the strong spin-orbit interaction yields to a ground state with a total angular momentum of $j = 5/2$. The first excited level with respect to the spin orbit coupling is $j = 7/2$, which lies more than 100 meV above the ground state. All the contributions of that multiplet are usually neglected.

This approach yields a Kondo effect if the effective exchange interaction is negative and can be applied only if the valence of the cerium impurities is almost integer, i.e. the $4f$ level

is occupied by one electron. The proposed scenario is known in the literature as Coqblin-Schrieffer model and method of its solution as Schrieffer-Wolff-transformation (for detailed derivation and further theoretical consequences, please see e.g. [32]). Usually the Kondo effect is considered in the presence of strong crystal field splitting.

In the following sections some physical quantities like the electrical resistivity or the specific heat are discussed.

Electrical resistivity of anomalous $4f$ systems

In a general treatment the application of the linearized Boltzmann equation yields the following transport coefficient for electrical resistivity, ρ:

$$\sigma = 1/\rho = e^2 K_0 \tag{2.60}$$

K_0 is the first order transport integral:

$$K_0 = \frac{k_F^3}{3\pi^2 m} \int \tau(\epsilon_k) d\epsilon_k - \frac{df_k}{d\epsilon} \tag{2.61}$$

Once, the relaxation time τ is known for a particular interaction process, the transport coefficient(s) can be calculated.[19]

In the scope of a perturbation type calculation in $J_{s-f}N(E_F)$ Cornut and Coqblin demonstrated for the first time the simultaneous acting of the Kondo effect in the presence of crystal field splitting. Results of their model have been applied to $CeAl_2$ and $CeAl_3$. The cubic crystal structure of $CeAl_2$ creates from the 6-fold degenerate state of the $j = 5/2$ total angular momentum a doublet as the crystal field ground state and a quartet as the first excited crystal field level. Both states are separated from each other by a certain energy Δ. The hexagonal crystal structure of $CeAl_3$ leads in the contrary to 3 doublets with the eigenstates $\pm 1/2$, $\pm 3/2$ and $\pm 5/2$. The crystal electric field is therefore responsible for, at least, a partial lifting of the ground state degeneracy. In the scope of the ansatz of Cornut and Coqblin the relaxation time is calculated in a third order perturbation type calculation.

From the direct and the resonant (Kondo) scattering, the temperature dependence of the magnetic contribution to the electrical resistivity ρ_{mag} can be calculated:

$$\rho_{mag} = AJ^2 N(E_F)(\rho_{spin} + \rho_{Kondo}), \tag{2.62}$$

where ρ_{spin} is the spin-disorder resistivity. The temperature dependence of this contribution results from the thermal population of the various crystal field levels.[20] The second term, ρ_{Kondo} is the Kondo resistivity.

[19] Other transport properties like thermal conductivity or thermoelectric power include up to second-order transport coefficients.

[20]
$$\rho_{spin} = \frac{\lambda_n^2 - 1}{\lambda_n(2j+1)} \tag{2.63}$$
where λ_n is the effective degeneracy of the populated $4f$ levels; for low temperatures $\lambda_n = 2$ and 4 for the doublet and quartet, respectively, since only the ground state level is populated.

The significant difference to the case of $3d$ impurities in a metallic host is the fact that there is a Kondo effect in each crystal field level. However, this can be observed only if the different crystal field levels are well separated. It is therefore possible to define a Kondo temperature for each crystal field level.

The most important results in the scope of this relaxation time approximation are:

- $\rho_{\mathrm{mag}}(T)$ is proportional to $(-\ln T)$ for temperatures which are much larger or much smaller than $\Delta_i\ k_{\mathrm{B}}$; $\rho_{\mathrm{mag}}(T)$ shows a maximum for temperature $\Delta_i \approx k_{\mathrm{B}}$.
- For $T << \Delta_2\ k_B$ and $T >> \Delta_n\ k_{\mathrm{B}}$ the ratio of the logarithmic temperature dependencies is given by $Q = (\alpha_1^2 - 1)/4j(j+1)$ (α_1 is the level degeneracy).

The value of Q is independent from the eigenstates of the involved crystal field levels; only the degeneracy α_1 determines this ratio. The slope of the lnT term is proportional to $J^3(N(E_{\mathrm{F}}))^2$. The validity of this calculation breaks down at $T \approx T_{\mathrm{K}}$.

Magnetoresistance

Since applied magnetic fields also influence fine details of the density of states, it can be anticipated that $\rho(T)$ of Kondo impurities, below and above T_{K}, is considerably altered under these fields. Within the simplest case, namely magnetic impurities embedded in a metallic host, $\rho(T)$ was found experimentally to decrease monotonically in an increasing magnetic field.

A calculation of the magnetoresistance requires knowledge of the occupation number of the Zeeman levels as a function of the field. It can be directly calculated in the scope of the Coqblin-Schrieffer model for the Kondo doublet only.

The universal behavior of $\rho(B)/\rho(0)$ vs. $\ln(B/B^*)$ shows that the physics of Kondo systems is determined from a single characteristic energy scale, $\mu_{\mathrm{B}}B^* \sim k_{\mathrm{B}}T_{\mathrm{K}}$.

For large magnetic fields, the magnetoresistance shows Kondo logarithms, which are features of asymptotic freedom, that is

$$\rho(T) \propto \ln^{-2}((B/T_{\mathrm{K}})^2) \tag{2.64}$$

An extension to finite temperatures has been presented by Batlogg (1987):

$$B^*(T) = B^*(0) + \frac{k_{\mathrm{B}}T}{g\mu}. \tag{2.65}$$

$B^*(0)$ has the meaning of the Kondo field and is related by the Kondo temperature T_{K} by:

$$T_{\mathrm{K}} = B^*(0)\frac{g\mu}{k_{\mathrm{B}}}. \tag{2.66}$$

Specific heat of strongly correlated systems

The specific heat anomaly due to the Kondo effect can be thought to arise from the thermal population of a triplet state which consists of conduction and localized electron states separated by an energy $k_{\mathrm{B}}T_{\mathrm{K}}$ from the singlet ground state. The first successful approach

to calculate the specific heat of Kondo systems was put forward by Schotte and Schotte (1975). They assumed a Lorentzian-like density of states at the Fermi energy for impurity spins $S = 1/2$. The width of this Lorentzian is $k_B T_K$[21]:

$$c_{imp} = k_B \frac{\Delta}{\pi k_B T}(1 - \frac{\Delta}{2\pi k_B T}\psi'[1/2 - \frac{\Delta}{2\pi k_B T}]) \tag{2.67}$$

This solution indicates that the specific heat exhibits a maximum in the vicinity of the Kondo temperature with a maximum value of about 1.5 J/molK. The entropy associated with this contribution tends at very large temperatures to a value of $R \ln 2$, since there, the spin moments recover their degrees of freedom. As already indicated, the specific heat follows from the thermal population of a triplet state above the non-magnetic ground state. If the temperature is increased, this state is populated, therefore the energy associated increases, too. This behavior is similar to the Schottky contribution to the specific heat in the case of crystal field levels. Oliveira and Wilkins (1981) have presented a renormalization group calculation of the impurity specific heat in a large temperature range. This calculation showed that the specific heat is a universal function of the temperature scaled by T_K. The specific heat in this model exhibits a maximum at $T = 0.67 T_K$ and a maximum value of roughly 1.5 J/molK. The entropy associated with this impurity contribution is consistent with the expected value of $R \ln 2$. At zero temperature this model yields:

$$\frac{c_{imp}(T \longrightarrow 0)}{T} \equiv \gamma = \frac{2\pi}{3} R \frac{0.013}{T_K} \approx 0.68 R/T_K \tag{2.68}$$

The relation shows a simple method to determine from low temperature specific heat measurements the characteristic temperature T_K.

More complex calculations based on either the large-N approximation or the Bethe ansatz method give again an universal behavior of the specific heat of $4f$ systems with maximum contributions depending on the total angular momentum j. The γ scales with the degeneracy, while the temperature behavior depends only on the Kondo temperature.

In addition the crystal field splitting of the 6- and 8-fold degenerate ground state of cerium and ytterbium, respectively, leads to a decrease of the effective degeneracy and to a an effective Kondo temperature, which can be very different from that of spin-1/2-systems.

Desgranges and Rasul showed in the scope of the Bethe ansatz solution numerical results for a quartet split into two doublets and for a $j = 5/2$ system which is split by the crystal field into 3 equidistant levels separated by the energy A. The effective Kondo temperatures are then (4, 6 represents the quartet and sextet state, respectively):

$$T_{K^{\text{eff}}4} = \frac{(T_K^{(4)})^2}{C_2 A} \tag{2.69}$$

$$T_{K^{\text{eff}}6} = \frac{(T_K^{(6)})^3}{C_4 A} \tag{2.70}$$

where $T_K^{(n)}$ is the Kondo temperature in absence of the crystal field splitting:

$$T_K^{(4)} \sim \frac{-\pi}{2J_{s-f}}, T_K^{(6)} \sim \frac{-\pi}{3J_{s-f}} \tag{2.71}$$

[21] ψ' is the derivative of the Digamma function[35]

and $C_2 = 3.34$, $C_4 = 34.13$ are constants, respectively.

There exists an analytical solution for the electronic contribution to the specific heat in the case of 2 doublets for T close to zero. For large values of the crystal field splitting the expression equals to that which is known for the spin-1/2 Kondo problem ($\gamma = \pi/3T_K$). The calculated Schottky contribution is smaller than that resulting from pure crystal field split magnetic systems. This is originated from the Kondo effect because the formation of the Kondo maximum requires entropy which is no longer available at high temperatures.

2.6.7 Heavy fermion superconductivity

Introduction

A number of Ce and U compounds like $CeCu_2Si_2$, UPt_3, $CeCoIn_5$ or UPd_2Al_3 show superconductivity below critical temperature, T_c about 2 K [36]-[39]. Additionally it was observed that the nonmagnetic isostructural compounds with lanthanum or thorium do not show superconductivity. At the superconducting phase transition, the weakly correlated quasi-particles condensate into an highly correlated state; the heavy quasi-particles couple into Cooper-pairs.

Additionally, 'magnetic' superconductors can be found (e.g. the UPd_2Al_3 case) where the system crosses over into a magnetically ordered state and well below that transition undergoes another phase transition into a superconducting ground state without loosing magnetic order. Mainly a local modulation of the superconducting state (FFLO SC, Fulde-Ferrell-Larkin-Ovchinikov) is thought to be responsible for such an unusual behavior.

The heavy fermion superconductivity occurs in spite of the fact that these compounds exhibit permanent magnetic moments, which in classical superconductors destroy the superconducting ground state. However, since the Kondo screening is observed in these systems from negative logarithmic contributions to the electrical resistivity it follows that the magnetic moments of the Ce or U ions are already compensated. A thorough theory of this phenomenon still does not exist.

Pairing mechanism in HFSC

Already discussed aspects of the heavy fermion superconductivity deal mainly with the following questions:

- Which pair state shows the system?
- What is the attractive force between the quasi-particles?

Generally, the superconducting state is characterized by a quantum mechanic order parameter, like the gap in the electronic excitation spectrum or the wave function of the Cooper-pair. A fundamental property of this wave function is its antisymmetry.

The order parameter can therefore be constructed by a superposition of odd (singlet) pair states (found in the common superconductors) and even (triplet) pair states (suprafluid ^{3}He). For few examples it is possible to discriminate exactly between different cases:

- The spin-orbit interaction is negligible; the spin is therefore a good quantum number; a classification according to the pair spin is possible: spin-singlet or spin-triplet superconductors.
- The crystal structure has an center of inversion; the pair wave function can then be classified according to the parity; there are superconductors with odd or even parity.

All the yet known heavy fermion superconductors belong to the second class: the spin-orbit coupling is strong, however the crystals exhibit a center of inversion, the order parameter can be classified according to its parity. An important criterion of the superconducting order parameter is its behavior under symmetry operations (see Figure 2.15):

- The order parameter shows the full lattice symmetry; this is valid for all conventional superconductors.
- The symmetry is broken, then such superconductors are termed unconventional superconductors. A state with odd parity in a crystal with inversion-symmetry leads always (from the group theoretical point of view) to an unconventional superconducting state.
- The crystal structure does not posses an inversion symmetry - unconventional superconductor with e.g. helical state.

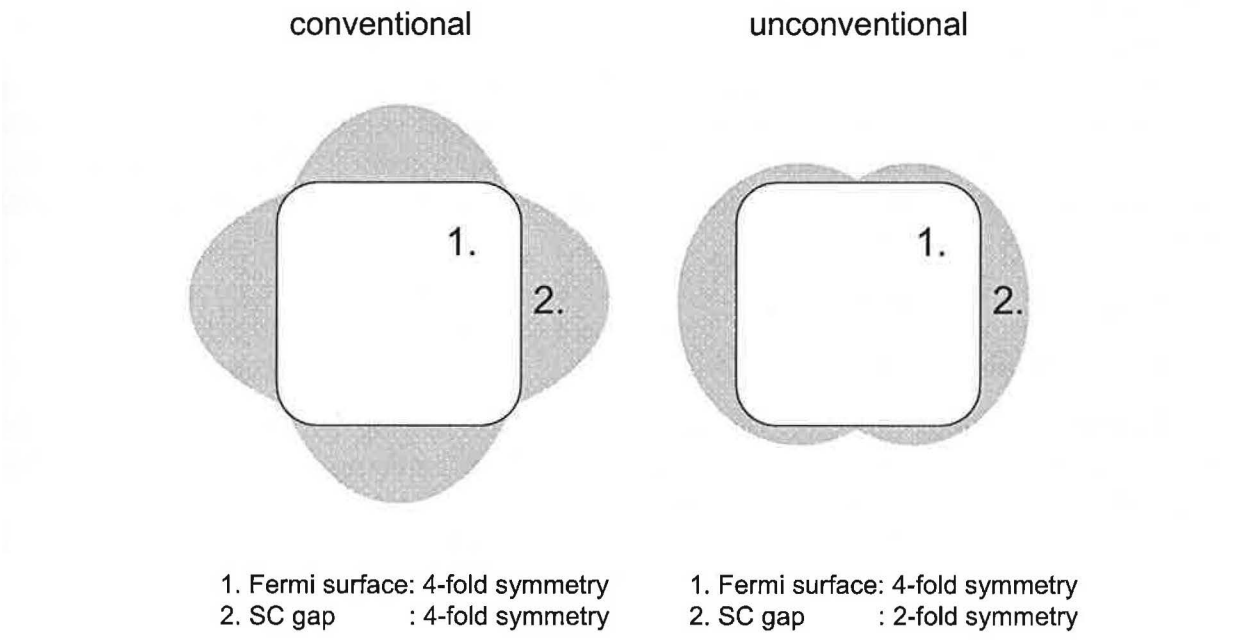

Figure 2.15: Symmetry of the order parameter and the Fermi surface in conventional and unconventional SC.

For both conventional and unconventional superconductors the order parameter can vanish on the Fermi surface. Therefore excitations are possible with any amount of energy. In such a case, transport properties like the thermal conductivity or the specific heat do not

case	SC gap vanishes	example
isotropic	everywhere	common SC
axial	at points	ABM SC in ^{3}He
polar	at lines	UPt_3
noncentrosymmetric	-	$CePt_3Si$

Table 2.2: Symmetry class of superconductors according to the gap vanishing mechanism.

show the famous exponential temperature dependence. Since each energy amount is possible for excitations the physical quantities show simple power laws.

Depending on the form of the superconducting gap in the excitation spectrum the superconductors can be divided into several classes as summarized in the Table 2.1.

Experimental evidence of HFSC state

Specific heat anomaly at T_c (ΔC_{SC})

The transition into the superconducting ground state is accompanied by a jump in the specific heat, which in terms of the BCS theory is given as $\Delta C_{SC} = 1.43 C_n(T_c)$. For $CeCu_2Si_2$ one obtains $\Delta C_{SC} = 1.1 C_n(T_c)$ contrary to the BCS theory. Similar disagreement has been observed experimentally in all HFSC.

The critical magnetic field H_{c2}

From analysis of the critical magnetic field, H_{c2} (by means of $H'_{c2} = (H_{c2}/dT|_{T=T_c})$) various parameters can be determined for conventional singlet superconductors. The important characteristics of the quasiparticles forming the Cooper pairs are their Fermi velocity, v_F and the mean free path, l_{mf}. Two different cases can be considered according to the limiting value of the mean free path, l_{mf} :

- $l_{mf} = \infty$: clean limit
- $l_{mf} = 0$: dirty limit

In the clean limit only the H'_{c2} increases with decreasing Fermi velocity, v_F . Heavy fermion systems are characterized by very low values of the Fermi velocity due to the unusual low value of the characteristic temperature.

In the dirty limit the H'_{c2} value is determined by the mean free path, l_{mf}. Assuming spherical Fermi surface, the H'_{c2} can be expressed as:

$$H'_{c2}(dirty) \sim const.T\gamma^2\rho_0 \tag{2.72}$$

The value and the temperature dependence of the critical field is determined from various mechanisms:

- The interaction of the magnetic field with the orbit motion of the electrons: orbital pair breaking
- and the interaction of the magnetic field with the spin: Pauli-limiting.

SC gap	isotropic	axial	polar
specific heat	$\sim \exp(-\Delta/T)$	$\sim (-\Delta/T)^3$	$\sim (-\Delta/T)^2$
NMR	$\sim \exp(-\Delta/T)$	$\sim (-\Delta/T)^4$	$\sim (-\Delta/T)^2$
thermal conductivity	$\sim \exp(-\Delta/T)$	$\sim (-\Delta/T)^3$	$\sim (-\Delta/T)^2$

Table 2.3: Temperature dependence of various physical quantities in the SC state for different shapes of the SC gap.

Orbital pair breaking is the most important mechanism in the low field limit, independent whether this SC is conventional or unconventional. It determines therefore H'_{c2}. The upper critical field, which is constrained by pair breaking, H^*_{c2} can be expressed as:

- $H^*_{c2} = 0.693 H'_{c2} T_c$; for a conventional SC in the dirty limit
- $H^*_{c2} = 0.850 H'_{c2} T_c$; for a polar, triplet SC.

Polar superconductors therefore exhibit the largest critical field for a given value of H'_{c2}.

For conventional SC with a total spin $S = 0 \longrightarrow \chi_s = 0$. For BCS SC with non-interacting electrons an upper border, the so called Clogston limit (H_p) is valid.

Let's consider two simple border cases within the Pauli limiting:

- conventional SC: $s = 0$, $l = 0$ and $s = 0$, $l = 2, 4, ... \longrightarrow \chi_s = 0$ - Pauli limiting appears to be maximum
- simple triplet state: $s = 1$, $l = 1$, 3, ... If the spin component is decoupled from the orbital one, there is no Pauli-limiting = no equal spin pairing.

Basic features of HFSC - summary

The characteristic behavior of selected physical quantities in the HF superconducting state are summarized in the Table 2.2 for different types of superconductors according to the SC gap symmetry.

SC	Sn	Y-Ba-Cu-O	$CeCu_2Si_2$	YNi_2B_2C	$CePt_3Si$
T_c (K)	3.7	100	0.6-0.8	15.5	2.2
structure			tetr.	tetr.	tetr.
order parameter	conv.	conv.	conv.	conv.	helical
γ (J/molK^2)	1.8	10	1000	20	300
$m/m*$	2	3-5	400	1.2	600
ξ (Å)	2300	14	100	80	100
λ (Å)	340	1400	5000	1200	1000
$\lambda\,\chi$	0.16	100	50	15	10
$B_{c2}(0)$ (T)	0.03	100	2	9	5
$-B'_{c2}$ (T/K)	0.014	2.7	27	0.3	8
other properties	-	HTSC	Kondo int.	-	Kondo int. AF ordering

Table 2.4: Some characteristics of classical-, high temperature-, heavy fermion - and borocarbide superconductors.

Remarks on Novel HFSC state in noncentrosymmetric systems

Most superconductors known to date are parity-conserving materials allowing the classification of their pairing states in spin singlets (even parity) or spin triplets (odd parity). The recently discovered heavy-fermion superconductors $CePt_3Si$ and $CeRhSi_3$ crystallizes in a tetragonal lattice with the point group C_{4v} [40, 41]. It has no spatial inversion symmetry, which implies that the spatial component of the wave function has no definite parity. To preserve the antisymmetry of the pairing, the same applies to the spin component.

The direct implication of the parity violation is that the pairing symmetry should, in principle, be a mixture of spin-singlet and spin-triplet states. The symmetry analysis for the superconducting pairing state becomes more complicated. Recent theoretical arguments indicate that such a mixture can be neglected under certain conditions; thus, the singlet and triplet pairing states can be considered separately as if parity is conserved.

In $CePt_3Si$ the upper critical field H_{c2} exceeds the paramagnetic limiting field, which readily points out to the occurrence of spin-triplet pairing in this material. This leads to a conflict because spin-triplet channels are known to be forbidden in the absence of inversion symmetry. Frigeri et al. showed, however, that spin-triplet states are not completely suppressed in the absence of an inversion center [42]. Considering the spin-orbit coupling (SOC) to be weak, they suggested the p wave ($\widehat{dk} = \widehat{x}k_y - \widehat{y}k_x$, odd parity) as the possible pairing state. The gap structure for this state has point nodes.

Further theoretical support for an odd-parity state was given by Samokhin et al., who showed that SOC in $CePt_3Si$ is strong and that this fact, along with the absence of inversion symmetry, always yields an odd-parity order parameter with line nodes for one-dimensional irreducible representations (IRs) [323]. In recent work, Sergienko and Curnoe proposed a

model for noncentrosymmetric superconductors with a strong SOC in which the temperature dependence of the thermodynamic properties would be governed by an even-parity function. Such a function would transform according to the IRs of the point group [45]. In this scenario, $\widehat{dk} = \widehat{x}k_y - \widehat{y}k_x$ corresponds to an isotropic and fully gapped even function.

As a consequence, these controversial discussions do not allow a definite conclusion on the symmetry and parity of the gap function in $CePt_3Si$ from a theoretical perspective. The parity conservation issues and the splitting of the spin degeneracy in the electronic energy bands by the SOC are of high relevance in unconventional superconductivity. Regardless of the pairing state multiplicity, the recent experimental results reported by Bonalde et al. suggest the existence of line nodes in the superconducting gap structure. The proposed state of art of the unconventional superconductivity in noncentrosymmetric $CePt_3Si$ will be given in the Chapter 4.

From the topological point of view, nontrivial nodal structures are one of the most noticeable features of the unconventional superconducting gap functions. Conventionally, the nodal structures have been investigated by power law behaviors of the temperature dependencies of the specific heat, the NMR relaxation rates and so on. Although the power law behaviors give a hint of the nodal structures, they can not give the details such as the number and the position of the nodes. Recently, the angular-controlled measurements of thermal conductivity and specific heat in a vortex state have been discovered as useful probes of the nodal structures determination. Some recent results on the noncentrosymmetric $CePt_3Si$ will be presented in the Chapter 4.

2.7 Electrons in submicron-scale and strongly disordered metals

The motion of an electron in a disordered system differs remarkably from the ideal crystal case due to interplay between its localization and system dimensionality. It was first shown already in 1960 that rapid quenching of certain alloys from the melt could form completely extended solid solutions, new metastable crystalline phases and amorphous solid phases.

According to the microscopic constitution of highly disordered metals/alloys we may distinguish the following categories:

- amorphous metals/metallic glasses
- quasicrystals
- nanocrystalline metals
- metals with micron-size grains and local structure disorder (intra-granular)
- crystalline metals with high concentration of structural defects(inter-granular)

The obtained phases exhibit often completely different physical properties in comparison to the crystalline phases of the same nominal composition [46]-[65].

The notoriously known is the strongly enhanced mechanical endurance due to lack of grain boundaries in metallic glasses.

The phenomena may be observed due to modification of the phonon spectra in disordered materials. In consistency with assumption of the distorted dimensionality, the corresponding response of phonons in the physical properties may reflect lower than 3-dimensionality.

Besides the macroscopic effects, the electronic properties of such systems are adapted to the reconstruction of their electronic band structure. From the fundamental point of view, the phenomena arise from the partly reduced dimensionality and local structural disorder of the system; the Fermi surface is modified and the loss of some degree(s) of freedom occurs.

The most illustrative effects can be observed on the transport properties (electrical resistivity, magnetoresistance, Hall coefficient) of disordered materials. In addition, heat capacity studies in magnetic fields (by means of the electronic contribution) serve as a useful tool to probe the change of electronic structure in comparison to the 'common' metallic state.

A number of experimental data on electron transport in disordered metal films and wires were shown to be in disagreement with the standard theory of electron dephasing in normal conductors. The saturation of conduction electron dephasing time appears in disordered conductors (and mesoscopic systems). In particular, it is of great interest whether the saturation might occurs universally in all materials and in all (zero, one, two and three) dimensions. It is also important to ask whether or not there might be a common, intrinsic source that causes the (almost) universally observed saturation.

The interest in this issue of the existence or not of a finite conduction electron dephasing time at absolute zero temperature is closely connected with the concern about the validity of the Fermi-liquid behavior, the possibility of the occurrence of a quantum phase transition, and also the feasibility of quantum computing. There are also works suggesting that this might explain the long-standing persistent current problem in metals. In practice, the value of the dephasing time can be reliably determined using quantum-interference studies such as weak-localization effects and universal conductance fluctuations.

The general approaches treating the electronic states in disordered metals are based on the disordered Anderson or Hubbard models via a random-phase-type approximation or the supersymmetry method [66].

However, the treatment of the submicron-scale and strongly disordered metals comprises numerous phenomenological approaches mostly. The experimental results are then interpreted in terms of 'deviation from the unperturbed crystalline state'.

2.8 Electrotransport phenomena in metals

Introduction

When an electric field is applied to a metallic rod, a small transport of matter occurs in addition to the electron flow. This process is referred to as electrodiffusion, electromigration or electrotransport. The following phenomena may occur in a solid medium:

- Self-transport in pure metals arising from the displacement of atoms into vacancies,
- the separation of components of a substitutional alloy resulting from their different rates or directions of migration,
- and the transport of interstitial solutes.

Form of migrating species	Electrotransport velocity per unit field
Self	$10^{-14} - 10^{-12}$
Substitutional solutes	$10^{-11} - 10^{-10}$
Interstitial solutes	$10^{-10} - 10^{-7}$

Table 2.5: Observed mobilities in solid metal system.

The orders of magnitude of the electrotransport velocities in the different systems are indicated in the Table 2.5 (according to [67]).

As almost all the current is carried by electrons, the electrotransport is very inefficient, typically 10^{-8} mol transported per 1 Faraday of charge in the case of self-transport. However, the phenomenon provides both interesting theoretical features and technological applications.

Theory of electrotransport

The motion of metal ion is primarily governed by momentum transfer from the charge carriers rather then the electrical field alone [68].Therefore, the total force exerted on the metal ion is a superposition of the electrical field and a so-called drag force resulting from the momentum exchange (Figure 2.16). The resultant net force, F_i, may be expressed using the equation 2.73.

$$F_i = eE(Z_i - \delta_{ei}/e) = eEZ_i^0 \tag{2.73}$$

The Z_i^0 is the effective valence of the ion given by the difference between the actual valence Z_i and the drag coefficient δ_{ei}. The direction of the resultant force acting on the metallic ion under external electrical field is therefore determined by the effective valence sign; if:

- $Z_i > \delta_{ei}/e$ - the resulting force is cathode-directed
- $Z_i < \delta_{ei}/e$ - the resulting force is anode-directed.

The ion migrates with a finite velocity, v_i, given by:

$$v_i = F_i B_i \tag{2.74}$$

where B_i is absolute mobility. Using the relation for diffusion modified for the solid-state conditions 2.75:

$$B_i = \frac{D_i}{fkT} \tag{2.75}$$

(D_i is the diffusion coefficient, and f is correlation coefficient, which describes the deviation from randomness) we may treat the electrotransport process as a diffusion process, which is biased in a particular direction by a force given by 2.73.

In general, three different approaches to the theoretical description of electrotransport were employed: methods of irreversible thermodynamics, semi-empirical methods, and recently those of quantum mechanics. The following part will briefly discuss the two most important models based on the quantum-mechanical approach.

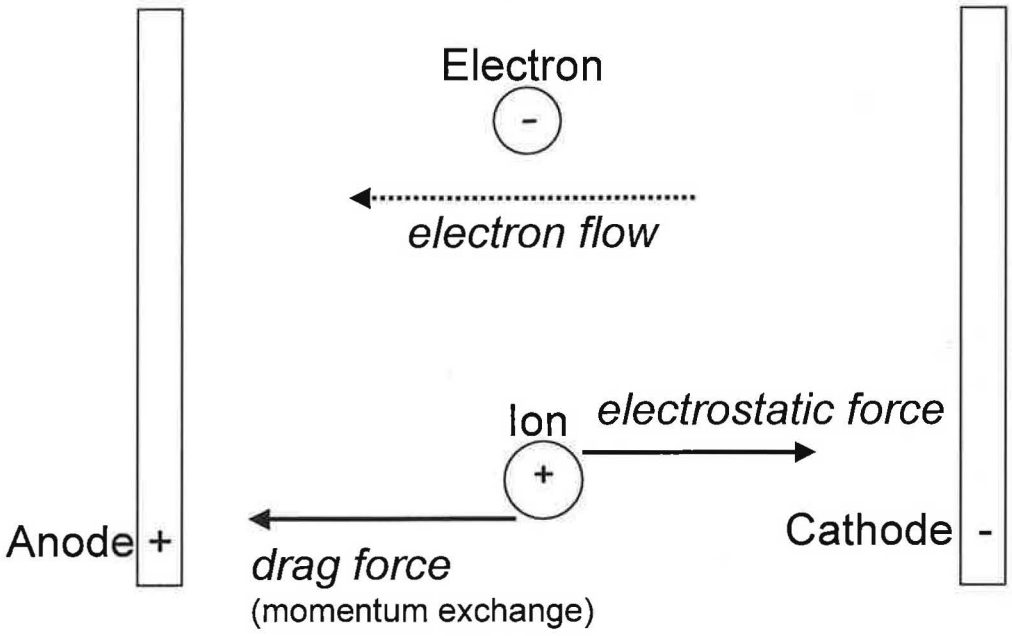

Figure 2.16: The forces acting on an ion during electrotransport.

The dynamical model

The proposed mechanism is given by momentum transfer from the current carriers to the scattering centers. The scattering rate is sufficiently high to justify the approximating effect as a continuous force. Assuming the closed Fermi surface, in the relaxation time approximation, the drag force may be expressed as:

$$F_{ei} = \frac{m*}{N_i e \tau_i} j \tag{2.76}$$

where N_i is the density of scattering centers, j is the current density, τ_i is the mean time between collisions and $m*$ is the effective electron mass. It is evident, that the sign of the drag force depends on the sign of $m*$ and hence, on the curvature of the Fermi surface. Calling the electron energy ϵ, we obtain the two experimentally observed cases:

- $\partial^2\epsilon/\partial k^2 > 0$, the force is the same direction as the electron flow (to the anode)
- $\partial^2\epsilon/\partial k^2 < 0$, the force is cathode-directed and the electrons act like holes.

Further details including the used formalism and partial steps of the calculations are presented in the original literature [69, 70]. However, it has been assumed so far, that the electrostatic component is just due to the interaction of the electric field with the unscreened ion. The polarization model extents this assumption.[22]

[22]In the relaxation time approximation it is inferred that some time after scattering has occurred the electron distribution does not depend on the non-equilibrium distribution just before the scattering. Additionally, if electrons have the equilibrium distribution with local temperature the collisions do not affect the form of the distribution function.

The polarization model

The total force acting on the interstitial atoms and matrix atoms in metals is determined within the frame of the perturbation theory using the first Born approximation (the applied electrical field acts as the perturbation on the free-electron wave function). Both the direct polarization effect and the effect due to displacement of the Fermi surface due to electric current flow. The most important result is, that the interstitial atoms do not experience a direct force from the electrical field due to complete screening by the charge carriers. The polarization due to the Fermi surface displacement gives rise to the force which is parallel to and proportional to the applied electric field. In other words, if the current carriers are electrons, the displacement is equivalent to an increase of the number of electrons travelling towards the anode. These electrons are retarded on the anode side of the impurity and accelerated on the cathode side. As a result the electron density is increased on the anode side relative to the cathode side (= anode directed 'induced' polarization force). For further details, please, see [71, 72].

As shown later, the resultant force may be treated in the terms of the resistivity of the impurity in the matrix. The results based on both models are equal, independently on including screening effects on the interstitial ions. The force is the same direction as the motion of the charge carriers and does not depend on the ion valency. When a jump between two neighboring interstitial sites occurs, the screening charge remains tightly bound and so moves with the ion. Thus, the force remains constant thorough the jump and represents the average net force acting on an interstitial ion undergoing electrotransport.

In summary, there two main differences between the mentioned models:

- in the dynamical model the only force acting on the ion at the stable point is the direct electrostatic force, whereas in the polarization model the electrostatic force is augmented by a force arising from the modification of the charge distribution by the neighboring vacant site;

- in the dynamical model no account is taken of screening at the saddle point. In the polarization model the screening reduces the electrostatic force to zero.

Chapter 3

Experimental methods

3.1 Sample preparation

3.1.1 Polycrystalline compounds

Mono-arc furnace

High-quality samples were synthesized in the mono-arc furnace by arc melting of pure constituent elements, respectively. All samples were four times remelted to achieve the highest possible homogeneity of the bulk. A good sample is usually characterized with extreme fragility and unvarying color through the whole volume.

Mono-arc apparatus at the Department of Condensed Matter Physics consists of the following main compartments: sample chamber, torch (fabricated from W doped with Th), cooling water system, vacuum system and power supply for the arc; the whole apparatus is schematically shown in Figure 3.1.

First, after the sample is set inside the apparatus, the sample chamber must be evacuated (typically 1-4 hour(s), pressure $\sim 10^{-1}$ Pa) and then filled with the protective Ar atmosphere ($\sim$ 0.5 atm). A melt is kept in a massive cooper water-cooled crucible, which was designed with four symmetrically positioned 'sub-crucibles', that allow to prepare utmost four samples in one pumping cycle. As the crucible is continuously cooled, the surface tension of the melt holds the drop of the material without a thermal contact with the material of the crucible and avoids any contamination of the melt.

The most crucial moment of the process is the initial reaction of pure elements under arc, when part of the material might be flown away by the arc plasma and the sample could form few stable phases inside, which cannot be removed neither with further melting nor by annealing of a final product due to the local phase equilibria in the bulk.

Synthesis of polycrystalline $CePt_3Si$-related compounds

Numerous polycrystalline samples of the nominal 1:3:1 composition were fabricated for structure and electronic properties studies. The materials were investigated either in the 'as cast form' or after additional treatment. Several samples were melted for longer time in a tri-arc furnace (the apparatus is described in the next section). The list of prepared compounds together with the applied treatment conditions are summarized in the Table 3.1.

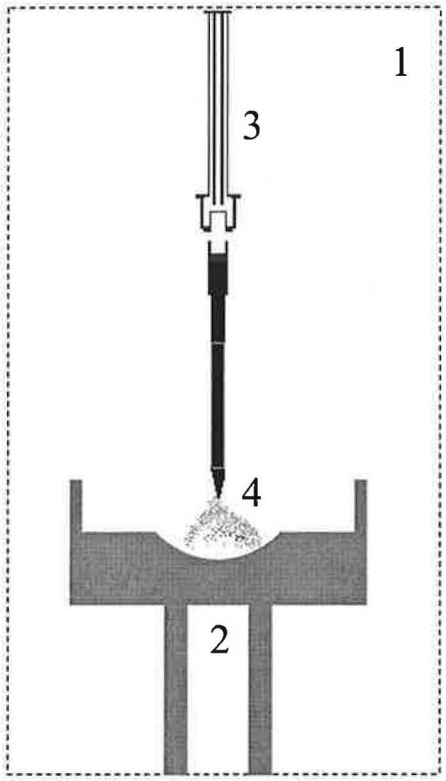

Figure 3.1: Scheme of a monoarc furnace.
1 - sample chamber, 2 - water cooled copper crucible 3 - water cooled torch holder with a tungsten torch, 4 - melted sample.

Furthermore, two groups of pseudoternary samples were prepared: $CePt_{1-x}T_xSi$ and $CePt_3Si_{1-x}X_x$, where T is a transition $3d$, $4d$ or $5d$ metal and X is a s- or p-element, respectively. The complete overview concerning preparation of those materials is summarized in the Table 3.2. In both Tables, the first-sight unsuccessful trials (in fact additional 38 samples of $x > 0.2$ or $x < 0.1$), it means evidently multi-phase/heterogeneous or not-reacting components, are not included.

To scrutinize the possibility of CeT_3Si formation in analogy with $CePt_3Si$, the interaction of components under different synthesis conditions starting from the 1 : 3 : 1 composition was investigated. The following transition metals were tested T = Ru, Rh, Pd, Os, Ir, Cu, Ag, Au. As cast samples (of $\sim$ 1.5 g each) were halved; one part was wrapped in a tantalum foil and seeled in a quartz tube under vacuum. It was annealed for 20 days. The samples were either cooled-down slowly or subsequently quenched into water.

$CePt_3X$	Label	Mass (g)	Melting	Annealing (time/temperature)	Cooling
B	1	1.2	3×	0	-
B	2	1.1	3×	8 days/950°C	slow
B	3	1.0	2×	8 days/950°C	quenched
B	4	1.0	2×	20 days/850°C	slow
B	5	1.0	2×	20 days/850°C	quenched
B	6	7.0	1×/*2 hours	0	-
Al	1	1.1	3×	0	-
Al	2	0.9	3×	8 days/950°C	slow
Al	3	0.9	3×	8 days/950°C	quenched
Al	4	0.9	3×	20 days/850°C	slow
Al	5	1.0	3×	20 days/850°C	quenched
Al	6	7.8	1×/*2 hours		-
C	1	0	3×	0	-
C	1	0.6	3×	8 days/950°C	slow
C	2	0.9	3×	8 days/950°C	quenched
C	3	0.8	3×	20 days/850°C	slow
C	4	1.1	3×	20 days/850°C	quenched
C	5	1.2	3×	21 days/1050°C	slow
C	6	1.8	3×	21 days/1050°C	quenched
C	7	7.6	1×*2hours	0	-
Si	1	0.9	2×	0	slow
Si	1	0.8	2×	8 days/950°C	
Si	2	0.8	2×	8 days/950°C	quenched
Si	3	1.0	3×	20 days/850°C	slow
Si	4	1.0	3×	20 days/850°C	quenched
Si	5	8.1	1×*2hours	0	-
Ge	1	0.9	2×	0	-
Ge	2	0.9	2×	8 days/ 950°C	slow
Ge	3	0.9	2×	8 days/ 950°C	quenched
Ge	4	1.2	3×	20 days/ 850°C	slow
Ge	5	1.1	3×	20 days/ 850°C	quenched
Ge	6	1.2	3×	7 days/ 900°C	slow
Ge	7	1.1	3×	7 days/ 900°C	quenched
Ge	8	6.3	1×*1hour	0	-
Ge	9	7.2	1×*2hours	0	-

Table 3.1: Synthesis conditions of $CePt_3X$ compounds.* - melted in a tri-arc furnace

$CePt_{1-x}T_xSi$ x = 0.2	Label	Mass (g)	Melting	Annealing (time/temperature)	Cooling
Ru	1	1.0	3×	0	-
Ru	2	1.0	3×	8 days/950°C	quenched
Ru	3	1.0	3×	20 days/850°C	slow
Rh	1	1.0	2×	0	-
Rh	2	1.0	2×	8 days/950°C	quenched
Rh	3	1.0	2×	20 days/850°C	slow
Pd	1	1.0	2×	0	-
Pd	2	1.0	2×	8 days/950°C	quenched
Pd	3	1.0	2×	20 days/850°C	slow
Ir	1	1.0	3×	0	-
Ir	2	1.0	3×	8 days/950°C	quenched
Ir	3	1.0	2×	20 days/850°C	slow
Au	1	1.0	3×	0	-
Au	2	1.0	3×	8 days/950°C	quenched
Au	3	1.0	2×	20 days/850°C	slow
Cu	1	1.0	3×	0	-
Cu	2	1.0	3×	8 days/ 950°C	quenched
Cu	3	1.0	3×	20 days/ 850°C	slow
$CePt_3Si_{1-x}C_x$					
x = 0.1	1	0.6	3×	0	-
x = 0.2	1	0.9	3×	0	-
x = 0.2	2	0.8	3×	20 days/850°C	slow
x = 0.2	3	7.3	1×*2hours	0	-
x = 0.5	1	1.1	3×	0	-
x = 0.5	2	1.2	3×	20 days/850°C	slow
x = 0.5	3	6.4	1×*2hours	0	-
x = 0.8	1	1.8	3×	0	-
x = 0.8	2	1.2	3×	0	-
x = 0.8	1	7.6	1×	20 days/850°C	slow
x = 0.9	2	7.6	1×*2hours	0	-
$CePt_3Si_{1-x}Mg_x$					
x = 0.1	1	0.8	2×		-
x = 0.1	2	0.8	2×	8 days/950°C	quenched
x = 0.2	1	1.0	3×	0	-
x = 0.2	2	1.0	3×	8 days/950°C	quenched

Table 3.2: Synthesis conditions of $CePt_{1-x}T_xSi$ and $CePt_3Si_{1-x}X_x$ compounds.* - melted in the Tri-arc furnace

Synthesis of polycrystalline $CeRu_2$-related compounds

The series of Ce-Ru-Si-containing samples was prepared in the analogy with the $CePt_3Si$ - related systems. The initial compositions together with the heat treatment conditions are summarized in the Table 3.3.

3.1.2 Single-crystal growth

Tri-arc furnace

Figure 3.2: Tri-arc furnace from outside.

The growth of selected single-crystals (namely of the 1:3:1 compounds) was performed in the Tri-arc furnace at the Department of Condensed Matter Physics. Simultaneous growth-trials were done by prof. Takemi Komatsubara using Tetra-arc furnace at the Institute for Materials Research, Tohoku University, Sendai. The two apparatuses differ in their designs, which offer two possible experimental configurations to be compared by means of their suitability for the particular crystal-growth.

Briefly, the Japanese-design furnace differs mainly in the hot-zone geometry, due to much steeper position of the arcs with respect to the crucible. As a consequence, there is a sharper temperature gradient in the melt-interface area. In general, easily freezing melts are better treated in the furnace.

Si:Ru:Ce composition	Label	Mass (g)	Melting	Annealing (time/temperature)	Cooling
20 : 60 : 20	1	2.3	3×	21 d./1225 K	slow
20 : 60 : 20	2	1.6	3×	10 d./1125 K	slow
20 : 60 : 20	3	1.4	2×	21 d./1225 K	quenched
20 : 60 : 20	4	1.2	3×	10 d./1125 K	quenched
20 : 60 : 20	5	3.2	1×*1hour	0	-
9 : 57 : 34	6	1.5	3×	0	-
9 : 57 : 34	7	1.3	2×	10 d./1125 K	slow
9 : 57 : 34	8	1.3	3×	10 d./1125 K	quenched

Table 3.3: Synthesis conditions of Ce-Ru-Si based compounds.* - melted in the Tri-arc furnace

Only the home-laboratory furnace will be described more in detail. Tri-arc furnace has been designed and built in cooperation with VAKUUM Praha company as an upgraded version of the tri-arc furnace of the van der Waals-Zeeman laboratory, Amsterdam. It utilizes the Czochralski technique modified for the arc heating. This device consists of the following parts (for details see Figures 3.2. and 3.3):

- Sample chamber containing water-cooled Cu crucible with variable rotation
- Vacuum system
- Water-cooling system
- Power supplies for the three arcs (heating sources)
- Pulling head with continuously controllable rotation and translation (product of Crystalox company)

First, the sample chamber is evacuated and the walls are heated to desorb gases, typically overnight, to reach the lowest possible pressure ($\sim 5.10^{-2}$ Pa) in order to get rid of all oxygen, water vapors and other spurious gases. These are one of the crucial factors, which influence the crystal-growth process. Second, the chamber is filled with the Ar protective atmosphere (6N purity, 1.3 atm). The melt is then heated with three symmetrically positioned arcs while the crucible is rotating ($\sim$ 10 RPM - rotations per minute) and cooled.

Growth apparatus

The crucial parameter of the initial step is the homogeneity and shape of the melt. When the melt has too low surface tension, the gravitation force squeeze the melt into the flat-shaped button and it is not easy to obtain equilibrium state during the pulling process. On the other hand, when the surface tension is stronger than the gravitation force, the melt forms

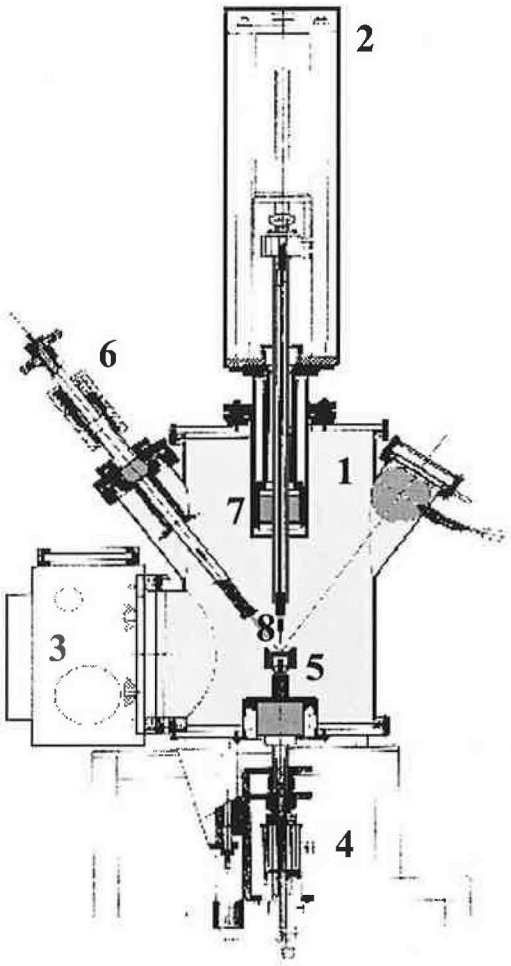

Figure 3.3: Schematic cross-section of a tri-arc furnace. Only one arc is shown. 1 - chamber, 2 - pulling head, 3 - glove box, 4 - rotating mechanism of crucible, 5 - crucible, 6 - torch, 7 - ferofluidix, 8 - sample.

ellipsoid and tends to stabilize itself and reach the equilibrium state, which is ideal to start the pulling procedure (see Figure 3.5).

When pulling from the polycrystalline seed or from unsolvable rod (tungsten), the so-called random necking process comes into play (see Figure 3.6). The aim of this technique is to propagate one crystalline grain and to enlarge it across the whole diameter of pulling ingot while decreasing the cross-section of the pulled ingot. This eliminates other site-grains. The neck thickness is typically $\sim$ 1 mm; the more slowly is the ingot necked, the better crystal and lower mosaicity is obtained. Generally, a higher pulling speed causes tapering of the ingot.

Within the next step, the ingot is broadened (up to typically 4 - 6 mm in diameter). A serious problem occurs when the melt surface becomes overcooled or when the crystals breaks itself in a too thin neck - one must be careful not to loose the whole grown sample. Enlarging

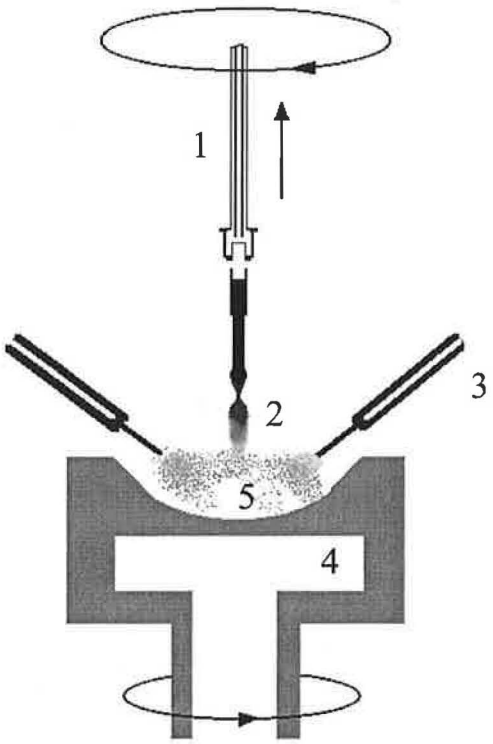

Figure 3.4: Modified Czochralski technique utilized in the tri-arc furnace at DCMP. 1 - pulling head, 2 - seed with a grown ingot, 3 - tungsten torch with arc, 4 - water-cooled crucible, 5 - melt.

of the ingot is often realized with the decrease of arc current and pulling speed. When the satisfactory piece of material has been grown, proper tapering of the sample separate the crystal from the melt.

One of the crucial parameters of the system is the position and shape of the so-called interface between the liquid state (melt) and the solid state (ingot). As the interface moves higher (up from the melt), the sample tends to slender, while it subsides, the diameter of the sample increases. While looking more in detail at the pictures of the crystal growth, one can see, that the curvature of the interface substantially differs when increasing or decreasing the diameter, respectively. When the interface follows an exponential-like shape, then the sample tends to increase the diameter (e.g. when enlarging ingot), while it follows tapering-like character the diameter decreases. A too steep exponential curvature of the interface generally signalizes strong tendency of the system to become overcooled, then the whole crystal might freeze and be lost.

An important criterium is the shape of an ingot after immediate pull-out from the melt. When the material is congruently melting, it tends to 'keep in touch' with its melt. The material then tends to form a long narrowing ingot. An opposite tendency can be observed in the case of incongruently melting material, which breaks apart forming a 'flat end'.

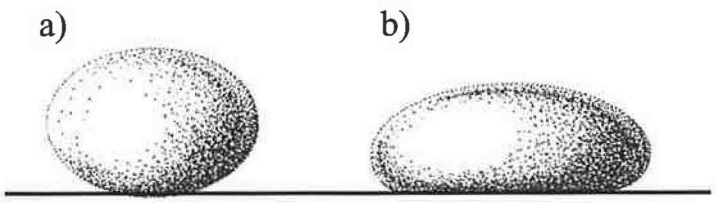

Figure 3.5: Ideal shape of melt (a) in comparison with a worst case (b).

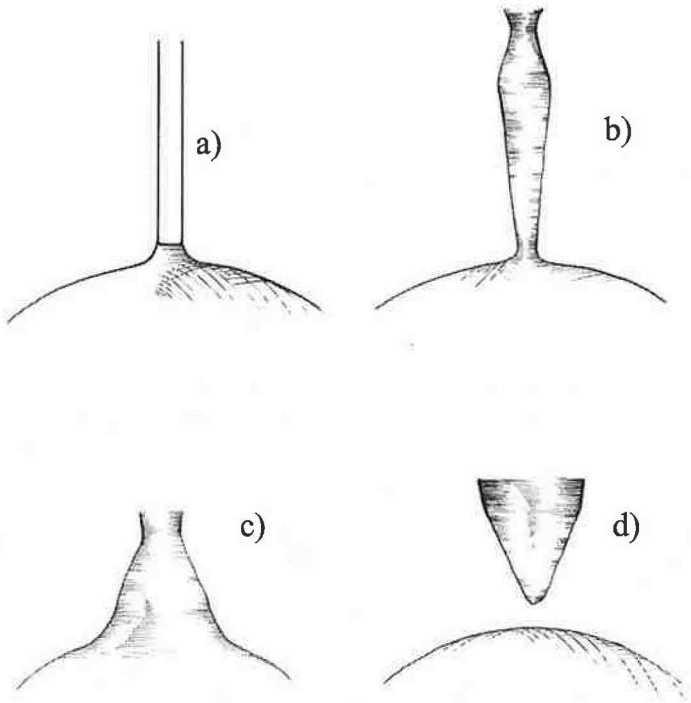

Figure 3.6: Growing process with random necking technique. (a) - initial step - dipping of a seed, (b) - necking, (c) - enlarging of an ingot, (d) - finishing procedure.

Synthesis of polycrystalline $CePt_3Si$-related compounds

Several trials of crystal growth of some 1:3:1 compounds were made. The materials were further studied either in the 'as cast form' or after additional treatment. The list of compounds together with the growth and applied treatment conditions are summarized in the Table 3.4.

3.1.3 Splat-cooling method

The samples of the nominal CePt3X, X = Si, B, Al, Ge composition were prepared by Antonio Gonçales in the splat apparatus of Instituto Technologico e Nuclear, Sacave'm, Portugal (*www.itn.pt*). The principle of the method is a rapid cooling of the liquid melt. Because of the very fast cooling rate (up to 10^5 K/s), the technique enables to stabilize meta-stable high-temperature phases or compounds formed by a peritectic reaction. In addition, different crystalline phases may be formed like quasicrystals, textures or completely amorphous/glassy metals. If a 'normal' polycrystalline material is formed, the grain size and layout often differs from those of the material prepared by simple re-melting.

In practise, the melt is rapidly splat by two massive water-cooled cooper blocks into a thin sheet. Recent modifications of the technique involve injection of the overheated melt on a fast-spinning plate or cylinder.

For further details concerning the splat-cooling, please see for example [73].

Before the splat-cooling procedure, the samples were melted in the mono-arc furnace and crushed into pieces of mass about 0.2 g. The list of materials treated by the splat technique is given in the Table 3.5. After the procedure, several samples were further annealed under different conditions (Table 3.5).

$CePt_3X$	label/ furnace	pulling speed (mm/hour)	seed/crucible rotation(RPM)	arc current (A)	additional treatment
B	A/1	8-10	4/4	19-32	-
B	B/1	8-12	2/2	18-28	annealed 8 days/950°C slow cooling
B	C/2	12-16	2/4	8-16	-
B	D/2	12-16	2/4	8-16	- 8 days/950°C slow cooling
Si	A/1	8-10	4/4	20-25	-
Si	B/1	6-8	4/4	25-28	-
Si	C/1	4-8	4/4	18-29	-
Si	D/1	4-8	4/4	12-16	- 8 days/950°C slow cooling
Si	E/2	8-14	2/4	12-16	-
Si	F/2	6-10	2/2	12-16	-
Si	G/2	6-10	2/2	12-16	- 8 days/950°C slow cooling
Ge	A/1	6-10	4/2	17-26	-
Ge	B/1	6-10	4/4	17-26	- 8 days/950°C slow cooling
Ge	C/1	6-10	4/4	17-26	-
Ge	D/2	6-10	4/4	12-16	-

Table 3.4: $CePt_3X$ compounds prepared treated by the Czochralski technique - growth parameters.
1 - Tri-arc furnace (DCMP), 2 - Tetra-arc furnace (IMR)

$CePt_3X$	Label	annealing (time/temperature)	cooling
B	1	0	-
B	2	8 days/950°C	slow
Al	1	0	-
Al	2	0	-
Al	3	8 days/950°C	slow
Si	1	0	-
Si	2	8 days/950°C	slow
Ge	1	0	-
Ge	2	0	-
Ge	3	8 days/950°C	slow
Ge	4	8 days/950°C	quenched

Table 3.5: Compounds prepared by the splat-cooling method.

3.1.4 Solid-state electrotransport

Introduction

In principal, the differential movement of solute ion with respect to solvent ions by electrotransport offers the possibility of purification. As already mentioned the electrotransport process is very inefficient, and so, in terms of purification per unit of energy consumed, any technique based on electrotransport would appear to be of limited value. Nevertheless, techniques have been developed which provide small quantities of high-purity metals, superior to that produced by other methods. Such materials are highly desirable in experimental solid state research, where the high-purity is a pre-requisite. The purification technique, often referred to as solid state electrotransport (SSE) processing, has certain advantages, particularly for reducing the concentration of interstitial impurities. The realization of a high degree of purification, however, does require careful attention to many experimental details.

Principle of SSE processing

During the SSE process, a metallic rod containing initially a dilute-uniform concentration, C_i^0, of a solute i is subjected to a direct current. As a consequence, the rod is heated (assuming constant temperature thorough its length). Furthermore, any solute flux through the ends or the surface of the rod is neglected. The migration of the solute (in the x direction) may be expressed as follows:

$$J_i = -U_i C_i E - D_i \frac{dC_i}{dx} \tag{3.1}$$

(U_i - solute i mobility, C_i - actual concentration of the solute i, E - electrical field intensity). After a sufficiently long time, the concentration at any point is time-independent (J_i) and a steady state is reached. The electrotransport flux (towards the anode) balances the back diffusion flux (towards the cathode). The concentration decays exponentially:

$$C(x, \infty) = K \exp \frac{-UEx}{D} \tag{3.2}$$

for interstitial solutes (and very short rod), the migration constant K is given by:

$$K = \frac{C_0 UEl}{D} \tag{3.3}$$

where l is the rod length. The general solution of the migration equation is more complicated and is given in [74].

Limiting factors

There are several limitations for the SSE processing, which are now briefly discussed.

- *Approach to the steady state*: to utilize the SSE technology efficiently, one must consider rather long time of processing. Obviously a time longer than l/UE is required in order to approach the steady state: in practice such times are about 100 - 300 hours.

- *The electric field*: the greatest degree of purification occurs when UE/D reaches a maximum. The value of E that can be used is governed by the rate at which the heat is removed from the rod. For a given geometry, the maximum value of E will be limited by the melting point of the purified metal or its volatility. In vacuum, the heat is lost just by radiation, so the electric field can be enhanced by decreasing the diameter of the processed rod contrary to reducing of the quantity of the purified material. As the ratio U/D does not necessarily increase with temperature (and so with E), the maximum value may occur well below the melting point. However, the "U/D maximum" criterion does not take into account the time necessary to reach the steady state. As U dramatically decreases with decreasing temperature, the processing time may become excessive at the lower temperature. The ratio U/D does not generally change markedly with temperature so it is usual in practice to maximize E.

  The purity of the material also increases with increasing length of the used rod. However, it must be balanced against a longer time to reach the steady state. Usually, typical rod diameters are up to 6 mm and length $\sim$ 100 mm, and $E \sim 10 - 40$ Vm^{-1}.

- *Flux through the ends*: a state of zero flux at the ends of the purified rod is nearly impossible to achieve in practice. It is very difficult to obtain contacts for the electrical current that do not react with the metal at the processing temperature, or are not themselves a source of contamination due to diffusion or electrotransport of impurities into the material. Two alternative methods have been used to reduce this problem. One way is to employ 'cold contacts'; the temperature of the ends of the rod are maintained several hundreds of degrees below that of the major portion of the rod. Although this

effectively reduces the flux of solutes into the rod to zero, the temperature gradients at the ends significantly reduce the mobilities of the migrating species and prevent the impurity concentration from reaching the ideal limits. By processing for a period of time, removing the ends and re-processing the central portion, notable improvements in purity have been obtained. The second method is to butt-weld a length of rod previously purified by SSE to the end of the specimen rod.

- *Contamination by the environment* is probably the most significant limiting factor. It has been shown that at pressures larger then 10^{-7} Pa such contamination can seriously limit the amount of purification possible. The vacuum level is nowadays kept in the range of $10^{-9} - 10^{-10}$ Pa. If the metal exhibit a very high vapor pressure at the desired processing temperature, inert gas must be used to reduce the rate of vaporization. High-purity He or Ar are employed with strict requirements on the partial pressures of diluted contaminants (below 10^{-7} Pa).

- *Types of impurities*: whether a metal may be efficiently and effectively purified by SSE technique depends on the mobilities of the impurities. The process is only really applicable for solutes for which $U >\sim 10^{-8}m^2$ and $U/D >\sim 10^2V^{-1}$. Such conditions are usually satisfied by intersticial solutes only. To achieve a high-purity product, the rod should initially contain as low concentration of the slow-moving substitutional impurities as possible. The presence of such impurities will often impose a limit on the maximum purity obtainable. Earlier studies in 1970's [75] discovered that cerium and/or gadolinium impurities, which one may expect to be substitutional and therefore slow-moving, migrate rapidly with $U \sim 10^{-7}m^2V^{-1}s^{-1}$ and $U/D \sim 10^2V^{-1}$. Examples include iron and cobalt in cerium and silicon in gadolinium. Therefore, these particular impurities may be effectively removed by SEE in a reasonable length of time.

Refining of rare-earth metals

The rare-earth metals have a very high affinity for the interstitial impurities like hydrogen, carbon, nitrogen and oxygen. Moreover, they are difficult to prepare with low-impurity content. Typical absolute purities of commercially available materials are 99 - 99.5 %. Impurities, even in small quantities, can influence to an appreciable extent the intrinsic properties of rare-earth containing materials. Therefore, high-purity metals must be used in any experimental investigations. Numerous investigations of the SSE treated rare earths showed positive effect on the interstitial impurities content [75]-[80]. As an example results of gadolinium investigations are presented in the Table 3.6. It has been further observed that carbon, oxygen and nitrogen migrate towards the anode [81].

Under certain conditions crystal growth may occur simultaneously with the purification processing [82]. The resultant crystals exhibit a high degree of structural perfection, as well as high purity. One disadvantage is that the orientation of single-crystals grown in polycrystalline specimen rod is not controllable. The problem has been overcome using the augmented SSE technique [82] in which the advantage of zone-melting in providing an orientated sample of a suitable shape have been combined with refining by SSE. Two effects accrue simultaneously - any substructure is significantly reduced and the overall purity is enhanced whilst the original orientation is maintained. To account for the removal of the

Original Gd ppm at.	Impurity	Purest section ppm at.
472-708	H	
-	N	-
4699-5210	O	106
1000	C	< 100
200-400	others	50
99.25 - 99.36 %	Total purity	99.94 - 99.95 %

Table 3.6: The purification of Gd by SSE processing according to [82]. Conditions - Rod diameter: 5.5 mm, Processing time: 140 - 169.5 hours, Temperature: 1100°C, Pressure: $\sim 2 \times 10^{-8}$ Pa

defect substructure, the electric field is though to assist the migration of sub-boundaries (defects) within the crystal and so enhance its quality.

Nowadays the SSE technology is mainly used for preparation of high-quality starting materials (rare earths) for crystal-growth of intermetallic compounds. In addition, the grown samples may be secondary treated by SSE to enhance the structural perfection and to decrease the impurity level as low as possible. The high-quality crystals are then used in many areas of solid-state research, namely for fine investigations of transport properties and electronic structure [84, 85, 86, 87].

SSE apparatus

Recently the new-generation SSE apparatus was designed and installed in the Department of Condensed Matter Physics (DCMP). The device was constructed by Vakuum Praha company under our supervision. The development process was strongly supported by fruitful consultations provided by prof. Kunihiko Maezawa from Toyama Prefectural University, Japan, who has more than 25 years of experience in the SSE technique. The power supply and control electronic was designed and fabricated by Jan Matlák (DCMP).

The most crucial aspects of the SSE processing were engineered by modification of the so far employed features. The most important points were the long-term stability of ultra-high vacuum (10^{-9} - 10^{-10} Pa) and special design of the sample holders. In addition a quadrupolar mass spectrometer (QMS) was involved to analyze the evaporants in the working chamber during the purification process. The prototype of the SSE system is depicted in the Figure 3.7. In the following part, the most important constituents of the device are discussed.

- *Working chamber*

  The working chamber is fabricated from stainless steel equipped with a chamber-baking system. The few-day baking procedure always starts the SSE processing in order to degas the chamber from residual gases and possible contaminants (e.g. traces of solvents used for cleaning).

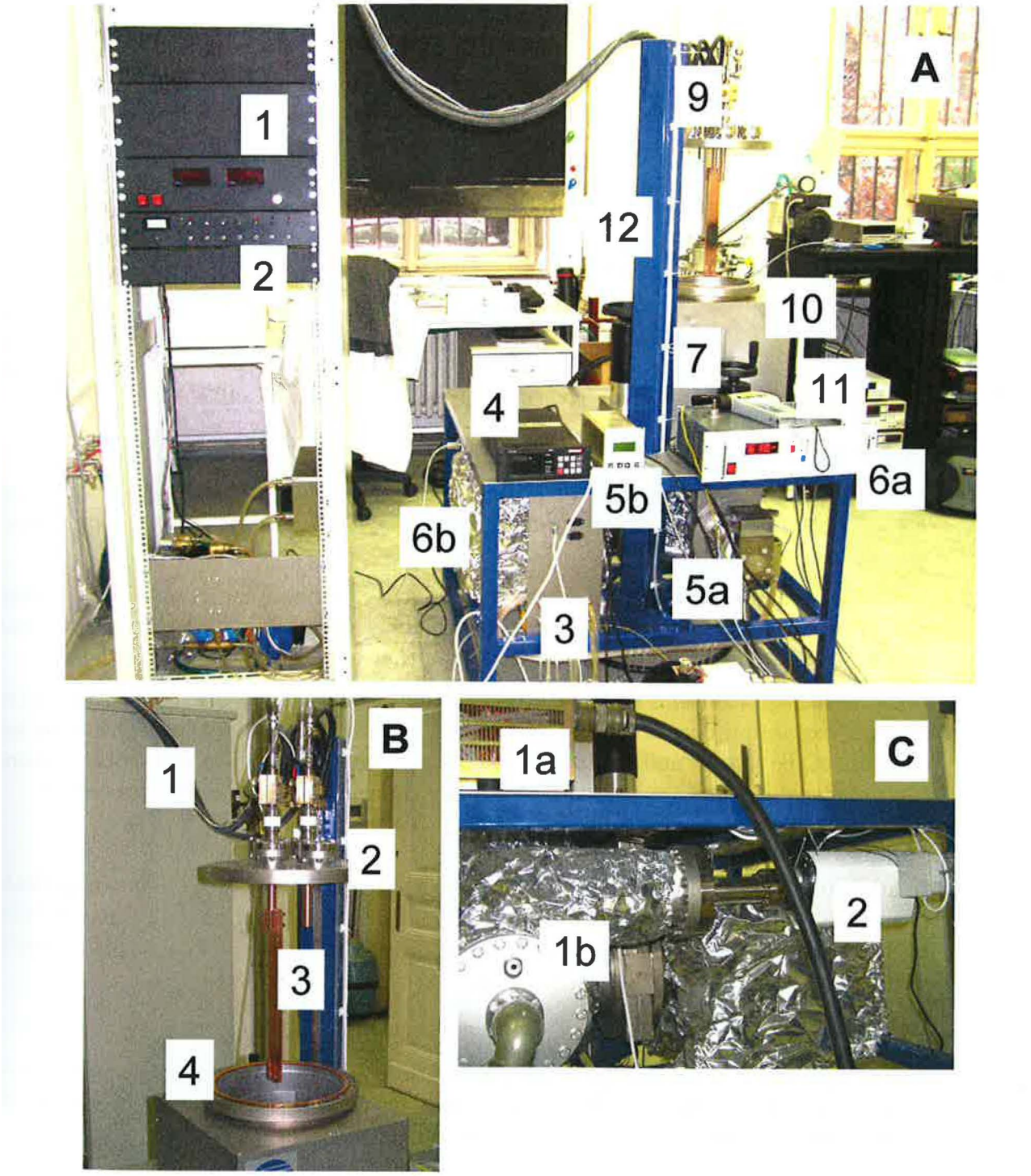

Figure 3.7: The SSE apparatus.
A - The SSE apparatus during testing period in technological laboratory, DCMP.B - Detail of the upper flange.C - Detail of the Ti-sublimation pump and QMS connections to the SSE system. For labels, please, see the text.

- *Pumping system*

  The evacuating aggregate consists of a combination of four powerful pumps employed to subsequently evacuate down the working ultra-high vacuum conditions. The pre-vacuum is managed using the oil-free rotatory pump (TriScroll TM 300, by Varian). The satisfactory pressure (10^{-4} Pa) for the ultra-high vacuum pumps to be started is obtained using the turbomolecular pump (Turbomolekular-Drag-Pumpe TC 600, by Pfeiffer Vacuum). The high-capacity ionic pump (Ultra-high vacuum ion sputter triode pump - ISP, by Vakuum Praha) enables to decrease the chamber pressure to 10^{-7} Pa. In synergy with the sublimation titanium pump equipped with a liquid-nitrogen cryopanel (TSP 929, by Varian) the pressure in order of 10^{-10} Pa can be stabilized in a long term period. The sublimation pump can adsorb large portions of gas in a very short time and is namely effective when the chamber pressure steeply rises, usually after the current value is changed.

- *Sample maintaining*

  Sample holder was constructed with respect to the mentioned difficulties (Figure 3.8). To ensure effective electrical and heat conductivity through the system, cooper metal was used as the main constructing material.

  To eliminate diffusion of the holder-material into the sample, molybdenum spacers placed between the sample and the cooper holders were fabricated (the molybdenum diffusion rate is negligible in comparison with that of cooper).

  Because the treated rod is supposed to be heated close to its melting point, a significant thermal expansion occurs during the current loading. To avoid any deformation and cracking of the sample and to keep the current and heat transfer smooth, springy cooper contacts were designed to respect the volume changes during the SSE procedure.

- *Cooling system*

  In addition, cooling closed-cycle was built for cooling the turbomolecular pump, chamber walls, and the high-current bushings. Finally, the working chamber may be filled by high-purity argon atmosphere to avoid a direct contact of a SSE-purified material with the air.

- *Sample-temperature control*

  The temperature of the sample during rafination, which is one of the important controlling parameters besides the pressure and the applied current, is detected by the optical infrared thermometers covering the range: 0 - 2500 °C.

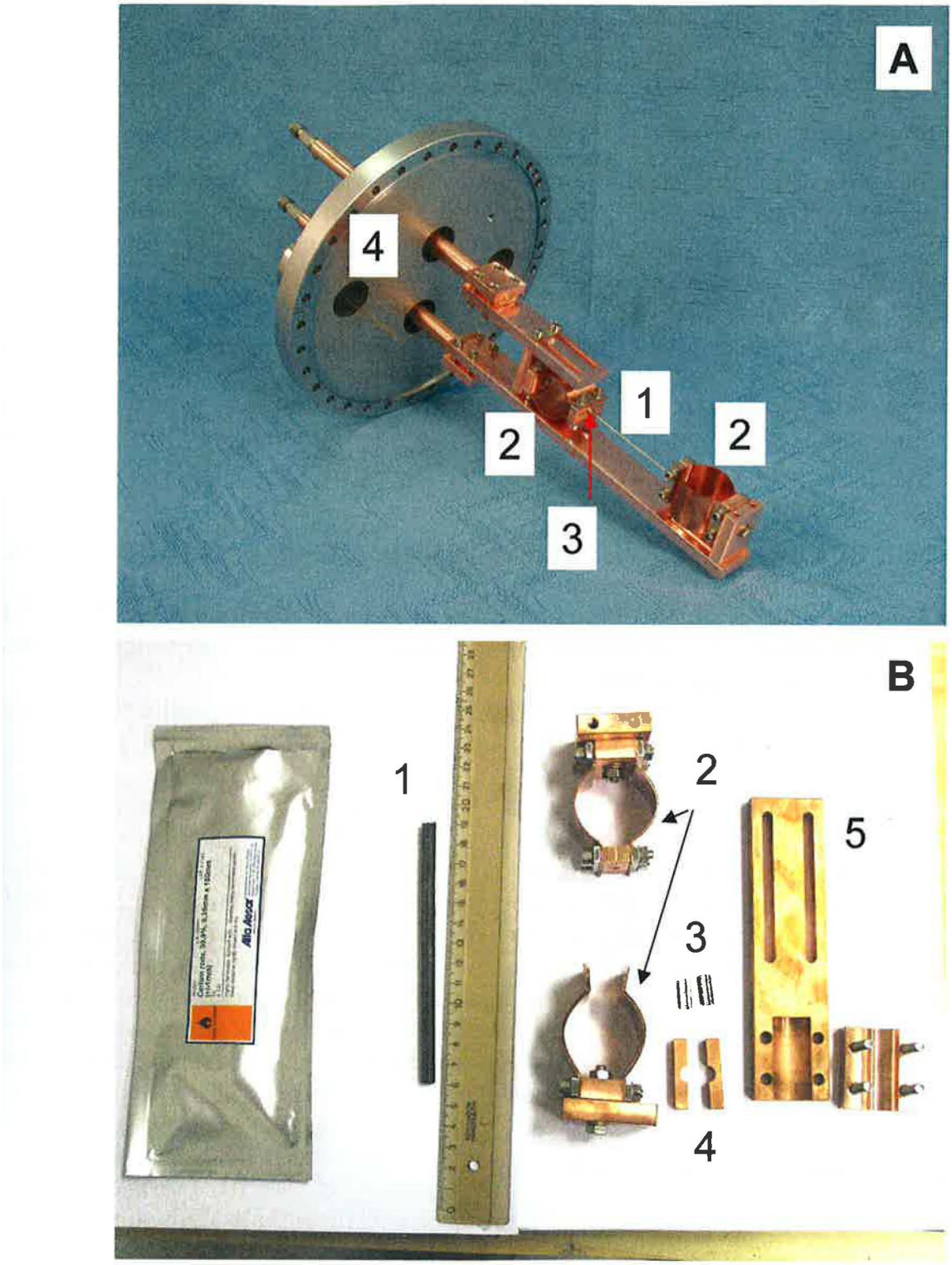

Figure 3.8: The SSE sample holder with the rare earth rod used as a sample.
A: 1 - testing sample (tungsten wire), 2 - springy cooper contacts, 3 - gripping of the sample.
B: 1 - the Ce rod, 2 - the sample holder, 3 - molybdenum spacers, 4 - cooper holders, 5 - parts of the holder, which are connected to the current supply.

3.2 Sample characterization

3.2.1 X-ray diffraction

Experimental setup

The samples have been investigated by x-ray powder diffraction (XRD) at ambient conditions with a conventional diffractometer (Seifert, installed at the Department of Condensed Matter Physics). The diffractometer was set up in the Bragg-Bretano geometry using the α_1Cu irradiation + monochromator.

The samples were investigated either directly in the bulk form or as powders. For the latter experiment, of about 300 mg of each sample were carefully powderized in a agate bowl under aceton (to decrease oxidation rate during the procedure), subsequently placed on a glass and fixed by aceton (or ethanol) solvent. Experimental results were further compared in order to inspect texture (preferred orientation) and/or strain in the prepared materials.

Basic data analysis

All the XRD data have been analyzed by the FullProf program [88], which enables to refine data from x-ray and neutron scattering.

The Rietveld analysis of the diffraction patterns [89] was performed according to the guidelines of the Commission on Powder Diffraction of the International Union of Crystallography for Rietveld refinement [90].

The basic principles of the Rietveld refinement are included in Appendix together with the instrumental function parameters of the Seifert diffractometer (Table C.1).

3.2.2 Laue method

The standard Laue method (in the reflection configuration [91]) has been used both to determine the single-crystallinity of the grown ingot and subsequently to orient the sample for further experiments. Laue patterns were taken on Micrometa 600 apparatus (Department of Condensed Matter Physics) with polychromatic W-radiation. Triple-axis goniometric head was used to fix a proper orientation of an ingot. When the orientation of a sample was fixed, the crystal was cut for further experiments using a fine spark cutter using a special sample holder, which enables to attach the goniometric head with the sample in the proper orientation.

3.2.3 Scanning electron microscopy

Microstructure and phase composition of all samples were investigated by scanning electron microscopy (SEM) at three collaborating institutes:

- Research Institute for Metals, Panenské Břežany, responsible contact: Jaroslav Uhlíř, device description: ZEISS DSM 940 equipped with wave X-ray micro-analyzer MICROSPEC WDX-3PC.

- Czech Academy of Sciences, Institute of Inorganic Chemistry, Řež u Prahy, responsible contact: Václav Tyrpekl, device description: PHILIPS XL 30 CP equipped with SE detector, Solid State and Robinson BSE detectors and EDX detector.

- Czech Academy of Sciences, Institute of Physics, Praha 6, responsible contact: Jiří Jurek, device description: microanalyser JXA-733(JEOL) equipped with BSE and EDX detectors.

For metallographic studies, the samples were polished with a diamond paste (up to the 0.5 μm roughness) and etched in a very diluted nitric acid.

Microstructures of all samples were examined using both back-scattered electrons and primary-emitted electron contrasts. Dispersion of the principal constituent elements was checked as well. Pure elements were used as standards. The weight concentrations have been obtained from the measured relative intensities (i.e. ratios to the standards). The data analysis was performed using standard procedures employing the corresponding company-provided software.

3.2.4 Residual electrical resistivity

The important aspect of the electrical resistivity measurements (the technique is described more in detail at the following subsection) is determination of the so-called *RRR* (residual resistivity ratio), which is a very important characteristic of a quality of the material.

A shown in the theoretical part, the total electrical resistivity ρ_{tot} can be described as the sum of following contributions:

$$\rho_{tot} = \rho_{\mathrm{ph}} + \rho_e + \rho_{\mathrm{mag}} + \rho_{\mathrm{imp}} \tag{3.4}$$

where ρ_{ph} is the phonon, ρ_{e} electronic and ρ_{mag} magnetic contribution, respectively. The ρ_{imp} is originated by disorder scattering of electrons on impurities and other imperfections in the lattice and is supposed to be temperature independent. As the *RRR* is obtained as a ratio of the electrical resistivity at room and at the lowest available temperature:

$$RRR = \rho_{T_{\mathrm{room}}}/\rho_{T_{\mathrm{low}}}. \tag{3.5}$$

the *RRR* (as a ratio of two experimental values obtained in the same configuration) is independent on the geometry of the sample and obviously is not affected by the absolute experimental error.

In fact, the *RRR* reflects the purity/quality of the material. Generally, a good single crystal has the *RRR* over 30. A sample suitable for the fine Fermi surface investigations by means of the deHaas - van Alphen effect must have the *RRR* over 100, and additionally the absolute value of the ρ_{T_low} should not exceed 1 $\mu\Omega$cm.

3.3 Macroscopic investigation techniques

The magnetic and transport properties were investigated using the PPMS - Physical Properties Measurements System by Quantum Design, San Diego (*www.qdusa.com*). It is an

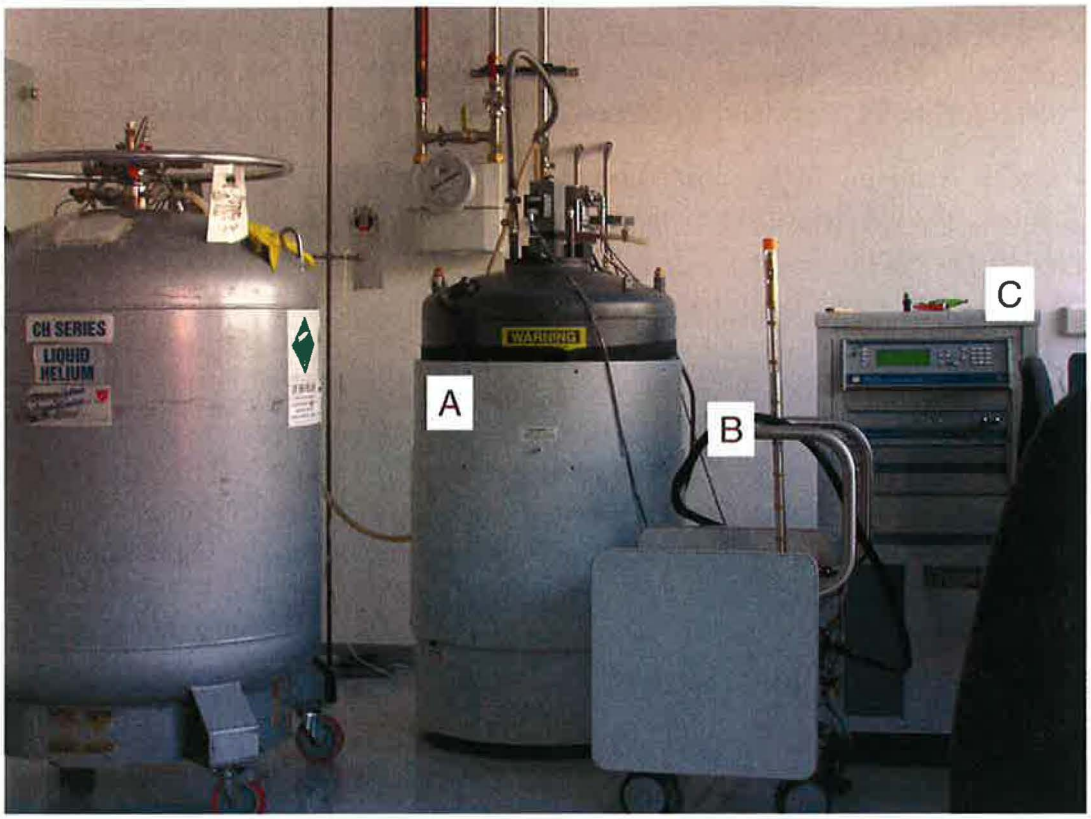

Figure 3.9: Installation of the PPMS 14 T.
A - He cryostat with the LN_2 shielding, B - ^{3}He system, C - controllers.

open-architecture, variable temperature-field system that is optimized for variety of experiments as listed further. PPMS is controlled via the MultiVu Windows-based software that contains all the functions essential for each measurement application. The system comprises a He cryostat with liquid N_2 shielding. The sample chamber involves sample mounts coupled to the 12 electrical leads built into the cryostat insert. The standard configuration allows to measure in the temperature range 1.9 - 400 K (1000 K[1]). In addition, ^{3}He closed-system enables to investigate heat capacity and transport properties down to 0.35 K. PPMS devices equipped with 14 T and 9 T superconducting coils (installed in the Joint Laboratory for Magnetic Studies) were at disposal.

Specific heat

The Heat capacity option in PPMS implements a 2τ-relaxation method. During the experiment the sample is placed on a sample holder ('addenda' - thin sapphire plate) and high vacuum is kept. The heat pulse and the measured sample temperature is maintained by 8 wires (4 wires in case of the ^{3}He option) connected directly to the sapphire plate. For further details concerning the experimental method and raw data evaluation, please see [94].

[1]High-temperature vibrating sample magnetometer only.

Measurements were done on plate-shaped samples of a weight of 2 - 10 mg. One surface of the sample was adjusted to a very smooth plane by which was the sample coupled to the heat capacity measuring system. To improve the thermal link between the sample and the sample holder a small amount of apiezon grace was used as a contact-fixing medium.

Magnetization and a.c. susceptibility

Majority of the samples was investigated using the standard PPMS ACMS option, which enables to measure both the magnetization and the a.c. susceptibility. The magnetization is recorded by the extraction technique and the absolute value of the magnetic moment is obtained by fitting the resulting signal to the standard-calibrated curve. Some materials (those with a very low response) were also measured using the VSM option (vibrating sample magnetometer), however, only the magnetization (and therefore static susceptibility) can be obtained. For further details concerning the methods, please see [94].

The samples for magnetization measurements were used in different forms. All polycrystalline samples were used as powders consisting of randomly oriented grains fixed by a nonmagnetic glue in a small gelatine ampule. The mass of those samples was approximately 50 - 150 mg depending on the measured signal. The pure rare earths and the samples prepared by the splat-cooling technique were investigated in the bulk pieces (the sample mass was adjusted according to the absolute measured signal). The single-crystalline or highly textured materials were investigated with orientation of the magnetic field along the principal crystallographic directions. For some compounds, both the bulk and the powder forms were measured in order to compare the obtained results.

Electrical resistivity and magnetoresistance

The a.c. electrical resistivity and magnetoresistance measurements were performed on PPMS apparatus by standard four-probe method using the ACT option [94]. The current and voltage contacts were made by silver or gold paste using silver wires. Two independent channels were available to measure two samples in one run. The excitation current was 0.5 - 10 mA and the frequency 30 - 80 Hz.

The absolute error of resistivity measurements (about 10%) was mainly caused by the uncertainty of the geometrical factors and from the occasionally appearing microcracks in the samples.

Thermal expansion and magnetostriction, thermal conductivity

Minority of the samples were investigated by additional techniques. The thermal expansion and magnetostriction was measured on the pure Ce using a capacitance cell implemented in the PPMS apparatus. Thermal conductivity of pure Ce was measured using the TTO option in the PPMS. For further details of the techniques, see e.g. [94, 95].

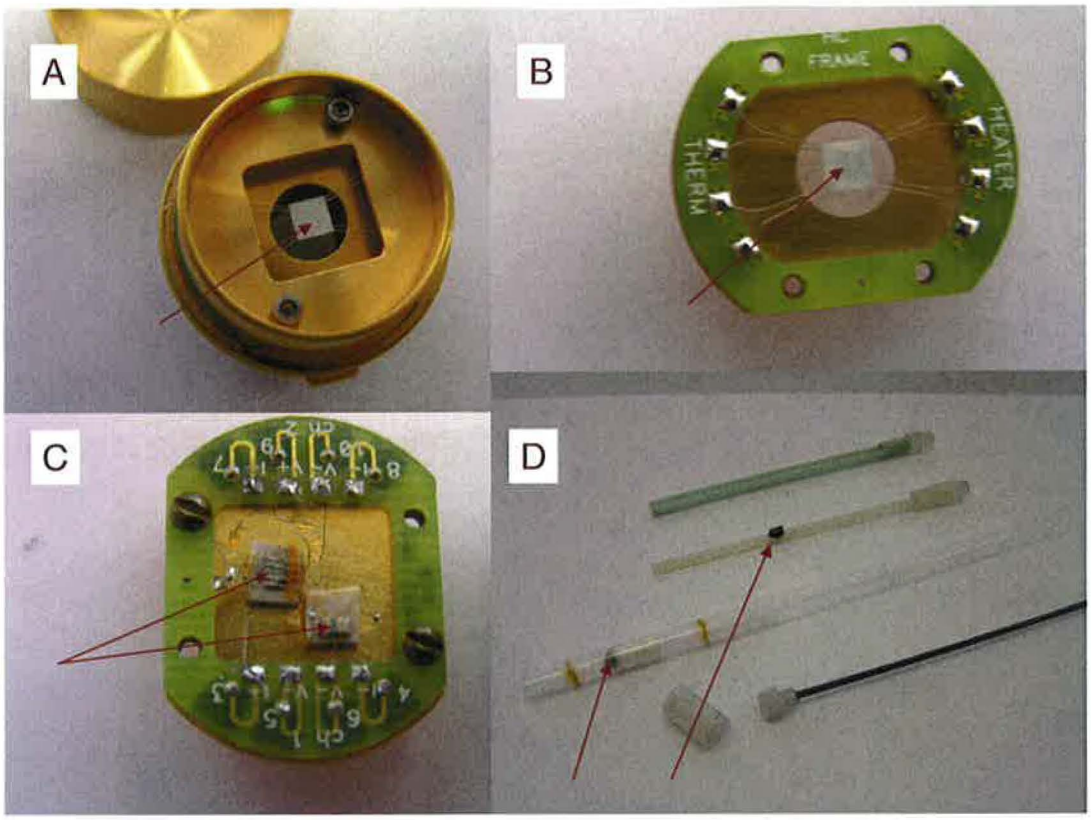

Figure 3.10: Sample set up used in the PPMS equipment.
A - puck for the heat capacity measurements, B - heat capacity puck for the ^{3}He option, C - puck for the electrical resistivity measurements, D - sample holders for the magnetization measurements. The arrows points to the sample position on the holders.

3.3.1 High-field magnetization and magnetoresistance

Magnetization and magnetoresistance were measured up to 48 T in the temperature range from 1.6 to 10 K in the Leibniz-Institut für Festkörper- und Werkstoffforschung (IFW), Labor für hohe gepulste Magnetfelder, Dresden in cooperation with Nadjezda Kozlowa. The most important experimental facts are discussed below. For more details concerning the high-field facility, see e.g. [96, 97, 98], *http://www.ifw-dresden.de/eindex.htm.*

Magnetic field time-dependence

The maximum field of 48 T is reached about 10 ms after the start of the measurement. The pulse shape of the field can be described as a sinusoidal oscillation of one period with decreasing amplitude as a function of time. The typical signal time-dependence during the pulse together with the used equipment is depicted in the Figure 3.3.1.

Magnetization

The high-field magnetization measurements were used for determination of the trend to saturation and metamagnetism in the $CePt_3Si$ related compounds.

The typical sample mass was set in correspondence to the expected measured signal $\sim$ 2 - 5 emu based upon the preliminary 9 T - measurements (performed in PPMS apparatus).

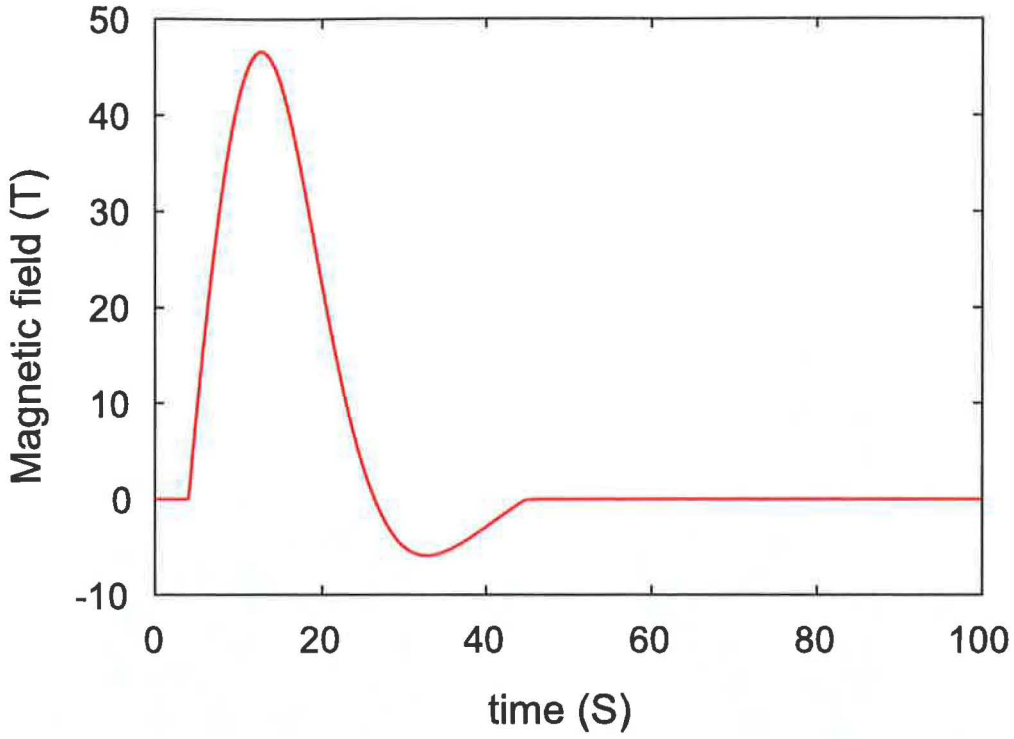

Figure 3.11: Time-dependence of the 50 T-field pulse.

Except series of polycrystalline samples, several highly-textured materials were investigated in principal orientations with respect to the magnetic field.

The magnetization measurement system was calibrated by low field data (up to 7 T) with a SQUID (Quantum Design) using a Ba-ferrite sphere and Ni.

Magnetoresistance

Measurements of magnetotransport phenomena of the $CePt_3Si$ related compounds in high magnetic fields allow to investigate electronic properties of metals such as the shape of the Fermi surface at the Fermi energy and the charge carrier concentration, since the current originates from states near the Fermi surface (as described in the theoretical part of the thesis).

The magnetotransport measurements were performed by four-probe a.c. current (alternating current) technique. The a.c. current was applied with the frequencies 10 kHz - 150 kHz.

The developed data acquisition magnetotransport measurement system consists of hardware and software subsystems. The hardware system includes digital oscilloscopes, generator, amplifiers. A fiber optic GPIB interface is used as the communication interface. This and the use of non-interruptible power supplies for oscilloscopes and generator, and the inner battery for the amplifiers allows one to reduce noise voltages and currents caused by ground loops and the 220 V power systems. The generator is used in the burst modulation mode. In that mode the duration of the generator signal is set equal to the time of the field pulse (e.g. 100 ms), and the signal is synchronized with the magnetic field pulse. This allows the

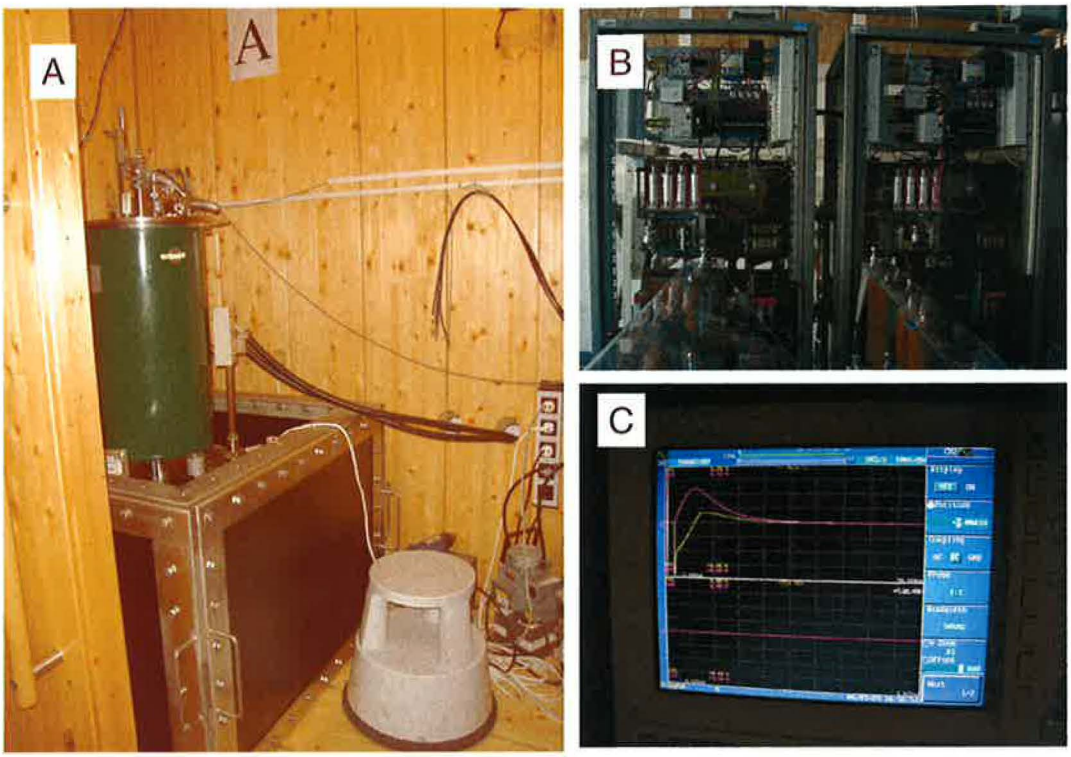

Figure 3.12: Pulsed-field facility in IFW, Dresden.
A - cryostat with the coil, B - capacitor bank, C - signal dependence during the pulse recorded on the oscilloscope.

enhancement of the signal to noise ratio by means of increasing the amplitude of the current applied through the sample without strong Joule heating.

Upon completion of the measurement, the experimental data are transmitted from the oscilloscope to the measuring computer and saved on hard disk for further analysis by the data processing program. The program includes algorithms based on DFS (Discrete Fourier Series), LSM (Least Square Method) approaches as well as on a new approach based on the FIR (Finite Impulse Response) filtering.

The requirements on the sample used in the experiment are: resistance at least 1 mΩ, the maximum length below 4 mm, and precise full-contact connection of the current and voltage contacts. The last condition ensures suppression of the parasitic voltage signal/loops, which might be induced during the magnetic field pulse. To fix the above mentioned conditions preliminary transport experiments were performed in the PPMS on the same samples as used for the high-field measurements.

3.4 Microscopic investigation techniques

Microscopic nature of magnetic interaction in some $CePt_3X$ compounds together with their crystal structures were investigated by neutron scattering. In the following section, some introduction to the neutron diffraction with focus on magnetic scattering is given. Finally,

experimental arrangement used in the investigations is briefly described.

3.4.1 Neutron diffraction

The essential advantage of the neutron diffraction compared to the X-rays is the capability to register elements with small atomic radius (e.g. H, C, N). The non-zero spin of neutrons is another feature, which distinguishes them from x-rays. As a result, the neutrons are scattered not only by nuclei but also by magnetic moments of magnetic ions. This makes them suitable not only for structural but also for magnetic studies.[2]

Introduction to the neutron scattering theory

The scattering amplitude of an individual nucleus for neutrons at a scattering wave vector Q is given by:

$$a_{N_j} = b_j + c_j \sigma I_j \tag{3.6}$$

where $1/2\sigma$ is the neutron spin operator and I_j is the spin of nucleus. In the majority of cases the nuclear spins are randomly oriented (they order usually at 10^{-3} K), therefore, the second term does not contribute to the interference effects or coherent scattering. Then the scattering amplitude is equal to:

$$a_{N_j}(Q) = b_j \tag{3.7}$$

It does not depend on the scattering vector and has a constant value for each element. In the contrast to X-rays the scattering amplitude b_j for neutrons does not follow any general dependence and can be even negative.

The interaction of neutrons with some material is given by the scattering cross-section, which is equal to the number of neutrons scattered in a solid unit angle. For a fully ordered crystal with atoms occupying positions R_{lj}, the scattering is proportional to the square of the modulus of the scattering amplitude:

$$\frac{d\sigma}{d\Omega} = |\sum_{lj} b_j e^{iqR_{lj}}|^2 = \frac{8\pi^3}{V_0} \sum_{\tau} |F_N|^2 \delta(Q - \tau) \tag{3.8}$$

where τ are the positions of nodes in reciprocal space, and F_N is the nuclear structure factor:

$$F_N(Q) = \sum_j b_j e^{iQr_j - W_j} \tag{3.9}$$

with W - the Debye-Waller factor.

The interaction between neutron spin and atomic magnetic moment m_j, which includes both spin and orbital components, is a dipole-dipole interaction. The magnetic scattering amplitude is given by:

$$a_{M_j}(Q) = p\sigma M_{\perp j}(Q) \tag{3.10}$$

[2]For the main aspects of the neutron diffraction, please see further e.g. [99, 100, 101].

where $1/2\sigma$ is the spin operator of neutron $M_{\perp j}$ is the projection of vector $M_j(Q)$ - the Fourier transform of the magnetization density $M_j(r)$ around nucleus - onto plane perpendicular to the scattering vector Q, and:

$$p = \frac{\gamma e^2}{2m_e c^2} = \frac{\gamma r_o}{2} = 0.2696.10^{-12} cm. \tag{3.11}$$

In terms of magnetic form factor $f_j(Q)$ and projection of the magnetic moment m_j onto the scattering plane, the magnetic scattering amplitude can be rewritten also as:

$$a_{M_j}(Q) = p\sigma f(Q) m_{\perp j} \tag{3.12}$$

Because of the $m_{\perp j}$ term the magnetic scattering amplitude is highly anisotropic as expected from the dipole-dipole interaction. The anisotropy depends on the mutual orientation of the magnetic moment m_j and scattering vector Q.

The magnetic scattering cross-section, similarly to the nuclear one, is proportional to the square of the corresponding scattering amplitude summed over all crystal:

$$\frac{d\sigma}{d\Omega} = |\sum_{ij} a_{M_j}(Q) e^{iQ} R_{ij}|^2 = \frac{8\pi^3}{V_0} \sum_k \sum_r |F_{M\perp}(Q)|^2 \delta(Q - k - \tau) \tag{3.13}$$

with k - the propagation vector coming from the Fourier expansion of the magnetic moment distribution on position j of cell l:

$$m_{ij} = \sum_k m_j^k e^{-ikl} \tag{3.14}$$

and the magnetic structure factor given by:

$$F_{\mathrm{M}}(Q) = p \sum_j f_j(q) m_j^k e^{ikr_j} e^{-W_j} \tag{3.15}$$

Note that the magnetic structure factor is a complex vector, while the nuclear structure factor is a complex scalar. For a perfect crystal the intensity due to nuclear scattering corresponds to the delta functions at the nodes of the reciprocal space, and for a perfect magnetic structures the intensity due to magnetic scattering concentrates on delta functions located at:

$$Q = \tau + k \tag{3.16}$$

for different τ nodes of the reciprocal lattice and for the different propagation vectors k.

Magnetic structures description

In the general case, the k vector may be at any point of the first Brillouin zone, and will define either an incommensurate structure or a long period commensurate one. The latter behaves like the former from the neutron diffraction point of view. Two types of incommensurate structure exist, depending on the dimension of the irreducible representation:

- **Sine-wave modulated structures** - all magnetic moments are of different lengths. Such structures are often observed at higher temperatures, in the vicinity of T_N, where the differences in the length of ordered moments are due to the thermal disorder. In the low temperatures, unless ground state is a singlet, the length of the ordered moments tend to become equal by squaring of the modulation, and the occurrence of new harmonics of k.

- **Helical structures** - magnetic moments are ordered in a helix and can be described with propagation vectors parallel to a 3, 4 or 6-fold symmetry axis with moments rotating in an easy plane perpendicular to this axis. In contrast to a sine wave modulation, a helical structure can remain stable down to low temperature.

Although the general case for propagation vector is any point of the first Brillouin zone, certain points of this zone are symmetrical for all the properties of the crystal, including the magnetic hamiltonian. Therefore the hamiltonian presents extremum for these k values, possibly a minimum which defines a commensurate magnetic structure.

An important point to notice, in the case of commensurate structures, is that the Fourier coefficients are real, and imply the modulation of the magnetic moments.

Magnetic correlations, short-range order

In many systems with unpaired electrons, no long-range magnetic order exists, however, a kind of local interspinal exchange develops below a characteristic temperature. In general, the local exchange may be of ferro- or antiferromagnetic nature. The typical examples are the so-called spin glasses.

A spin glass is a disordered material exhibiting high magnetic frustration. The origin of the behavior can be either a disordered structure (such as that of a conventional, chemical glass) or a disordered magnetic doping in an otherwise regular structure. Frustration refers to the inability of the system to remain in a single lowest energy state (the ground state). Spin glasses have many ground states which are never explored on experimental time scales. In fact, it is the 'time dependence' which distinguishes spin glasses from other magnetic systems.

In addition, elastic neutron scattering may serve as a probe for magnetic correlations. For example, it may help to distinguish between crossover in the local dynamics or cooperative short-range magnetic ordering in systems with Kondo-type interaction.

In case of intrinsic inhomogeneities, a long-range magnetic order may be reached through a percolating processes of nascent magnetic clusters (e.g. CeNi - CeCu system, [102]). In this regime, the system shows a kind of temperature-dependent short range order.

Concerning the diffraction on non-ordered solid, the total intensity ma be written in the form:

$$I(Q) = I^S(Q) + i(Q), \tag{3.17}$$

where I^S is the self-dependent scattering and i is the distinct (interference)s scattering. The required structural (or 'magnetic') information may be obtained by means of sine Fourier transformation of the interference function $Qi(Q)$.

In a magnetic system, the difference between the diffraction pattern in the 'ordered' and paramagnetic state yields the corresponding magnetic differential correlation function

($Q_i^M(Q)$). For a system without any correlation between the magnetic moment directions and the interatomic vectors, the $Q_i^M(Q)$ may be transformed as described above to give directly the magnetic correlation function. It depends on the relative positions and the magnetic moments of the magnetic ions and hence it is possible to extract information concerning both the atomic and magnetic structure.

Measurements on magnetic systems are usually limited to $Q < 10$ Å^{-1} due to fall off in the intensity of magnetic scattering with increasing Q.

Powder neutron diffraction experiments

The neutron diffraction studies were performed in the Institute Laue-Langevin, Grenoble (*www.ill.fr*). Since the powder neutron diffraction is well known technique and does not belong to the key techniques related to the thesis, only the most important facts are summarized below together with relevant references to the literature.

The high-resolution powder and stress scanning diffractometer D1A was used for room temperature structure measurements of $CePt_3X$, X = Si, C or Ge samples.

The D20 - 2-axis high intensity diffractometer equipped with a large microstrip detector was employed for the ultra-low temperature scattering on $CePt_3C$ and $CePt_3Ge$, respectively. Because of very low magnetic moments expected on the Ce ions, the D20 was selected because of very high neutron flux ($\sim 10^8$ neutrons per second on cm^2) and possibility of dilution refrigerator maintenance without significant intensity reduction.

Approximately 6 grams of each sample was used for the diffraction experiment. For the room-temperature diffraction, the samples were crashed onto rough powders $\sim 100\mu$m (to eliminate texture effect) and placed in a vanadium container. The ultralow temperature investigations required $\sim 50\mu$m grain size of the used powders. The samples were kept in a massive cooper container, which ensured adequate thermal exchange between the cryosystem and the sample.

The pseudo-Voight function was adapted for the data analysis. The instrumental parameters fixed for the neutron diffractometers are summarized in the Appendix, Table C.2.

Chapter 4

Rare earth transition metals

I am rare earth metal.
I temper last forever and ever with internal constancy,
and when I am in air, blue night air, I burn.
I am loose and wild with the momentum of the things I hold inside.
I am dangerous a threat to myself and others.
Tonight there will be nothing in which to put my passion
but to run run and run and run into this night fall to the lawn
press my face to cool grass smell the must of earth,
the only crucible vast enough for yearning.

Rare Earth Metal by Erin L. King

4.1 Remarks on to-date knowledge

The rare earth elements form a chemically uniform group and include yttrium (Y), lanthanum (La) and the lanthanides cerium (Ce), praseodymium (Pr), neodymium (Nd), promethium (Pm), samarium (Sm), europium (Eu), gadolinium (Gd), terbium (Tb), dysprosium (Dy), holmium (Ho), erbium (Er), thulium (Tm), ytterbium (Yb), and lutetium (Lu).

The name 'rare earth' meant something else to early chemists. It was used because the rare earth elements were very difficult to separate from each other. They were not 'rare' in the Earth, but they were 'rarely' used for anything.

The outer electron shells of the lanthanides do not change within the period, therefore their chemical behavior is very similar. The differing atomic and ionic radii does affect their chemistry. As a result of the increased attraction of the outer shell electrons across the lanthanide period, the following effects are observed. Each of these effects is sometimes referred to as the famous *lanthanide contraction*[1]:

- The atomic radii of the lanthanides are smaller than would normally be expected.

[1]Without the lanthanide contraction a chemical separation of lanthanides would be extremely difficult.

- The ionic radii of the lanthanides decrease from 0.117 nm (La^{3+}) to 0.100 nm (Lu^{3+}) in the lanthanide period.[2]
- The third row of d block elements have only marginally larger atomic radii than the second transition series.
- The radii of the elements following the lanthanides is smaller than would be expected if there were no f-transition metals.

The physical properties are in contrast strongly dependent on the number of electrons in the $4f$ shell of rare earth metals. A large amount of experimental and theoretical work on the magnetic and transport properties of rare earth elements, alloys and compounds have been reported. In this chapter, brief outline focused on important aspects of the rare earth research is presented.

In spite of some new data in this chapter, for a main survey the reader is referred to [103].[3] However, most of the recent investigations are dealing with the magnetic properties of rare earth elements in their artificial form like ultrathin films or multilayer superstructures. The last part of this chapter is a *bonus* devoted to the surface magnetic behavior of some lanthanides deposited on the surface of nonmagnetic metals.

The following three sections comprise the most important aspects of solid-state chemistry and physics of Ce, Tb and Er - the rare earth elements considered in the experiment within the scope of the thesis.

4.2 Cerium

Cerium is one of the most fascinating elements of the periodic system. In its elemental form it exhibits several phases like an antiferromagnetic-, a paramagnetic- and a superconducting-phase. It is the only element with a solid-solid critical point and Kondo scattering. Many of these properties are attributed to the single localized $4f$ electron state close to the Fermi level.

Pure metallic cerium is of little use for practical purposes, it oxidizes very rapidly under exposure to (moist) air. It the most reactive element of the rare earth metals except for europium.

Alloys containing cerium though, are widely used. For instance inst used in cigarette lighters are made of a pyrophoric alloy. Other applications are in the manufacturing of glass and in the carbon-arc lighting used in the picture industry. Cerium oxides are used as glass polishing agent and in the walls of self-cleaning ovens as hydrocarbon catalyst. Cerous nitrate has even been used in medical treatment of seasickness and chronic vomiting.

Cerium is named after the asteroid Ceres which was discovered in 1801, only two years before the discovery of cerium in 1803 by the Swedish chemists Berzelius and Hisinger. It was first prepared as a metal in 1875 by Hillebrand and Norton. It is the most abundant of the

[2]Due to more stable 2+ valence in Eu and Yb in most common compounds, their metallic radii, however, surpass the monotonous trend.

[3]The most general information about physics and chemistry of rare earths are included in the well-known reviews: [104, 105, 106].

rare earth metals and is found in a number of minerals like: allanite, monazite, bastnasite, cerite and samarskite.

With an atomic number of 58 it is the first of the Lanthanide series. Much later, several phases were found. Only in the early fifties the purification of cerium improved sufficiently, that a reliable phase diagram could be made. Probably the most interesting phenomena of cerium is the isostructural phase transition which ends in a solid-solid critical point, where the phases on either side of the transition become indistinguishable. In the last fifty years, many theories have been proposed to explain this peculiar phase transition [109]. For a long time Cerium was known as the sole exception within elements revealing magnetism and superconductivity (in the α phase above 50 kbar), however, in 2001 superconductivity under pressure was amazingly found in the archetypal ferromagnet [108] - iron as predicted already in 1979.

The low pressure part of the cerium phase diagram is shown in Figure 4.1. The superconducting α' phase ($T_c = 1.8$ K) lies at much higher pressures and cerium turns into liquid at 947 K (0 GPa). The α and γ phases are believed to have the same crystallographic structure, the face-centered cubic structure (or fcc), but the α phase volume is 14 - 17 % smaller. The phase boundary ends in a critical point where the two fcc phases become indistinguishable.

At low pressures the β phase lies in between the α and γ phase and it has a hexagonal close-packed (or dhcp) structure. The phase is a nightmare for investigators who want to study the $\alpha \leftrightarrows \gamma$ phase transition.

The $\alpha \leftrightarrows \gamma$ phase boundary is an increasing line with increasing pressure and temperature. The phase boundary is not a line with a negative slope, with the γ phase below, because at constant pressure and increasing temperature the entropy should increase, which will only be the case if the volume increases. The transition is a order isostructural phase transition, which implies that hysteresis to be expected. Koskenmaki and Gschneidner combined data from several authors in a non-equilibrium phase diagram [110], which is redrawn in the right panel of the Figure 4.1.

The different phases with their crystallographic properties are summarized in Table 4.1. Up to now it is believed that there are no broken symmetries, which are obligatory for a critical point, although there is still reason for some doubt. In order to go smoothly from one phase to the other by applying pressure and raising the temperature, it is not possible that a symmetry is altered. A change in symmetry can not go smoothly and will thus involve a phase transition.[4] The phase transition from an fcc to a distorted fcc lattice was already found in lanthanum and praseodymium, the neighbors of cerium in the periodic table.

The valency is defined as the number of electron states in the occupied part of the conduction band that are participating in the conduction: the free electrons; thus not counting the $4f$ electrons. A change in $4f$ occupancy must therefore be accompanied by a change in

[4]Eliasberg and Capellman put forward that the critical point in cerium is in fact a "critical point of a continuous phase transition", which is now called a tricritical point [111]. The basis for this conclusion is an (additional) observation by Davis and Adams where they found singular behavior of the thermal expansion and of compressibility occurring only in the α phase.According to Landau, a first order phase transition between two phases having different symmetry continues beyond the tricritical point as a second order phase transition. In the vicinity of the tricritical point the compressibility etc. diverge, but only in that phase which has lowest symmetry of the two. Apparently, α phase cerium should have a lower symmetry then γ phase cerium. This was exactly observed by Davis and Adams, but not recognized [112].

Phase	Crystal structure	a (nm)	b (nm)	c (nm)	T (K)	p (GPa)	At. radius* (nm)	Metallic vol.* (nm^3/Ce)
α'	orth.	0.3049	0.5998	0.5215	298	5.8	0.1615	0.02384
α	fcc	0.4824			298	0.81	0.1706	0.02806
β	dhcp	0.3681	1.1857		298	0	0.18321	0.034784
γ	fcc	0.5161			298	0	0.18245	0.034367
δ	bcc	0.411			1041	0	0.183	0.0347

Table 4.1: Crystal structures, lattice parameters, metallic radii and atomic volumes of Ce phases (* for coordination number 12).

	Ce^{3+} teor.	Ce^{4+} teor.	α	β	γ
Radius (nm)	0.1846	0.1672	0.173	0.18321	0.18245
Valence	3	4	3.67	3.04	3.06
T(K)		300	300	116	

Table 4.2: Ionic radii and valence of Ce in its modifications in comparison with the theoretical values for the Ce^{3+} and Ce^{4+}.

valency. In the early days of the cerium investigation it was believed that the $4f$ occupancy and thus the valency changed by one electron, but more recent experiments show that the valence of cerium does not change by 1 but at most by 0.5 or less. Many authors have attempted to measure the valence of cerium in its different phases. Table 4.2 is a compilation of several different types of experiments up to 1981. The valency of cerium is still a matter of controversy.

The single $4f$ electron plays a dominant role in the properties of cerium. Although it is an nearly empty shell the spatial localization of the $4f$ electron in cerium is well within the $5d$ and even $5p$ shell. The $4f$ radial extent in cerium is smaller because only one electron is put into the new shell. Since it will be orthogonal to all other electrons and the Pauli principle does not apply, the radius can be very small indeed. The $4f$ electron, at least in the phase, is localized whereas the $5d$, $6s$ band is a 8-10 eV wide itinerant band. From susceptibility measurements (Figures 4.2 and 4.3) it is known that the γ phase is paramagnetic with well-defined spins and that the α phase in nonmagnetic. The β phase shows antiferromagnetic ordering at 12.5 K [116].

A very interesting observations were recently published by Aoki et al [114] who investigated the effect of thickness of the Ce thin films on the magnetic moment per Ce ion (Figure 4.3).

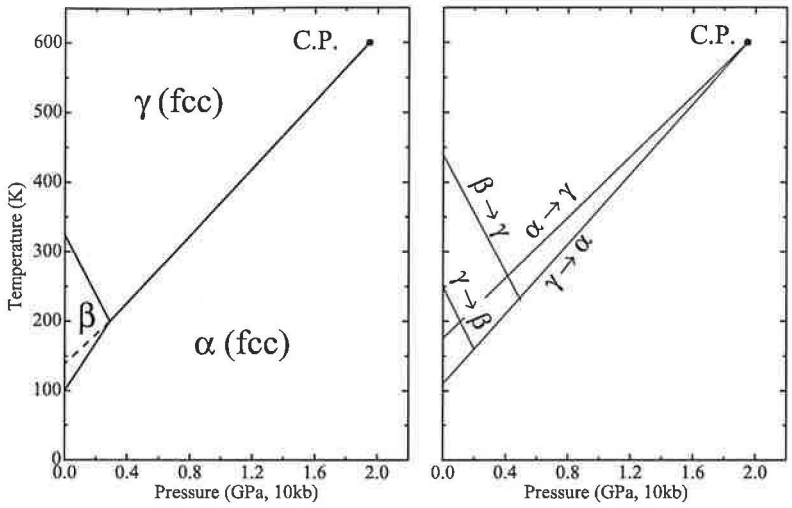

Figure 4.1: Phase diagram of Cerium.
From [110].

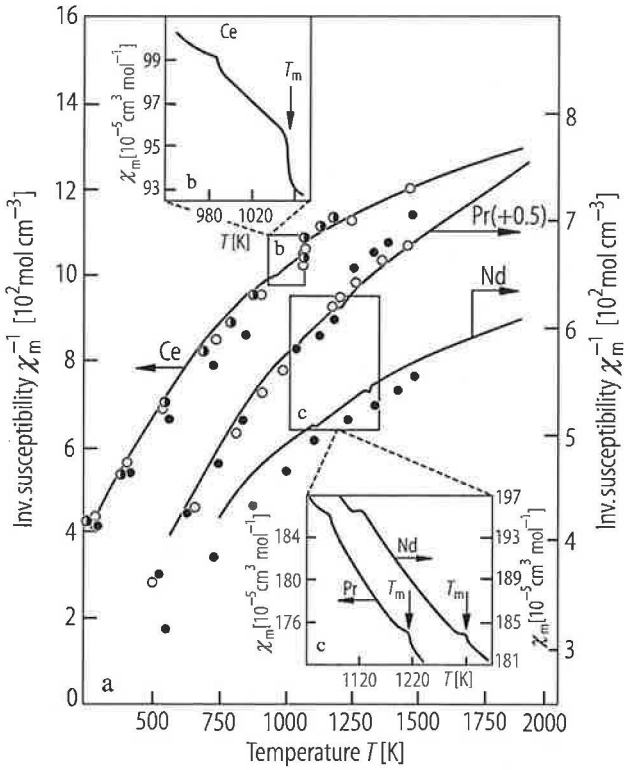

Figure 4.2: High-temperature magnetic susceptibility of Ce, Pr and Nd.
From [113].

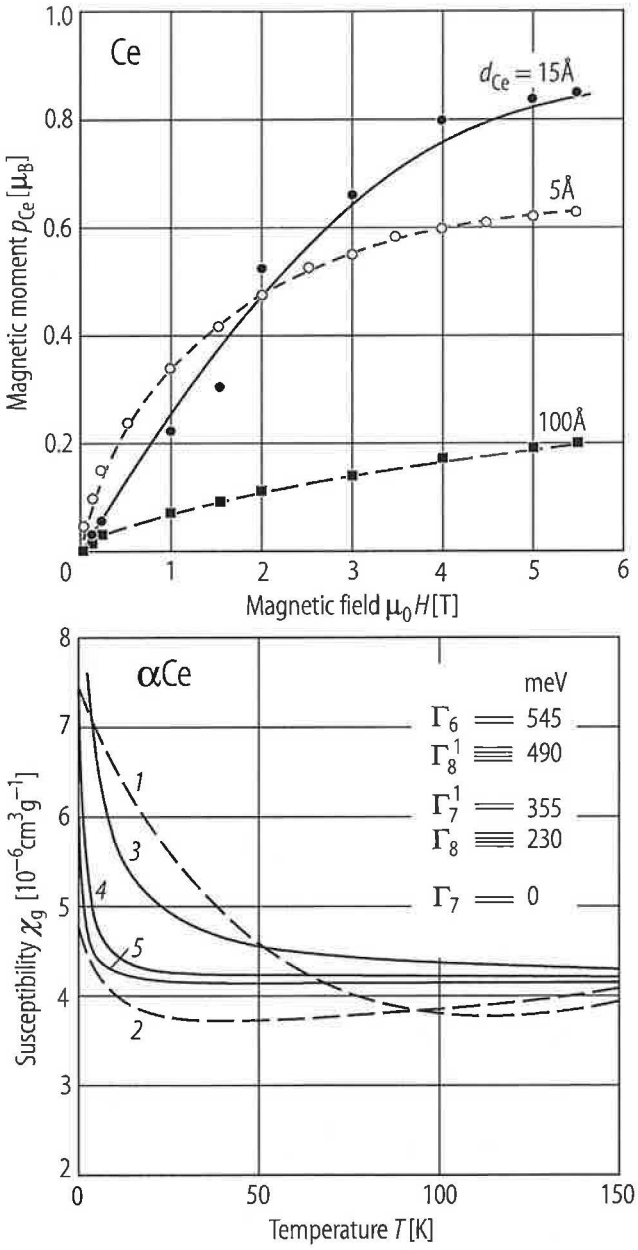

Figure 4.3: Magnetic properties of the Ce metal.
Magnetization curves of the Ce thin films with respect to its thickness (upper)[114]. Magnetic susceptibility of α-Ce (bottom)[115].

4.3 Terbium

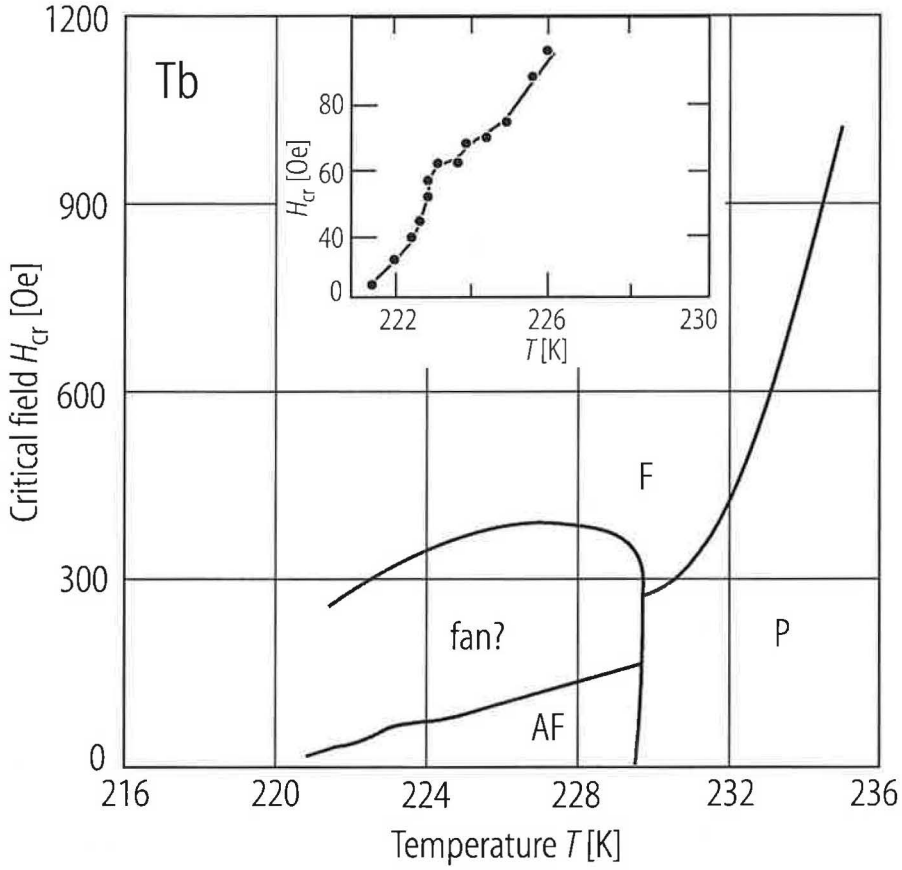

Figure 4.4: Magnetic phase diagram of Tb.
According to [118]

Terbium was discovered in 1843 by Swedish chemist Mosander, who detected it as an impurity in yttrium-oxide and named after the village Ytterby in Sweden. It was not isolated in pure form until the recent advent of ion exchange techniques.

Terbium is never found in nature as the free element, but it is contained in many minerals, including cerite, gadolinite, monazite, xenotime and euxenite. As with the other lanthanides, terbium compounds are of low to moderate toxicity, although their toxicity has not been investigated in detail. Terbium has no known biological role. Sodium terbium boride is used in solid-state devices, the oxide has application as activator of green phosphorus in the television tubes. It can be used with zinc oxide as a crystal stabilizer in fuel cells operating at elevated temperatures.

As most rare earths it crystallizes in the hexagonal-closed packed structure (space group: $P6_{3/m}m$, a = 0.36010 nm, c = 0.56936, $\gamma = 120$ ° [117]).

Terbium show rather complex magnetic ordering as depicted in the magnetic phase diagram (Figure 4.4). On cooling it orders antiferromagnetically at $T_N = 230$ K and undergoes an additional order-to-order phase transition at to the ferromagnetic phase at $T_C = 221$ K.

In the intermediate phase region and low magnetic fields, the complex fan spin structure has been reported.

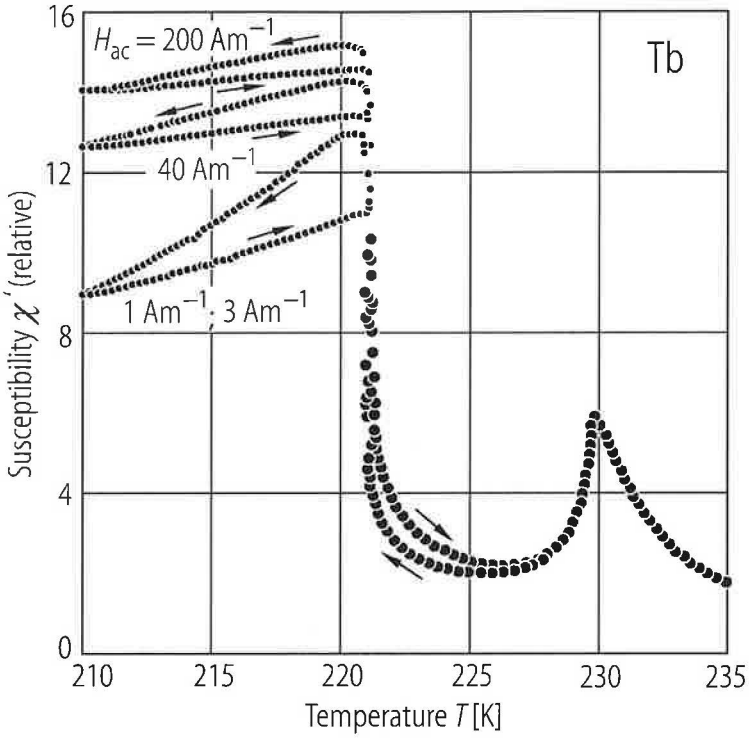

Figure 4.5: Magnetic susceptibility of the Tb metal.

The findings of a detailed a.c. magnetic susceptibility study of the antiferromagnetic (AF) suggested existence of spiral-spin domains in the AF region. The formation of an spiral-spin domain structure which was found to be different on warming the sample from the ferromagnetic region to the AF region, compared with that obtained when the sample was cooled from the paramagnetic region to the AF region. The related susceptibility data from reference [134] are presented in Figure 4.5. Further it was shown by authors of [119] that the thickness of the spiral-spin domain walls in the AF region decreases with increasing temperature.

Interesting magnetic impurity effects were observed, when warming the high-purity single-crystals, from the ferromagnetic to the fan/helimagnetic region. An extra positive contribution to the temperature modulation signal of the a.c. susceptibility is present throughout most of the AF region. This 'anti-hysteretic' behavior in the AF region is due to aligned ferromagnetic islands (centered around magnetic impurities) and/or to thicker domain walls of ferromagnetic character retained as a result of the imperfect first-order phase transition of the sample as a whole.

In addition, terbium shows significant magnetocaloric effect in the order-to-disorder region as depicted in the Figure 4.7.

Additional investigations of the Tb metal can be found in the references [121]-[133].

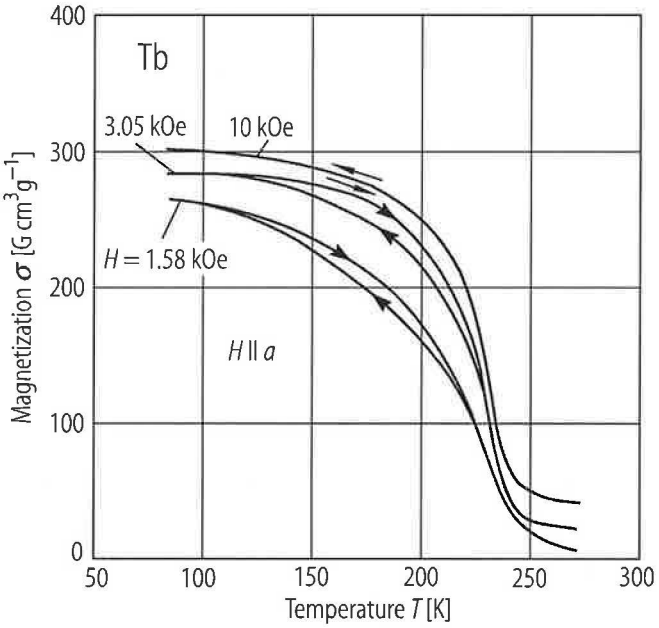

Figure 4.6: Temperature dependence of the magnetization of Tb single-crystal in fixed magnetic fields.
From [134].

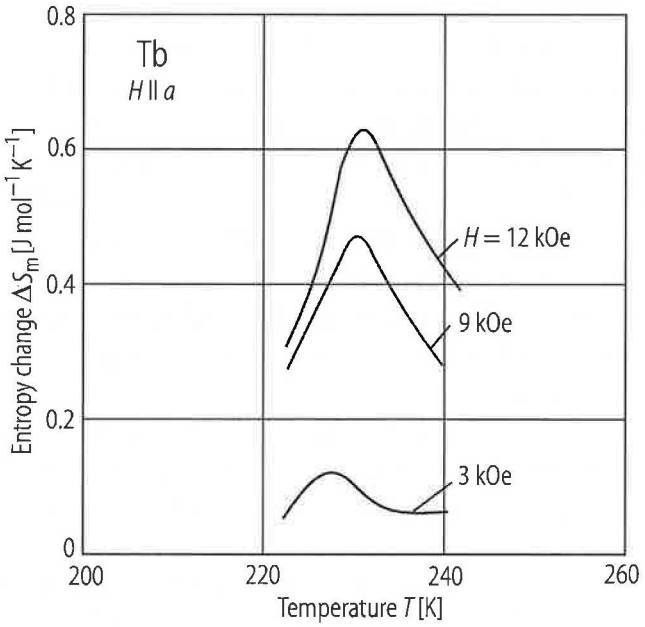

Figure 4.7: Magnetocaloric effect in Tb.

According to [134].

4.4 Erbium

Klemm and Bommer first produced reasonably pure erbium metal in 1934 by reducing the anhydrous chloride with potassium vapor.[5]

The following uses for erbium are generally reported. It is added to vanadium, because it lowers hardness and improves workability. It is used in nuclear industry. Erbium oxide is pink and serves as a colorant in glasses and porcelain enamel glazes. It's also used in photographic filters.

It posses the hexagonal-closed packed structure (a = 0.3588 nm, c = 0.55874, $\gamma = 120^\circ$ [117]).

Erbium, has the most complex magnetic phase diagram of any of the heavy rare earths. The numerous magnetic structures of erbium have been studied in several neutron diffraction and xray scattering studies [135, 136, 137, 138, 139].

The magnetic structure of erbium in zero applied field was determined by Cable et al by magnetoresistance experiments [2] and revealed three primary ordered states. The Néel temperature, T_N has been denoted as longitudinal, $T_{N\|}$ and basal, $T_{N\perp}$ with respect to the type of magnetic moments ordered.

Below the longitudinal $T_{N\|} = 89$ K, erbium orders antiferromagnetically along the c-axis with a sinusoidal wave vector of approximately seven atomic planes. Below the basal $T_{N\perp} = 53$ K , the basal plane moments become ordered as well with the same modulation as the c-axis. Below the Curie temperature at T_C 18 K, erbium orders ferromagnetically into a conical structure along the c-axis.

As the temperature is lowered below $T_{N\perp}$, the period of the c-axis wave vector increases from less than seven atomic layers to eight atomic layers. Also, the c-axis wave vector begins to lose its sinusoidal modulation and square up, until T_C is reached, when erbium attains an alternating cone structure. The magnetic structure in this intermediate region, between T_C and $T_{N\|}$, has been described in a synchrotron x-ray scattering study by Gibbs et al [137].

In this study, they found that as the temperature is lowered the c-axis wave vector does not change continuously but rather locks in to rational values. These rational wave vectors follow the form $q = n(4n-1)^{-1}c^*$ where $n = 2, 3, 4, \ldots$, suggesting that at certain temperatures the magnetic structure of erbium is commensurate with the lattice. The configuration of magnetic moments in the intermediate phase region (at 4 K and 22 K, respectively) is depicted in the Figure 4.9 (from reference [138]). Further the calculated stages in the collapse of the (2/7)c* structure of Er with a magnetic field along the a axis at 35 K is depicted in the Figure 4.10 according to [139].

The zero-field magnetic structures of Er are summarized in the Table 4.3.

Under applied magnetic field, much complex scenario occurs. The sketch of the magnetic phase diagram for field applied along the b and c axis, respectively, is presented in the Figure 4.10.

It is also worth to notice that all the listed order-to-order magnetic phase transitions are

[5] In 1842 Gustav Mosander separated 'yttria', found in the mineral gadolinite, into three fractions which he called yttria, erbia, and terbia. The names erbia and terbia became confused in this early period. After 1860, Mosander's terbia was known as erbia, and after 1877, the earlier known erbia became terbia. The erbia of this period was later shown to consist of five oxides, now known as erbia, scandia, holmia, thulia and ytterbia.

q	structure	T (K)
5/21	ferromagnetic	18
1/4	2(44)	18 - 25
6/23	2(444443)	25.5 - 28.5
5/19	2(44443)	29
4/15	2(4443)	32.5 - 35.5
3/11	2(443)	40
2/7	2(43)	49.5 - 52.5
		$T_{N,\parallel} = 53$; $T_{N,\perp} = 89$

Table 4.3: Magnetic structures of erbium.
The notation (43) means that four magnetic moments are aligned parallel to the c-axis and three moments are antiparallel. Because the hexagonal close-packed structure contains two inequivalent sublattices, the structure is more accurately referred to as 2(43).

difficult to be found on the macroscopic physical quantities like magnetization, specific heat or a.c. susceptibility. Figure 4.11 serves as a demonstration of the bulk properties of Er.

The complexity of magnetic interaction in erbium does not refer to the wild magnetic phase diagram only. In ultra-pure erbium studies exotic thermal effects at the first order magnetic transformation at around 19 K were observed [141].

The phenomena include (1) superheating (i.e., the metal is colder after heat has been added to it than before the heat pulse), (2) supercooling, and (3) the existence of metastable intermediate phases during this phase transformation in erbium (four on heating and two on cooling). None of these effects are observed in less pure metals. The specific heat of Er, supercooling/superheating effects together with the time-dependence of the heat capacity after a sequence of three successive heat pulses are presented in Figures 4.12 and 4.13.

Although the experimental evidence that superheating and supercooling in ultra-pure erbium occurs during the first order magnetic phase transition without or with (respectively) a crystal structure change, it has been noted earlier that magnetoelastic interactions may strongly influence equilibrium properties of the lanthanide metals.

The existence of metastable intermediate phases during the first order transition is not too surprising considering the number of complex magnetic phases that exist, including the various spin-slip transitions in addition to the three main magnetically ordered structures, which are rather exotic.

Thus it is not unreasonable that as the antipasto domain + cone + helix phase transforms to the ferromagnetic cone + helix magnetic structure on cooling, the transformation would proceed through two intermediate structures. Also, the reverse pathway from the low temperature phase to the high temperature one does not necessarily need to be the same, and so the existence of four intermediate magnetic structures is plausible.

Finally, additional reports on physical properties of the Er metal are summarized in the references [142]-[160].

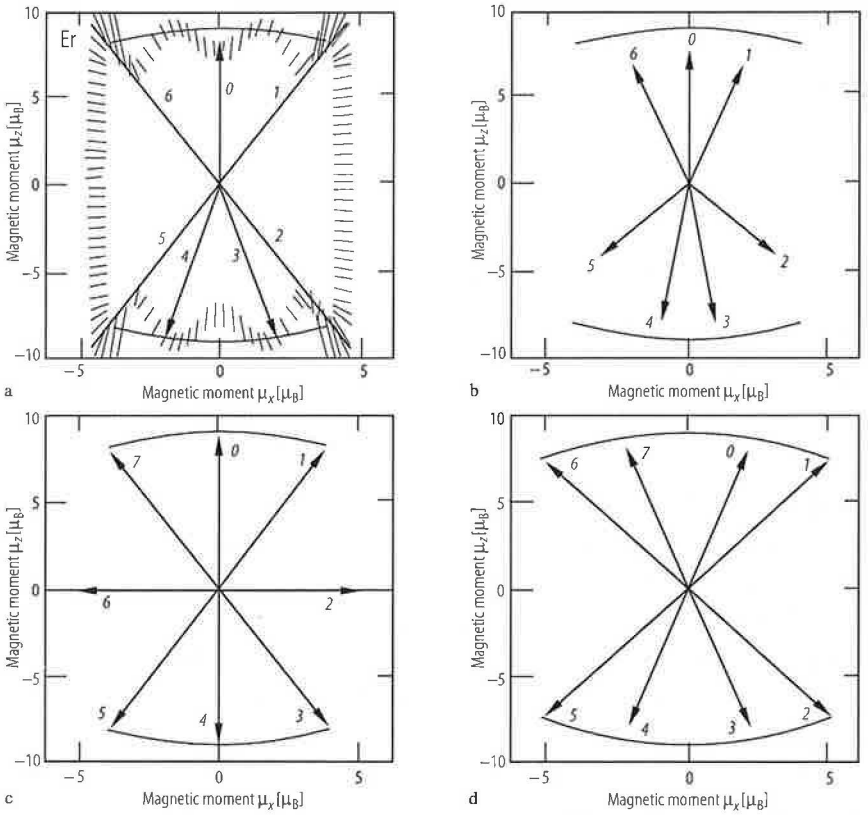

Figure 4.8: Spin configuration for a cycloidal structure of Er at 4.5 K and at 11.5 kbar hydrostatic pressure determined by the neutron diffraction studies.
The moments have been projected onto the zz-plane and displaced to a common origin. The numbers i = 0, 1, 2, 6, 7 refer to spins in the i-th layer of atoms. The moment components along the y axis were assumed to be zero. The two arcs mark the 9 μ_B upper limits of the total Er moment per atom. The borders of the hatched areas in (a) are given by the two curves calculated for an incommensurate structure by using the upper and lower limits for the ordered moment amplitudes. Figures (c) and (d) show similar diagrams derived for Er at 22 K and at ambient pressure. Figure (b) shows the spin configuration for Er at ambient pressure and 49 K.

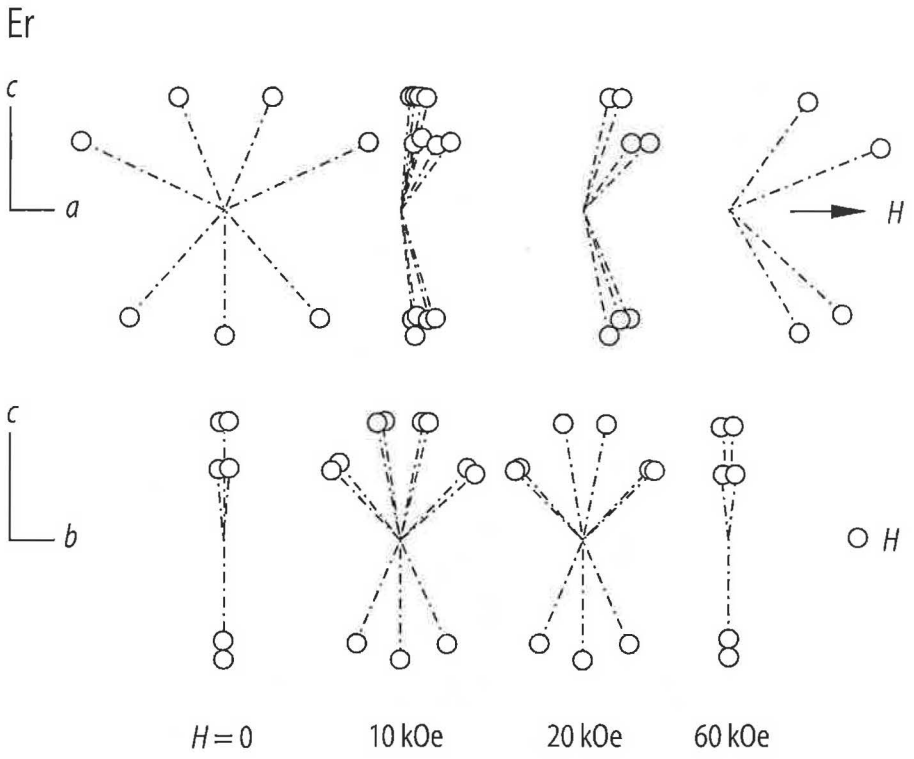

Figure 4.9: Calculated stages in the collapse of the (2/7)c* structure of Er with a magnetic field along the a axis at 35 K.

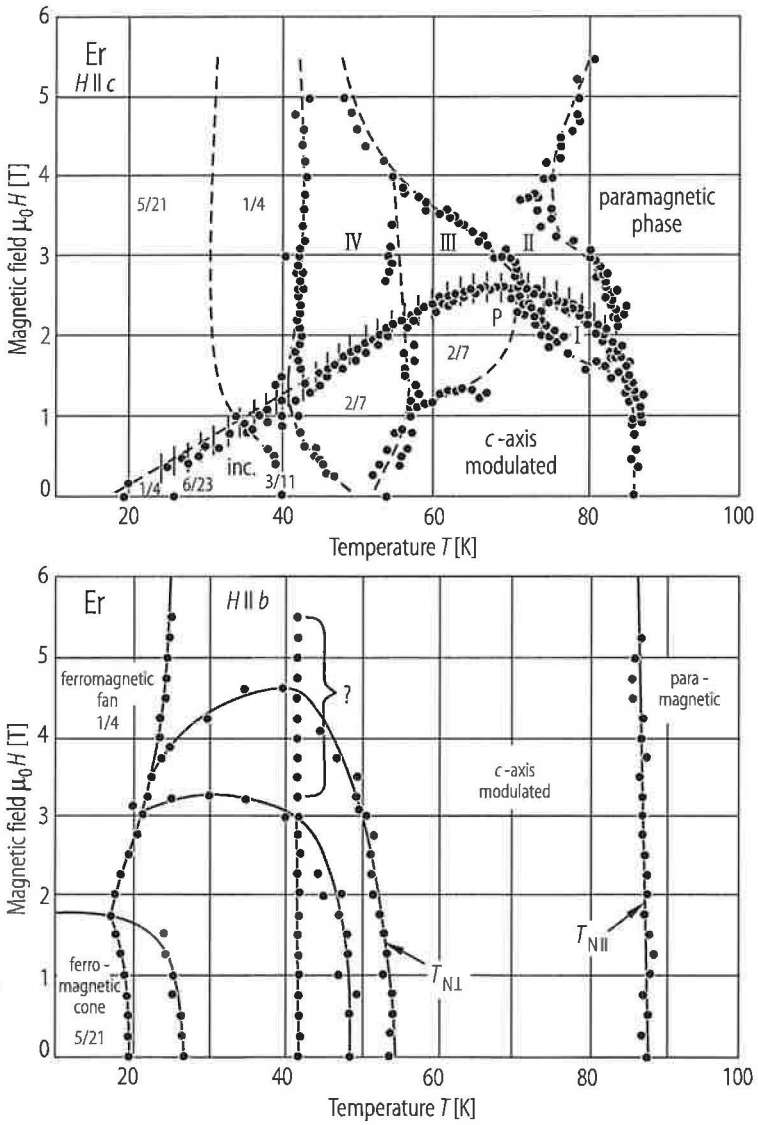

Figure 4.10: Magnetic phase diagram of the Er metal for the magnetic field applied along the c and b axis, respectively.

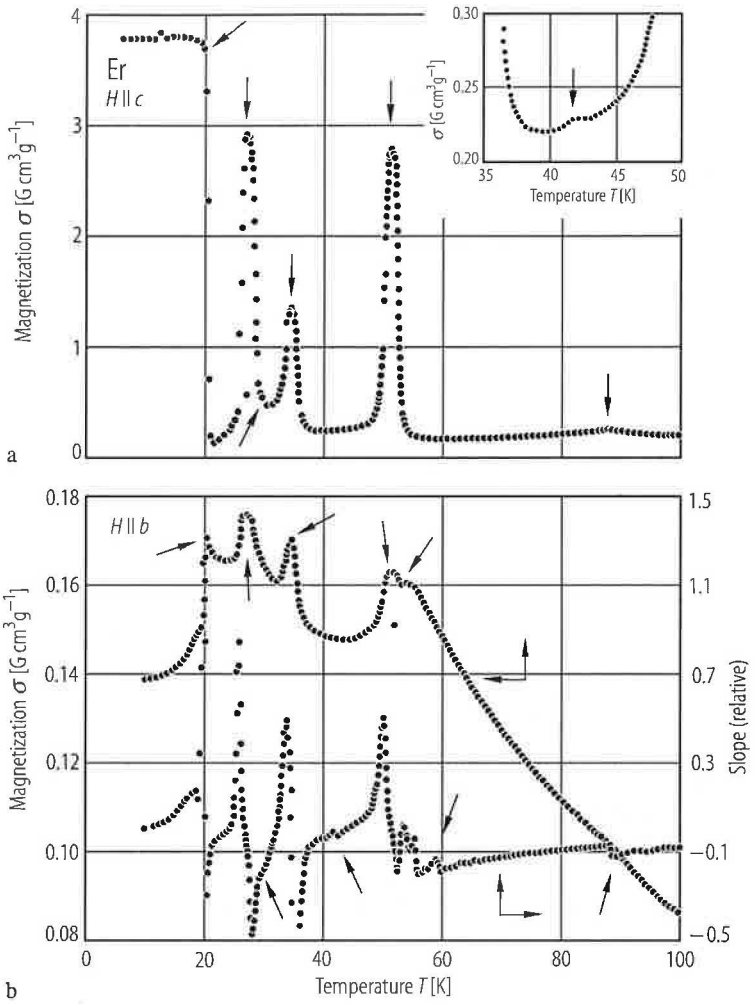

Figure 4.11: Magnetization of single-crystal Er along the c and b axis, respectively. (a) Magnetization of single-crystal Er along the c axis as a function of temperature in a constant magnetic field of 100 G. The inset shows magnetization against T for the c axis near 42 K. (b) The upper curve is the magnetization of Er along the b axis as a function of temperature for a constant magnetic field of 100 G. The lower curve is the slope of the b axis σ-T plot for Er, from reference [140].

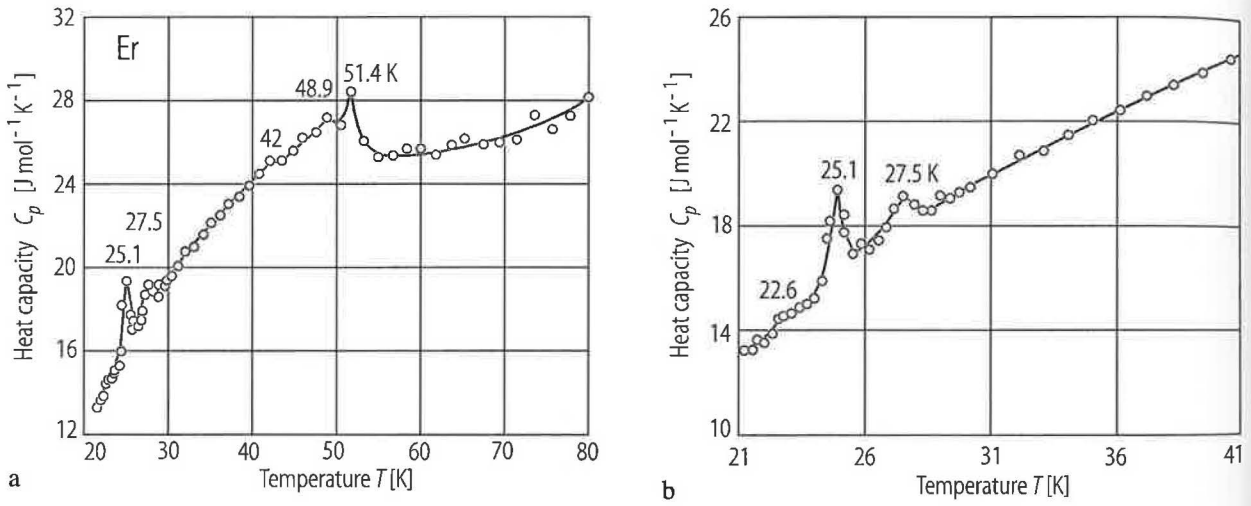

Figure 4.12: Heat capacity of erbium.

From [141].

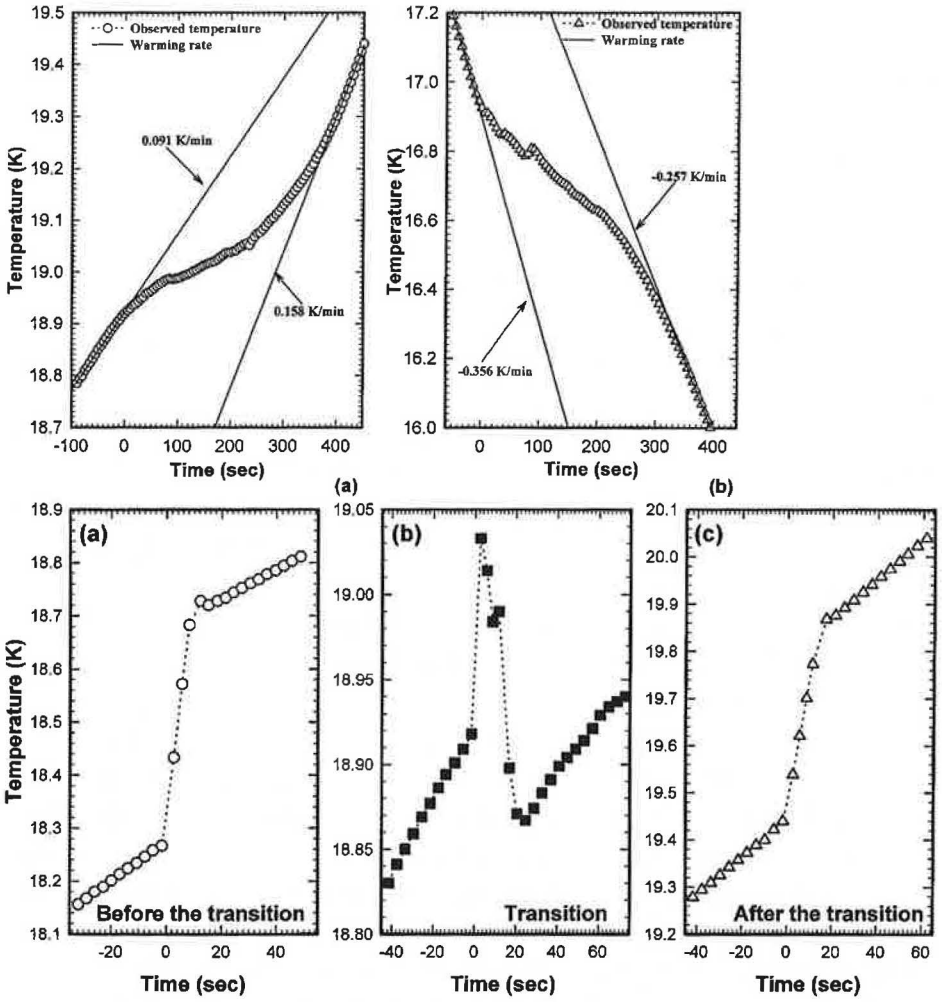

Figure 4.13: Supercooling effect in Er metal.
upper - The time-temperature behavior during heat pulse measurements near the first order magnetic phase transition of erbium for three successive heat pulses. lower - Time-temperature heating (a) and cooling (b) curves for routinely prepared high purity Ames Laboratory erbium. From [141].

4.5 Rare earths in reduced dimensions

It is well known that the magnetic order can be modified at the surface of a ferromagnetic material. The loss of the transitional symmetry perpendicular to the surface plane and the reduced atomic coordination can result in magnetic interactions which differ from those in the bulk. It is to be expected that the magnetic ordering will be weakened at the surface by the reduced atomic coordination.

Contrary to these expectations the enhanced surface ordering temperatures and the surface magnetic reconstruction (SMR) (i. e., a different orientation of the spins at the surface than in the bulk) are among the most intriguing phenomena found in surface magnetism [161]. For example, the results obtained from the spin-resolved photoemission experiment performed on ultrathin Gd films grown on W(110) [162] indicate that the in-plane ordering temperature of the surface is by 80 K higher than that of the inner layers. These data show also a complex and unexpected temperature dependence of the magnetization. At high temperatures the polarization of the $4f$ states at the surface differs from that of the underlaying layers. Extensive studies have failed to demonstrate the existence of such phenomenon in the $3d$ transition metals.

Evidence for an enhanced surface ordering temperature over the bulk Curie temperature T_B was found by Rau et al. [163] on polycrystalline Gd surfaces. A similar observation has been reported for epitaxial Tb films [164]. In a nearestneighbor Ising model with bulk coupling constant J, there exists a critical value of the surface coupling constant J_s, above which the surface orders at temperature (T_S) higher than the bulk Curie temperature (T_B). In this case the surface critical behavior at T_S is known as a "surface transition". For $T_B < T < T_S$ the surface behaves as a two-dimensional system, with the magnetic order decaying almost exponentially within the bulk.

There also exist a few experimental cases for which $T_B < T_S$. Farle et al [165] reported that the Curie temperature depends on the film thickness; T_C of a Gd monolayer on W(110) is 20 K below T_C for bulk sample. It is worthwhile to point out that, despite of these findings, the mechanism responsible for the enhancement of the surface Curie temperature in these systems is still not at all understood in terms of fundamental atomic properties.

The synthesis of artificially layered materials has attracted much attention in the last decade. The discovery of techniques to produce multilayers of rare earth elements that alternate with the non-magnetic hexagonal structure elements Y or Lu has opened up broad new opportunities to study the magnetic coupling in rare earth systems. Y and Lu have similar physical and electronic properties to the magnetic heavy rare earth and, because of the relatively small mismatch between the basal plane lattice parameters (e.g. 1.6 % for Dy and Y), good epitaxial growth is achieved. Artificial single crystal superlattices of GdY, DyY, ErY, and HoY, have been produced and extensively studied [168, 169].

These and similar systems offer a near ideal opportunity to investigate the magnetic exchange couplings and interaction strengths in a system consisting of magnetically concentrated layers (e.g. Dy) interleaved, in a controlled fashion, with magnetically inert layers (e.g. Y, Lu). It should be noted that such a system is unique and can never be simulated by bulk dilute alloys because of the attendant reduction in the average exchange interaction with the decreased density of magnetic ions, and the probability of some nearest neighbors even in very dilute samples.

Magnetic long-range coupling in layered metallic structures has become a key issue in thin-film magnetism since the observation of oscillatory exchange coupling across non-ferromagnetic spacer layers [166, 167]. Although this phenomenon was first discovered in rare earth superlattices most studies today deal with transition metal systems because of their technological relevance to magnetic storage devices.

The present theoretical understanding of transition metal multilayers has been developed on the basic of detailed observations revealing, e.g. short-period oscillations not extend beyond several atomic planes [170] as well as 90 degrees coupling [171]. In metallic RE systems, due to the localized nature of the $4f$ electrons, the exchange coupling is well described by the Heisenberg Hamiltonian $H = JS_iS_j$, where J denotes the effective coupling strength between the localized $4f$-spin moments S_i and S_j. The exchange coupling in rare earth metals is indirect, relatively long range, mediated through the 6s and 5d conduction electrons it is oscillatory and usually described in a Ruderman-Kittel-Kasuya-Yosida picture.

Hence, magnetic superlattices containing magnetic rare earth elements, e.g. Gd or Dy, alternating with a nonmagnetic analogue such as Y, Lu, W, would seem to be promising systems for investigating the modulation effects derived from a long-range interlayer exchange coupling.

The Y, Lu or other nonmagnetic metal block (Zr, Mo) does not simply act as an inert spacer between the blocks of magnetic material. Instead, it is found that there is a phase shift, proportional to the length of the Y, Lu or W block, introduced between neighboring magnetically active (Gd, Dy or Tb) blocks.

Neutron and X-ray studies of the rare earth films and multilayers have revealed numerous magnetic phases which could not have been predicted from the behavior of the pure bulk magnetic systems [172]. This is caused due to the lattice strain and clamping originating at layer interfaces. The epitaxial strain and clamping imposed at the film-substrate interfaces alters the detailed temperature dependence of the magnetic structures most notably by the introduction of multiphase coexistence.

Moreover, while the crystal symmetries of the film remain unchanged from the bulk, the lattice and magnetic correlation lengths are reduced, consistent with a high degree of disorder. This disorder may play a significant role in the resulting magnetic order. Indeed, in the low temperature Er/Y superstructure the magnetic correlation lengths are comparable to the unit-cell size of magnetic structures and two new magnetic wave vectors falling between 5/21 and 1/4 were observed ([173]). It has been found that the driving energy for the ferromagnetic transition in Er multilayers varies linearly with the strain [164], implying that strain effects are more important than even the artificial modulation of multilayers. The complexity of these interfaces and their dependence on growth conditions, continue to challenge systematic studies [174]-[181].

However, not only the fundamental magnetic interaction is the pivotal topic in the rare earth research.

The contemporary boom of nanoparticle investigations motivated few groups to develop suitable synthetic methods to obtain spherical particles, nanotubes and nanowires of some rare earth elements [182]-[187].

There are plenty of motivational reasons for this peculiar work. One of them is the use of lanthanides as radionuclides in nuclear medicine is well-known (detecting and treating cancerous tumors). The possibility of obtaining controlled-size lanthanide nanoparticles

opens a wide scope for their application in nuclear medicine.

However, because of the extremely high chemical reactivity and hence the considerably rigorous equipment requirements to preserve a high purity of the product, the preparation and characterization of nanostructured pure rare-earth metals are still big challenges in nanoscience and nanotechnology.

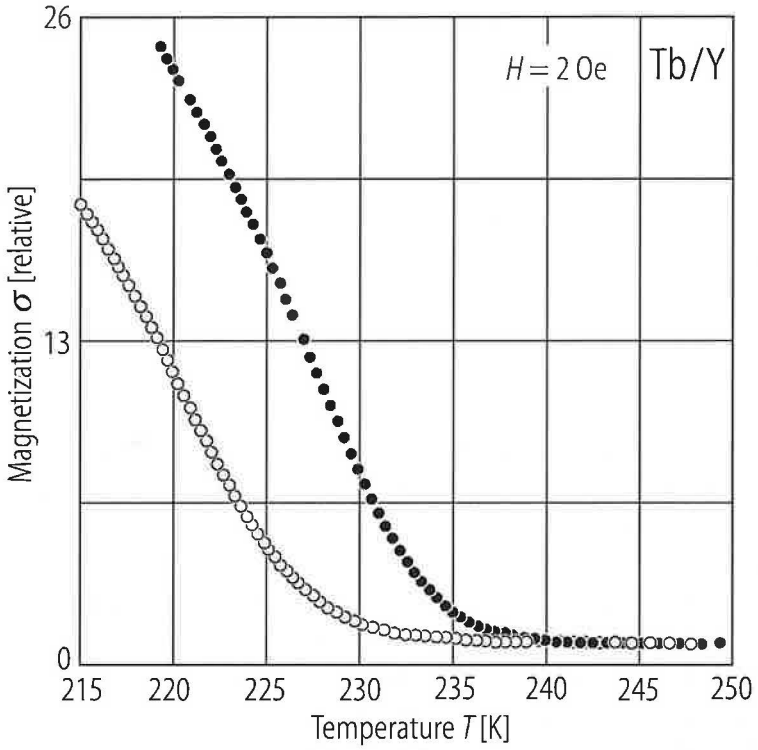

Figure 4.14: Thermal dependence of the magnetization of 100 nm Tb film epitaxially grown on Y (solid circles), and Tb (2.6 nm)/Y(4.4 nm) superlattice (open circles) under 2 Oe magnetic field applied in the basal plane. Tb directly undergoes a transition from the paramagnetic phase to the ferromagnetic one whereas there is no ferromagnetic long range order in the superlattice [180].

4.6 Additional remarks on rare earths - production, usage, magnetism in applications

Due to notoriously known issue of rare earth metals numerous reports and reviews on are available. Therefore only the list of actual and relevant references is added to the succinct introduction:

- In [188]-[192] the recent development in their industry is given.
- In references [193]-[207] the progress in production including separation and recovery is summarized.

- The effect of rare earths on materials properties and chemical catalysis are listed in [208]-[220].
- Production of L-Xray light is described in references [221]-[226].
- Studies presented in references [227]-[252] give additional knowledge about magnetism.
- Because one of the hot topics in the solid state science is the magnetic refrigeration, references [253]-[259] comprise the most important aspects of this environment-friendly technology related to rare earths.
- References [260]-[266] deal with the rare earths in context of health and biological research.
- Nuclear and radiochemical applications are summarized in [267]-[281].

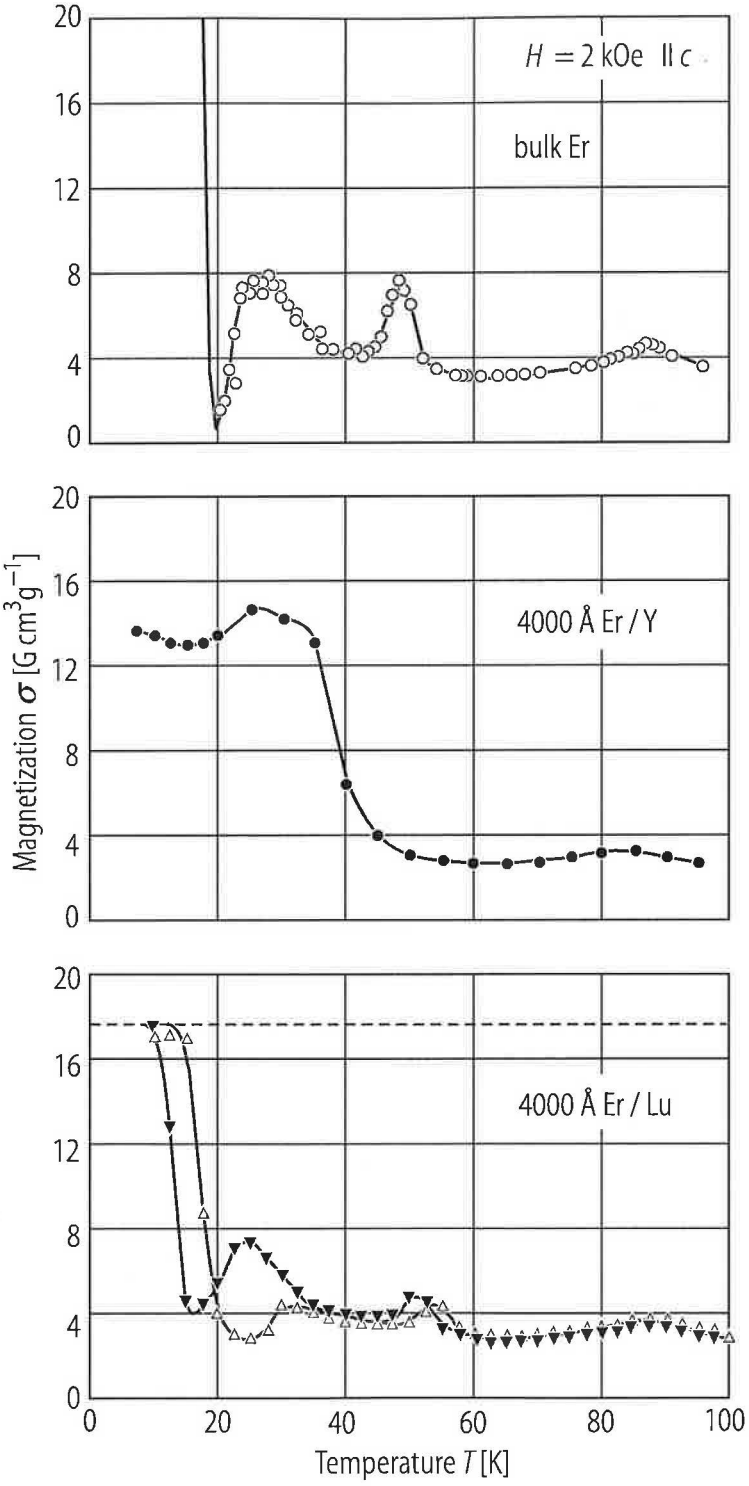

Figure 4.15: Magnetization as a function of temperature applied along the c axis for a 400 nm Er film grown on Lu (closed symbols are field cooled and open symbols are zero-field cooled) and a 400 nm Er film on Y (field cooled). The dashed line marks the maximum magnetization allowed by demagnetization effects in the field. Magnetization data for bulk Er are shown for comparison [181].

Chapter 5

$CePt_3Si$ and related compounds - the state of art

5.1 Preface

[1]

Symmetry is central to our understanding and description of natural phenomena. The fundamental conservation laws of physics, such as the conservation of momentum and energy, are the consequences of symmetries in space and time. Also, our understanding of the forces of nature is based on a local symmetry known as "gauge symmetry". However, the world is often unsymmetrical: in the process of nuclear beta-decay, there is an absence of inversion or mirror symmetry, known as "parity violation"; another example is that the structure of DNA is not mirror symmetric.

The consequences of broken symmetries can be dramatic. The breaking of gauge invariance, for example, is associated with the onset of superconductivity - the resistance-less flow of electric current, usually at very low temperatures. Recently, Bauer et al presented a material in which space and time inversion symmetries and gauge symmetry are broken: $CePt_3Si$ is the first example of a magnetic superconductor that has no mirror symmetry, an observation that lead to a re-examination of current understanding of the superconductivity phenomena.

In 1957, Bardeen, Cooper and Schrieffer (BCS) explained the origin of superconductivity in simple metals such as aluminum. In BCS theory, electrons joined into "Cooper pairs" are the mediators of the supercurrent flow. The quantum wave-function (or description) of the superconductor is a coherent superposition of paired-electron states. The Cooper states of lowest energy have overall zero momentum and so there must be pairing of electrons of momenta equal in magnitude, but opposite in direction. Moreover, the pair states depend not only on the coordinates of the electrons but also on their spin orientation. Because the electrons in the Cooper-pair state are fermions (with one half-unit of spin each), the pair-state wave-function must be anti-symmetric under interchange of the two electrons. This is the origin of the familiar Pauli exclusion principle.

In simple metals such as aluminum, the Cooper-state wave-function can be separated

[1] based on conclusions by Saxena [282]

into two parts, one that depends only on the spatial coordinates and the other only on the spin coordinates. In crystals with space-inversion symmetry, an interchange of the spatial coordinates of the electrons leads to a state that is indistinguishable from the original. Hence, the probability distribution of the electrons in the Cooper state must be unchanged. The Cooper-state wave-function can only change by a phase factor under this transformation. Because a second interchange must lead back to the original quantum state, the phase factor must be therefore +1 or -1. This simply means that the spatial part of the Cooper state must be either symmetric or anti-symmetric.

5.2 First heavy fermion superconductor without inversion symmetry: $CePt_3Si$

The symmetry of the crystal structure is the crucial point for classification of the order parameter in unconventional superconductors. In context of the underlying electron correlations it is the essence of pairing in the superconducting (*bosonic*) state.

The recently discovered heavy-fermion superconductor (HFSC) $CePt_3Si$ has no spatial inversion symmetry due to lacking of inversion center in its unit cell. This absence implies that the spatial component of the wave function cannot be defined straightforwardly.

The direct implication of the parity violation is that the pairing symmetry should, in principle, be a mixture of spin-singlet and spin-triplet states. This leads to a conflict because the spin-triplet channels are known to be forbidden in the absence of inversion symmetry.

In addition, $CePt_3Si$ exhibits microscopic coexistence of long-range antiferromagnetic ordering (T_N = 2.2 K) with the unconventional HFSC state below 0.7 K. The first results of the specific heat and electrical resistivity measurements according to [40], which served as the proof of coexistence of magnetic ordering and HFSC state are depicted in Figures 5.1 and 5.2.

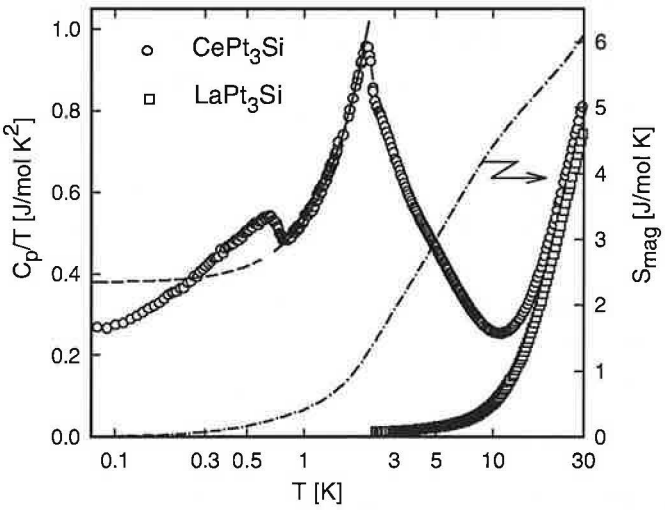

Figure 5.1: Specific heat of $CePt_3Si$ according to [40].

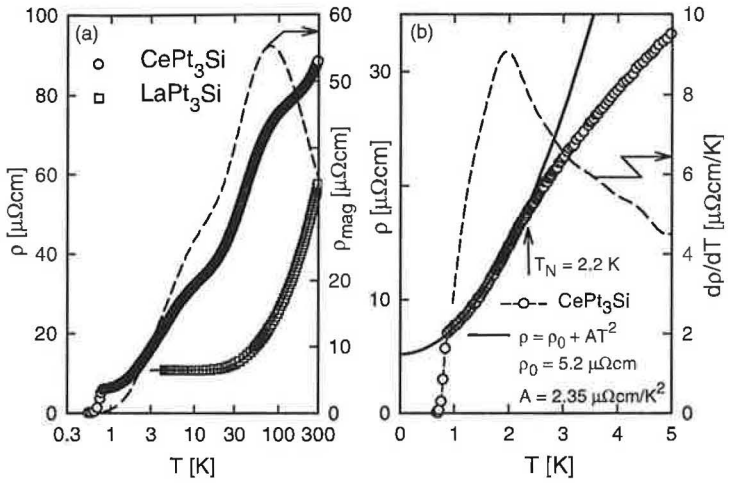

Figure 5.2: Electrical resistivity of $CePt_3Si$ according to [40].

a(pm)	c(pm)	Ce(1b)	Pt(2c)	Pt(1a)	Si(1a)
407.2	544.2	1/2 1/2 0.1468	1/2 0 0.6504	0 0 0	0 0 0.4118

Table 5.1: Crystallographic data of $CePt_3Si$ according to [40].

5.2.1 Crystal structure

The crystal structure of $CePt_3Si$ is tetragonal with the space group $P4mm$. It was first time reported for the isotypic ternary boride $CePt_3B$ [283], which is related to the three common structure types as shown in Figure 5.3. The lattice parameters together with the atomic position in the unit cell are summarized in the Table 5.1. The correspondence of the cubic $CePt_3$ and the tetragonal $CePt_3B$-type structures is depicted in Figure 5.4.

The structure can be hypothetically derived from the $CePt_3$ with cubic $AuCu_3$ structure by filling the void with Si, which in addition causes a tetragonal distortion of the unit cell.[2]

5.2.2 Kondo effect, antiferromagnetic ordering and paramagnetic state properties

$CePt_3Si$ orders antiferromagnetically at the Néel temperature, $T_N = 2.2$ K, as originally observed on electrical resistivity and specific heat data. The AF ordering is accompanied by pronounced magnetic fluctuations above T_N as indicated by logarithmic tail on the heat capacity data. The anisotropy of the crystal structure ($c/a \sim 1.34$) may be the additional reason for enhance of the short range magnetic correlations.

The microscopic origin of the long-range AF ordering was proved by neutron scattering experiments [285] yielding a strongly reduced magnetic moment of 0.16(1) μ_B/Ce atom.

[2]Filling of voids in structures with large cages may dramatically influence physical properties as evidenced in detail for skutterudites REM_4X_{12} (RE - rare earths; M - transition metals; X - p element) [284].

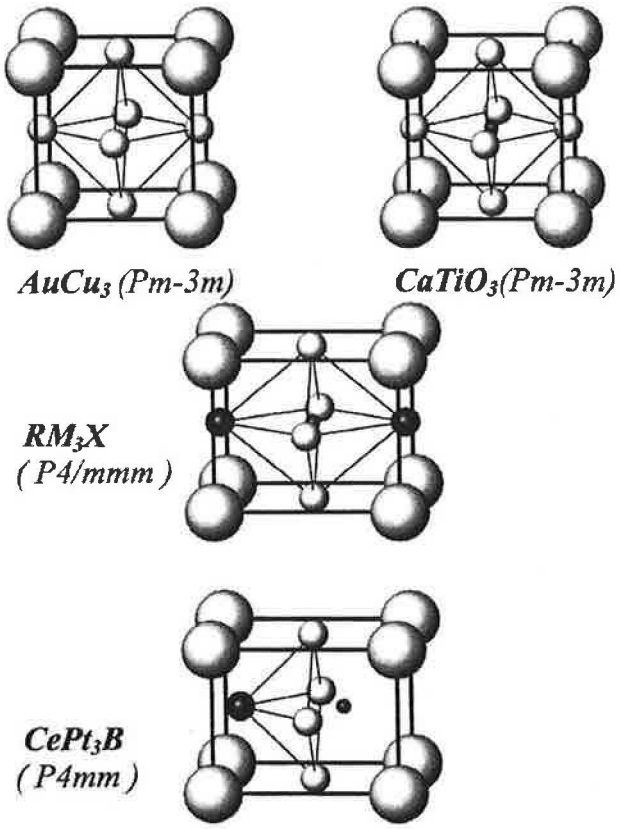

Figure 5.3: Genesis of the $CePt_3B$-type lattice and related structures. From reference [283].

The observed Bragg reflections with the propagation (0 0 1/2) below and above the critical temperature, T_c, indicated microscopic coexistence of AF order and heavy fermion superconductivity.

The AF structure can be described as follows: it consists of ferromagnetic layers of the Ce $4f$ magnetic moments aligned along the a-axis. The ferromagnetic layers are stacked along the c-axis in the sequence + - + - and so on. Within a localized model of the Ce $4f$ moment, on simultaneous spacetime inversion a given magnetic sublattice is centrosymmetric and a pairing of spin-triplet character may be favorable. In other words, the two interleaved ferromagnetic sublattices of the local Ce moments, have inversion symmetry under simultaneous spacetime reversal. However, the $4f$-ligan hybridization with Pt and Si breaks this degeneracy and a combination of these two competing effects may be relevant to understanding of the simultaneous occurrence of superconductivity and AF order.

The characterization of the paramagnetic state of $CePt_3Si$ from susceptibility measurements reveals a Curie-Weiss behavior with an effective Ce moment 2.54 μ_B/f.u. and paramagnetic Curie temperature θ_P = -45 K. While the former quantity indicates a rather stable Ce^{3+} state at high temperatures, the large negative θ_P value refers to pronounced antiferromagnetic interactions and/or considerable $4f$-ligand hybridization. In terms of Kondo-type interactions, neglecting crystal field effects, the Kondo temperature would follow from $T_K =$

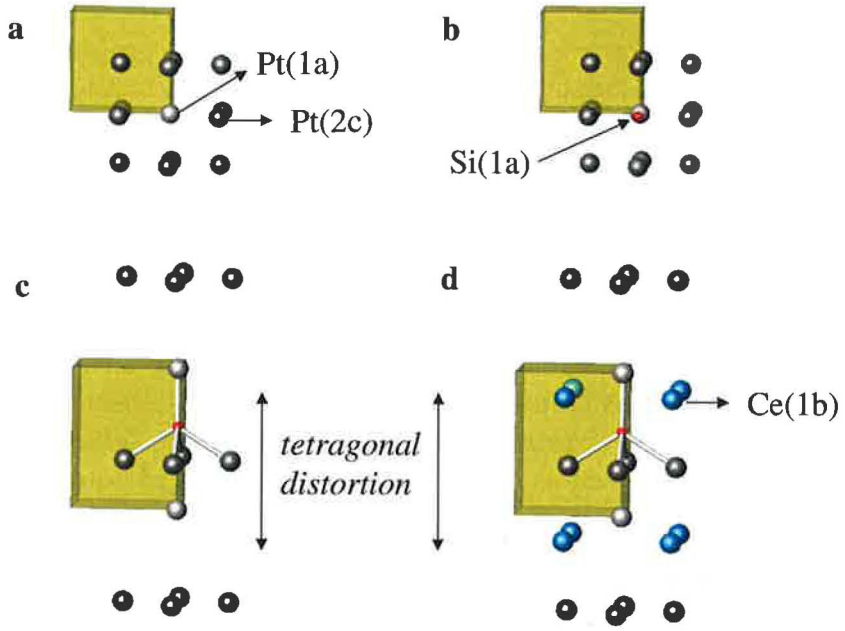

Figure 5.4: Relation between the cubic $CePt_3$ lattice and the $CePt_3Si$ structure. a - only Pt sublattice, the yellow polyhedron corresponds to the unit cell in the $CePt_3B$-type structure, b - insertion of Si atom, c - distortion due to Si, d - all atoms including Ce.

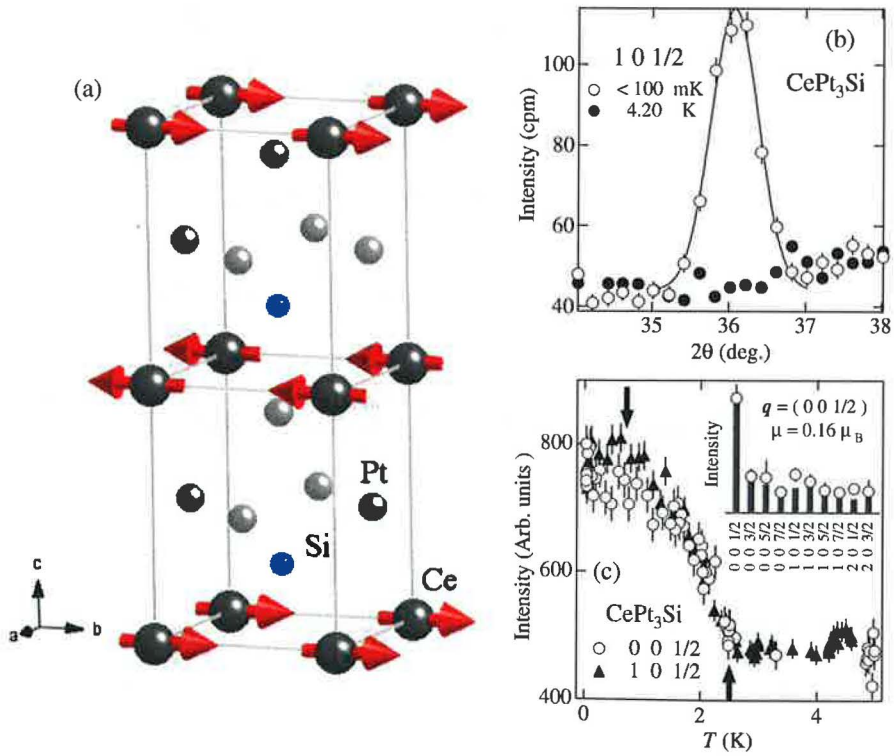

Figure 5.5: Magnetic structure and neutron diffraction results of $CePt_3Si$, from [285].

$-\theta_P/4 = 11$ K.

The magnetic moment 0.16(1) μ_B/Ce observed by neutron diffraction is strongly reduced in comparison with the CurieWeiss effective moment 2.54 μ_B/Ce (obtained from the paramagnetic susceptibility data). The reduction is in agreement with the expected Kondo-type interaction in the compound.

The entropy gain 0.22 $R \ln 2$ at the ordering temperature supports presence of the Kondo phenomena. The $R \ln 2$ value is reached at around 25 K only.

Surprisingly, crystal-field excitations were indicated by curvature of the temperature dependence of the electrical resistivity at $\sim$ 80 K. Clear crystal field excitations at 1 and 24 meV were observed by inelastic neutron scattering and later by nuclear magnetic resonance. In the simplest case, no clear crystal field excitation should be observable in a Kondo-lattice system in which the $4f$ levels are strongly hybridized with the conduction states, and possess an itinerant character expressed as a renormalized heavy Fermi liquid phase.[3]

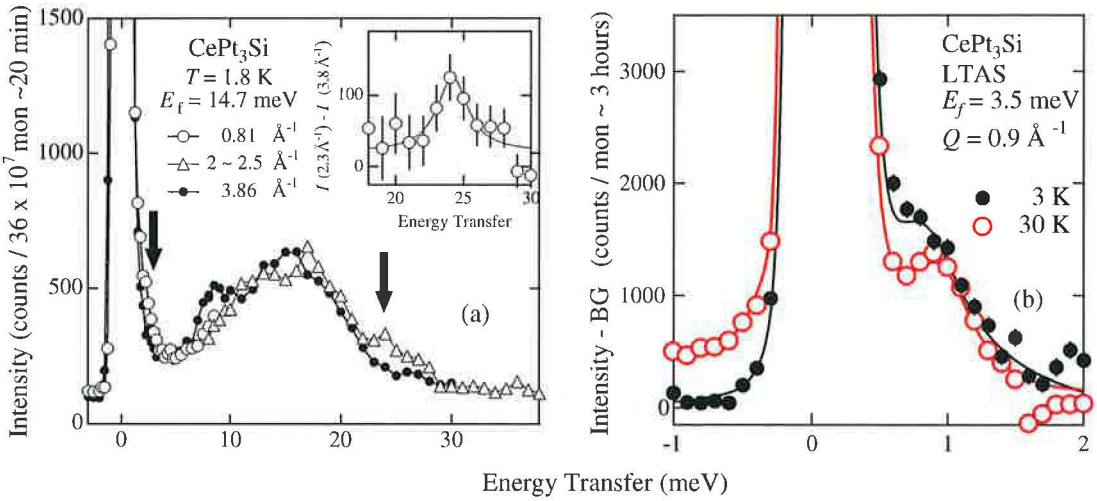

Figure 5.6: Results of inelastic neutron scattering of $CePt_3Si$, according to [285].

5.2.3 Heavy fermion superconducting state

In all previously studied unconventional superconductors, the governing property for description of the SC state was the relative symmetry of the order parameter in comparison to that of the Fermi surface (for details, please see Chapter 2).

[3]No crystal field excitation has been reported in $CeCu_6$ or $CeRu_2Si_2$ [286, 287], instead a quasi-elastic response, the so-called Kondo resonance peak is superposed on the AFM fluctuations as the relevant low-energy excitation. It has been reported that a broad CEF excitation can be observed in the heavy fermion superconductor $CeCu_2Si_2$; again its ordered state is unclear yet [288, 289]. An example of a heavy fermion superconductor based on Pr which shows clear CEF excitations is $PrOs_4Sb_{12}$. The Fermi surfaces of $PrOs_4Sb_{12}$ are understood in terms of a localized $4f$ band structure. Very recently a remarkable low energy excitation was observed at $q = (100)$, which corresponds to the propagation of the field-induced antiferro-quadrupolar order [290, 291].

	S-O coupling	parity	dimension	gap/nodes	ref.
1	weak	odd	1D	points	[42]
2	strong	even	1D	lines	[43]
3	strong	even	3D	isotropic	[45]

Table 5.2: Scenarios of pairing in the HFSC of $CePt_3Si$.

In case of non-centrosymmetric structures many theoretical and experimental studies were recently stimulated by the discovery of the $CePt_3Si$ compound. The most obvious and unusual characteristics of the HFSC state of $CePt_3Si$ are summarized here:

- The coexistence of HFSC and AF ordering does not simply imply unconventional SC state.
- The high value of the upper critical field $H_{c2}(0) = 5$ T far exceeds the Pauli-Clogston limit (~ 1 T). Spin-singlet pairing mechanism is therefore incompatible.
- Contrary, the lack of symmetry center prevents in general spin-triplet pairing.
- Special property of the $P4mm$ space group is the absence of the mirror plane $z \rightarrow -z$ which yields a Rashba-type spin orbit coupling and leaves the triplet pairing state: $\mathbf{d}(\mathbf{k}) = \widehat{x}k_y - \widehat{y}k_x$, represented by A_{2u} irreducible representation of the $P4mm$.
- the SC emerges under the AF order, therefore it seems to be more natural to assume spin-singlet type of pairing, because the Pauli paramagnetic limit is rendered less effectively by presence of spin-orbit coupling arising from the broken symmetry.

Recent band structure calculation revealed that a possible gap appears on the Fermi surface, depending on the dimensionality of the order parameter. In case of one-dimensional order-parameter, the gap has line nodes at crossing between the Fermi surface and the high-symmetry plane of the Brillouin zone or at the Brillouin zone boundaries.

The general polemics on symmetry of pairing state was given in the Chapter 2. The most important theoretical results based on different approaches are summarized in the Table 5.2[4].

Several fine experimental investigations were performed to support one of the proposed scenarios [292]-[296]. The $CePt_3Si$ was investigated by penetration depth measurements, nuclear magnetic resonance (NMR) and angular-dependent thermal transport. The penetration-depth and thermal-transport studies uniformly revealed model of energy gap with line nodes as the only possible interpretation for the experimental observations. In addition, the penetration depth experiments suggested two-dimensional spin-singlet symmetry. The NMR results excluded isotropic spin-triplet state, however, suggested point-gap structure.

[4]The authors of 3 considered the symmetry properties of the gap function in superconductors with lifted spin degeneracy. Phase factors which appear with the gap function under point group operations and time reversal may be handled by the introduction of an even auxiliary function, which transforms according to the irreducible representations of the point group. This function defines the behavior of the superconductor in terms of thermodynamic and tunnelling properties.

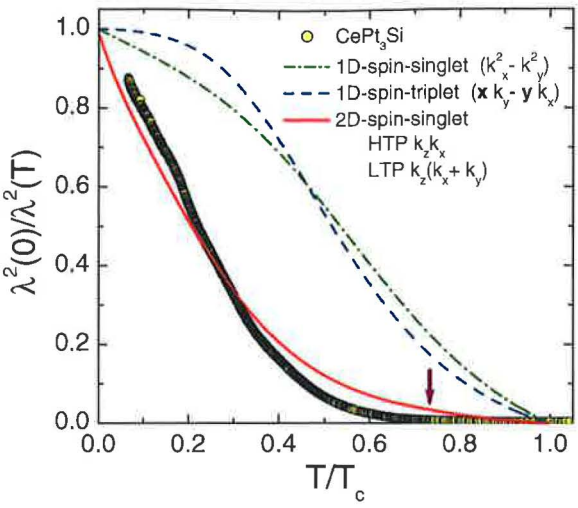

Figure 5.7: Results of the numerical evaluations of the models discussed in the text and for the polycrystalline $CePt_3Si$ sample.
The arrow indicates the point where the T behavior of the superfluid density should have a crossover from the high- to low-temperature phase.

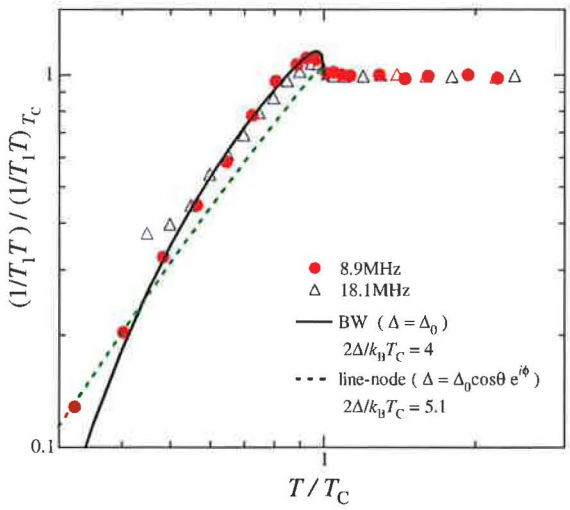

Figure 5.8: The plot of $(1/T_1T)_{SC}/(1/T_1T)_N$ vs $T = T_c$ of $CePt_3Si$ at 8.9 (circles) and 18.1 MHz (triangles). Here $(1/T_1T)_N$ corresponds to the value at the normal state at 8.9 ($H =$ 1 T) and 18.1 MHz ($H = 2$ T). The solid line is a tentative fit calculated by applying the Balian-Werthamer model (BW isotropic triplet SC state) with a value of $2\Delta/k_BT_c = 4$. The dashed line indicates a fit by a line-node gap model with $2\Delta/k_BT_c = 5.1$.

The role of magnetic fields on HFSC state in $CePt_3Si$ was theoretically investigated by Kaur et al [297]. Using a two-band theory with a Rashba spin-orbit interaction, they obtained behavior of the upper critical field for the field along the c axis as if it would be in a conventional superconductor independent of the paramagnetic (Zeeman) field. While there is a paramagnetic limiting effect for magnetic fields applied in the basal plane, the

high-field superconducting phase has pronounced differences for field-directions parallel and perpendicular to the c axis. For the field parallel to the c axis, the paramagnetic limiting is basically absent and the vortex phase is quite conventional. For the perpendicular field direction, the field can induce a phase which gives rise to an additional phase factor in the many body wave function with q perpendicular to the applied field: a helical vortex phase.[5]

In fact the real nature of the superconductivity in $CePt_3Si$ is still unclear. For instance no theoretical study involving the full Shubnikov symmetry of the problem has been published. This approach is substantiated because of unconventional superconductivity in presence long-range antiferromagnetic ordering. The transfer of the question, in fact one dimension higher because of the colored symmetry, might supply new insight into it.

5.2.4 Influence of composition on electronic properties

It's generally known, that any metallurgical modification of a superconductor modifies its properties, namely in the SC state. The family of unconventional superconductors based on Ce is extremely sensitive to material purity, crystallinity and any alloying effects. $CePt_3Si$ is not an exception.

Preparation regime

There are two important aspects of 'sample dependence' in $CePt_3Si$:[6]

- annealing and subsequent cooling rate
- off-stoichiometry

There are only few reports on annealing effect in the $CePt_3Si$ compound. According to Ishikawa [298] the quenched sample revealed a sharp cusp at 3.7 K on the temperature dependence of the magnetic susceptibility, while the annealed one seemed to be nonmagnetic without showing such a cusp down to 2 K at least. The effect suggested that the AF found in quenched $CePt_3Si$ samples may be spurious, probably induced by disorder due to quenching.[7]

Motoyama [299] investigated effect of concentration variation. The static magnetic susceptibility at low temperatures enhances with increasing Pt content. This enhancement started around 100 K and became larger around 10 K. The effect was explained by increasing Pt concentration causing, that 1a positions are occupied by Pt atoms, partially. These Pt-chains cause the enhancement of magnetic susceptibility. Therefore, the Pt-chain seems to influence the character of the susceptibility in the vicinity of the AF ordering temperature.

The off-stoichiometry was also the reason for spurious observation of the double SC phase transition on specific heat reported in [300]. In fact, when lowering the Ce content

[5]The proposed Josephson junction experiment can unambiguously identify the helical order and discussed the appearance of a transverse magnetization related to the helical order.

[6]The 'sample dependence' is sometimes used in literature to mask shady nature of the investigated samples. In sophisticated works it represents deviations in material behavior with respect to its preparation procedure. Namely in intermetallic phases, variable composition keeping the same crystal structure is very common. So it is a tough question, whether the set of samples can be treated as the same phase or not.

[7]Both samples were annealed at 850 ° for 3weeks. The first one was quenched, the second annealed at 650 ° for 2weeks and cooled down slowly.

a new phase $Ce_3Pt_{23}Si_{11}$ forms. The two compositions are very close and cannot be easily distinguished by microprobe analysis. The phase orders antiferromagnetically at ~ 0.4 K. The AF ordering is associated with a huge λ-type anomaly. Because of that, the 'double-effect' can be observed in samples with minimum content ~ 0.05 % of the $Ce_3Pt_{23}Si_{11}$ phase [301].

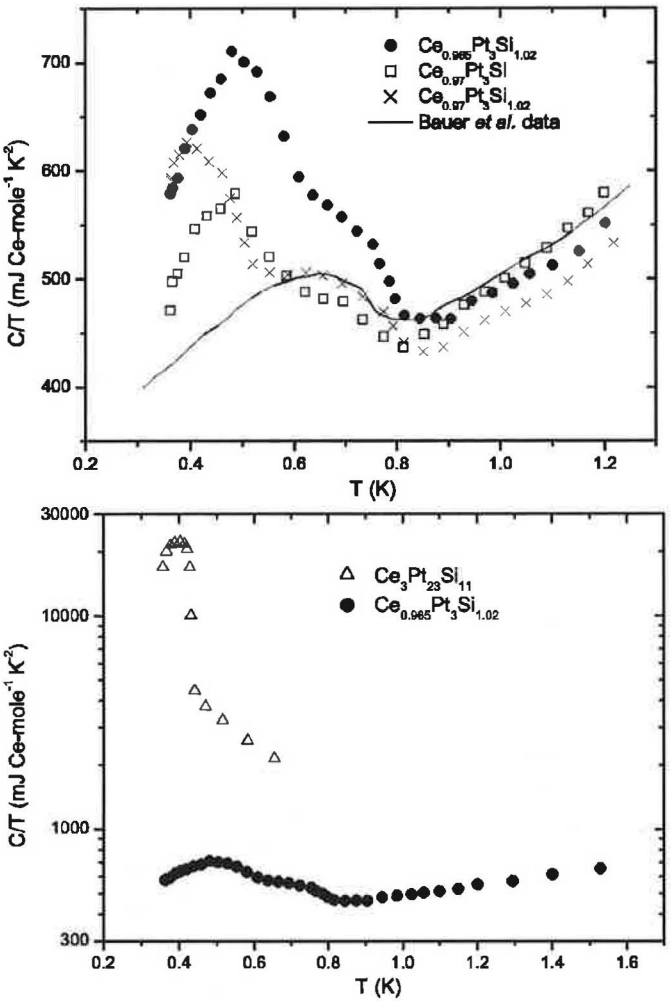

Figure 5.9: Sign of spurious double superconducting transition in $CePt_3Si$. Upper - various specific heat data, lower - specific heat of the spurious phase in comparison with that of the contaminated $CePt_3Si$ sample.

Substitutions

Only doping effects of La and Ge in $CePt_3Si$ were investigated, respectively [302]-[305].

The extraordinary sensitivity of the material on La doping is comparable to the alloying effect of a magnetic impurity in a conventional superconductor. Only ~ 2 atomic % of La completely suppress superconductivity. The abrupt attenuation of the critical temperature is assumed to be a pair breaking effect. This supports the unconventional SC state formed

in the $CePt_3Si$, simultaneously the enhanced spin-orbit scattering originates pronounced sensitivity to impurities. The 2 atomic % of La substitution causes a rapid shift of the Néel temperature below 1.8 K [302].

Substitution of Si by Ge was investigated by Bauer et al [303]. The Ge atoms randomly occupy the 1a sites of space group $P4/mmm$ up to 20 atomic % of Ge. The monotonic increase of both a and c parameters yields a growing unit cell volume upon substitution with increasing Ge concentration. The investigated samples are characterized by a concentration dependent onset of SC, where the Si/Ge substitution suppresses the SC roughly above 10 atomic % of Ge. A magnetic instability is referred to broadened magnetic phase transitions; the respective temperatures increase continuously with increasing Ge content. The Si/Ge substitution simply drives a volume expansion, thus magnetism is stabilized and SC finally ceases to exist.

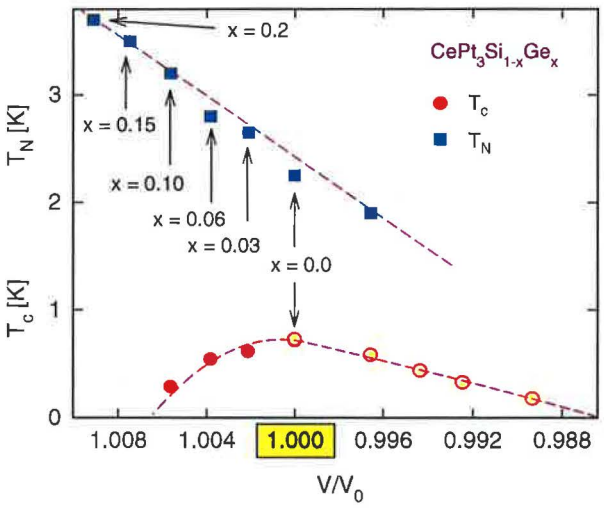

Figure 5.10: Evolution of T_c and T_N with the Ge substitution in $CePt_3Si$ according to ....

5.3 Isostructural RPt_3X compounds, R = La, Ce, Pr, Nd, Sm, Gd, R = Si, B

5.3.1 RPt_3Si, R = La, Ce, Pr, Nd, Sm, Gd

The series ternary $CePt_3Si$ homologous compounds RPt_3Si for R = La, Pr, Nd, Sm, Gd has been investigated by Bauer et al. [304]. Long-range antiferromagnetic order was encountered for R = Nd, Sm, and Gd. $PrPt_3Si$, however, does not show any sign of magnetic order down to 400 mK due to a nonmagnetic crystal effect field ground state arising for the non-Kramers Pr^{3+} ion in tetragonal symmetry.[8]

[8]Our recent specific heat investigations down to 400 mK and magnetic field up to 9 T suggested rather complex behavior. A well-defined anomaly was observed at $\sim$ 1 K. It's significantly supported by the applied magnetic field, however, it's smeared out by field-enhanced nuclear contribution of the Pr^{3+} ion. We

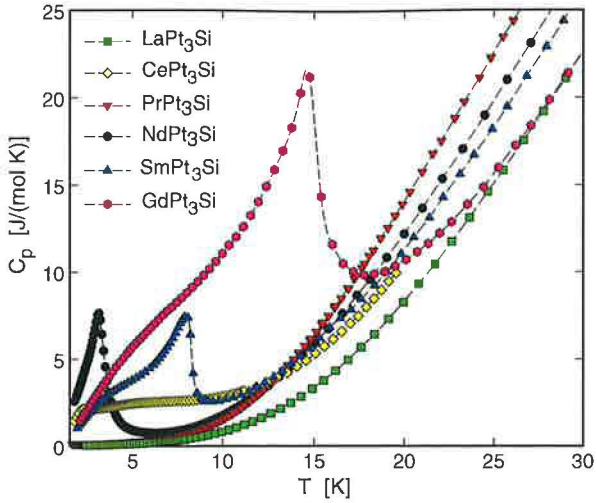

Figure 5.11: Specific heat of RPt_3Si, R = La, Ce, Pr, Nd, Sm, Gd compounds according to [313].

RPt_3Si	a(nm)	c(nm)	T_N (K)	μ_{eff}	θ_P
La	0.411 27	0.543 16	-	-	-
Pr	0.406 83	0.544 43	-	3.51	-15
Nd	0.405 58	0.543 88	3.3	3.58	-7
Sm	0.403 38	0.541 47	8.3	0.74	1
Gd	0.403 02	0.538 96	15.1	7.73	11.5

Table 5.3: Lattice parameters and magnetic characteristics of the RPt_3Si compounds.

A mean-field type of order is revealed for the spin-only case $GdPt_3Si$. CEF effects were conceived to be responsible for the observed deviation of the Néel temperature, T_N from the de Gennes scaling.

The most important structural and magnetic characteristics of the isostructural RPt_3Si compounds are summarized in the Table 5.3.

5.3.2 RPt_3B, R = La, Ce, Pr, Nd

The only group of compounds keeping the same crystal structure as the light-rare earth RPt_3Si (R = La - Gd) silicides are the analogues borides.

The $CePt_3B$ is actually the model compound for the non-centrosymmetric tetragonal structure with the *P4mm* space group. It has been first time reported by Süllow et al.

speculate about possible nuclear and $4f$ spin coupling yielding intra-mixed nuclear-electronic spin order. The hypothesis is supported by the electrical resistivity experiments. The resistivity remains intact in magnetic fields. As the nuclear-electronic spin order is the matter of intra-ionic exchange, the electrical transport should not be significantly affected.

Its recent re-investigation stimulated by the discovery of the exotic $CePt_3Si$ was performed by Bauer et al (specific heat analysis [308]) and Vejpravova et al [306, 307](comprehensive results will be presented in the Chapter 8).

In contrast to its Si isotype, the compound do not show superconductivity. It undergoes two successive magnetic phase transitions, paramagnetic to an antiferromagnetic phase at $T_N = 7.8$ K and at $T_C = 6$ K from the antiferromagnetic phase to a reduced-moment ferromagnetic state.[9] This interpretation is supported by the absence of hysteresis between T_C and T_N and the susceptibility plateau. Although metallurgical analysis revealed no impurity phase causing the ferromagnetism, a trace amount of ferromagnetic impurity originating the ferromagnetic-like behavior cannot be excluded. The Ce effective moment was reported of about 2.3 μ_B/f.u. and the paramagnetic Curie temperature θ_P = - 12 K. A possible Kondo effect in the compound is found to be rather week.

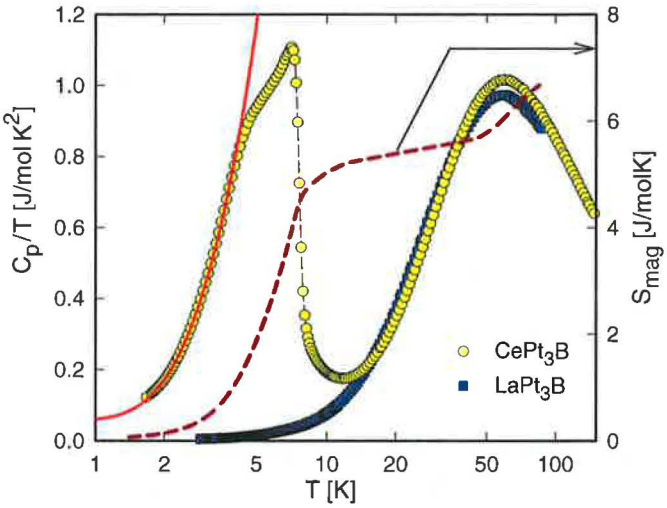

Figure 5.12: Specific heat of $CePt_3B$ according to [308].

The crystal structure and magnetic properties of ternary rare-earth platinum borides RPt_3B (R = La, Pr, Nd) has been studied in [309]. The tetragonal $CePt_3B$ structure type has been confirmed for all the three compounds.

$LaPt_3B$ exhibits temperature independent Pauli-type paramagnetic response. $PrPt_3B$ orders antiferromagnetically at $T_N = 15$ K followed by a ferromagnetic spin flip at $T_C = 5$ K.[10] $NdPt_3B$ exhibits an antiferromagnetic spin alignment at $T_N = 7$ K.

The most important structural and magnetic characteristics of the isostructural RPt_3B compounds are summarized in the Table 5.4.

[9] Both transitions have been observed in the recent studies as well, however, the absolute values of T_N and T_C are slightly varying.

[10] Our investigations by specific heat and magnetic susceptibility revealed contrary results. The compound remains unordered down to 400 mK. The data presented in [309] are rather strange and do not clearly prove the proposed ordering in the compound.

RPt_3B	a(nm)	c(nm)	T_N/T_C (K)	μ_{eff}	θ_P
La	0.40317(3)	0.51066(4)	-	-	-
Pr	0.39950(1)	0.50610(2)	15/5	3.59	-11
Nd	0.39890(3)	0.50475(5)	7	3.61	-5

Table 5.4: Lattice parameters and magnetic characteristics of the RPt_3B compounds.

5.4 Other isotypic RPt_3Si compounds

The heavier rare-earth elements and Y seem to form structure variants with much larger unit cells and centrosymmetry in contrast to the $CePt_3B$-structure type kept in the La - $GdPt_3Si$ series. The structures are known for the Y, Er, Dy and Yb cases only. They are rather complicated and therefore cannot be easily deduced from the powder diffraction data.[11] The corresponding crystallographic parameters are summarized in the Table 5.5. Except the Yb system [312], the compounds were not further investigated by means of their magnetic and transport properties.

There is only a short report on $TmPt_3Si$ - it is crystallizing in a derivative structure type of $CePt_3B$ (not described in detail) and reveals a negative temperature coefficient of the electrical resistivity below the room temperature [312].

$Yb_{18}Pt_{51.1}Si_{15.1} \sim YbPt_3Si$

Yb containing compounds in many cases exhibit anomalous physical properties at low temperature, similar to Ce systems. This fact is often simply attributed to the mirror-like electronic configuration of Ce and Yb systems. Superconductivity, however, has never been encountered in heavy-fermion-based Yb systems. The $YbPt_3Si$ shows no superconductivity in contrast to its isotype $CePt_3Si$.

Besides the general observation mentioned above, the compound shows a slightly different stoichiometry and a centrosymmetric tetragonal structure consisting of $CePt_3B$-type building units with areas of strongly distorted regions in between.

[11] The Er structure may be described as a supercell of the Dy and Y structures, respectively, with the P4/mbm symmetry, doubled along the c axis.

Table 5.5: Crystallographic data of the RPt_3Si compounds.

$RPt_{\sim 3}Si$	space group	a (nm)	c (nm)	exact composition R:Pt:Si
Y	$P4/mbm$	1.87778	0.40897	18 : 50.56 : 15.44
Er	$P4_{2/m}nm$	1.86723	0.81734	36 : 102 : 32
Dy	$P4/mbm$	1.7777	0.40891	18 : 50.28 : 15.72
Yb	$P4/mbm$	1.86246	0.40513	18 : 51.1 : 15.1

The Yb ion is in the trivalent ground state, giving rise to a stable $4f^{13}$ electronic configuration of the system. A long-range antiferromagnetic order sets in at $T_N = 1.8$ K with a spin-wave gap of the order of 1 K. Below 0.5 K a further magnetically ordered state occurs.

The paramagnetic temperature regime is characterized by the interaction of the Kondo effect and crystal electric field splitting. The tetragonal crystal structure causes a lifting of the eightfold degenerate $j = 7/2$ total angular moment of the Yb ion, resulting in a manifold of four doublets with the first excited CEF level separated by more than 100 K from the ground state. Hence, magnetic order occurs within the ground-state doublet which, additionally, is evidenced from magnetic entropy data.

Referring to [312] the field dependence of the heat capacity supports a considerable magnetocaloric effect around 2 K, revealing a high potential to realize efficient sample cooling to temperatures well below 1 K.

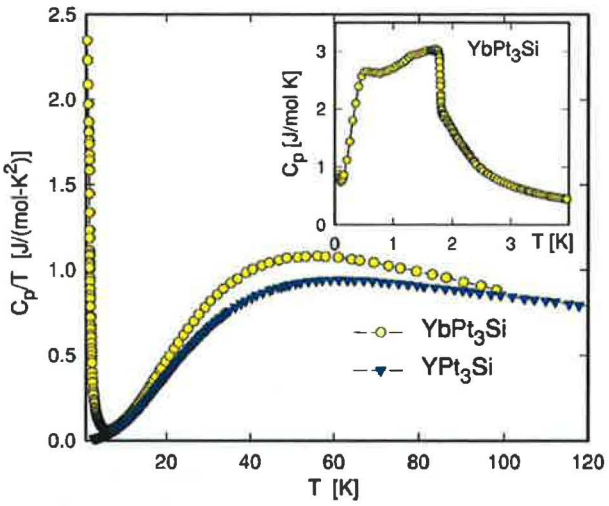

Figure 5.13: Specific heat of $\sim$ $YbPt_3Si$ compound according to [312].

Additional references to $CePt_3Si$ and related compounds

There have been published much work on the $CePt_3Si$ so far. The most crucial references, which were not discussed in the previous text are presented in the bibliography as well: [313]-[329].

Chapter 6

Ferromagnetic (or not) SC $CeRu_2$ and relatives

[1]

Laves phase $CeRu_2$ belongs to the exotic group of intermetallic compounds known as unconventional superconductors. It stands out from the class of 'conventional superconductors' in extreme type II behavior (Ginsburg-Landau parameter, $\kappa = 16$), whilst permitting the possibility of sample preparation in a metallurgically clean state. The superconductivity is originated by the Ce $4f$ electron states as supported by additional alloying with magnetic ions on Ru sites - there is no detrimental effect to the superconductivity. The $4f$-nature of the SC state in $CeRu_2$ is also corroborated by the fact, that its analogue $LaRu_2$ show conventional type-II superconductivity below 4.4 K.

Furthermore, the $CeRu_2$ is known as the sole ferromagnetic superconductor based on Ce.

The compound was earlier assumed to be tetravalent due to its small lattice parameter and lack of localized magnetic moment. The high degree of delocalization is explained by the large value of the hybridization energy ($\sim$ 120 meV). This picture is supported by the photoemission resonant studies, which clearly demonstrate a $4f$ derived emission within 1 eV below the Fermi level (E_F) and more vaguely at 2.5 eV below E_F, respectively.

[1]The overview of $CeRu_2$ up to date knowledge was composed from references [330] - [410]. The literature interpreting the physics of $CeRu_2$ in context of other Ce based strongly correlated materials is given in references [411] - [464].

$CeRu_2$	structure	space group	a(pm)	T_m (K)	T_c (K)
	C15	$Fd\bar{3}m$	754.5	40	5.6
	($MgCu_2$-type)		T = 300 K		

Table 6.1: Basic characteristics of $CeRu_2$.

6.1 Superconductivity and ferromagnetism in $CeRu_2$

6.1.1 $CeRu_2$

The coexistence of the two collective phenomena, superconductivity and magnetism, was first extensively studied in the Chevrel phases, where in certain pure compounds magnetic order appears below the superconducting transition temperature. In these materials the magnetically ordered ions are only weakly coupled to the conduction electrons. A different situation pertains for some of the heavy fermion superconductors (like $CeCu_2Si_2$, UPt_3 or URu_2Si_2; for details, please see the previous Chapter 5). The small size of the ordered magnetic moments in these compounds relative to their Néel temperatures attests to the more complex many-body origins of their magnetism.

$CeRu_2$ surpass other unconventional Ce superconductors; it is the only one HFSC with a ferromagnetic exchange interaction between the Ce magnetic moments, whilst the other Ce HFSC with coexistence of magnetic ordering exhibit solely antiferromagnetic arrangement. It condenses into a static magnetic state at the temperature $T_m = 40$ K, which persists into the superconducting state below $T_c = 5.6$ K.

The evidence of static ferromagnetic ordering comes from both muon-spin relaxation measurements and a.c. susceptibility measurements on a single crystal (see Figure 6.1).

In the superconducting state of $CeRu_2$ an abrupt transition from irreversible magnetic behavior near the upper critical field to almost perfectly reversible behavior at lower fields occurs. The robustness and well-defined nature of this transition has led to the contention that it might be due to some underlying transition within the superconducting state, rather than due to a continuous evolution of flux pinning effects alone. The correlation length of the flux line lattice interpreted within a theory of weak collective pinning yielded a pin spacing of the order of the superconducting coherence length. So far no evidence of the pinning mechanism has been forthcoming.

In this light, the existence of magnetic order raises the possibility that the pinning is magnetic in origin and not necessarily related to crystalline defects. In the pure compound the transition is indeed quite subtle and therefore it was not probably picked up in pilot dc magnetization studies.

The mentioned evidences of extremely small-moment ferromagnetism in $CeRu_2$ seems to be rather doubtful (in fact they are the reason for the 'or not' appending remark in the title of the Chapter). The peradventures may be summarized as follows:

- The effect of muon injection into the structure is comparable to the hydrogen substitution on the same lattice site (for the hydrogenation effect, please see the next section). There are several reports on effect of hydrogenation in $CeRu_2$; the most important conclusion is the abrupt change of the Ce ion valency by means of localization of the Ce $4f$ states. However, similar effect of muon cannot be excluded. The partial localization may enhance or in fact originate the proposed static ferromagnetic ordering reflected by muon life-time decay.

- Due to complexity of the ternary Ce - Ru - Si phase diagram it is very difficult to prepare any Ce - Ru (- Si) sample in a single-phase and impurity free state. Moreover, the Ce

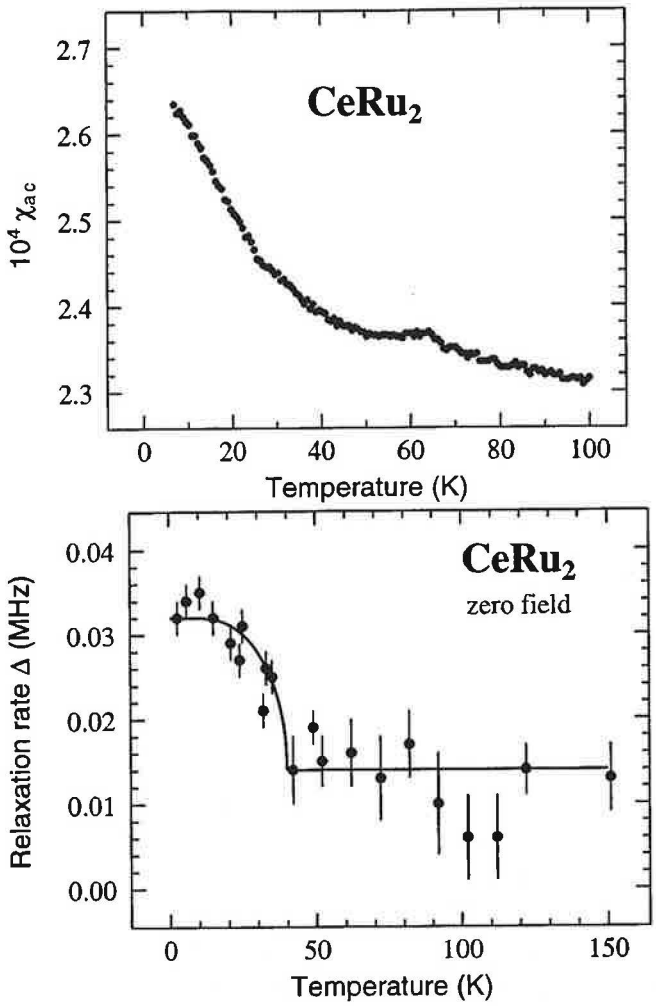

Figure 6.1: Temperature dependencies of the a.c. susceptibility and the muon relaxation rate in $CeRu_2$ according to [330].

metal itself usually contains a pretty large amount of spurious entities. The known a.c. susceptibility data purportedly demonstrate formation of the ferromagnetic state. An analogues dependence may be observed in any Pauli metal with a small amount of paramagnetic or ferromagnetic impurity.

- There are no additional proofs of ferromagnetic ordering in $CeRu_2$ except the muon-spin polarization investigations. In contrast the indirect evidence from the in-field pinning phenomena in the superconducting state supports some kind of magnetic condensation.

6.1.2 Superconductivity and ferromagnetism of $CeRu_2$ under substitution

Effect of hydrogenation

Like many other Laves phases, $CeRu_2$ absorbs hydrogen up to $CeRu_2H_{\sim 4}$. The protons occupy interstitial sites preserving the C15 structure with the relative lattice expansion of about 12 %. The simultaneous disappearance of the superconductivity and resulting paramagnetic behavior (with the Ce magnetic moment $\sim 0.65\ \mu_B$) point out to the localization of the Ce $4f$ states upon hydriding. The fully trivalent Ce in $CeRu_2$ hydrides was also confirmed by X-ray photoemission core-level spectroscopy (Figure 6.2).

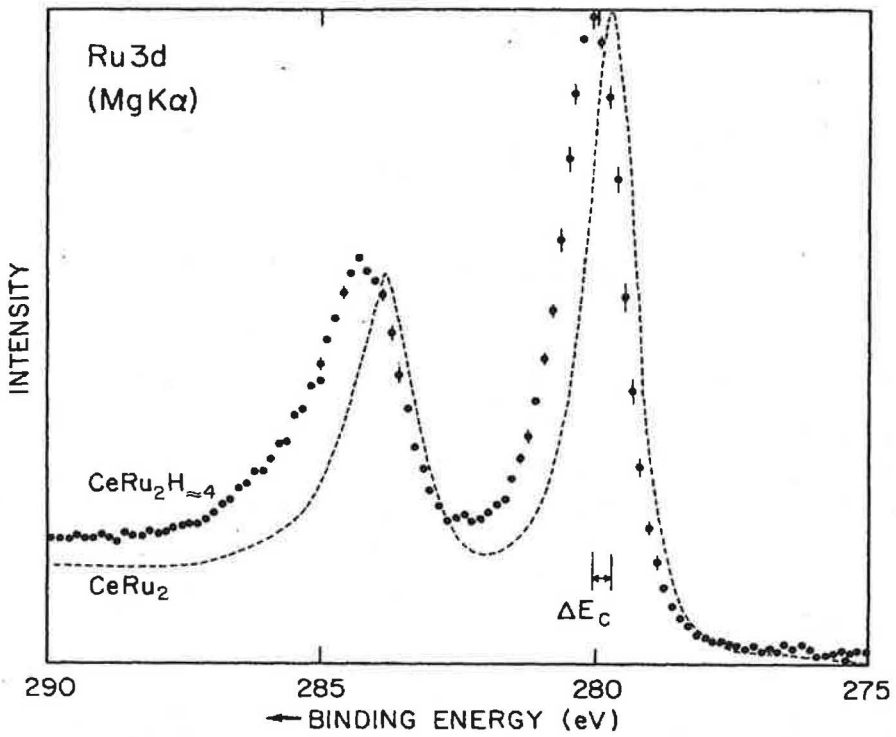

Figure 6.2: Photoemission data on $CeRu_2$ and its hydride according to [330].

Alloying by other RE

[2]

Early studies concerning the coexistence of magnetism and superconductivity related to $CeRu_2$ considered compounds where the Ce had been partially substituted by a third ionique species. It was found that the replacement of Ce with significant quantities of other lanthanide metals can give rise to short-range ferromagnetic correlations. On substituting higher concentrations of these elements the superconductivity is eventually destroyed and replaced by a long-range ferromagnetic order.

[2]The overview about the role of alloying and disorder in $CeRu_2$ is based on the references [465]-[483].

Chemical substitution at the Ce site by La has been one of the approaches used, to explore the rich physics involved with the interplay of the localized and itinerant character of the Ce $4f$ electrons, and to get a further insight on the superconductivity of this system. The $Ce_{1-x}La_xRu_2$ provides a model case with the end member $LaRu_2$ to be a formally $4f^0$ system, showing superconductivity at 4.4 K. The T_c shows an anomalous change from 6.2 K, 0.3 K, and 4.4 K, respectively, at x = 0, 0.5, and 1 (while a continuous expansion of the unit cell with increasing of the La concentration occurs.

In addition, at low concentration, $0 < x < 0.15$, an anomalous T_c behavior has been observed with an increase of T_c with a maximum of 6.7 K in the range of x = 0.07 before the decrease with further increasing of the La concentration. This abnormal change in T_c with external pressure indicates an interesting behavior of the electronic correlations in the $Ce_{1-x}La_xRu_2$ system.

The anomalous T_c dependence on the pressure appears similar to the one found in the $Au_{1-x}Pd_xGa_2$ alloys, which has been assigned to a Fermi surface transition. Also, the new structural phases appearing under external pressure in the $CeRu_2$ and their possible relation with the superconductivity motivates further studies on this $4f$ superconductor.

6.2 Strongly correlated Ce - Ru - Si compounds

The ternary Ce - Ru - Si phase diagram is considerably rich. It comprises (besides 20 binary phases) 9 ternary compounds. The unique constellation of the Ce, Ru and Si electronic states incorporated in few common crystal structures results in exotic phenomena like intermediate valency, anomalous magnetism or heavy fermion behavior, usually accompanied with unconventional superconductivity. In this section, the most crucial cases will be briefly discussed.

6.2.1 $CeRu_2Si_2$

3

The $ThCr_2Si_2$ is a well-known and prevailing tetragonal crystal structure in the intermetallic compounds of 1:2:2 stoichiometry. When the Ce, Ru and Si atoms occupy the corresponding positions in the structure, one of the most famous representatives of the non-Fermi liquid/heavy fermion compounds without superconductivity is formed.

The $CeRu_2Si_2$ is characterized by the large value of the Sommerfeld coefficient (γ = 385 mJ/molK^2) and magnetic susceptibility flattening below 10 K. Despite some anomalous properties, like the linear low-temperature resistivity, $CeRu_2Si_2$ is in fact a Kondo lattice. Below a characteristic temperature T_K the system undergoes a cross-over from the high-temperature moment freedom regime to the low-temperature strongly correlated state described by heavy fermion (j ¿ 1/2) and particulary a Kondo system ($s = 1/2$) behaviors. This scenario has been demonstrated by Y and La substitutions on the Ce sites, resulting in enhancement/suppression of the NFL behavior, respectively.

Additionally, the compound exhibits a metamagnetic-like phase transition (MMT) accompanied by abrupt localization of the $4f$ states in high magnetic fields (Figure 6.3). In

[3]The overview of $CeRu_2Si_2$ up to date knowledge was composed from the references [484] - [516].

fact, the magnetic field acts as a switch between the delocalized and localized moment behavior. Due to many discrepancies between the proposed mechanism (based on the de Haas - van Alphen measurements) and the experimental data (high-field specific heat) a new mechanism of the MMT was recently proposed. The high-field effect involves a continuous evolution of the Fermi surface. The transition conserves the Fermi surface volume, it's topologically driven and keeps Fermi liquid behavior in al fields.

In essence the continuous Fermi surface transition can be described with a spin-split Fermi surface in a simple parabolic (but not necessarily isotropic) band. To quantify the spin (Zeeman) splitting, it is taken proportional to the applied magnetic field while the total Fermi volume is held constant. The conductivity contributions of both Fermi surface 'sheets' can be added, and the resulting resistivity and Hall resistivity are depicted in Figure 6.4, respectively.

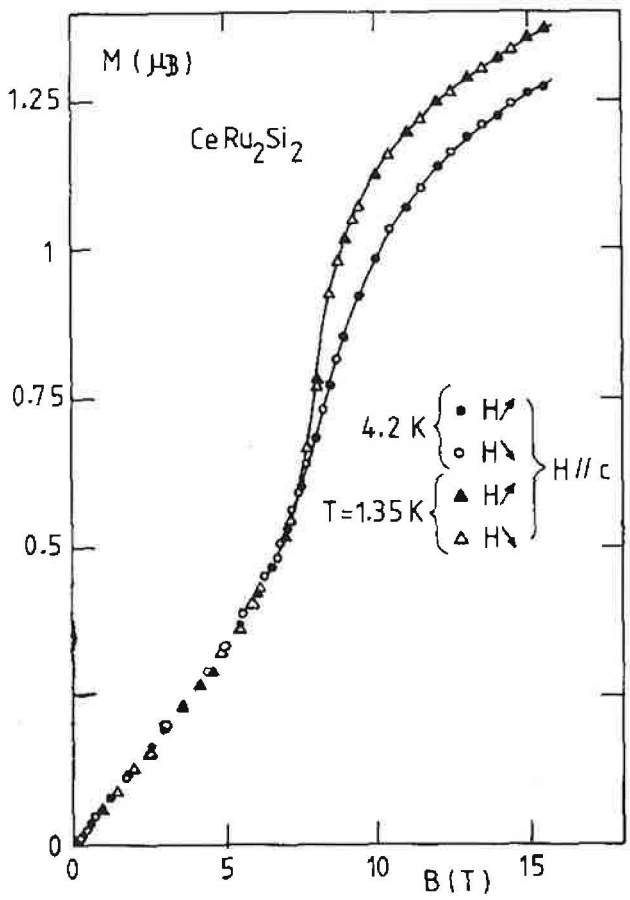

Figure 6.3: Magnetization curve of $CeRu_2Si_2$ [510].

Because the compound is the archetype of the heavy fermion behavior, there's enormous number of references available (more then 350 since the first report). For concrete details concerning alloying effects on electronic properties, specific experiments etc., please see the selected significant references ([484] - [516]).

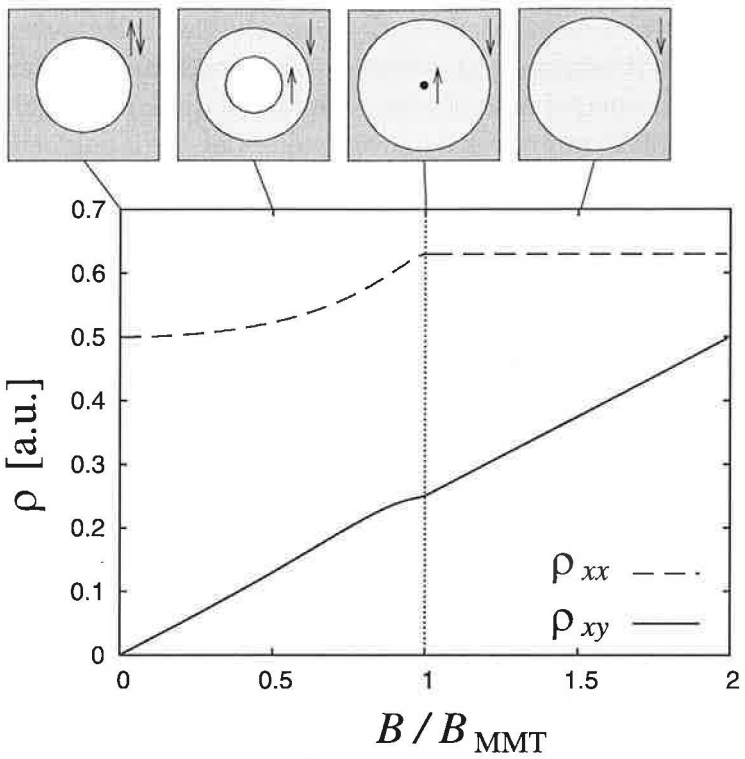

Figure 6.4: Magnetoresistivity and Hall resistivity of a model system consisting of a spin-split, hole-like spherical Fermi surface where one of the spin sheets shrinks to a point at BMMT.
The pictures show the field evolution of the Fermi surface.

6.2.2 CeRuSi

CeRuSi crystallizes in the orthorhombic TiNiSi-type structure (space group *Pnma*). In fact it is the less investigated heavy fermion Ce - Ru - Si containing compound. Besides the report on its formation and crystal structure, only one reference with respect to its electronic properties was published. The compound is reported as medium heavy fermion with the enhanced γ coefficient 220 mJ/molK^2. A shallow maximum at around 0.5 K was attributed to coherence effects. However, the quality of the presented data and consequent interpretations is slightly controversial [517, 518].

6.2.3 $CeRuSi_2$

$CeRuSi_2$ belongs to the rare family of compounds, where the Kondo effect coexists with ferromagnetism. Its crystal structure ($NdRuSi_2$-type, space group $P2_1/m$) is monoclinic.

Magnetic and specific heat measurements demonstrate the presence of a ferromagnetic transition with Curie temperature $T_C \sim 10$ K. The maximum on the temperature-dependence of the electrical resistivity and enhanced electron specific heat with Sommerfield coefficient ~ 100 mJ/molK^2 suggest its classification as the concentrated Kondo system.

The ferromagnetism in $CeRuSi_2$ was further suggested by recent muon spectroscopy in-

vestigations. However, presence of muon-spin relaxation in high longitudinal fields below and above the T_C indicated also fluctuations of the cerium magnetic moment in the compound.

The most important references on the $CeRuSi_2$ system are: [519]-[526].

6.2.4 $CeRu_3Si_2$

The $CeRu_3Si_2$ compound was reported in [527]-[536]. The $CeRu_3Si_2$ crystallizes in the hexagonal structure ($P6_3/m$, $LaRu_3Si_2$-type). The compound is a mixed-valent system corroborated by the enhanced Pauli-type magnetic susceptibility. It undergoes a superconducting transition below 1 K, which is much smaller then the value of T_c in its analogue $LaRu_3Si_2$ (7 K). The upper critical field, $H_{c,2} = 0.24$ T proves the type-II behavior. The Ginzburg-Landau parameter is estimated to $\kappa \sim 6$.

Chapter 7

Results and discussion - rare-earth metals

Typical representatives of systems, in which the purity crucially influences electronic properties are the rare-earth metals. Part of the work was therefore focused on purification and further investigations with respect to the purity of investigated metals. The following chapter comprises:

- reports on the solid-state electrotransport experiments performed on the Ce, Tb and Er metals,
- results of macroscopic investigations of the Ce, Er and Tb, metals
- discussion of the obtained results.

7.1 Treatment by solid state electrotransport

7.1.1 SSE apparatus testing

As already mentioned the electrotransport process is ultra-high-vacuum (UHV) demanding, therefore the apparatus was examined for long-term stability of the UHV conditions. The pressure dependence during the testing procedure is depicted in the Figure 7.1.a. The results confirmed excellent stability of the UHV below 10^{-12} mbar for $\sim$ 3500 hours. The time dependence of the ion current of the Tri-Scroll pump (Figure 7.1.b) corroborates the retentive pumping capacity of the utilized four-stage pumping system.

In addition the chamber-baking procedure was monitored as well. The pressure dependence is shown in the Figure 7.1.c. The maximum baking temperature (T_{max}) was set to 300 °C to evaporate heavier organic contaminants from the chamber. The process was continuously monitored by a quadrupolar mass spectrometer (QMS). The typical QMS spectrum is demonstrated in the Figure 7.2. Besides the characteristic fragments of ambient atmosphere (H_2O, N_2, CO_2 and O_2), a series of peaks above m/z = 40 appeared due to presence of organic compounds. The organic impurities usually come from the sample surface (aceton, residua of the storage wax etc.) and experimentalist's treatment (biological constituents, polishing materials etc.).

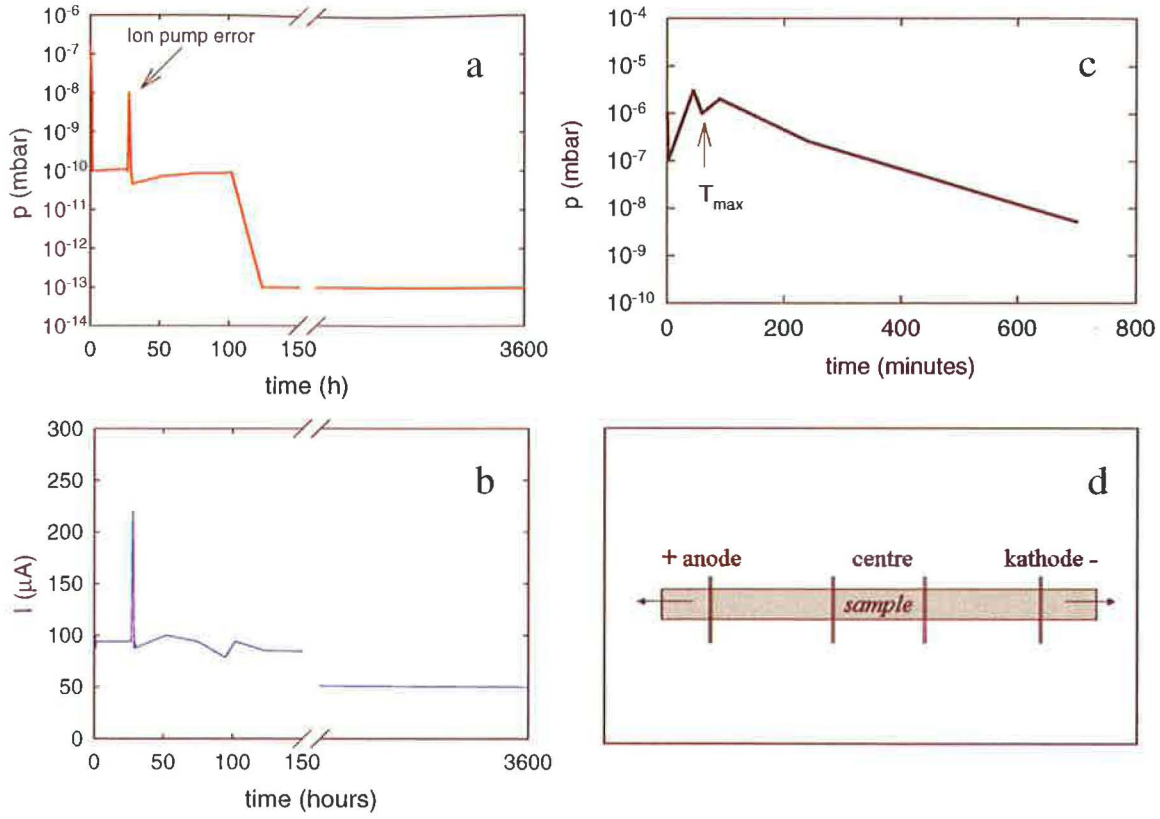

Figure 7.1: a - Pressure dependence during the long-term SSE chamber testing. b - Ion current dependence of the TriScroll ion pump during the long-term SSE chamber testing. c - Pressure dependence during the SSE chamber baking. d - Scheme of the zones of the SSE-treated sample .

Ce, Tb and Er rods were chosen for our studies. The nominal purity of the samples was 99.9 %. The original length of each sample was reduced from 150 to 120 mm; the cut-off piece was used for reference measurements of the electrical resistivity (to determine the *RRR*) and other properties. The samples were mounted inside the SSE apparatus as described in detail in the Chapter 3. For further description of the sample parts, the rod was imaginarily divided into three main areas with respect to the current flow: cathodic, center and anodic, as shown in the Figure 7.1.d.

Contrary to the previous works, we did not applied the maximum acceptable current (corresponding roughly to the 9/10 of the melting point), but kept the optimum lower values for much longer time. The choice of our *long-term regime* is also corroborated by the theory of electrotransport, which implies longer processing times to be better for reaching the steady state redistribution of the impurities in the specimen. We tried to validate the positive effect experimentally. The typical SSE parameters of the purified compounds are summarized in the Table 7.1.

We must stress out that we did not use complementary Ar (or He) atmosphere as suggested by Fort during purification of Er or Tb as metals with higher volatility at the typical SSE-processing temperatures. [77, 76].

	$0.9T_m$ (°C)	v.p. (mbar)	t	t_O (h)	T_N (h)	T_C(h)
Ce	691	3×10^{-14}	9×10^5 y	520	5167	4660
Tb	1201	6×10^{-5}	5 h	120	367	797
Er	1349	4×10^{-2}	30 s	98	131	393

Table 7.1: SSE characteristics of the treated samples.
T_m - melting temperature, v.p. - vapor pressure at 0.9 T_m, t - time to lose 1% of the sample at $0.9T_m$ by vaporization, $t_{O(N,C)}$ - time to approach the steady state for the oxygen, nitrogen and carbon impurities.

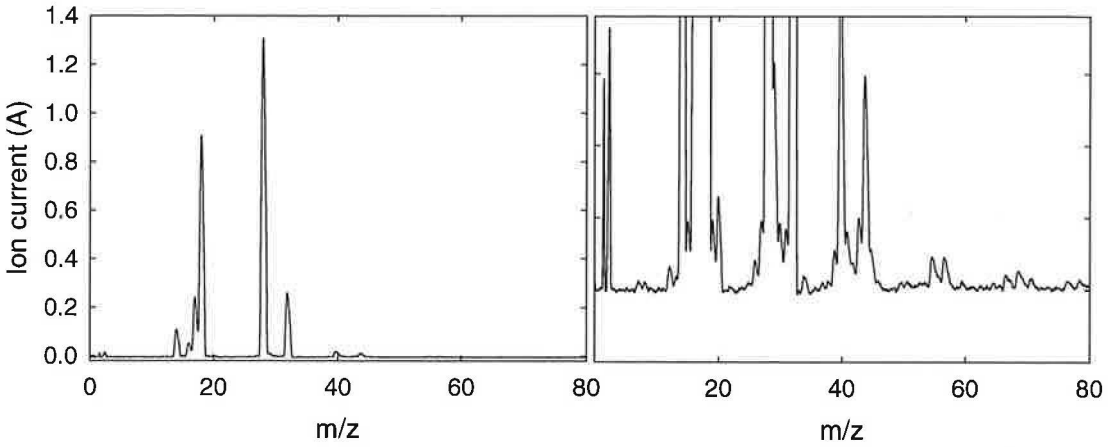

Figure 7.2: QMS spectrum during the baking procedure.
The detail of the weaker peaks (left) reveals presence of various organic contaminants up to high m/z.

7.1.2 SSE treatment of Ce, Tb and Er metals

A this point, the key experimental results of the SSE process are presented.

The characteristics, which must be monitored during the SSE treatment are:

- chamber pressure,
- applied current,
- sample voltage,
- sample temperature (and its distribution along the rod),
- processing time and
- ion current, respectively.

The crucial criterion of the purity improvement is the time dependence of the relative electrical resistivity (the actual resistivity reduced by the initial one). If the value saturates or even decreases during the experiment, the process is obviously effective.

The above mentioned dependencies are depicted in the Figure 7.3 for the Ce and Tb samples, respectively. It's clearly seen, that after reaching the *steady state* (for its definition, please see the Chapter 2), the chamber pressure and the ion current stay almost constant, so the value of the relative resistivity.

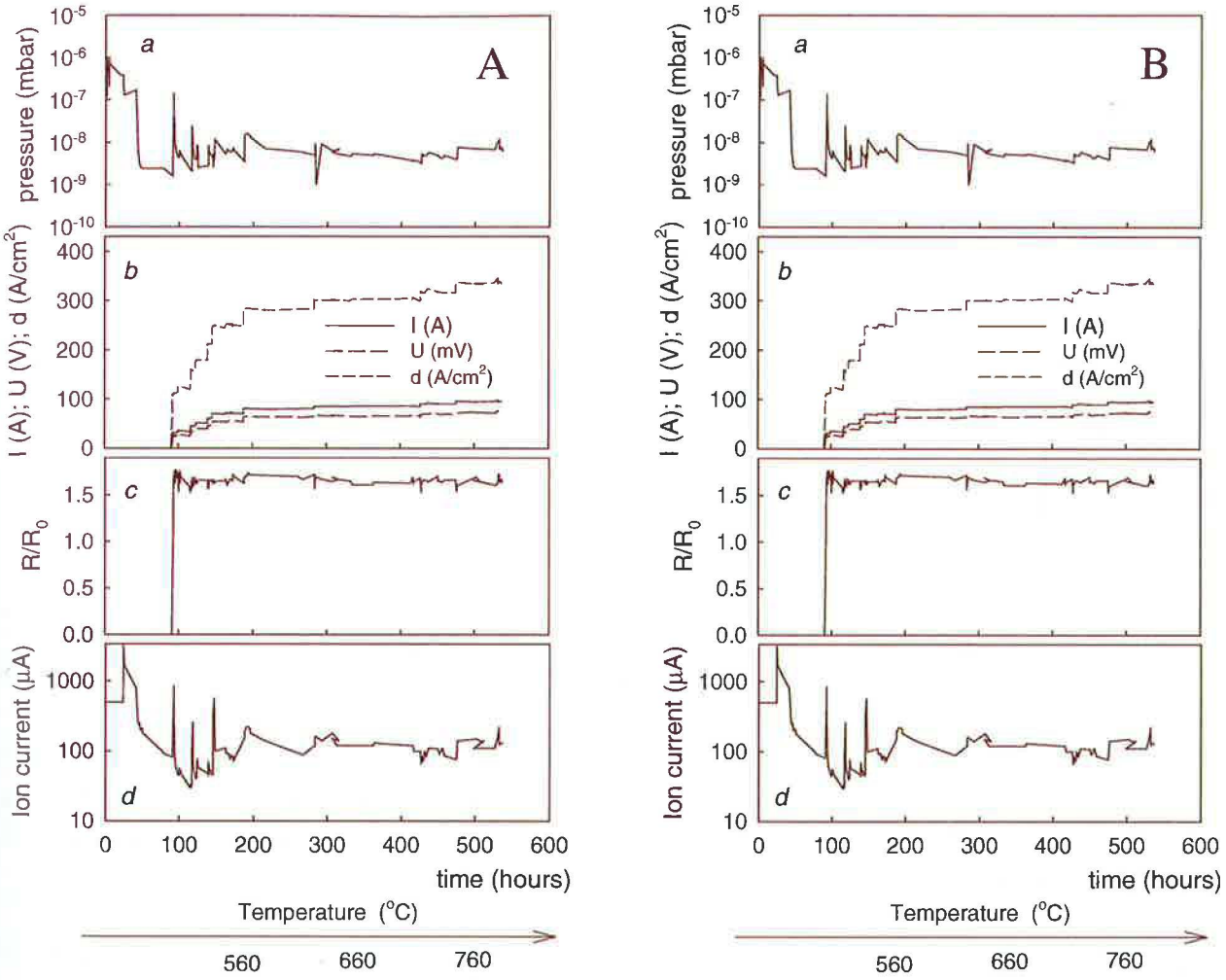

Figure 7.3: Experimental parameters of the SSE process.
Pressure (a), sample current, voltage, and current density (b), relative change of the sample resistivity (c), on current dependence of the TriScroll ion pump(d)in the SSE process for the Ce (A) and Tb (B) samples, respectively.

The composition of the residual atmosphere in the chamber was continuously monitored by QMS to analyze gaseous impurities evaporated from the treated sample. The values were not corrected to the residual atmosphere because of the time-dependence of the background gases. The partial pressure of the gases desorbed from the SSE chamber during the process is obviously not constant - it is reduced after long-term evacuating in comparison to the initial (just after the chamber baking) level. Therefore, no base line was measured to be subtracted from the recorded m/z spectra.

A typical QMS spectrum before and after application of the current to the sample, respectively, is depicted in the Figure 7.4.a (Ce metal). The difference between the two spectra revealed a significant contribution of the hydrogen, oxygen and water components.

The evolution of the water, hydrogen and nitrogen components under current of 100 A in the Ce sample is shown in the Figure 7.4.b, expressed as the relative ion current. After applying the 100 A (maximum loaded current) the sample gradually heats up and vaporizes a fraction of dissolved impurity gases. After approximately tens of hours, both the temperature and concentration of the evaporated gases saturate and the value of the applied current can be increased.

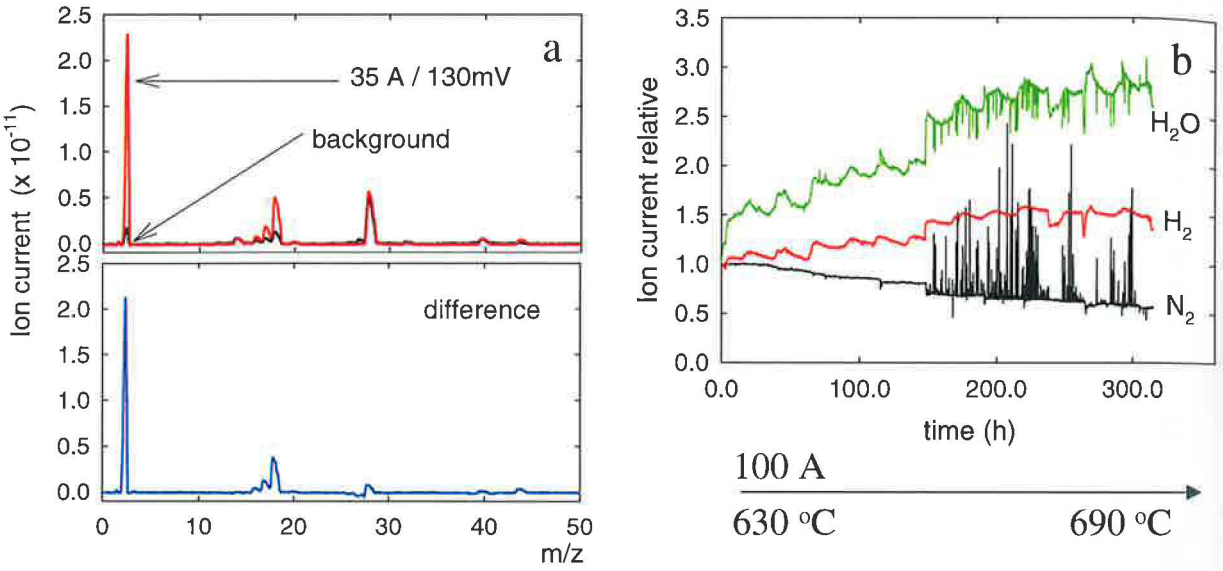

Figure 7.4: QMS spectra of the SSE-treated Ce sample.
a - residual gas spectrum (black line) in comparison to the spectrum after application of 35 A (red line) on the Ce sample. b - pressure time dependence of the gases evaporated from the Ce sample during the maximum loaded current.

Similar dependencies of the ion current in different timescales and stages of the SSE process are shown in the Figure 7.5 for the Er and Tb samples, respectively. It is evident, that both the elements dissolve different ratio of the spurious gases; hydrogen is the dominant contaminant in the Er while nitrogen in the Tb metal. Nevertheless, H_20, H_2, N_2 and O_2 are the major detected impurities in all investigated samples.

The most important experimental parameters, which were carefully controlled during the whole process, are summarized in the Table 7.2. Let's give some comments on their relation to the experiment control.

The very important characteristics are the sample temperature and temperature distribution along the sample rod. Evidently, we must not reach the melting point. The center part of the sample is the most heated, sometimes reaches over 100 ° higher temperature then the cathodic and anodic zones, respectively. Therefore, the maximum applied current is driven by the center zone temperature. The temperature of other parts of the sample was monitored as well to discover possible discrepancies in the current flow and heat convection

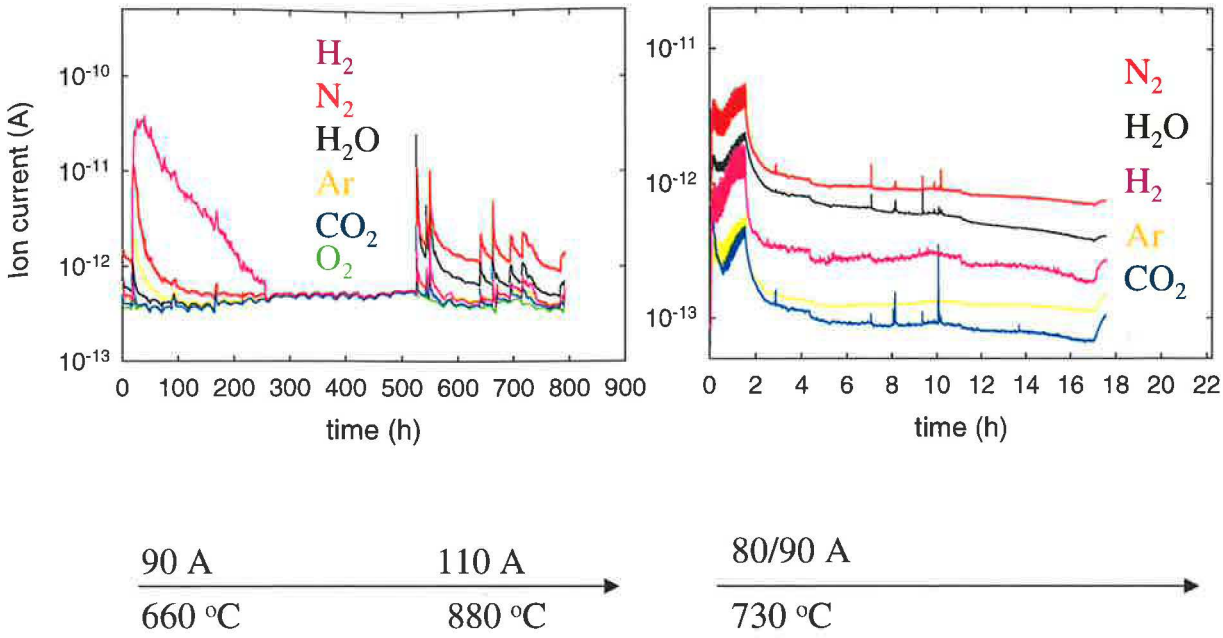

Figure 7.5: QMS spectra of the SSE-treated Er (a) and Tb (b) samples. The pressure time dependencies of the gases evaporated from the samples were selected at different stages of the SSE process.

due to e.g. potential cracking of the material. The temperature values under the maximum applied current and their average are depicted in the Table 7.2 for all three sample zones.

All three samples were further characterized by measuring of the residual resistivity ratio (RRR), which is presented in the Table 7.2 together with the low-temperature resistivity ρ_0. The resistivity of the Ce sample was measured in 0.9 GPa pressure to avoid the effect of the $\alpha \longleftrightarrow \beta$ phase transformation below 200 K.[1]

The RRR significantly increased and the ρ_0 decreased in all treated samples. The most distinct change has been observed in the cathodic zone of the Er and Tb samples, respectively. In case of the Ce metal, only the center part was investigated, however, dramatic improvement of the sample quality was found. In comparison to the available literature data, the obtained values of RRR and ρ_0 are in a good agreement, even better. We may in addition point out, that we worked in the long-term and semi-maximal current regime in contrast to the so far presented studies.

[1]Our investigation of impurity concentration on the ppm level by the available ICP and SIMS techniques did not revealed sufficiently consistent results with respect to the detection limits of the methods and their volume/surface and element sensitivity.

	T (C°)	time (h)	*RRR*	ρ_0 ($\mu\Omega$cm)
Ce	620*	2800	7	8.0
A	580		-	-
C	690		54	2.4
K	590		-	-
Er	1000*	480	4	33
A	890		7	23.0
C	1190		12	11.8
K	920		19	4.5
Tb	1200*	960	15	5.0
A	1120		28	4.2
C	1400		36	2.8
K	1080		43	1.0

Table 7.2: Experimental conditions of the SSE procedure. The first line of *RRR* and ρ_0 in each compartment represents the reference sample values. * marks the average temperature value.

7.2 Cerium

In this section, the results of comparative investigations of the Ce metal will be presented. The reference and the SSE-treated samples were investigated by the X-ray diffraction, electrical resistivity, thermal expansion, magnetization, a.c. susceptibility and thermal conductivity.

7.2.1 X-ray diffraction

The X-ray diffraction patterns of the bulk pieces of the Ce rod are depicted in the Figure 7.6. The rod was cut perpendicularly to the cylinder's axis and the X-ray beam diffracted from the resulting plane. The reference sample is denoted as R, the SSE treated one as SSE. The Bragg positions of the expected β and γ phases are shown as well.

As already mentioned in the introductory part (Chapter 5), the Ce phase diagram comprises three ambient-pressure phases. At the room temperature the β-phase should be stable, however, the γ phase forms just above 300 K and the complete transformation to the β phase occurs below 260 K. Therefore, either the coexistence γ-β regime and/or a high strain is observed in the Ce samples.

While the pattern of the reference sample shows no additional reflections except the dominant (100) one of the β phase, the SSE-treated sample exhibits additional distinct peaks, which suggest presence of the high-temperature γ phase. The additional small reflection at around 20° 2θ could not be attributed to any known simple Ce phase or other lanthanide.

Our further measurements on the same batch of the Ce reference samples always revealed

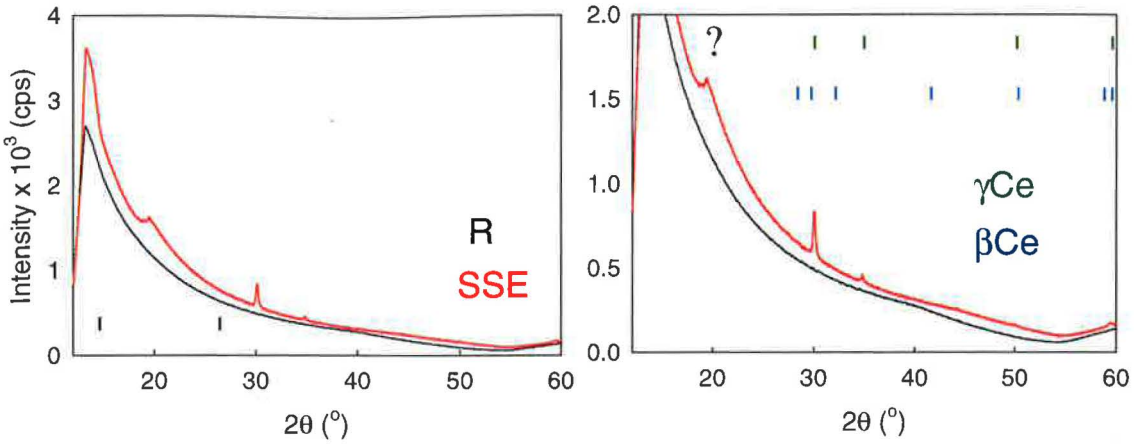

Figure 7.6: X-ray diffraction pattern of the Ce samples.
X-ray diffraction pattern of the SSE-treated (red) and reference (black) Ce samples. The black vertical lines in the left figure correspond to the major Bragg positions of the β phase.

the same pattern appearance. The only difference observed was the time effect on the ratio of the relative γ- to β-content in the SSE-purified material. Performing the analogues diffraction experiment after one year, the content of the γ phase was considerably reduced, but remained almost unchanged after two years.

We may speculate, that at least our regime of the SSE process extends the stability range of the γ phase.

7.2.2 Transport and dilatometric properties

The temperature dependencies of the electrical resistivity and the thermal expansion of the two representative Ce samples are presented in the Figure 7.7. The curve related to the SSE-purified sample in the Figure 7.7.a exhibits a moderate maximum at around 250 K, which is connected to the γ-β phases transformation. This observation is consistent with the results of the X-ray diffraction investigations taking into account, that the content of the high-temperature γ phase is enhanced in the SSE-treated Ce metal.

Further on cooling, both dependencies show a large step-like anomaly below $\sim$ 100 K attributed to the β to α phase transition. While the purified sample transforms already at 92 K, the reference one undergoes the transition at 80 K as deduced from the temperature derivative of the electrical resistivity (7.7.b). The volume change connected with the aforementioned transformation below 100 K prevented measurements down to low temperatures due to damage of the proper electrical contact.[2]

The temperature dependencies of the relative contraction/expansion (dl/l) and the isobaric relative volume change (α) are shown in the Figures 7.7.c,d. The dilatometric experiment was performed as follows: the sample was cooled down to 2 K (run 1), heated up to

[2]The volume and thermal effects accompanying the crystallographic phase transition were the reason of the fail of the heat capacity measurements by the relaxation method.

300 K (run 2), cooled down to 2 K (run 3) and finally heated up to 300 K (run 4, SSE sample only).

The run 1 - related curves are almost identical; the transformation temperature determined as the maximum of the α coefficient is 78 K for the SSE-treated and 76 K for the reference Ce samples, respectively. During heating (run 2), the re-transformation occurs at 181 K (an additional shoulder appears on the α vs T curve at 183 K) in the purified, and at 185 K in the reference sample, respectively. On second cooling (run 3) the transformation occurs at 95 K (SSE) and 98 K (R), respectively. Final heating of the SSE-sample revealed double anomaly with maxima at 183 K and 185 K.

Our observations are indicative of extension of the hysteresis region in the vicinity of the α-β transformation in the SSE-purified material. Moreover, the absolute values of the isobaric α coefficient are of about 25 % larger in the pure Ce sample.

The fine structure of the higher-lying anomaly in the SSE-sample is definitely not of the spurious experimental origin. It has not been reported yet and cannot be explained within the up to date knowledge.

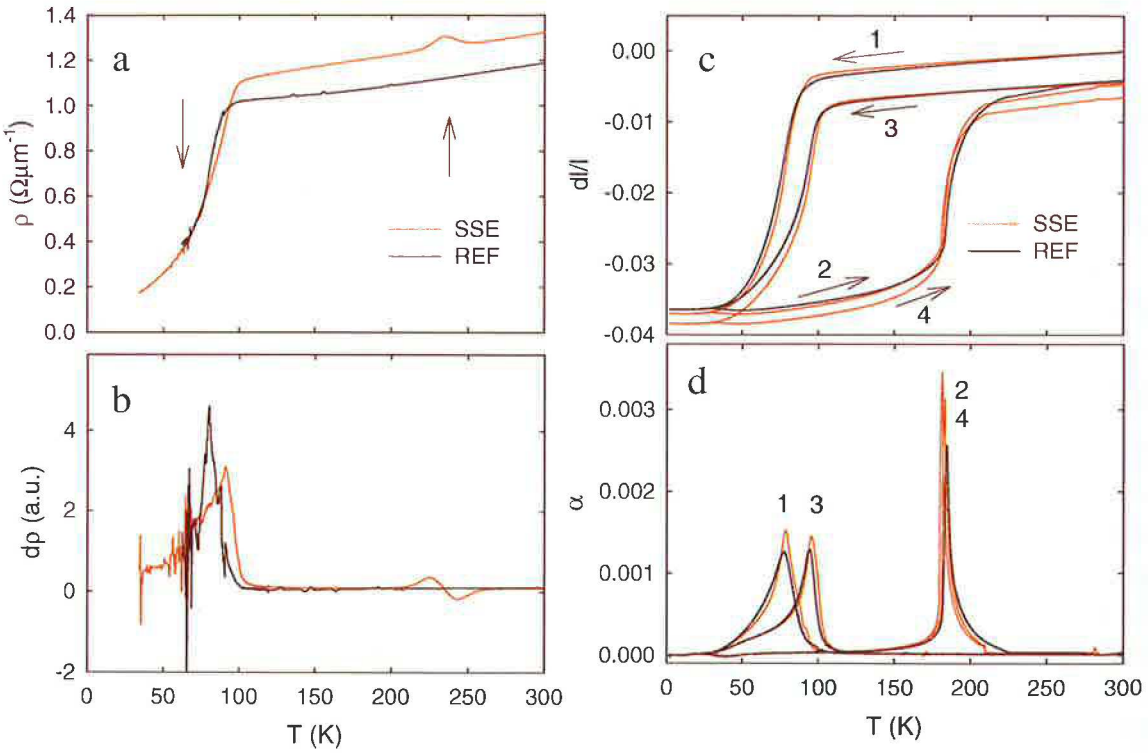

Figure 7.7: Temperature dependencies of the specific electrical resistivity (ρ) (a), its 1^{st} derivative (b), the relative contraction/expansion (dl/l)(c) and isobaric relative volume change (α)(d) of the SSE-treated (SSE) and reference (REF) Ce samples. For the numbers 1 - 4 meaning, please see the text.

The thermal conductivity (κ) (by means of its temperature dependence) of the SSE-purified and reference samples is shown in the Figure 7.8. The absolute value of κ is slightly higher in the reference sample. The purified material show only a moderate minimum at

around the α-β transformation temperature. The thermal conductivity of the reference sample increases on cooling below 120 K, yielding a kink at $\sim$ 100 K followed by a peak at 80 K. Both curves turn to decay on cooling below 40 K reaching 2 W/Km and 4 W/Km in the SSE-treated and the reference sample, respectively. No effects were observed in the vicinity of the β-γ transformation temperature.

The results of the thermal conductivity experiments are somewhat unmeaning. One cannot easily distinguish, especially due to the structural phase transitions involved, which of the contributions to the conductivity is modified the most (like in case of electrical resistivity). Moreover, the α phase orders antiferromagnetically below 20 K [3]

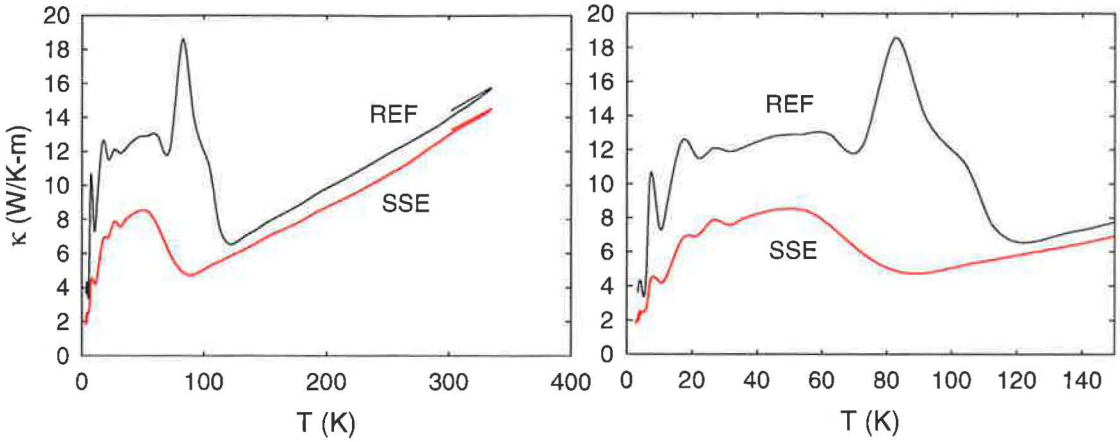

Figure 7.8: Temperature dependence of the thermal conductivity (κ) for the SSE-treated (SSE) and reference (REF) Ce samples, respectively.

7.2.3 Magnetic properties

The effect of SSE-treatment on the magnetic properties of Ce was also investigated. The zero-field cooled (ZFC) and field-cooled (FC) temperature dependencies of the static magnetic susceptibility are depicted in the Figure 7.9.a,b. While the Ce1-related ZFC dependence changes its slope at 14 K, then increases and finally saturates, the two other curves decay below 14 K and show mirror character. The FC curves have the same trend in all three samples, only the 2-K value varies from 1.75 to 0.6 x 10^{-8}m^3/mol. We attribute the observed anomaly to the magnetic ordering of the remnant β phase.

The real part of the a.c. susceptibility is depicted in the Figure 7.9.d. A single sharp anomaly peaks at 13 K in Ce1 and Ce2-related curves, and is rather well-detectable in the Ce3 sample (reference material). In consistency with the reported data and our static measurements, the anomaly corresponds to the para-to antiferromagnetic phase transition of the β phase.

[3]The thermal resistivity (1/conductivity) can be expressed as a sum of the two contributions: 1. due to electron scattering on static imperfections ($\sim 1/T$) determining namely the low temperature part of κ, and 2. due to scattering on the thermally excited phonons. In case of simple metals, the lowering of the thermal conductivity would correspond to the enhanced purity. However, this is not the Ce case.

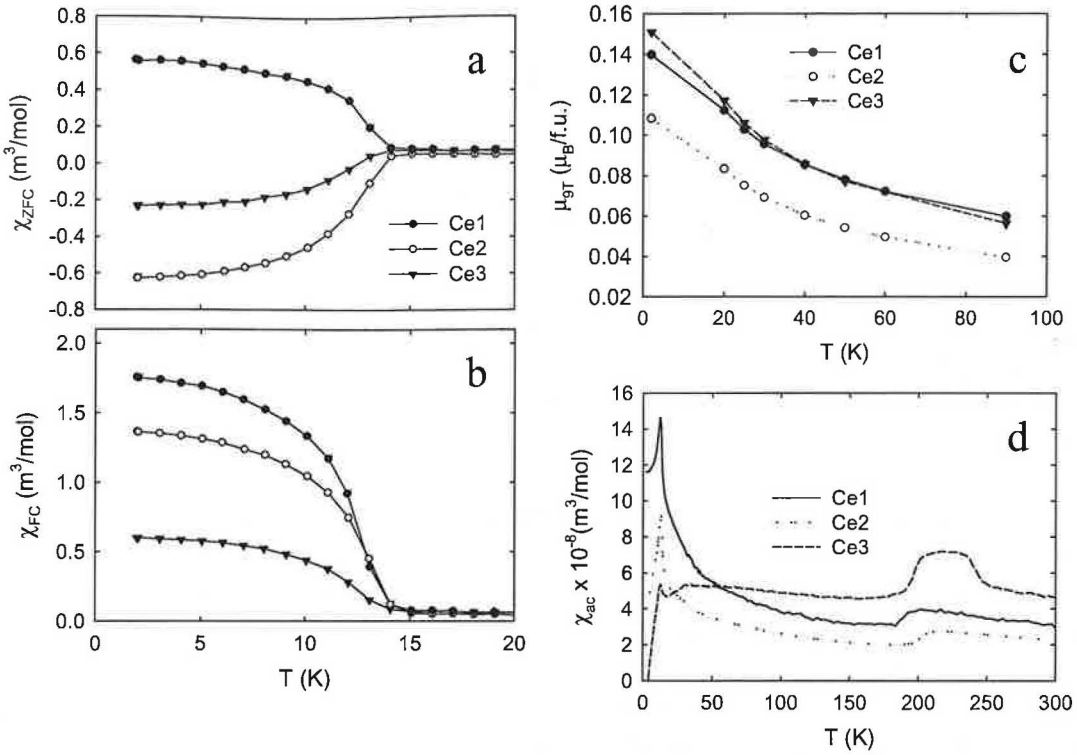

Figure 7.9: Magnetization and a.c. susceptibility measurements of the Ce samples; Ce1 - center Ce2 - cathode Ce3 - reference. a - ZFC magnetic susceptibility at 1 mT, b - FC magnetic susceptibility at 1 mT, c - temperature dependence of the magnetic moment at 9 T, d - real part of the a.c. magnetic susceptibility.

7.3 Terbium

In this section, the results of comparative investigations of the Tb metal will be presented, including investigations of a nanoscaled Tb sample. the samples were labelled as follows: C-center, A - anode, K - cathode parts, R - reference, N - nanoscaled. The reference and the SSE-treated samples were investigated by the X-ray diffraction, heat capacity, electrical resistivity, magnetization and a.c. susceptibility.

7.3.1 X-ray diffraction

The X-ray diffraction patterns of the bulk pieces of the Tb samples are depicted in the Figure 7.10. The rod was cut perpendicularly to the cylinder's axis and the X-ray beam diffracted from the resulting plane. The patterns are almost identical in case of the SSE treated and reference samples (Figures 7.10. a,b), and can be indexed with the Tb crystal structure. Three impurity peaks were found at around 25°, 29° and 36° 2θ in the reference sample, and their intensity was significantly reduced in the purified samples.

The intensity of the (002) reflection is enhanced in all presented data, suggesting preferential orientation in the (00l) crystallographic direction along the ingot. The texture is the most suppressed in the center part of the sample rod. The resulting values of the lattice

	R	C	A	K	N1	N2	N3
a (Å)	3.6118	3.6120	3.6121	3.6120	3.6010	3.6005	3.5993
c (Å)	5.7133	5.7131	5.7161	5.7143	5.6947	5.6954	5.6969

Table 7.3: Lattice parameters of the Tb samples.

parameters obtained by the Rietveld analysis are summarized in the Table 7.3.

The diffraction patterns of the nano-Tb material are shown in the Figures 7.10.c,d for X-ray and neutron irradiation, respectively. We investigated three different areas of the sample as shown in the Figure 7.10.c. While the areas 1 and 2 give almost the same diffraction response, the area 3 is characterized by enhanced intensity on the (100) reflection. The two broad maxima at low angles 25° 2θ probably correspond to amorphous fractions of the sample.

Similar impurity peaks as in the reference and SSE-treated samples were observed at 25° and 29° in the X-ray pattern, respectively, but not in the neutron data. We may speculate, that the impurity forms only on the surface, therefore its content is negligible with respect to the sample volume (seen by neutrons). However, the peak cannot be attributed to any simple Tb (e.g. oxide) or lanthanide phase.

7.3.2 Heat capacity and entropy

The temperature dependence of the specific heat of the reference and the nano Tb samples is shown in the Figure 7.11. The most significant differences can be found in the low temperature region (Figure 7.11.a,c) and in the vicinity of the magnetic phase transitions in the temperature range 220 - 230 K, respectively.

The low-temperature specific heat is considerably enhanced in case of the nano Tb sample, but still holds the $\gamma T + \beta T^3$ dependence expected for the three-dimensional metallic system. The estimated Sommerfeld γ coefficient is of about 30 mJ/molK^2 in the nano Tb in contrast to the reference sample with 20 mJ/molK^2.

The $C_p$anomaly at T_N peaks at 227 K and 223 K in the nano and reference sample, respectively. The shape of the anomaly is in an excellent agreement with the literature data in the reference sample. In the Tb metal the para-to- antiferromagnetic phase transition occurs at $T_N = 228$ K, at $T_C = 220$ K, it undergoes an antiferro-to-ferromagnetic phase transition. The specific heat data suggest lack of the T_N-related transition in the nano Tb.

In order to inspect the temperature dependence of the zero-field entropy in both materials, the relative isothermal entropy change (ΔS) and the relative adiabatic temperature change (ΔT)) was calculated by subtraction of the corresponding entropy data of the nano Tb from the reference. The idea is to estimate the effect of different aggregation state in the material, which we define as a *disorder-caloric effect* or *scale-caloric effect.* [4] The results

[4]We assumed the disorder to be the external field similarly as the magnetic or electric field acting on the magnetic or dielectric state of the system. The temperature or entropy change under applied magnetic field is known as the magneto-caloric effect, while the same phenomenon under electric field as the electro-caloric effect.

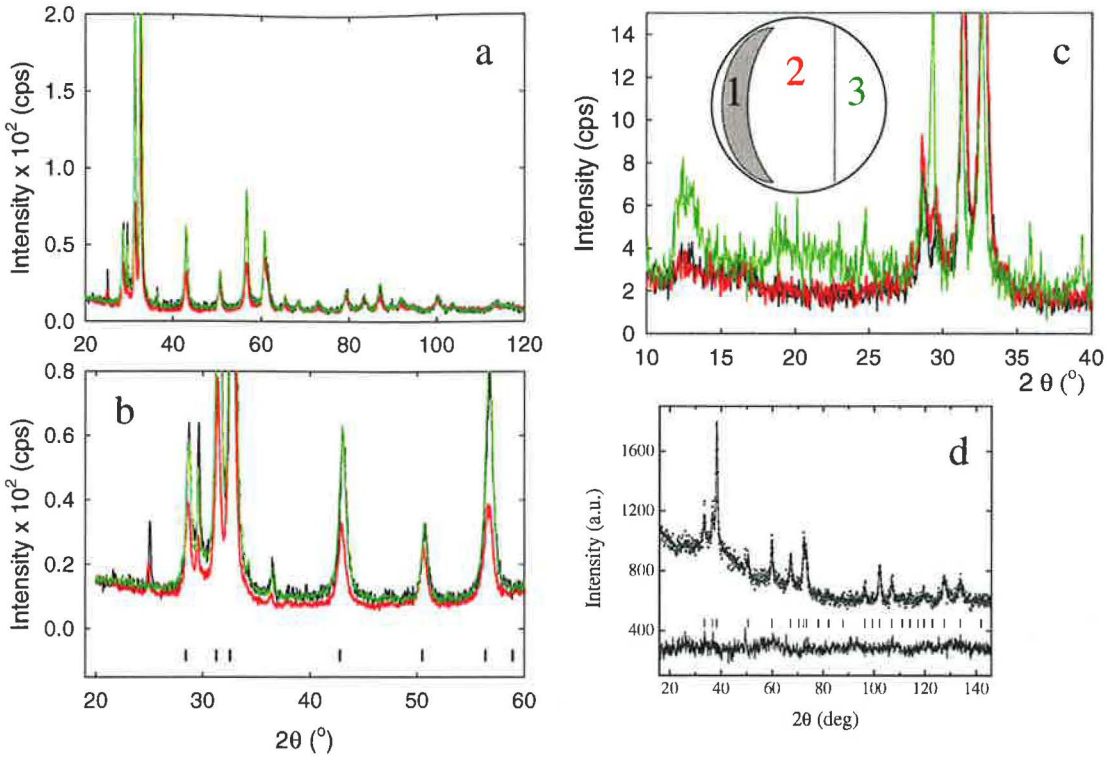

Figure 7.10: X-ray diffraction patterns of the Tb samples. a - R (black), C (red), K (green) samples, b - detail of a, the black markers correspond to the Tb diffraction lines positions, c - pattern of the nano Tb sample at three points of the ingot, d - neutron diffraction pattern of the nano Tb by Moze et al.

are depicted in the Figure 7.12. a,b. The low-temperature entropy of the nano Tb is larger by 0.6 J/molK^2, while the T_N and T_C-related entropy is lowered of about the same value. Similarly, the ΔT yields -1.5 K at 2 K and rises up to almost 5K in the magnetic transition region.

The observed low-temperature caloric effects can be interpreted as the entropy contribution due to formation (or annihilation) of the arrangement different from the common polycrystalline state. If we treat the contribution as some kind of electron/quasiparticle scattering on inhomogeneously distributed scattering centers, the effect would be dominant at low temperatures as observed. The opposite ΔS and ΔT effects in the vicinity of T_C and T_N are more probably ascribed to the lack of antiferromagnetic ordering in the nano Tb sample. However, the hypothesis must be proved on the microscopic scale.

The influence of SSE treatment on the magneto-caloric properties of the Tb samples was also investigated, namely due to its substantial importance for the applications. The results are depicted in the Figure 7.12.c,d. Its evident, that the purification procedure do not significantly influence the absolute values of ΔS and ΔT, respectively. The lowest absolute value was found in the anodic are of the sample, suggesting lowering of the absolute effect with lower purity of the material.

7.3.3 Electrical resistivity

The temperature dependence of the electrical resistivity is depicted in the Figure 7.13. The effect of the SSE purification is demonstrated by almost two-order of magnitude decrease of the resistivity in the treated sample (7.13.a). The improvement of the residual resistivity is shown in the Figure 7.13.b as a relative change of resistivity to the 300 K value. The lowest value was observed in the cathode part of the sample. The absolute values were already presented in the section 7.1. The temperature derivative of the electrical resistivity of the reference and the center-area sample is shown in the Figure 7.13.c, respectively, demonstrating negligible shift of the resistivity anomaly connected with the magnetic ordering at $\sim$ 225 K.

A very interesting feature was observed when investigating the most pure (cathode area) sample in the intermediate antiferromagnetic helical region. Previous magnetization and a.c. susceptibility studies proposed formation of the so-called antiferromagnetic domain walls when heating from the ferromagnetic to the helical phase just below the T_N. The effect is accompanied by furcation of the a.c. susceptibility curves measured during heating and cooling in zero magnetic field between 221 - 226 K. Analogues furcation was observed on the temperature dependence of the electrical resistivity as shown in the Figure 7.14. as the relative resistivity (a) and the difference between the cooling and heating branches (b).

7.3.4 Magnetic properties

The temperature dependence of the static magnetic susceptibility and hysteresis loops of all samples are presented in the Figure 7.15.

The character of the 5-T field-cooled curve is almost identical in all investigated samples. The 2-K value ranges from 1.0 - 1.2 $\times$ 10^{-4} m^3/mol for the SSE treated materials and the nano Tb sample, and 0.7 $\times$ 10^{-4} m^3/mol in the reference material. Such minority deviations can be ascribed to partial change of the texture (in fact observed by X-ray diffraction) of the Tb material during the SSE process.[5]

The ZFC and FC dependencies recorded at 10 mT are depicted in the Figure 7.15.b. Except the enhanced susceptibility values in the reference sample, the most crucial is the shape of the curves in the magnetic phase transition region, when comparing the 'common' and the nano material. While all polycrystalline samples show sign of multiple anomaly corresponding to the two consecutive magnetic phase transitions, the nano Tb material reveals rather a single anomaly. In addition the shape of its FC curve is smooth in the in contrast to the double kink feature on the other FC dependencies, suggesting a single ordered phase i the nano Tb sample.

Hysteresis loops measured at 2 K are shown in the Figures 7.14. c,d. The reference sample shows lower a value of the magnetic moment at 9-T and slightly larger coercivity field, H_C $\sim$ 0.2 T the SSE treated samples ($H_C \sim 0.1$ T). The curve for the nano Tb measured for the field perpendicular to the sample plane (and so the original ingot) is added for comparison. We must also point out, that relevant correction to the demagnetization factor could not be

[5]To avoid effect of demagnetization we used samples of the identical mass and shape, and oriented the rotational axis of the cylinder parallel to the magnetic field as shown in the Figure 7.15.

performed, because we could not reach saturation in the available magnetic field. Therefore we used identical samples (except the nano Tb) to get somehow comparable results.

The hysteresis loops at 2 K of the nanoscaled Tb for a magnetic field applied parallel and perpendicular to the sample plane are presented in the Figure 7.16 together with the magnetoresistance. The coercivity field is definitely larger then in the 'ordinary' samples, however it can be quantitatively evaluated for the parallel orientation only $\sim$ 0.2 T.

The magnetoresistance is negative yielding 14 % at 9 T. The remnant MR is of about 2% at 2 K.

The a.c. susceptibility is shown in the Figure 7.17. for the reference and the central-part of the purified Tb samples. Except the expected anomaly at $\sim$ 220-230 K, additional minority features can be observed, namely on the imaginary part of the dynamic susceptibility. The curve related to the reference sample exhibits a series of kinks, which may come from impurity heavy rare earths diluted in the material. Contrary, the purified sample yields just one pronounced spurious peak at around 25 K of unknown origin, which is enhanced with increasing frequency of the applied a.c. magnetic field.

We may speculate, that some part of the sample may form grains of $\sim$ nm size, which enter the blocked state at the anomaly temperature. Because of the inter-grain interaction, the frequency dependence of the maximum on the a.c. susceptibility is not observed. However, lack of the other spurious anomalies suggest higher level of purity in the SSE treated sample.

The experiments suggesting formation of the antiferromagnetic domain walls in the intermediate helical phase region were performed, as well. The results of the a.c. susceptibility investigations are shown in the Figure 7.18. for the SSE treated samples. We tried different regimes of heating/cooling. The furcation was observed in all samples and depended on the interval of the heating/cooling hysteresis. In agreement with the previous results the cooling-curve is situated below the heating-curve. Investigations of the after-effect of the applied magnetic field revealed slight enhancement of the absolute values of the susceptibility, but did not modify the character of the furcation significantly.

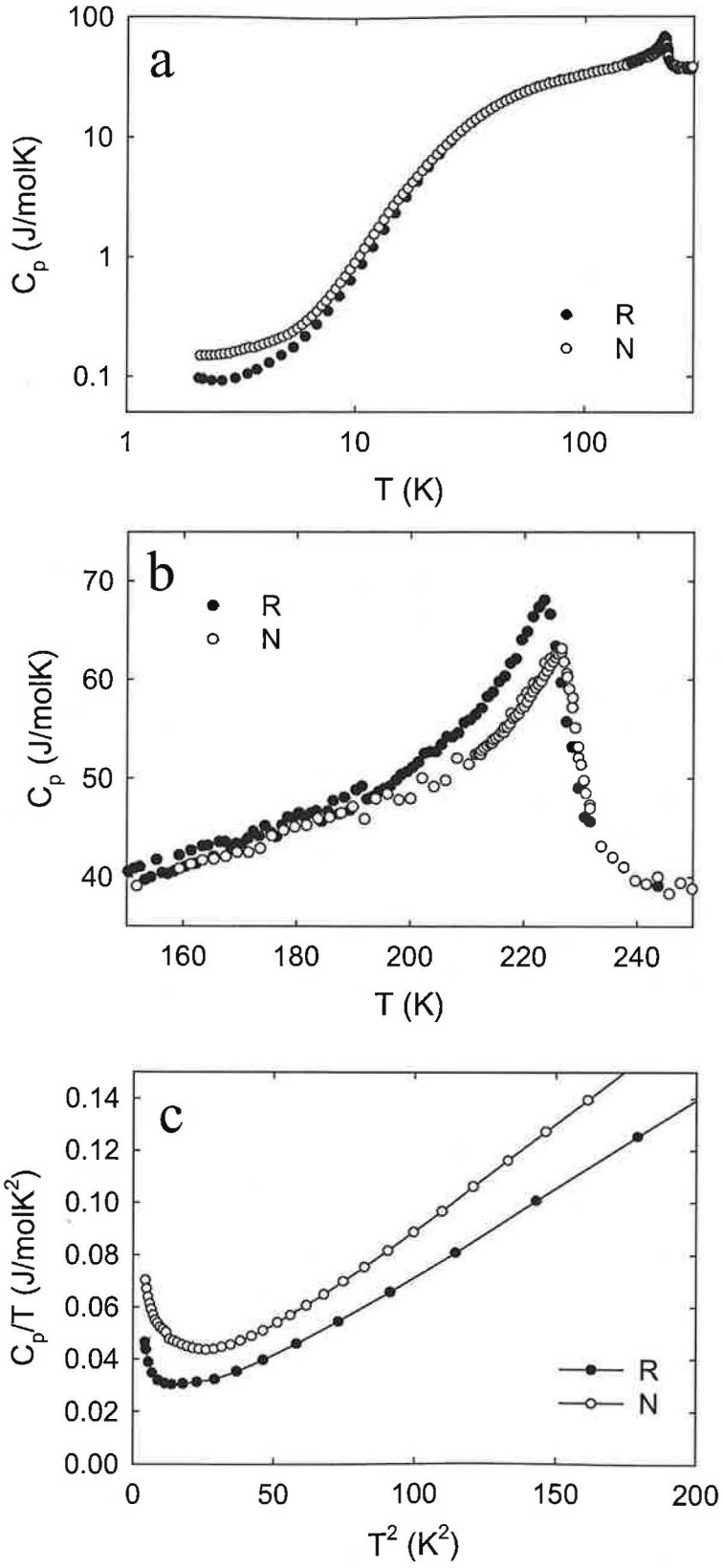

Figure 7.11: Temperature dependence of the specific heat of the reference (R) and nano (N) Tb samples. a - The $C_p$in the whole measured temperature range. b - Detail of $C_p$in the vicinity of T_N. c - Comparison of the low-temperature $C_p$part.

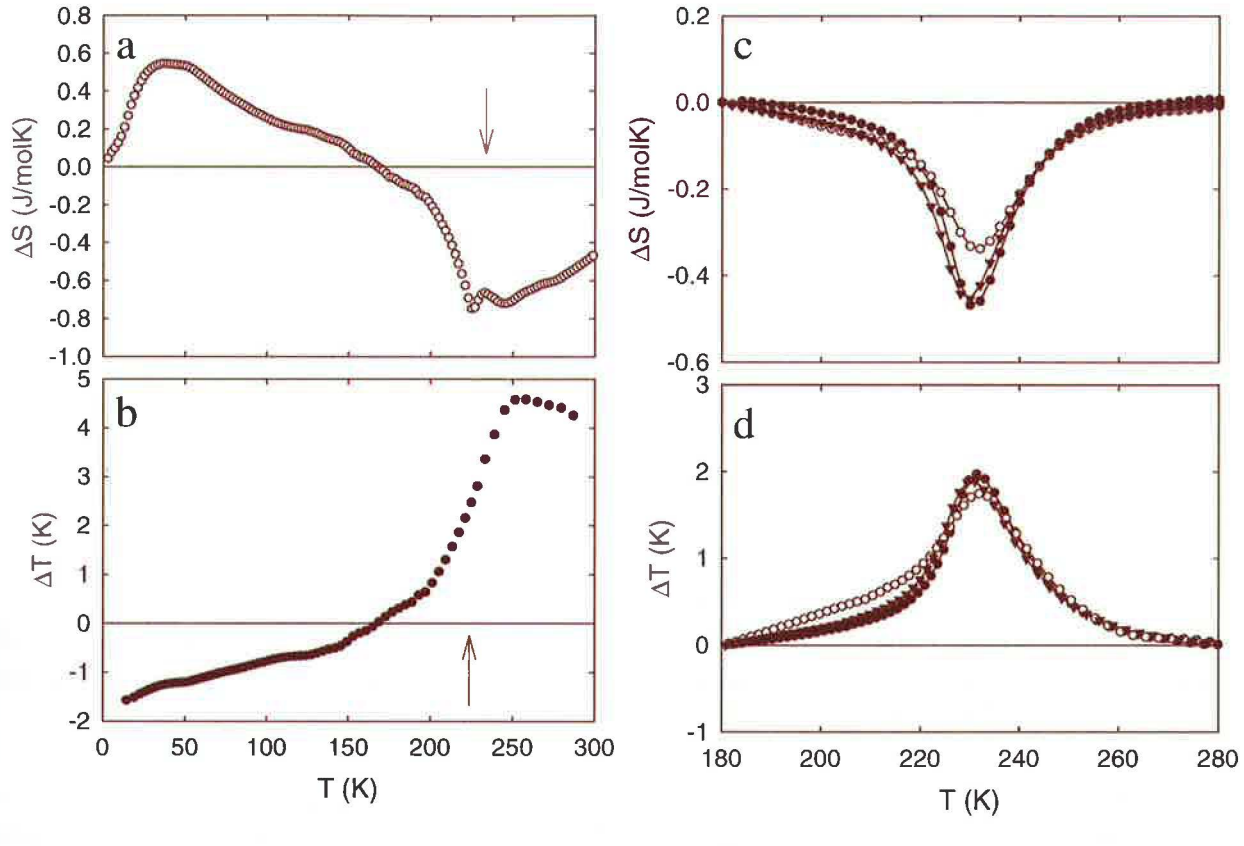

Figure 7.12: Magnetocaloric effects in Tb samples. a - relative isothermal entropy change (ΔS) of the reference (R) and nano (N) samples. b - relative adiabatic temperature change (ΔT) of the reference (R) and nano (N) samples. c - (ΔS) of the purified Tb samples. d - (ΔT) of the purified Tb samples. ○ - A ● - C ▼ - R.

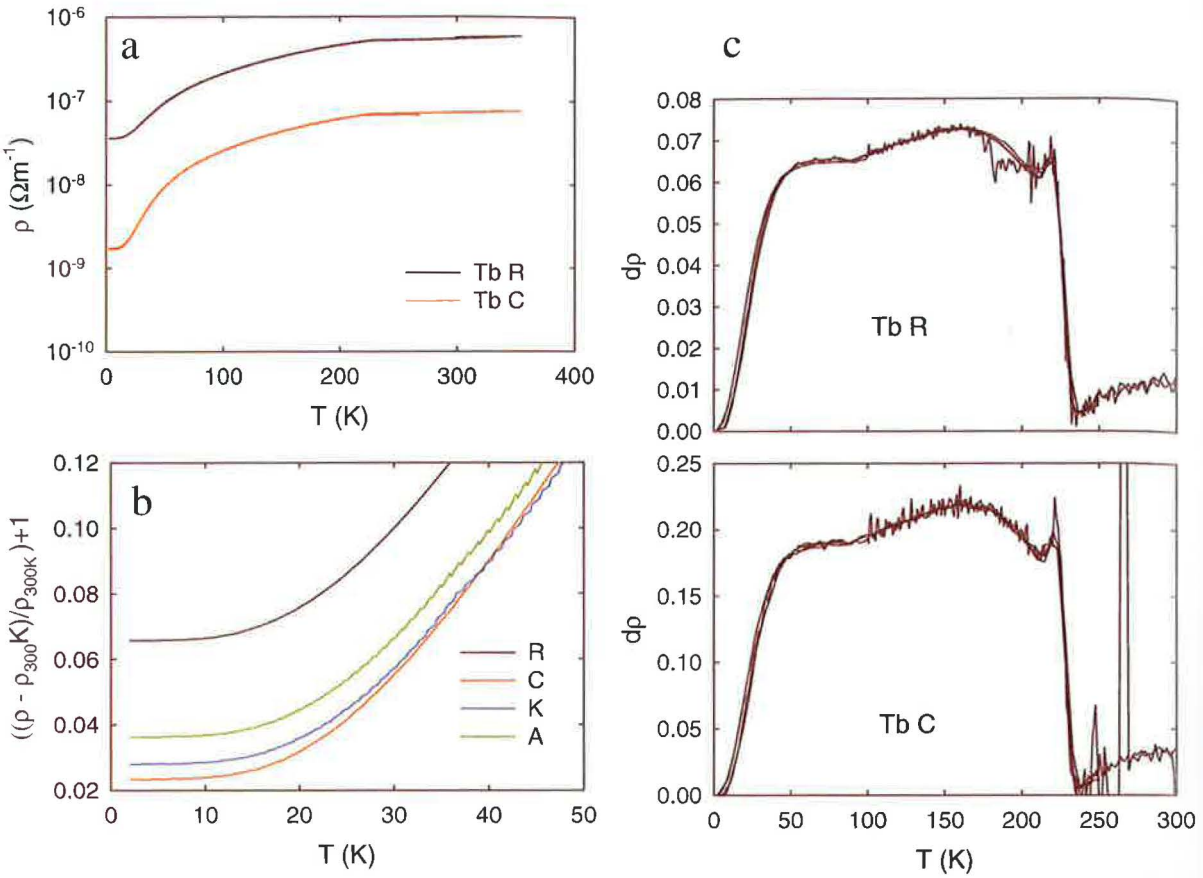

Figure 7.13: Electrical resistivity of the Tb samples.
Electrical resistivity of the Tb samples: a - comparison of the C and R samples, b - detail of the low-temperature region, c - Temperature dependence of the 1^{st} derivative of the electrical resistivity of the C and R Tb samples.

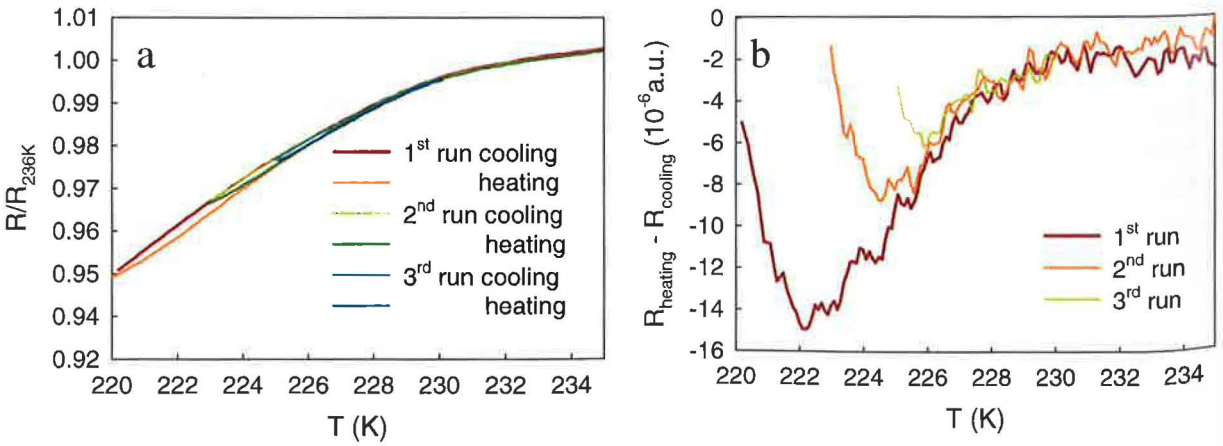

Figure 7.14: Effect of the AF domain formation on the electrical resistivity of the SSE treated samples in the intermediate region: $T_C < T < T_N$.

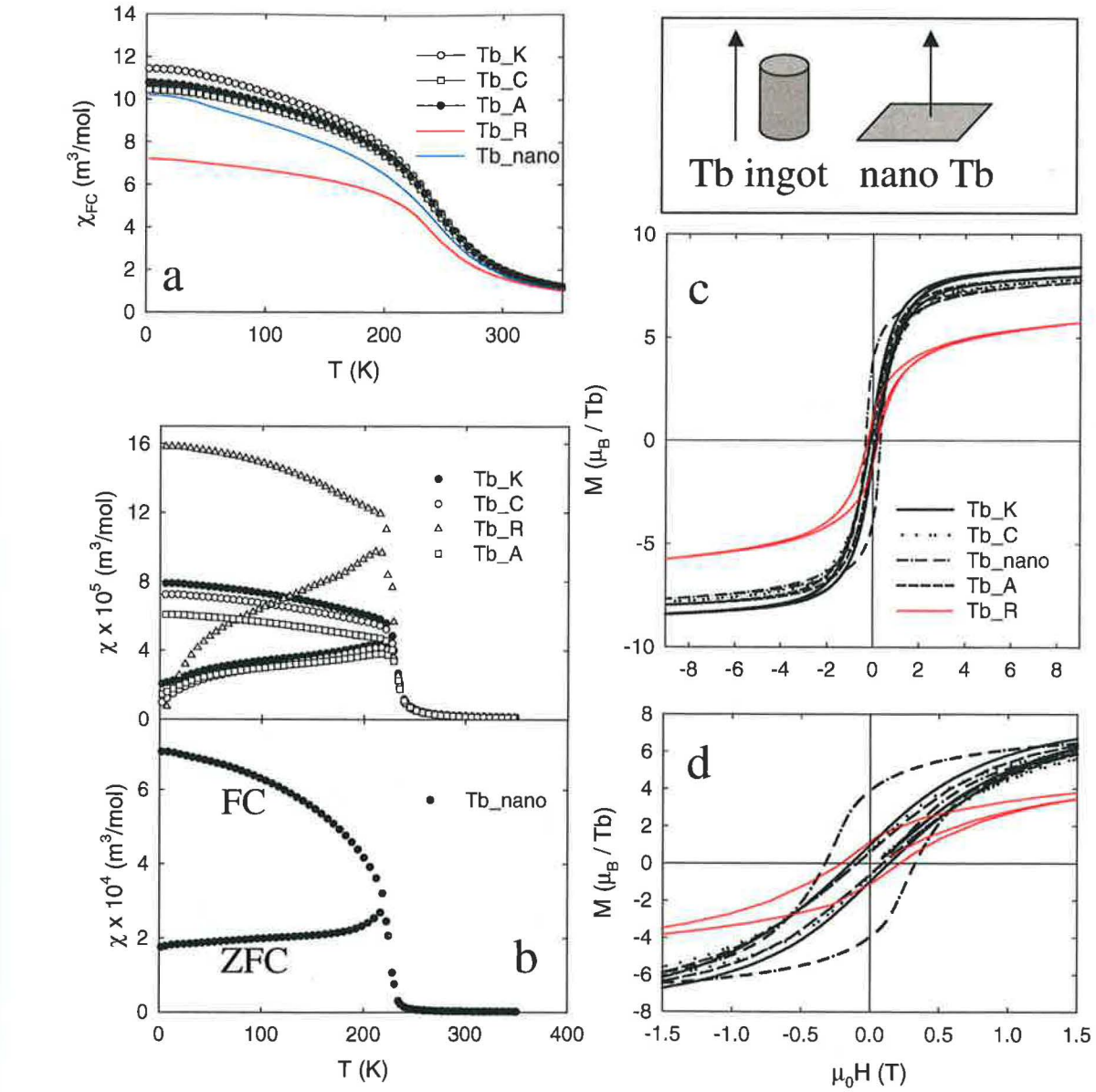

Figure 7.15: Magnetic properties of the Tb samples.
Magnetic properties of the Tb samples. a - Temperature dependence of the FC magnetization at 5 T. b - Temperature dependence of the ZFC and FC magnetic susceptibility at 10 mT. c - Hysteresis loops at 2 K. d - Low-field detail of the hysteresis loops. The picture in the right upper corner depicts the orientation of magnetic field with respect to the samples.

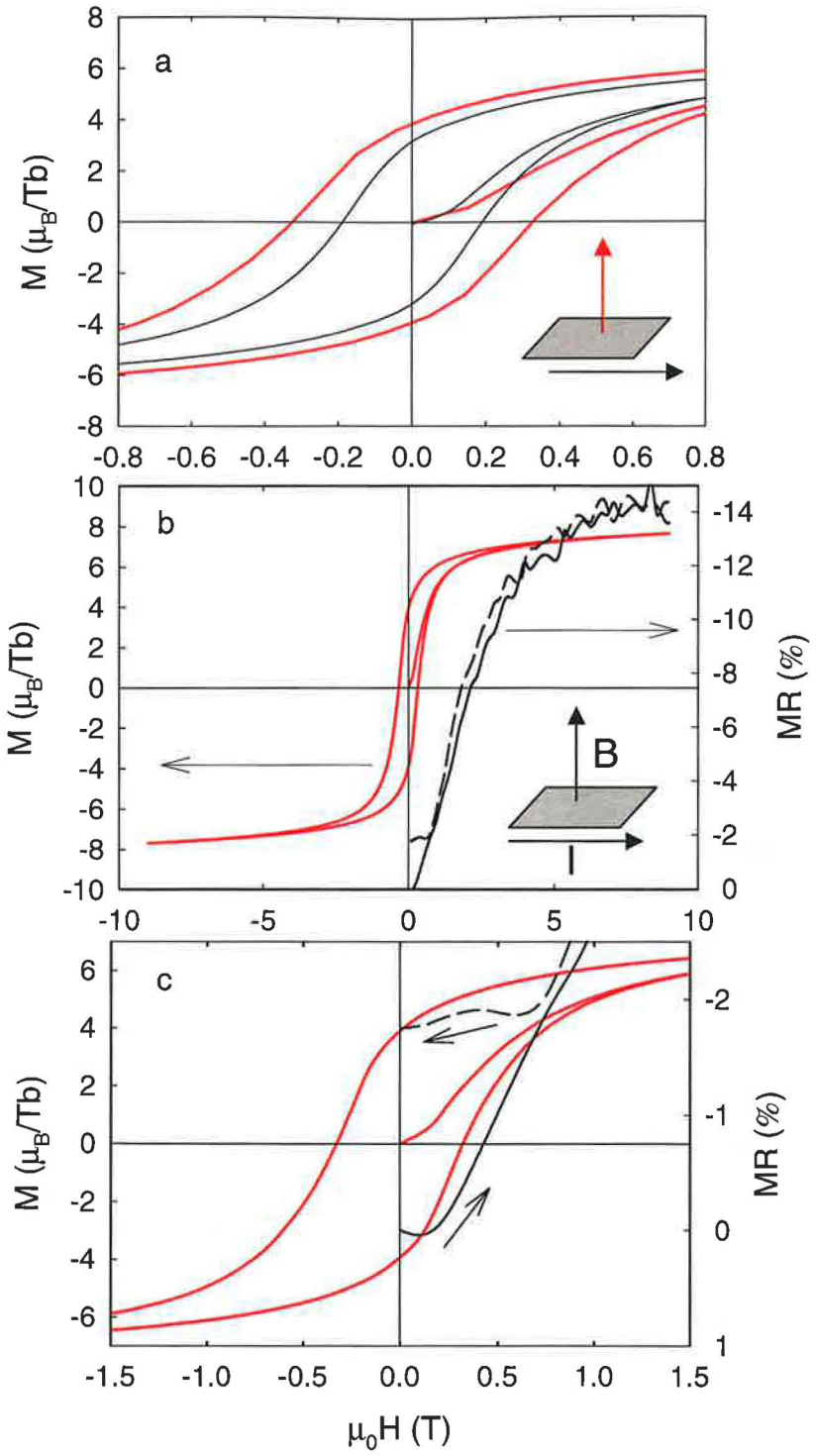

Figure 7.16: Magnetic behavior of the nano Tb sample. a - Detail of the hysteresis loop at 2 K for field applied parallel and perpendicularly to the sample plane. b - Hysteresis loop in comparison with magnetoresistance at 2 K. c - Detail of the hysteresis loop and magnetoresistance at 2 K for field applied perpendicularly to the sample plane.

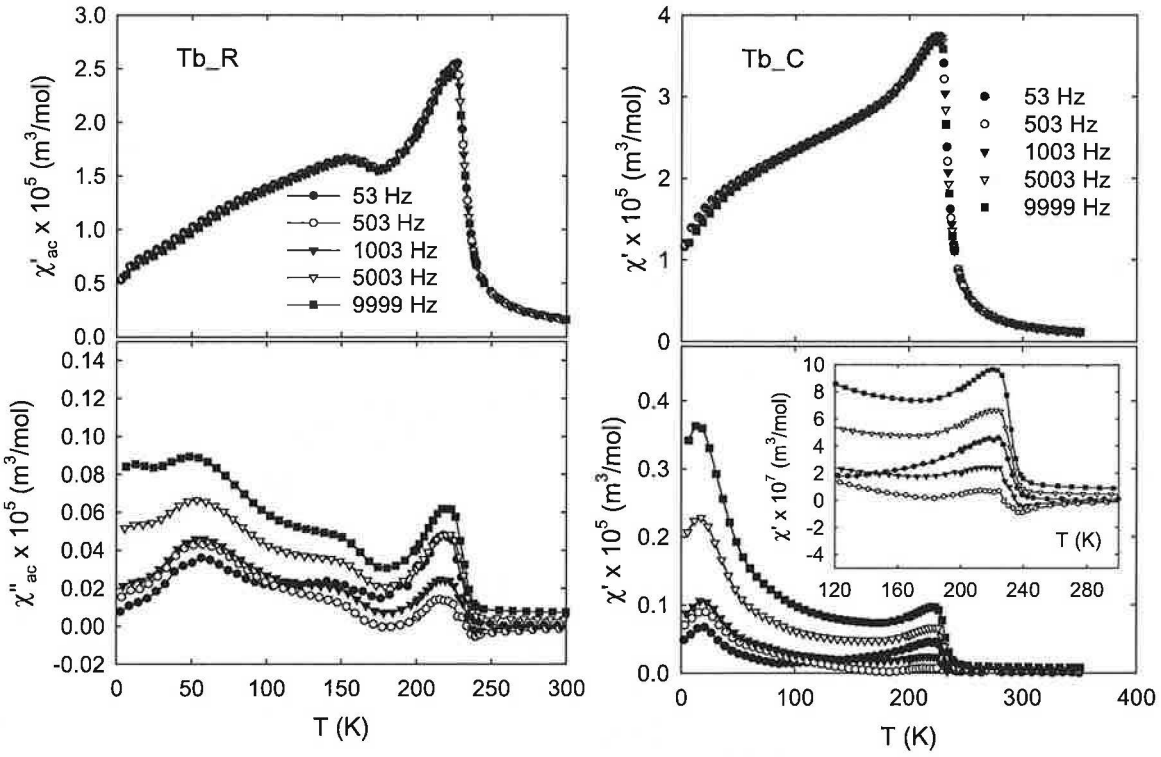

Figure 7.17: Temperature dependence of the real and imaginary parts of the a.c. magnetic susceptibility at several frequencies of the a.c. magnetic field.

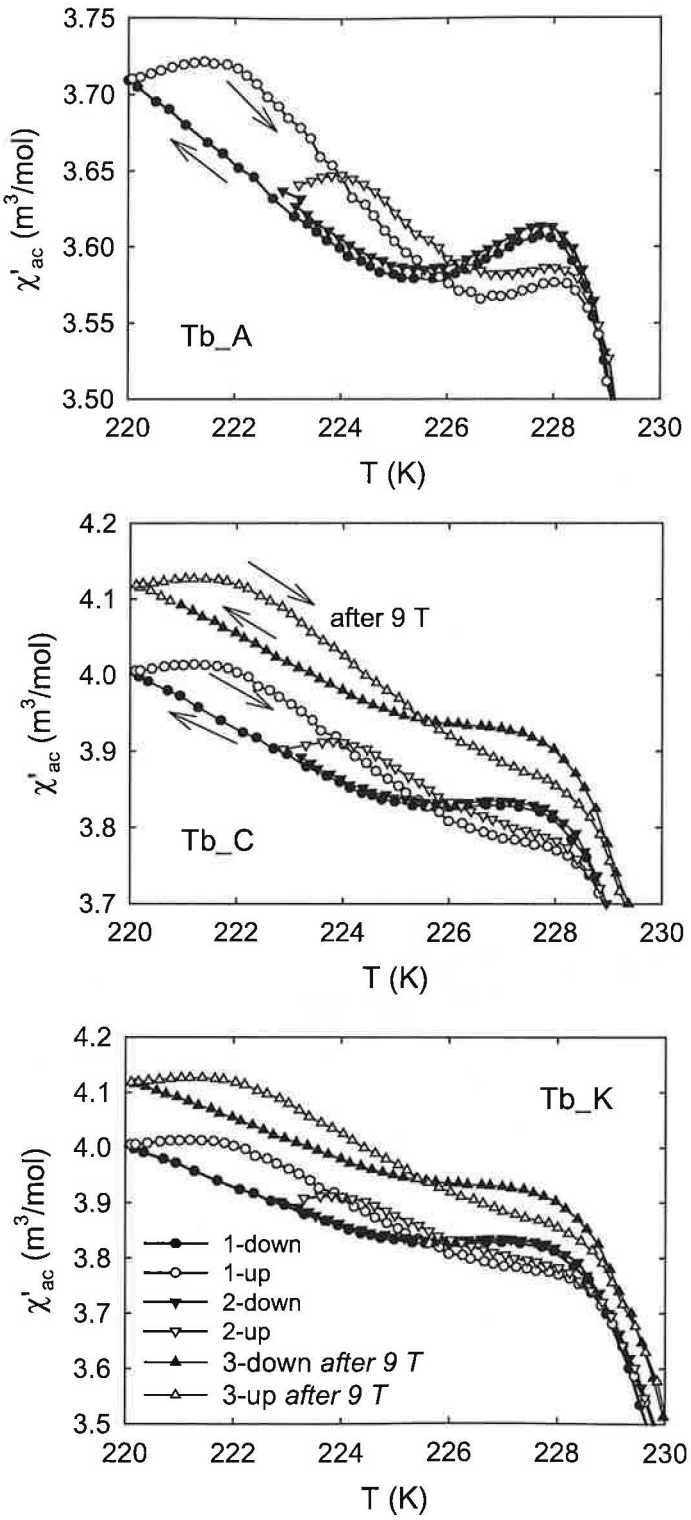

Figure 7.18: Effect of the AF domain formation on the a.c. susceptibility of the SSE treated samples in the intermediate region: $T_C < T < T_N$.

7.4 Erbium

In this section, the results of comparative investigations of the Er metal will be presented. The samples were labelled as follows: C-center, A-anode, K-cathode parts, R-reference, S - sublimed. The reference and the SSE-treated samples were investigated by the X-ray diffraction, heat capacity, electrical resistivity, magnetization and a.c. susceptibility.

Because the X-ray diffraction investigations did not reveal any considerable differences in the reference and the SSE treated samples, there is no special subsection focused on this research. The commercial Er sample obtained by sublimation technique was oriented by the Laue method, yielding the *b*-axis parallel to the 'needle'.

7.4.1 Heat capacity

The temperature dependence of the heat capacity is presented in the Figure 7.19. The anomaly at 80 K is related to the para-to-antiferromagnetic phase transition and its character do not significantly vary in the investigated samples. Contrary, the complex magnetic ordering at lower temperatures is characterized by anomalies of different appearance depending on the sample treatment. While the reference Er material shows only a broad kink in this region, the SSE purified Er samples exhibit a distinct anomaly at $\sim$ 20 K followed by a kink at $\sim$ 28 K. The profile of the consecutive anomalies is the most illustrative in the most pure sample - the cathodic-part and the least in the least pure anodic-area sample.

The influence of the sample purity on the magnetocaloric effect was also investigated. The plots of the isothermal entropy change and the adiabatic temperature change against temperature in several magnetic fields are presented in the Figure 7.20. The temperature dependence of both quantities do not vary much, so only the ΔS of the cathode and ΔT of the anode samples are depicted for illustration (Figure 7.20.a,c).

The absolute 7-T values are the largest in the center part of the sample the least in the reference, but the deviation is in fact within the error of the calculation.

7.4.2 Electrical resistivity

The temperature dependence of the electrical resistivity is depicted in the Figure 7.21. The SSE treatment reduced both the residual resistivity and the *RRR* as already presented in the Section 7.1.

7.4.3 Magnetic measurements

The effect of the SSE purification on the character of multiple magnetic phase transitions in the Er metal was investigated by magnetization and a.c. susceptibility measurements. The results are shown in the Figure 7.22 for all polycrystalline and the single crystalline Er materials, respectively.

The ZFC and FC static susceptibility (for magnetic field applied along the *b*-axis) of the sublimed single-crystal exhibits a series of anomalies, which can be well-ascribed to the referred magnetic phase transitions. Contrary, the curves of the reference and purified samples are almost identical with much broader features in the ordered state.

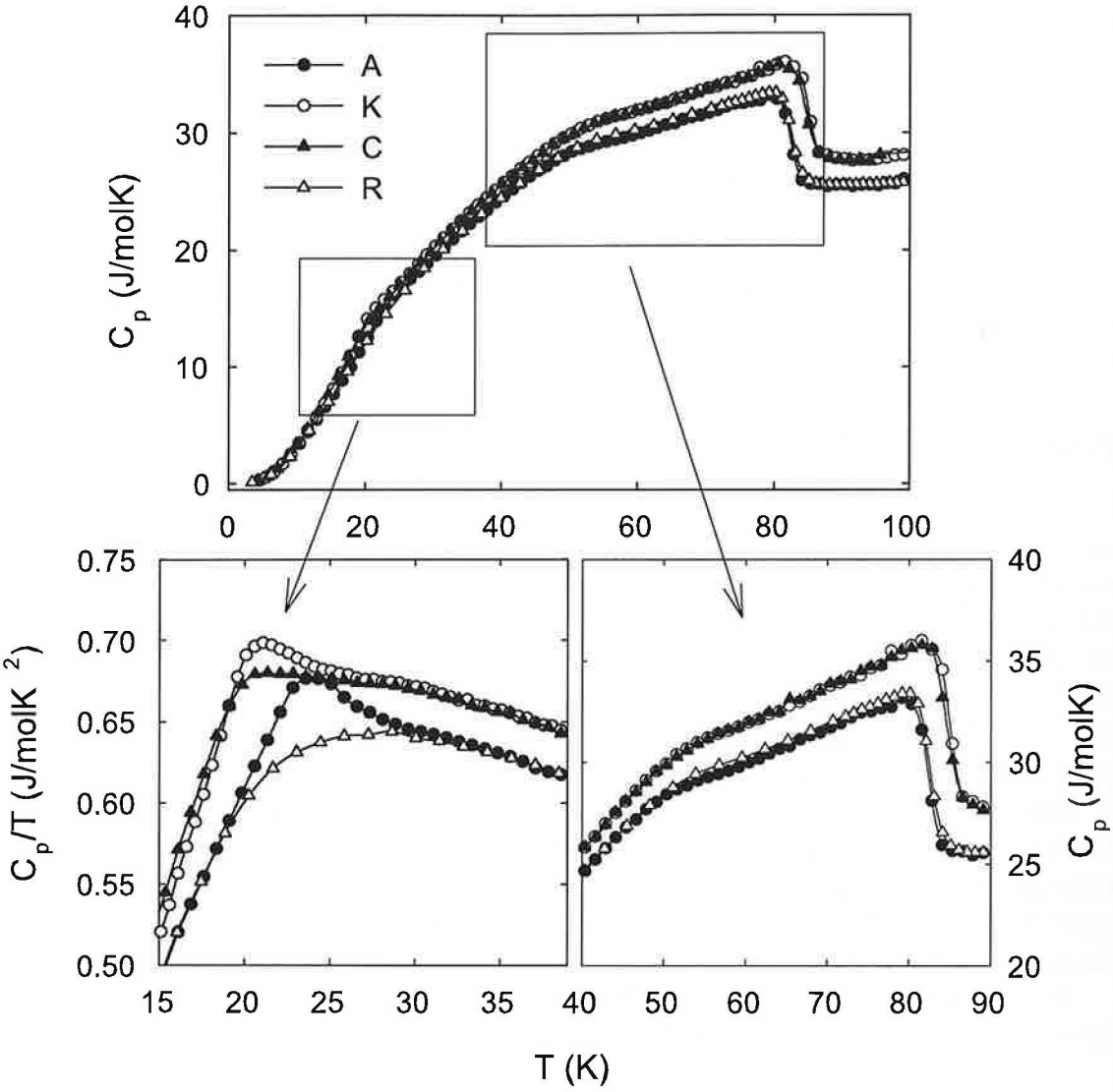

Figure 7.19: Specific heat of the Er samples. The insets present the regions, where the magnetic phase transitions occur.

Analogues character of the a.c. susceptibility dependencies (Figure 7.22.b.) was observed.

Only negligible differences were observed when inspecting the magnetization processes in the Er samples. The magnetization curves at 2 K and 50 K of the center-part and sublimed samples, respectively, are presented in the Figure 7.23 together with their 1^{st} derivative.

It is evident, that the SSE treatment did not significantly modified magnetic properties of the Er sample.

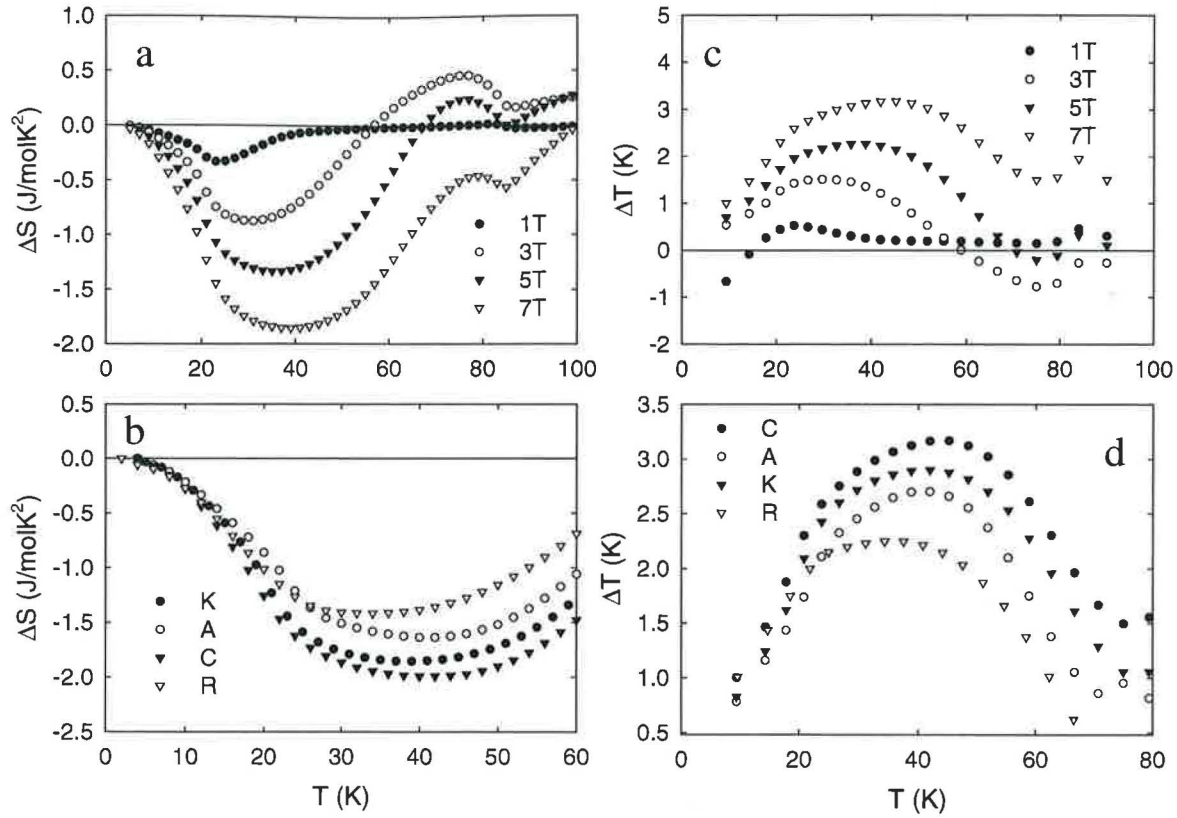

Figure 7.20: Magnetocaloric effects in Er samples. a - isothermic entropy change (ΔS) of the K sample. b - ΔS of the K, A, C and R samples. c - (ΔT) of the C sample. d - (ΔT) of the all Er samples.

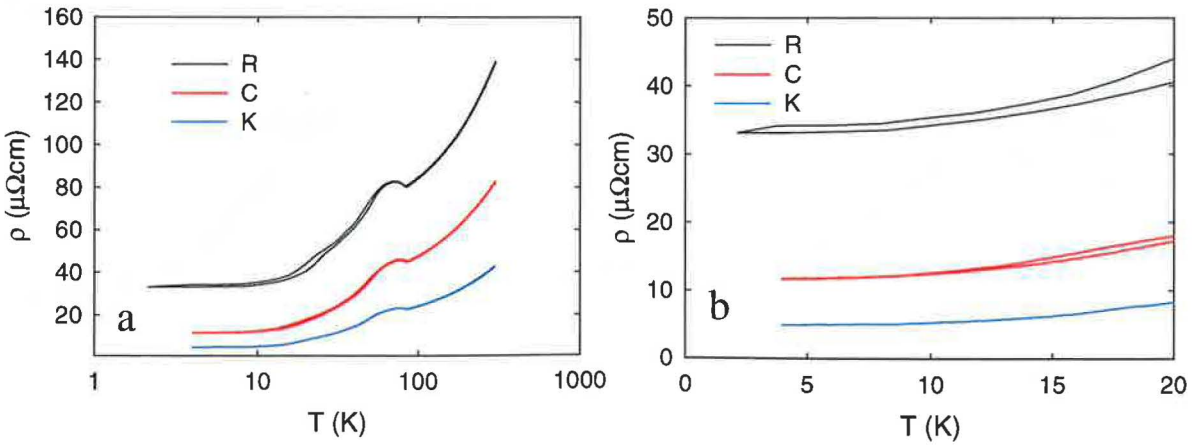

Figure 7.21: Electrical resistivity of the Er samples: a - comparison of the C, K and R samples, b - detail of the low-temperature region.

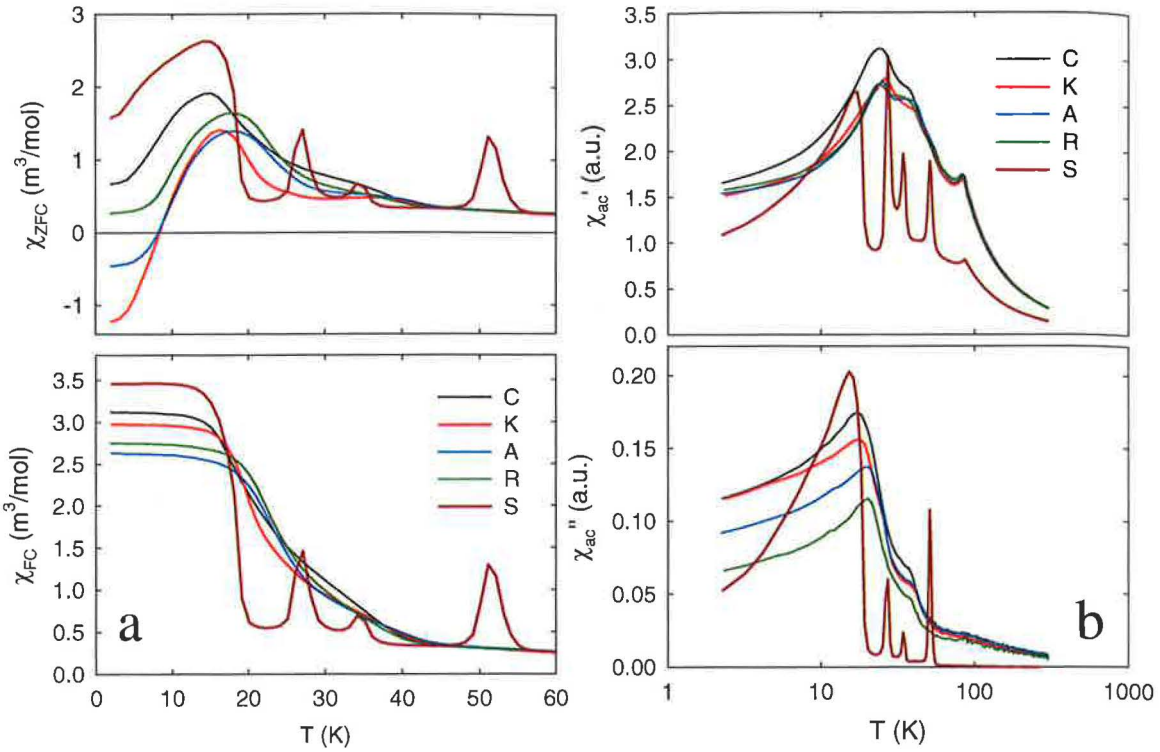

Figure 7.22: Temperature dependence of magnetization and a.c. susceptibility of the Er samples. a - ZFC and FC magnetic susceptibility at 10 mT. b - Real and imaginary parts of the a.c. magnetic susceptibility at f = 1003 Hz, A = 1mT.

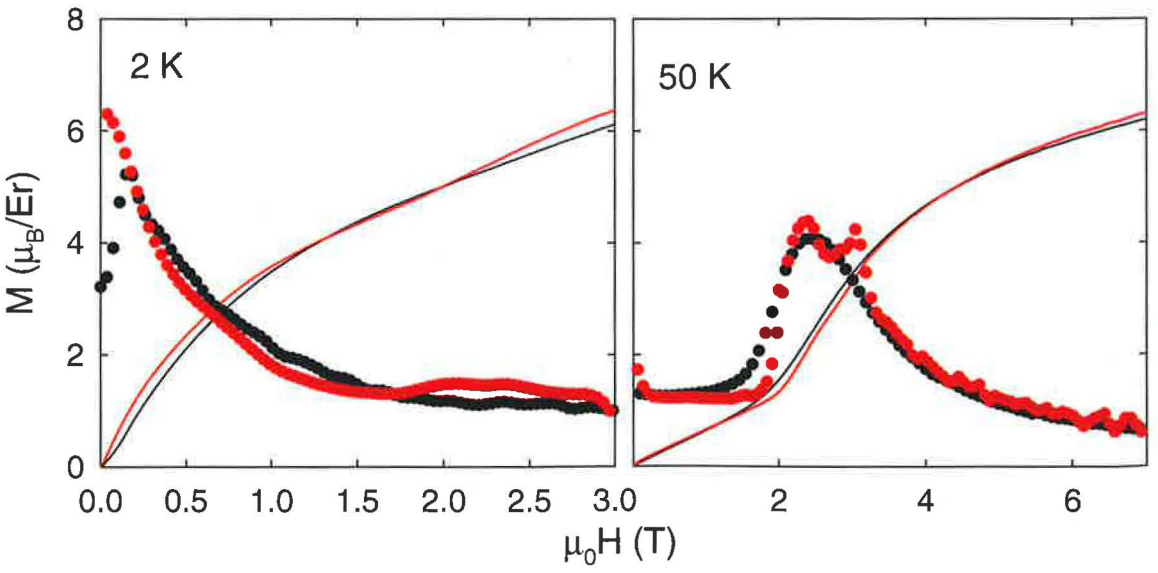

Figure 7.23: Magnetization curves of the Er C(black) and S(red) samples at 2 and 50 K. The circles demonstrate the 1^{st} derivative of the magnetization curves.

Chapter 8

Results and discussion - $CePt_3Si$ related systems

One of the most fascinating systems in context of the impurity phenomenon are the strongly-correlated Ce based compounds. The extreme case is the non-centrosymmetric heavy fermion superconductor with coexisting long-range antiferromagnetic ordering: $CePt_3Si$. This chapter is focused on the comprehensive investigation of compounds related to this unique system. The research was focused on the following aspects:

- influence of Ce metal purity on the formation of $CePt_3Si$ and related phases
- influence of the aggregation state of the material on its structural and electronic properties
- effect of *p*- and *d*-metal substitution and doping on the formation of the related ternary and pseudoternary phases
- effect of *p*-metal and *d*-metal doping on magnetic ordering and superconductivity in $CePt_3Si$

The spectrum of the elements involved in the synthesis experiments is shown in the Figure 8.1. We tried both the 100% substitution of a single element and in case that no single phase was formed, gradual doping of the element was performed starting from 2% and varying up to the highest possible level. The successfully obtained phases (at least with 2% doping) are depicted in the Figure 8.1 in contrast to the attempts, where the substitution failed.

The at least dominant-phase materials were characterized by microprobe analysis (SEM - Scanning Electron Microscope) and X-ray diffraction (XRD), and investigated by various experimental techniques. To enable transparent discussion of each material properties, the chapter is structured in the two main sections related to $CePt_3X$ isotypes (X = B, Al, Ge, C Si) and $CePt_3Si$ substitutions (doping by *p*- and *d*- elements).

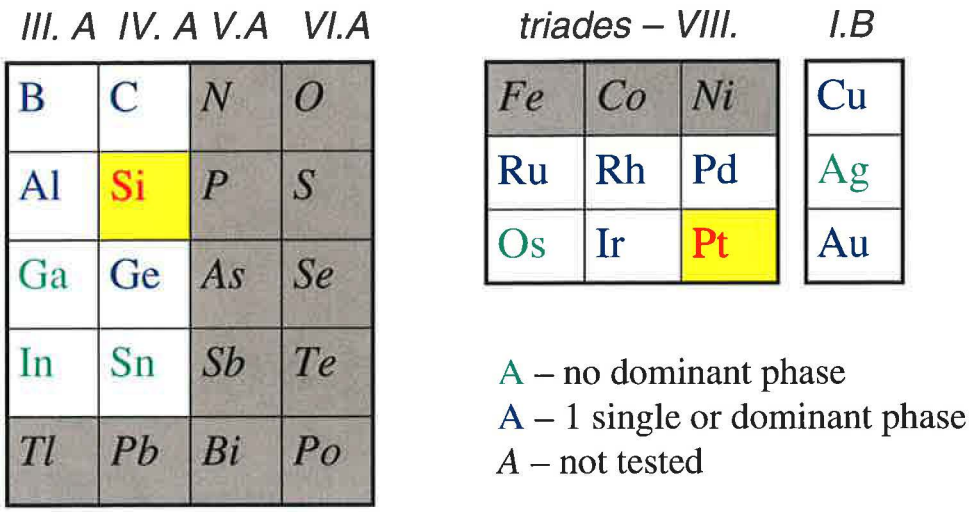

Figure 8.1: Fragments of the periodic table with depicted elements used in substitutions.

8.1 $CePt_3X$ isotypes

In this section, namely the relation between the material's microstructure and its properties is presented. Beside the already known phases $CePt_3B$ and $CePt_3Si$, the three novel systems are discussed: $CePt_3Ge$, $CePt_3Al$ and $CePt_3C$. We have investigated various synthesis regimes on the formation of the 1:3:1 stoichiometry:

- effect of the Ce purity - we used commercial and the SSE purified material
- influence of annealing
- effect of the cooling rate (and additional annealing)

8.1.1 $CePt_3B$

The compound is known for more then 10 years, however, it's re-investigation was stimulated by the discovery of its Si isostructural analogue.

We have prepared and investigated a series of samples as summarized in the Table 8.1, the details concerning the preparation procedures are presented in the Chapter 3.

We have not observed any difference when melting the components with the commercial or SSE treated Ce metal. In contrast, the crystal growth led to successful stabilization of the grown ingot in case of the SSE purified Ce only. However, no bulk single-crystal was obtained in any of the performed trials.

X-ray diffraction and SEM analysis

The X-ray diffraction patterns of the selected $CePt_3B$ samples are depicted in the Figure 8.2 together with the Bragg positions of the neighboring phases in the ternary Ce-Pt-B phase diagram. No binary phases were detected in the diffraction patterns.

Label	preparation	annealing	cooling
1	arc melted	N	-
2	arc melted	Y	S
3	arc melted	Y	Q
4	arc melted	Y	S
5	arc melted	Y	Q
6	arc melted	N	-
A/1	grown	N	-
B/1	grown	Y	S
C/2	grown	N	-
D/2	grown	N	-
1	splat-cooled	N	-
2	splat-cooled	Y	S

Table 8.1: Summary of the investigated $CePt_3B$ samples.
Y/N - yes/no; S/Q - slow/quenched.

It is evident, that the as cast sample melted in the nominal 1:3:1 stoichiometry contained also the $CePt_4B$ phase (Figure 8.2.a). The annealing successfully stabilized the $CePt_3B$ phase (not shown), but just after rapid quenching. Slow cooling from the annealing temperature revealed formation of the mixture of $CePt_xB$, x = 2-4 phases (Figure 8.2.c).

The splat cooling method provided a mixture of $CePt_xB$ phases together with an amorphous fraction suggested by a broad bump below 20° 2θ (Figure 8.2.d). Annealing of the splat-cooled sample supported formation of the $CePt_3B$ phase and recrystallization of the amorphous fraction (not shown).

Selected SEM micrographs are shown in the Figure 8.3. The quantitative analysis of all investigated samples revealed the nominal 1:3:1 stoichiometry. Almost homogeneous appearance of the micrographs contrasted to the X-ray diffraction results. However, when we take into account, that the molecular weights of the Ce - Pt - B neighboring phases do not differ significantly, the SEM analysis do not reveal enough convincing proof of single-phase material. The microstructure of the single-phase sample (observed also by the diffraction experiment) is shown in the Figure 8.3.c.

Most crucial was the investigation of microstructure of the splat-cooled materials (Figure 8.3. a,b). The bulk is formed of irregular grains with the diameter within 200 nm - 2 μm. The annealing transformed the microstructure to rather common, similar to the annealed bulk sample (Figure 8.3.c).

Specific heat

The temperature dependence of the specific heat of the as cast and annealed samples (1,2) is presented in the Figure 8.4.a. We can clearly identify anomalies attributed to the magnetic

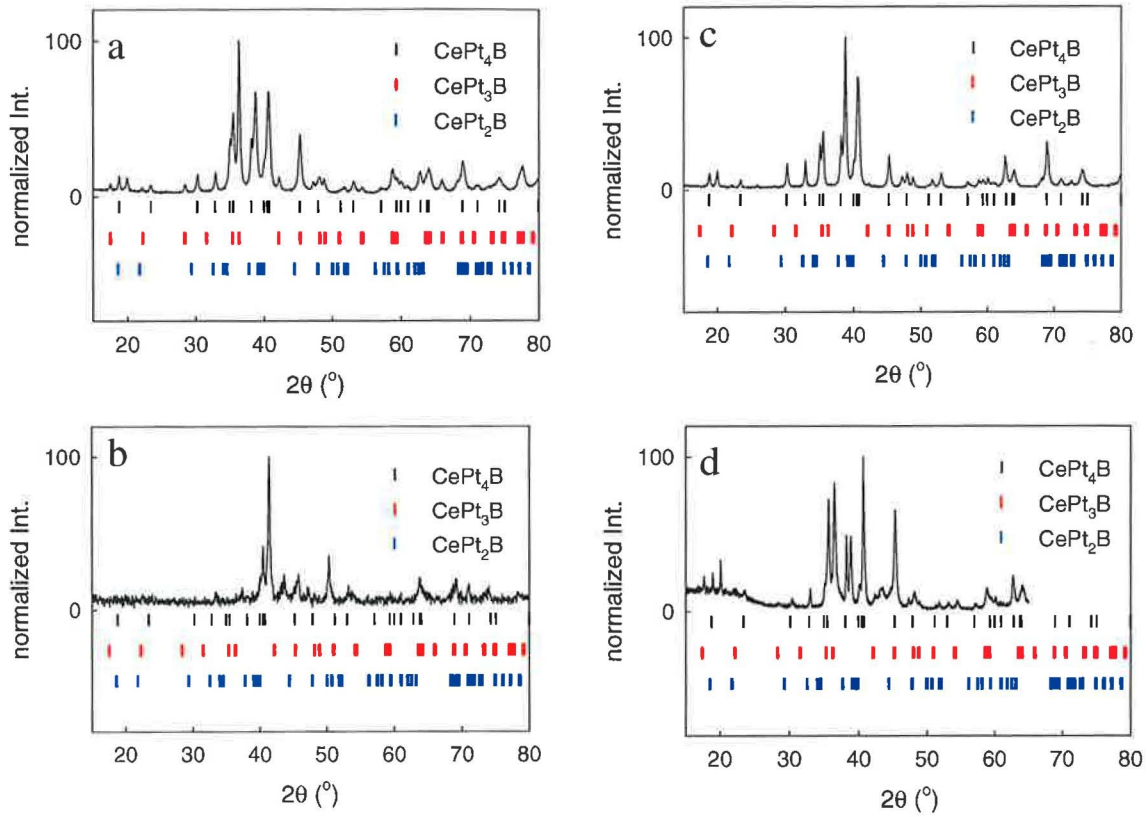

Figure 8.2: Powder XRD data from selected $CePt_3B$ samples.
Powder XRD data from selected $CePt_3B$ samples. a - as cast sample, 1. b - melt after crystal growth, C/2. c - annealed, 2. d - splat-cooled, 1.

Figure 8.3: SEM micrographs of selected $CePt_3B$ samples.
SEM micrographs of selected $CePt_3B$ samples. a - splat-cooled, 1. b - splat-cooled, 2. c - annealed, 2. The small black spots on the surface correspond to the oxidized surface layer.

ordering in the $CePt_3B$ ($T_N \sim 8$ K, $T_C \sim 5$ K) and $CePt_4B$ ($T_N \sim 2$ K). We must point out, that the annealed sample contains a large fraction of the Pt rich phase and the T_C-related transition in the $CePt_3B$ is much suppressed. For comparison the specific heat and

its evolution in magnetic fields of the single $CePt_4B$ phase is depicted in the Figure 8.5.a. The isothermal entropy change in the vicinity of T_N is also presented (Figure 8.5.b).

The specific heat of the annealed splat-cooled sample shows a single broad bump at around 5 K in contrast to expected double-character of the anomaly observed in the single-phase $CePt_3B$ sample (Figure 8.4.b). The anomaly is gradually suppressed by the applied magnetic field. In comparison, the two-phase polycrystalline sample exhibits much defined evolution of the anomalies with applied magnetic field as shown in the Figure 8.4.c,d. We may speculate, that the microstructure of the recrystallized splat-cooled material is still disordered on a submicron scale, causing violation of the magnetic exchange interactions in the system. Therefore, the anomaly connected with the magnetic ordering is diffused.

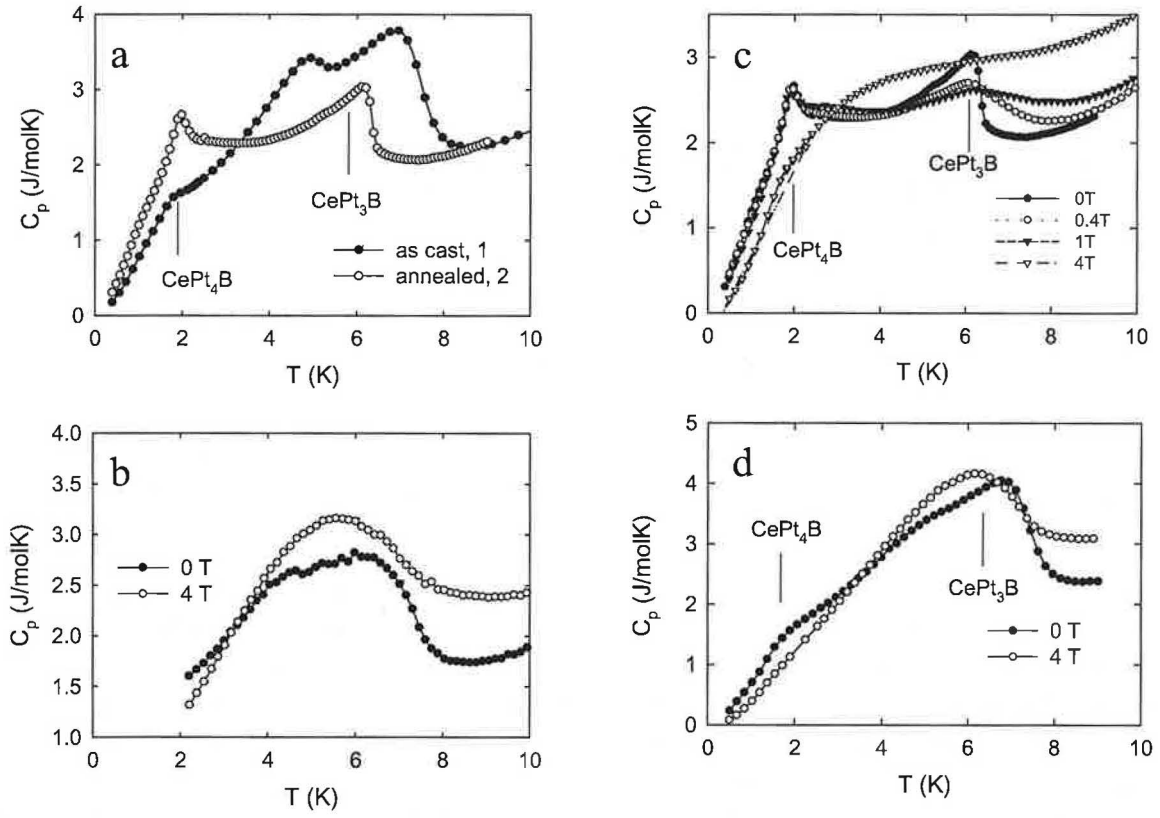

Figure 8.4: Specific heat, $C_p$of selected $CePt_3B$ samples.
Specific heat, $C_p$of selected $CePt_3B$ samples. a - as cast, 1 and annealed, 2 samples. b - splat-cooled, 2. c - annealed, 2. d - as cast, 1.

The detailed measurements of the specific heat of the single-phase ingot of $CePt_3B$ (sample D/2) is summarized in the Figures 8.6 and 8.7. A single λ-type anomaly peaks at T_N = 7.8 K and the T_C-related transition can be manifested as a kink at $\sim$ 6 K. The evolution of the specific heat in magnetic fields is rather complex suggesting complicated magnetic phase diagram in magnetic fields (Figure 8.6.a). Namely the rapid enhancement of the T_N-connected anomaly at 2 T suggests either a dramatic change of the magnetic structure or

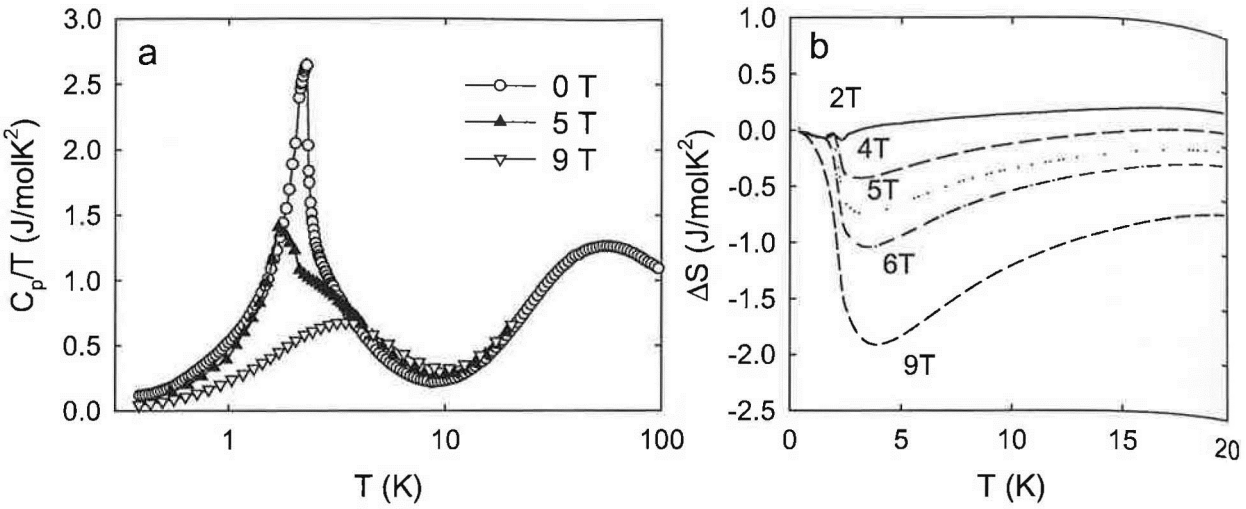

Figure 8.5: Specific heat, $C_p$of $CePt_4B$.
Specific heat, $C_p$of $CePt_4B$. a - $C_p$in magnetic fields. b - isothermal entropy change, ΔS in magnetic fields up to 9 T.

	γ (J/molK^2)	Θ_D (K)	Θ_{E1} (K)	n1	Θ_{E2} (K)	n2	Θ_{E3} (K)	n3
$LaPt_3B$	5.6	143	116	4	207	4	507	4
$CePt_3B$	8.0	150	150	2	165	6	290	2

Table 8.2: Parameters of the electronic and phonon specific heat of $LaPt_3B$ and $CePt_3B$.

probably localization effects of the $4f$ electron density in the compound. [1]

Focusing on the low temperature limit of the C_p/T vs T^2 dependence, we observe a considerable reduction of its 2-K value with increasing magnetic field up to 9 T (Figure 8.6.b). There are two suggested scenarios for this observation. First, the crystal-field level scheme is modified under the magnetic field, second, a gap may form on the Fermi surface leading to the observed decrease.

To estimate the magneto-caloric effects in this material, we have calculated the isothermal entropy change in magnetic fields up to 9 T (Figure 8.7.b). The 9 T - value falls in the interval of ΔS observed in similar medium-correlated Ce compounds with magnetic ordering.

Besides, we tried to treat the heat capacity data by much detailed analysis. First, the whole temperature dependence of the specific heat was fitted by the sum of the electron, phonon and Schottky contributions, respectively. The specific heat of the non-magnetic analogue $LaPt_3B$ was described by the relevant γT and phonon contribution and those parameters were used for further analysis of the isostructural Ce compound. The resulting values are summarized in the Table 8.2. for both compounds.

Finally, the crystal-field (CF) level scheme was estimated by fitting of the Schottky formula for the 6-level system (Ce^{3+}: J = 5/2). The best fit yielded Δ_i = 5±0.4 K, 80±3

[1]Unfortunately, the alocated neutron diffraction experiment in HMI Berlin was cancelled due to persisting technical difficulties on the neutron diffractometer.

K - doublet, 120±10 K - doublet. The calculated magnetic entropy is shown in the Figure 8.7.a reaching the Rln6 value at ~ 120 K as expected from the calculated CF level scheme.

We must also mention, that our analysis revealed a much lower value of the γ coefficient than the approach applied further. The reason is, that our model includes the γ coefficient related to the 'free electron states', it means that any huge enhancement of the γ value would be in contradiction with the free electron gas model used for its derivation.

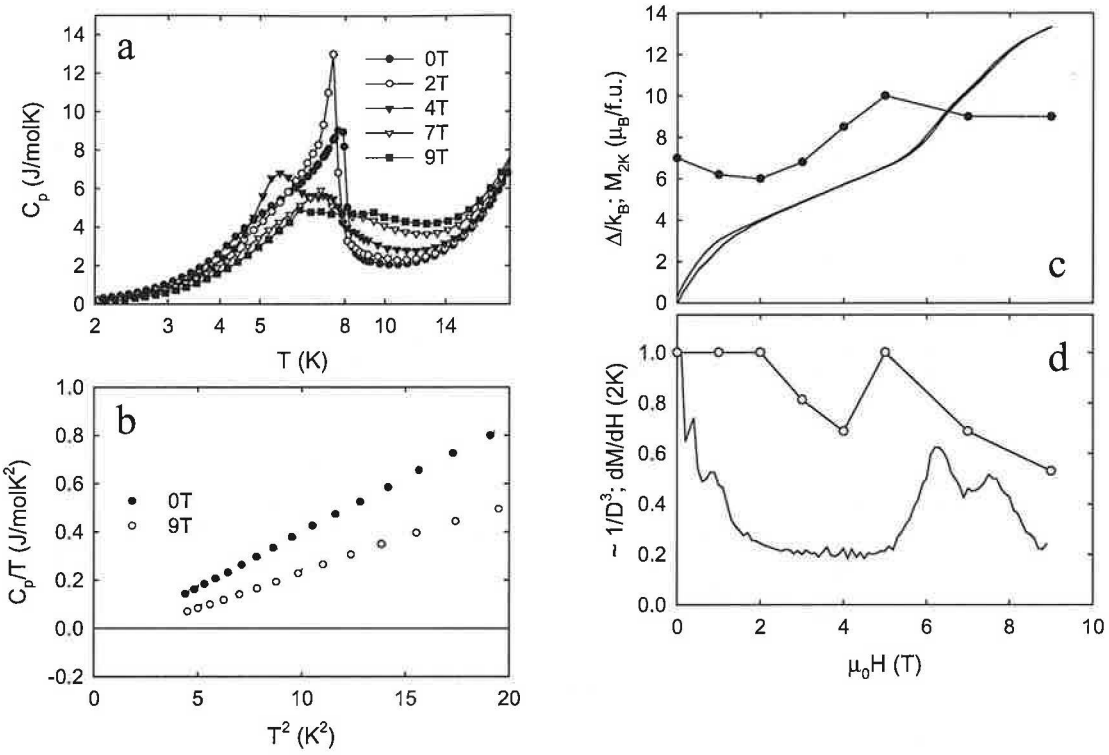

Figure 8.6: Specific heat, $C_p$of $CePt_3B$ in magnetic fields.
Specific heat, $C_p$of $CePt_3B$ in magnetic fields. a - $C_p$in magnetic fields. b - detail of the low-temperature part of C_p/T vs T^2 at zero field and 9 T. c - field dependence of the Δ value obtained from equations 8.1 and 8.2 in comparison with the magnetization curve at 2 K. d - field dependence of the $1/D^3$ parameter in comparison with the derivative of the magnetization curve.

The contribution of antiferromagnetic spin waves to the specific heat follows from the model [538]:

$$C = \gamma T + C_{\mathrm{mag}}; T \leq 0.65 T_{\mathrm{N}} \tag{8.1}$$

$$C_{\mathrm{mag}} = 1/D^3 \Delta^{7/2} T^{1/2} \exp^{-\Delta/T} \left[1 + \frac{39}{20}\frac{T}{\Delta} + \frac{51}{32}\frac{T^2}{\Delta^2} \right] \tag{8.2}$$

The quantity Δ corresponds to the spin-wave gap, which arises from anisotropy either in the magnetic interactions, or of the single-ion type, and D is the spin-wave velocity. It holds for temperatures smaller than the spin-wave gap ($\approx 0.65 T_{\mathrm{N}}$). A similar analysis based

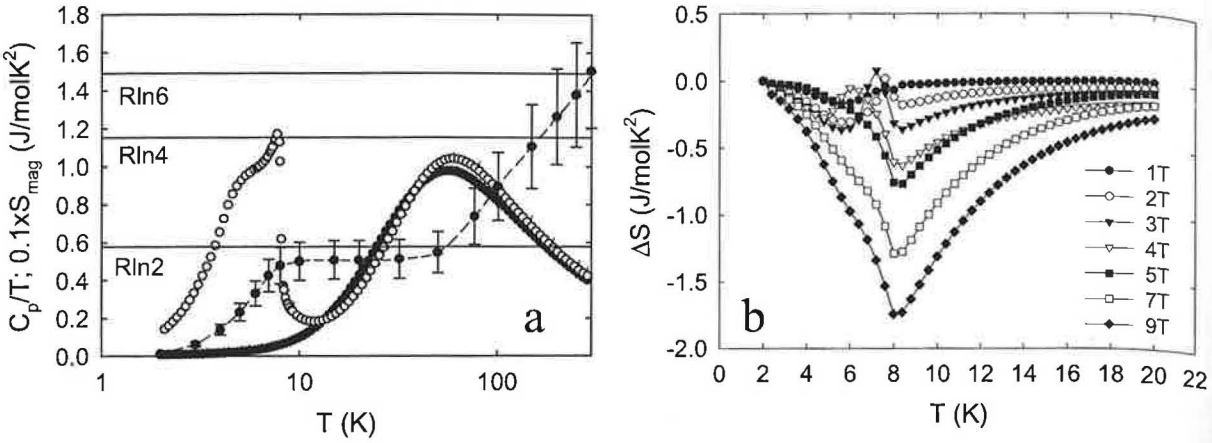

Figure 8.7: Specific heat, $C_p$and isothermal entropy change in magnetic fields, ΔS of $CePt_3B$. Specific heat, $C_p$and isothermal entropy change in magnetic fields, ΔS of $CePt_3B$. a - $C_p$of $CePt_3B$ (open circles) in comparison with that of $LaPt_3B$ (black circles). The dashed line corresponds to the calculated magnetic entropy. b - ΔS in magnetic fields up to 9 T.

on the same model was performed using the electrical resistivity data (equation 8.3). The results of the fit are presented in this subsection in the Table 8.3. The obtained γ value using the spin-wave gap approach was 7× larger in comparison to our analysis: 57 mJ/molK^2. We must stress out, that attributing this to the γ coefficient is not straightforward, however, it's still generally accepted.

$$\rho = \rho_0 A \Delta^{3/2} T^{1/2} \exp^{-\Delta/T} \left[1 + \frac{2}{3}\frac{T}{\Delta} + \frac{2}{15}\frac{T^2}{\Delta^2}\right] \tag{8.3}$$

The parameter A is related to the spin-wave velocity as $1/D^3$, ρ_0 is the residual resistivity (scaling parameter).

The evolution of the model parameters in magnetic field is depicted in the Figure 8.6.c,d.

	0T	1T	2T	3T	4T	5T	7T	9T	14 T
from C_p(T)									
Δ/k_B	7.0	6.2	6.0	6.8	8.5	10.0	9.0	9.0	
$1/D^3 \times 10^{-3}$	3.2	3.2	3.2	2.6	2.2	3.2	2.2	1.7	
from ρ (T)									
Δ/k_B	10.0			12.6		7.3			14.0
A	0.13			0.14		0.09			0.14
ρ_0	3.57			3.85		4.28			4.84

Table 8.3: Parameters of the AF magnon excitations in $CePt_3B$ determined from the heat capacity (for $\gamma = 56\pm1$ J/molK^2) and electrical resistivity data.

The anomalies on the field dependence of the spin-wave gap Δ roughly correspond to the critical field of the observed metamagnetic phase transitions on the 2 K magnetization curve. Similarly, the parameter A related to the spin-wave velocity sharply decreases at the magnetic field, where the metamagnetic transition occurs.

Electrical resistivity

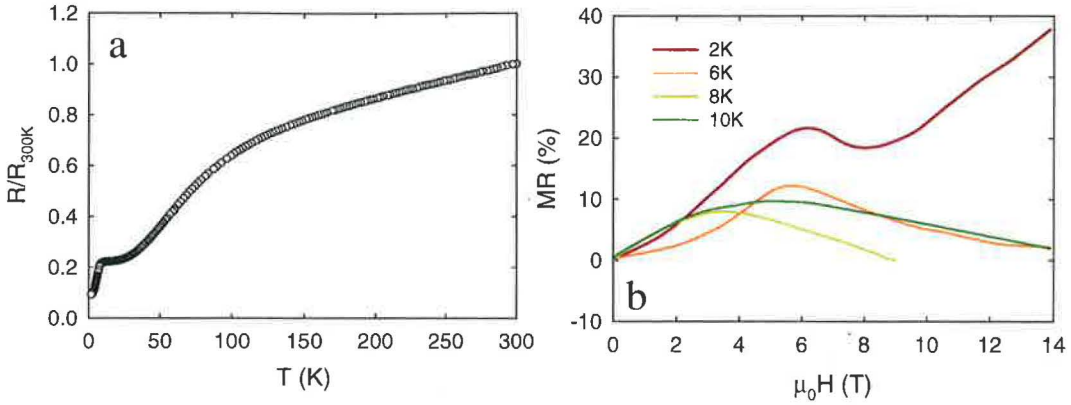

Figure 8.8: Electrical resistivity of $CePt_3B$.
Electrical resistivity of $CePt_3B$. a - temperature dependence of the electrical resistivity. b - magnetoresistance at selected temperatures.

The typical temperature dependence of the electrical resistivity of the $CePt_3$ sample is shown in the Figure 8.8. together with the magnetoresistance measurements. The 300 K value is of about 80 $\mu\Omega$cm and the residual resistivity, ρ_0 ranges from 8 to 14 $\mu\Omega$cm, respectively. The lowest values were observed in two samples, which were prepared from the SSE-treated Ce and annealed. The resistivity of the splat-cooled sample slightly increases on cooling (of about 2%) and the room temperature value was determined as $\sim$ 120 $\mu\Omega$cm.

The low-temperature drop of the resistivity occurs at T_N; the two consecutive transitions cannot be separated. The curvature of the electrical resistivity above 100 K is probably attributed to the population of the higher-lying CF states of the Ce ion. The hypothesis, however, deserves testing by any inelastic neutron scattering experiments.[2]

The magnetoresistance curves in the ordered state show a single maximum. The 2 K - curve exhibits a large positive contribution up to highest applied field 14 T with the 40 % MR, while the 6 K-related MR curve turns to almost negative values at 14 T. he position of the MR maximum is identical - at $\sim$ 5 T. Close to the T_N, the maximum shifts to 3 T and the MR tends to negative values above the observed metamagnetic transition. The 10 K - curve forms a diffuse bump at around 5 T and the high-field values turns to the positive values again.

[2]The bump in the temperature dependence of the electrical resistivity is by some authors attributed to Kondo-type contribution to the resistivity. But if have a rather good proof of the presence of the crystal-field splitting (Schottky-type contribution to the specific heat), the electron scattering must take place at least on the population of interacting Kondo and CF states. Therefore a simple explanation with $T_K \sim 100$ K, if the usually T_K scales in units of K in such systems seems to be a bit strange.

The analysis of the temperature dependence of the electrical resistivity data with respect to the magnetic field is presented in the previous section. The complex character of the MR behavior supports the picture of complex interplay between the applied magnetic field and Fermi surface reconstruction, but the details must be examined on the microscopic scale and by relevant theoretical calculations.

Magnetization and a.c. susceptibility measurements

The temperature dependence of the real and imaginary parts of the a.c. susceptibility (χ', χ'') of the annealed polycrystalline and splat-cooled samples, respectively, is shown in the Figure 8.9.a,b. Both data sets were recorded at the same frequency (103 Hz) and amplitude of 1mT.

Surprisingly, the real part of the susceptibility related to the former sample shows several anomalies and exhibits of two orders lower signal then the imaginary part with a single anomaly at around 6 K. The χ' curve of the disordered material is characterized with a broad maximum centered around 5 K and the χ" curve shows almost continuous increase on cooling. The diffuse character of the anomaly on the splat-cooled sample related χ' curve contrasts to the sharp peaks on the polycrystalline data. It suggests better nominal composition homogeneity of the material, but much disordered magnetic exchange interaction between the Ce magnetic moments.

The investigation of the effect of the applied a.c. field frequency on the anomalies (not shown) revealed strong frequency dependence of the dynamic susceptibility in the splat-cooled material. Its spin system is therefore much sensitive to the absorbed energy in the applied frequency range (10 - 10kHz), so the characteristic time scale of the magnetic moment reversal are of this order. The question is, what in fact is the basic 'magnetic unit' (single Ce spins, clusters or surface spin layers on the submicron scale grains) responsible for our observations.[3]

The temperature dependence of the zero-field cooled static susceptibility at several magnetic fields is shown in the Figure 8.9.c. The T_N-related anomaly can be detected as a small kink at 7.5 K; the transition to the ferromagnetic state at $\sim$ 5 K. The low-temperature susceptibility is gradually suppressed with the increasing magnetic field, suggesting presence of an induced ferromagnetic state.

For comparison, the temperature derivative of the electrical resistivity at selected magnetic fields is shown in the Figure 8.9.d. The evolution of the maximum on the dR/dT dependence follows the trend expected from the in-field specific heat and magnetization isotherms measurements.

The paramagnetic susceptibility of $CePt_3B$ (not shown) is well characterized by the modified Curie-Weiss law with the effective magnetic moment $\mu_{eff} = 2.52\ \mu_B$, the paramagnetic Curie temperature, θ_P = -26 K and $\chi_0 = 9.3\times10^{-9}m^3/mol$.

Finally, the magnetization curves of the ingot of $CePt_3B$ are depicted in the Figure 8.10. comprising the results in the static magnetic field up to 9 T together with the pulsed 50 T field (both measured on the identical sample). The low-temperature curves do not precisely correspond to each other due to heating of the sample during the field pulse. The hysteresis

[3]The detailed analysis of the dynamic behavior of the $CePt_3B$ splat system will be published elsewhere.

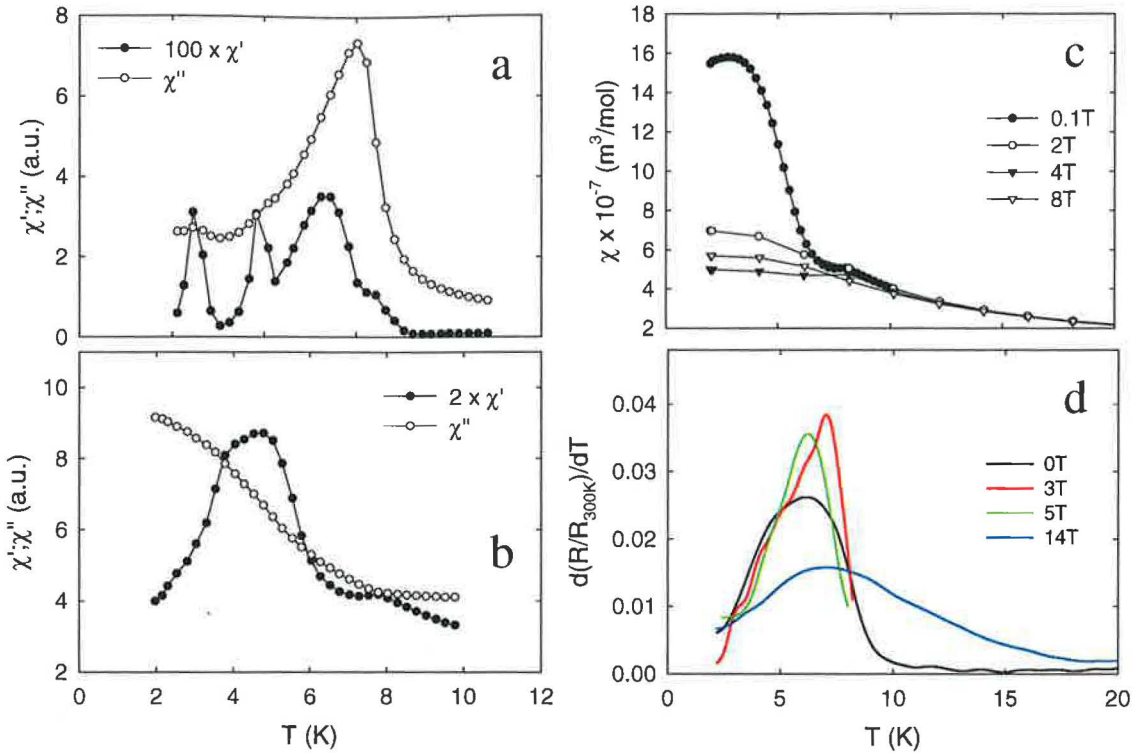

Figure 8.9: Static and dynamic magnetic susceptibility of $CePt_3B$.
Static and dynamic magnetic susceptibility of $CePt_3B$. a - real part of the a.c. susceptibility in the magnetic transition region. b - imaginary part of the a.c. susceptibility in the magnetic transition region. c - static magnetic susceptibility at several magnetic fields. d - temperature derivative of the electrical resistivity in selected magnetic fields in the magnetic transition region.

observed on the pulsed-field curves is attributed to the same effect.[4]

The static-field curve recorded at 2 K shows signs of two metamagnetic transitions up to 9 T at 3.5 and 7 T, respectively. The contribution of the expected ferromagnetic component, which is proposed to form below $T_C = 5.5$ K is estimated to $\sim 0.1\ \mu_B$/f.u. at 2 K. A suspicion of an additional metamagnetic transition is seen at ~ 30 T, but the effect may be originated by the sample-heating peculiarities.

[4]We also performed series of experiments using randomly fixed powders and powders oriented in the magnetic field. The results were more or less identical, only the sharpness of the metamagnetic phase transition slightly varied.

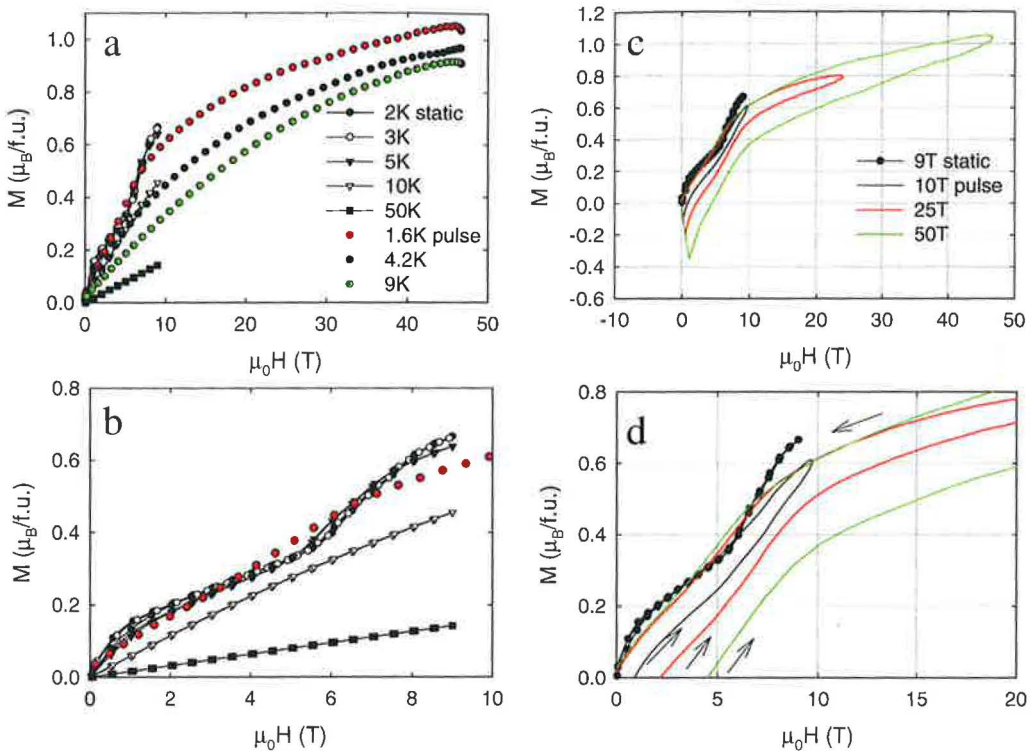

Figure 8.10: Magnetization curves of $CePt_3B$.
Magnetization curves of $CePt_3B$. a - measurements at pulsed magnetic field in comparison to the static results. b - detail of the magnetization curves up to 10 T. c,d - evolution of the magnetic moment in the pulsed magnetic field during the applied pulse. The arrows correspond to the increase/decrease of the applied pulsed field.

8.1.2 $CePt_3Al$

The synthesis of this novel compound was also stimulated by the $CePt_3Si$-connected research.

We have prepared and investigated a series of samples as summarized in the Table 8.4, the details concerning the preparation procedures are presented in the Chapter 3.

Similarly as in case of the B compound, we have not observed any difference when melting and further investigating samples prepared from the components with the commercial or SSE-treated Ce metal.

X-ray diffraction and SEM analysis

The SEM micrographs are presented in the Figure 8.11. All arc melted samples revealed homogeneous composition and microstructure. The materials prepared by the splat-cooling showed also excellent homogeneity of the nominal Ce - Pt3 - Al composition, but their microstructure consisted of ~200 nm or smaller aggregates (Figure 8.11.c).

The X-ray diffraction patterns of the $CePt_3Al$ samples are shown in the Figures 8.12 and 8.13, respectively. We tried to compare the $CePt_3B$ type structure to the data first to examine, if the compound is isostructural to the $CePt_3X$, X = Si, B. If we considered

Label	preparation	annealing	cooling
1	arc melted	N	-
2	arc melted	Y	S
3	arc melted	Y	Q
4	arc melted	Y	S
5	arc melted	Y	Q
6	arc melted	N	-
1	splat-cooled	N	-
2	splat-cooled	N	-
3	splat-cooled	Y	S

Table 8.4: Summary of the investigated $CePt_3Al$ samples.
Y/N - yes/no; S/Q - slow/quenched.

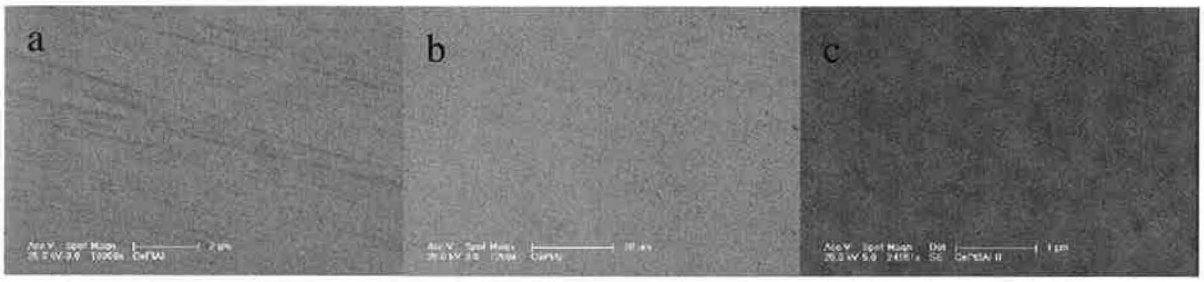

Figure 8.11: SEM micrographs of the $CePt_3Al$ samples.
a - arc melted sample 3; b,c - splat-cooled sample 2.

only selected reflections, the structure was rather well described by the tetragonal noncentrosymmetric $CePt_3B$-type, however, the remaining reflections could not be attributed to any known binary or ternary Ce - Pt - Al based phase. (The Bragg positions of the most probable candidates of the related ternary phases are depicted in the Figures 8.12 and 8.13 as well.)

To get some relation to the $CePt_3B$ structure, we assumed, that the Al atoms do not strictly occupy the appropriate crystallographic positions and part of them is located in some intersticial positions. This would lead to splitting of the reflections of the ordered $CePt_3B$ structure. Still, the structure was not well described.

Finally, we tried to index the diffraction pattern using a new structure type. The structure was finally described by a monoclinic unit cell with a = 19.797 Å, b = 4.671 Å, c = 14.436 Å, $\beta = 117.906°$.[5] When we consider the complex arrangements observed in the heavy rare earth RPt_3Si compounds with monoclinic unit cells of about the same dimensions ($YbPt_{\sim 3}Si$), the

[5]We used the DICVOL program for the procedure. The best agreement of the fit and the least unit cell was obtained for the mentioned parameters. However, we obtained three additional sets of lattice parameters and β angle.

proposed structure is not completely excluded.

Unfortunately, no single-crystalline sample was obtained after several trials using either stoichiometric and off-stoichiometric composition of the melt, therefore we were not able to determine the $CePt_3Al$ structure unambiguously. Moreover, it seems, that the phase is not congruently-melting and we obtained homogeneous samples just because of enough fast cooling of the melt after switching off the arc. The consequent annealing probably did not affected the stability of the phase, because we did not reach it's peritectic formation temperature.

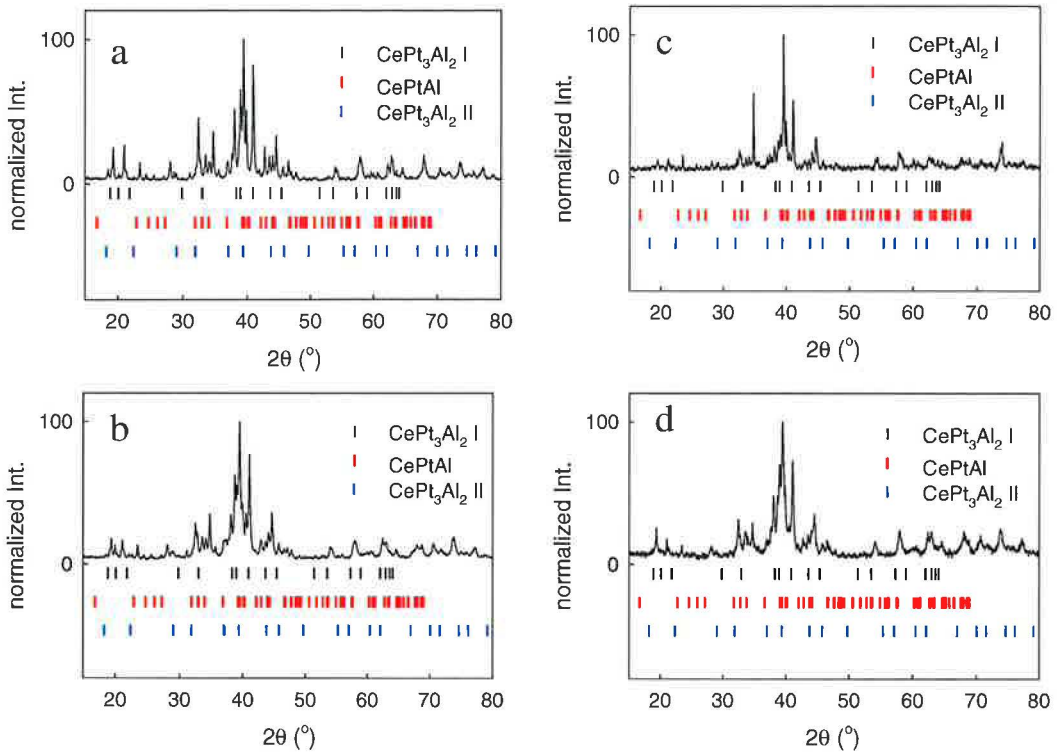

Figure 8.12: X-ray diffraction patterns of the $CePt_3Al$ samples
a - arc melted 1, b - arc melted 2, c - arc melted 3, d - arc melted 4 .

Let's focus on the diffraction pattern of the splat-cooled synthesized phases. The sample 1 provided a broad peak centered at around 35° 2θ (Figure 8.13.b) and the sample 2 revealed additional broad contribution around 20° of a fraction of the amorphous phase (Figure 8.13.c). The annealing surprisingly enhanced the ratio of the amorphous phase as demonstrated in the Figure 8.13.d.

Specific heat and caloric effects

The low-temperature detail of the specific heat is shown in the Figure 8.14. There are two anomalies at $T_1 = 1.9$ K and $T_2 = 0.8$ K. The annealing procedure considerably enhanced the T_1-related anomaly as demonstrated in the Figure 8.14.a. When we confront our results with the literature, no Ce - Pt - Al phase reveal specific heat anomalies at the temperatures we

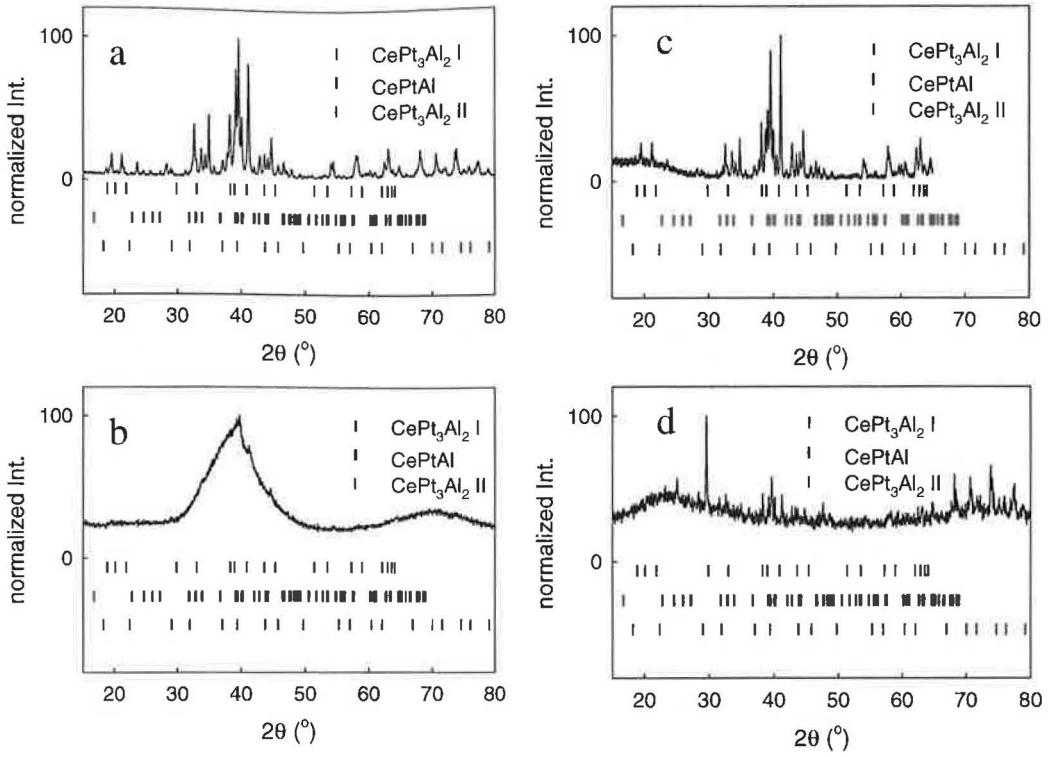

Figure 8.13: X-ray diffraction patterns of the $CePt_3Al$ samples
a - arc melted 5, b - splat-cooled 1, c - splat-cooled 2, d - splat-cooled 3.

observed [539, 540]. It corroborates the conclusion, that we have obtained a novel compound, which exhibits magnetic ordering of antiferromagnetic nature as suggested by the specific heat data in magnetic fields (Figure 8.14.c,d). The appearance of the T_2-connected kink is a bit disputable and it cannot be excluded, that it comes from a small amount of some impurity phase.

The low-temperature specific heat of the splat-cooled sample is shown in the Figure 8.15. together with the calculated isothermal entropy change (ΔS) in magnetic fields up to 9 T. In contrast to the polycrystalline samples, the splat-cooled material shows a single broad anomaly at $\sim$ 0.8 K, which is continuously smeared out and shifted to higher temperatures by applied magnetic field. Moreover, the logarithmic dependence of the C_p/T vs T signalizes, that pronounced spin instabilities at least just above the anomaly temperature occurs.

The suggested spin fluctuations are definitely enhanced in comparison to the arc melted samples, and beside the common effects of strong correlation in Ce heavy fermion systems, additional factors must play a great role. They are highly probably originated either by the disorder of the alloy or by the frustration of the system by means of its disturbed dimensionality.

The influence of the magnetic field on the entropy of the splat-cooled system is demonstrated in the Figure 8.15.b; the maximum of $\Delta S = 2.5$ J/molK^2 is observed at $\sim$ 3 K in 9 T. When we compare the observed 9 T value to that of the arc melted materials (not shown), we obtain a difference of about 1 J/molK^2 on behalf of the disordered phase. We may spec-

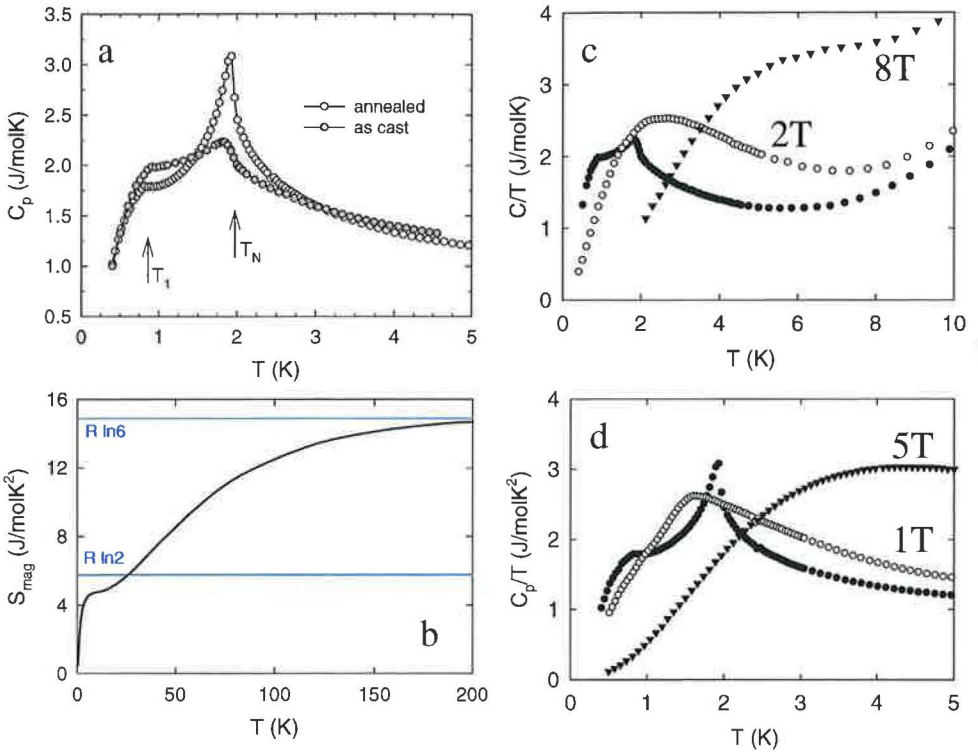

Figure 8.14: The low-temperature part of the specific heat of the $CePt_3Al$ samples. a - comparison of the as cast and annealed samples, b - calculated magnetic entropy of the annealed sample, c,d - specific heat in magnetic field of the sample 1, and of the sample 2, respectively.

ulate, that the extra entropy comes either from the formation of different aggregation state (similarly as in case of the nano Tb) or enhanced disorder in the splat-cooled system.

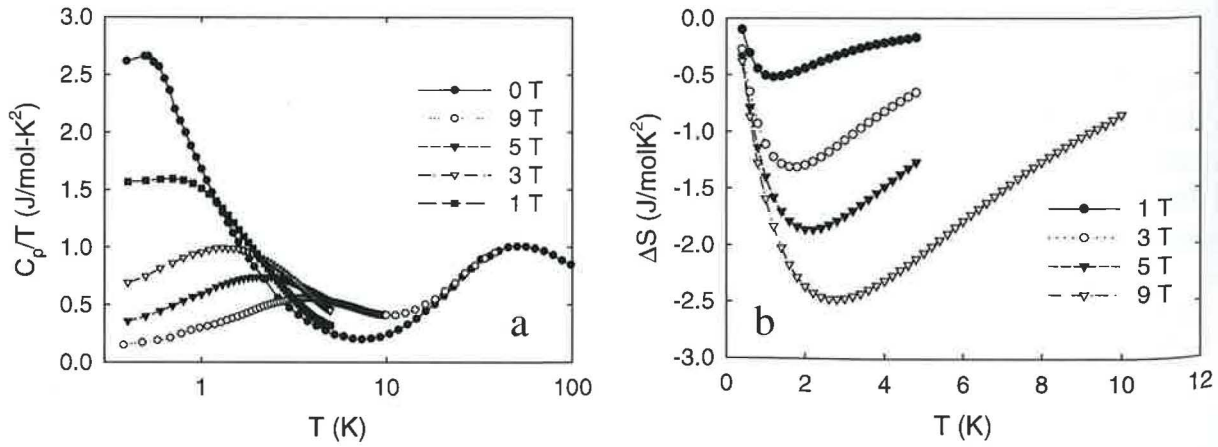

Figure 8.15: Specific heat and the isothermal entropy change of the $CePt_3Al$ splat-cooled sample.

	γ (J/molK^2)	Θ_D (K)	Θ_{E1} (K)	n1	Θ_{E2} (K)	n2	Θ_{E3} (K)	n3
$LaPt_3Al$	6.6	133	110	4	370	4	189	4
$CePt_3Al$	8.0	150	150	2	165	6	290	2

Table 8.5: Parameters of the electronic and phonon specific heat of $LaPt_3Al$ and $CePt_3Al$.

Finally, let's briefly discuss the temperature dependence of the magnetic entropy shown in the Figure 8.14.b. The curve was obtained by the standard procedure described already in the $CePt_3B$-related section. The used parameters of the electron and phonon parts of the specific heat are summarized in the Table 8.5. The entropy reaches the doublet-related Rln2 at $\sim$ 30 K and saturates to the Rln6 value above 200 K. The above described behavior is typical for the systems, where the Kondo-type interaction reduces the Ce magnetic moment at low-temperatures; the doublet-related value is not reached at the ordering temperature. Above 200 K, the Ce^{3+} configuration is expected to be stable.

Magnetization and susceptibility

The temperature dependence of the static magnetic susceptibility of the $CePt_3Al$ is shown in the Figure 8.16.a. The susceptibility below 10 K exhibits pronounced dependence on the applied magnetic field. With increasing the magnetic field, the low-temperature tail is suppressed and tends to saturate. The high-temperature curve can be successfully described using the modified Curie-Weiss law with the effective magnetic moment $\mu_{\text{eff}} = 2.38\ \mu_B$, the paramagnetic Curie temperature, θ_P = -19 K and $\chi_0 = 3.4\times10^{-9}\text{m}^3/\text{mol}$.

The magnetization isotherms measured at low temperatures are presented in the Figure 8.16.b. The characteristic Brillouin-like curvature suggests lack of magnetic ordering in the $CePt_3Al$ above 2 K. The 9 T magnetic moment ($\sim$ 0.9 μ_B) is consistent with the values observed in other Ce based compounds with low-temperature magnetic ordering and medium-strength Kondo-type screening.

The low-temperature behavior of the susceptibility under magnetic field is worth further of discussion. Similar trend can be observed in several heavy-fermion systems at low temperatures (T$\sim T_K$), the illustrative example is the CePtSi and $CePtSi_{1-x}Ge_x$ [541], known as a system with disorder-driven non-Fermi liquid (NFL) - Fermi liquid (FL) transition. The curvature of the temperature dependence of the susceptibility is a result of two competing phenomena, the CF splitting and magnetic disorder. The behavior of the magnetic susceptibility is almost identical in arc melted and splat-cooled samples.

Considering that the anomaly on the specific heat data of the splat-cooled sample is not attributed to the long-range magnetic ordering, discussion in the frame of the Kondo disorder model [542] or Griffiths phase model [543] becomes relevant. To estimate the susceptibility of $CePt_3Al$ at low temperatures (below 2 K), extrapolation of the Wilson ratio[6] using the

[6]The generally known Wilson ratio is defined as

$$R = (\pi^2 k_B^2 / 3\mu_{\text{eff}}^2)\chi T / C_p \tag{8.4}$$

, where χ is the magnetic susceptibility and C_p the heat capacity; other symbols have the usual meaning.

specific heat data (down to 0.4 K) was performed. We treated both the low-field and 8 T susceptibility data (of course with utilizing of the zero-field and 8 T specific heat data).

The obtained temperature dependence of the Wilson ratio is depicted in the Figure 8.16. c. The low-field data do not correspond to the behavior of a FL system (constant value) in the examined temperature range, however, comport with the results of the Kondo disorder model [542]. The linear part of the data (below 3 K) was used for extrapolation of the Wilson ratio. The 8 T - susceptibility is almost constant between 4 - 10 K and exhibits an abrupt increase below 3 K. Contrary to the low-field values, the 8 T data are reasonably close to the universal value R = 2 expected for a Kondo system.

The extrapolated low-temperature magnetic susceptibility is depicted in the Figure 8.16.d. It exhibits a logarithmic dependence on temperature as observed in NFL systems. Although the accuracy of the applied procedure is not very high, the relatively smooth dependence of the Wilson ratio and reproducible NFL behavior of the susceptibility suggest, that our estimation is rather well acceptable.

In consistency with the results of the heat capacity measurements, we speculate, that magnetic ordering may be suppressed in the splat-cooled material due to enhanced inter-electron correlations leading to the local spin instability, probably stimulated by the disorder.

Electrical resistivity

The electrical resistivity of the arc melted samples is presented in the Figure 8.17. The values of the room-temperature resistivity range from 66 to 72 $\mu\Omega$cm, and the residual resistivity, ρ_0 varies between 35 to 43 $\mu\Omega$cm. The $R(T)$ dependence is almost linear above 20 K, at low temperatures shows a broad maximum at 3 K. The peak transforms into a smooth drop-off when applying magnetic field (Figure 8.17.b). The zero-field data show a linear dependence on temperature, which expands into a larger temperature interval with increasing magnetic field. Such linear dependence is generally attributed to the onset of NFL behavior, but it must not be necessitously the case of $CePt_3Al$.

The electrical resistivity does not show any clear evidence of magnetic ordering, contrary to the observation on the specific heat data. However, if we expect the ordering to occur under relatively strong correlation of Kondo-type, the observed anomaly may comprise the two competitive contributions. Finally, the rather low RRR value of the investigated materials suggests not well-ordered crystalline phase, therefore the effects at low temperatures can be driven by the disorder scattering as well.

The resistivity data of the splat-cooled samples are shown in the Figure 8.18. The sample 1 (with a minority fraction of an amorphous phase, but with well-defined diffraction lines) exhibits a maximum on the $R(T)$ curve at $\sim$ 3 K, which is smeared out with the applied magnetic field. Above 5 T, the $R(T)$ curve turns into a monotonously decreasing with a change of slope at around 5 K. The observed behavior is rather similar to that observed in the arc melted samples. Contrary, the sample 2 revealed almost exponential dependence of the zero-field resistivity at low temperatures (Figure 8.18.b) and of one order higher value of the room-temperature resistivity, 653 $\mu\Omega$cm.

The reason for the observed character of the resistivity resides probably in the microstructure of the material. As it consists of 100 nm-large aggregates, the resistivity much resembles that of granular metals for example [544]. In those systems, the electrical resistivity is driven

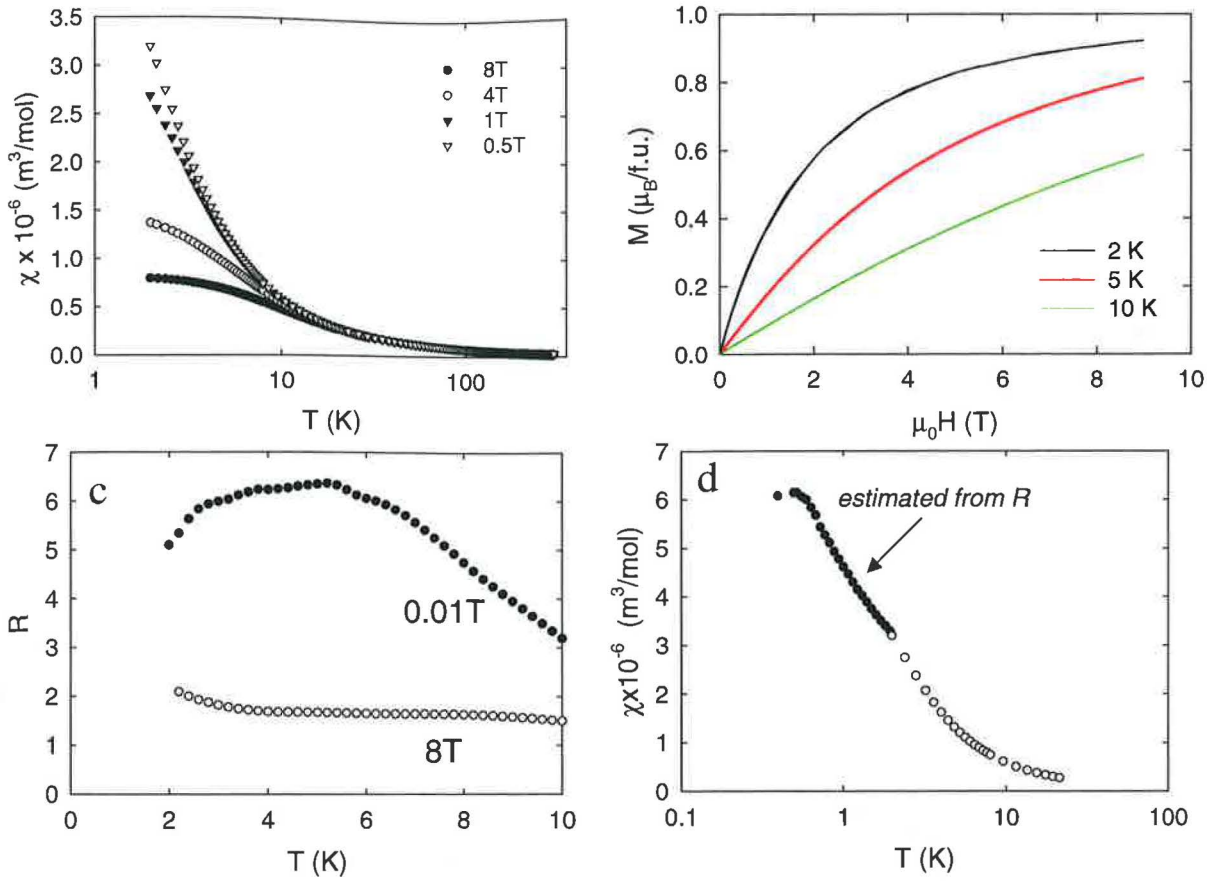

Figure 8.16: Magnetic properties of the $CePt_3Al$ samples.
a - magnetic susceptibility at several magnetic fields, b - magnetization isotherms at selected temperatures, c - temperature dependence of the Wilson ration, d - estimated and experimental low-field magnetic susceptibility

either by dominant electron localization or electron-electron interaction [545, 546].

The dominance of the electron localization mechanism is demonstrated by the linear dependence of $1/R$ on the square-root of the applied magnetic fields in fields above ~ 4 T (Figure 8.18.c). The idea is corroborated by the linear behavior of the $1/R$ vs $T^{1/2}$ dependence as depicted in the Figure 8.18.d. Contrary the analogues zero-field dependence (not shown) decays much faster suggesting admixture of the electron-interaction effects in low magnetic fields.

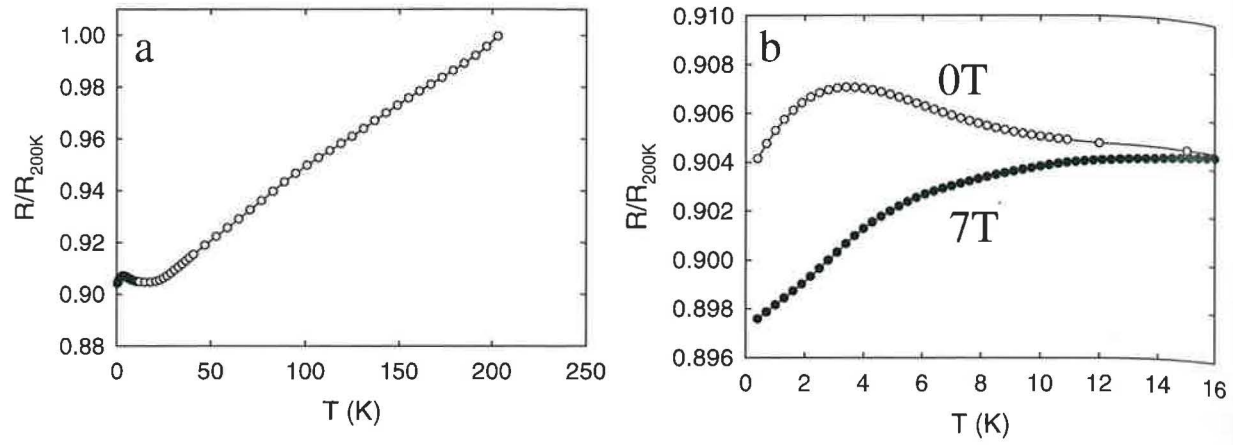

Figure 8.17: The electrical resistivity of $CePt_3Al$.
a - zero-field temperature dependence, b - low-temperature detail of the zero-field and 7 T curves.

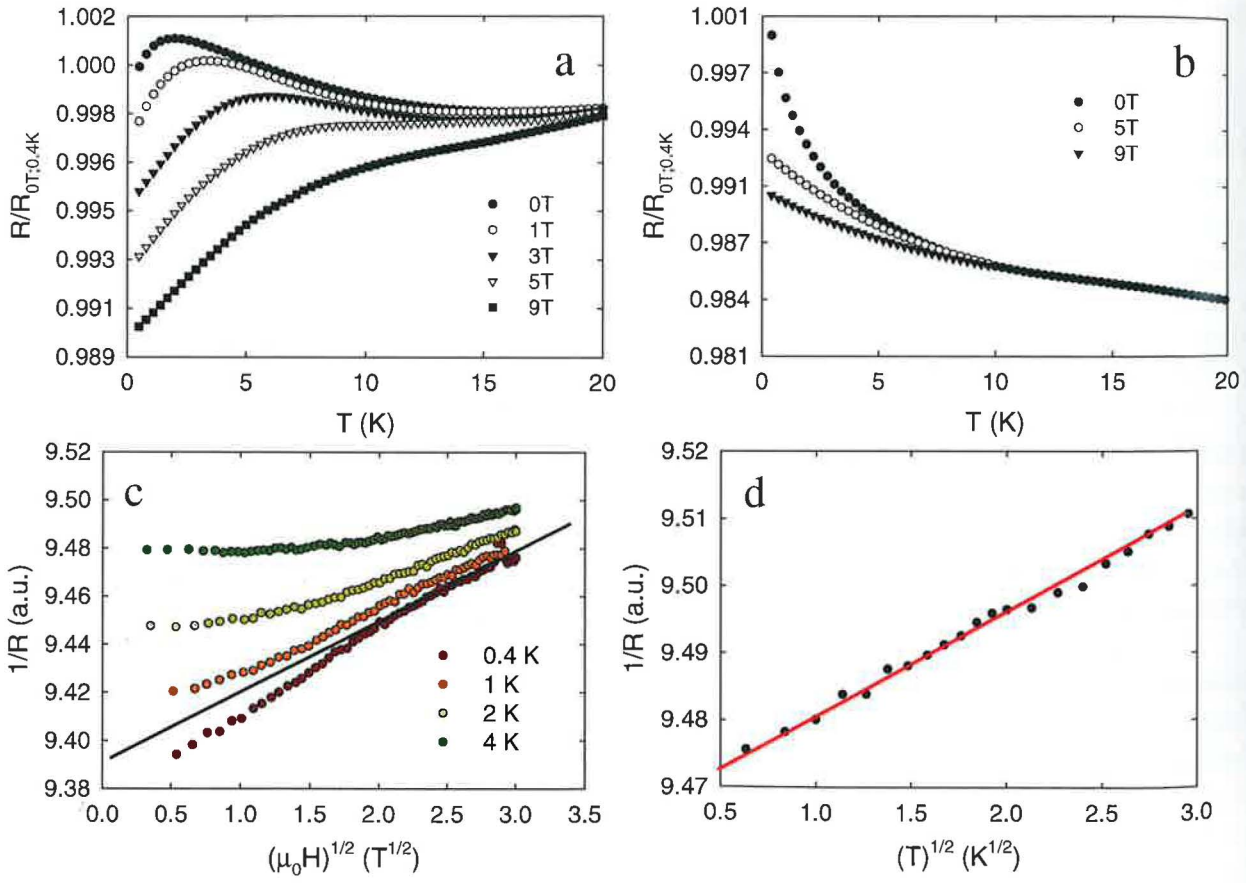

Figure 8.18: The electrical resistivity of splat-cooled $CePt_3Al$.
a - sample 1, b - sample 2. c - plot of the $1/R$ vs $H^{1/2}$ of sample 2, the line correspond to the fit of the 0.4 K curve, d - plot of the $1/R$ vs $T^{1/2}$ of sample 2, the red line represents the linear fit to the low-temperature data.

8.1.3 $CePt_3C$

The synthesis of this novel compound was also stimulated by the $CePt_3Si$-connected research. The most interesting was to explore, if the compound with C forms a single isostructural phase and what would be its properties in comparison to the HFSC Si-containing material. We also tried to substitute the Si by Mg and the results of the SEM analysis are presented in this subsection for comparison.

We have prepared and investigated a series of samples as summarized in the Table 8.7, the details concerning the preparation procedures are presented in the Chapter 3.

Contrary to the B and Al compounds, we observed an interesting melting effect depending on the purity of the used Ce. Surprisingly, the samples melted from the commercial Ce were much easier homogenized. The carbon diluted in the melt much faster and its rate of integration in the structure was much higher as shown further.

SEM analysis and diffraction experiments

The SEM micrographs are shown in the Figure 8.19. The microstructure of the as cast and quenched samples revealed formation of spherical cavities (approximately 50 μm in diameter and smaller), the detail of a representative is shown in the Figure 8.19.b. Inside the 'bubbles' the material formed a kind of lumps, which lead to enhanced surface-to-volume ratio in the cavities. The size of the 'bubble-like' defects is strongly reduced (below 1 μm) with annealing and subsequent slow cooling to room temperature as demonstrated in the Figure 8.19.c.

A very interesting microstructure is formed when introducing Mg in the material as shown in the Figure 8.19.d. The as cast samples revealed no special arrangement on the microscale, however, after annealing above 900 ° the Mg element evaporates from the material and a mesh of bend channels (each of $\sim$ 1μm long and below 1μm thick) is formed. The observed effect inspired us to propose a potential synthesis of porous metallic structures: using a highly-volatile element which can be additionally evaporated from the metallic matrix, which consequences formation of porous microstructure or even nanostructure.

The XRD and neutron diffraction patterns of $CePt_3C$ are shown in the Figure 8.20.a and b, respectively. The structure could not be described with the expected $CePt_3B$-type. Instead we successfully indexed the X-ray diffraction pattern with a cubic lattice. The resulting parameters are summarized in the Table 8.8. We were not able to distinguish, whether the C atoms occupy a defined crystallographic position of the $Fd\bar{3}m$ space group, stay irregularly in intersticial positions or disperse homogeneously in the material.

Moreover, in all as cast and quenched samples, the most intensive (002) line of C was detected. Therefore, only the Ce and Pt positions were determined. The arrangement is in analogy with the $CePt_{2+x}$ system [547].

The effect of the additional heat treatment on the ratio of carbon introduced in the structure was clearly seen when comparing the intensity of the C-related (002) line. In the as cast samples, the intensity was much enhanced in comparison to the annealed samples. Therefore, we decided to pack in more carbon to reach the desirable 1:3:1 stoichiometry in spite of some excess of carbon left in the material.

Those samples (4 and 6) revealed no significant differences in the X-ray diffraction data in comparison to the previous ones. To solve the problem of C accommodation in the structure,

Label	preparation	annealing	cooling
1	arc melted*	N	-
2	arc melted	Y	S
3	arc melted	Y	Q
4	arc melted*,**	Y	S
5	arc melted*	Y	Q
6	arc melted**	N	-
7	arc melted*	N	-

Table 8.6: Summary of the investigated $CePt_3C$ samples.
Y/N - yes/no; S/Q - slow/quenched. The * marks the samples prepared from the commercial 3N Ce, ** represent the samples, where access of C was used.

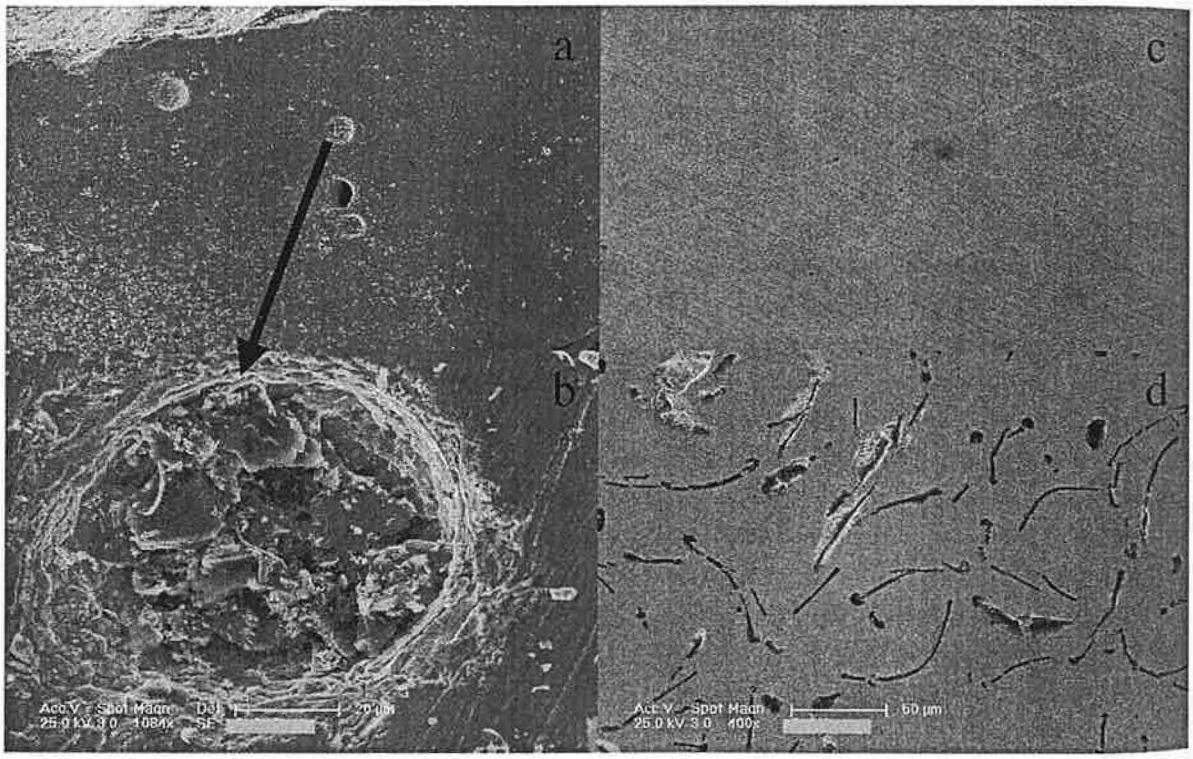

Figure 8.19: SEM micrographs of the $CePt_3C$ and $CePt_3Mg$ samples.
a - sample 1, detail of the characteristic defect in the sample 1, c - sample 2, d - annealed $CePt_3Mg$ material.

we performed a neutron diffraction experiment to observe the potential diffractions related to the carbon atoms. The results are shown in the Figure 8.20.b for the sample 6 with excess of carbon. We must point out, that the intensity of the carbon (002) line did not changed in comparison to the stoichiometrically melted samples. This observation suggest an idea,

space group: F $d\bar{3}m$	a = 7.65 - 7.63 Å
Ce (1/8 1/8 1/8)	Pt (1/2 1/2 1/2)

Table 8.7: Crystal structure of the majority of the $CePt_3C$ samples.

that when dissolving carbon in the Ce - Pt phase, certain fraction stays always dispersed in the structure, not due to kinetic but thermodynamic reason.

The analysis of the neutron diffraction pattern did not revealed any reflections, which would correspond to diffraction of regularly occupied C atoms. The comparison of the stoichiometric and carbon-excess samples revealed the same content of the dispersed carbon. The lattice parameters of the carbon were found to be slightly reduced in comparison to the literature data.

We may conclude, that the carbon crystallites are partly dispersed in the material (they probably function as the nucleation centers for the formation of the observed 'bubble' defects) and partly enter the crystal structure (probably the tetrahedral caverns formed of the Pt atoms in the proposed cubic structure), but not regularly.

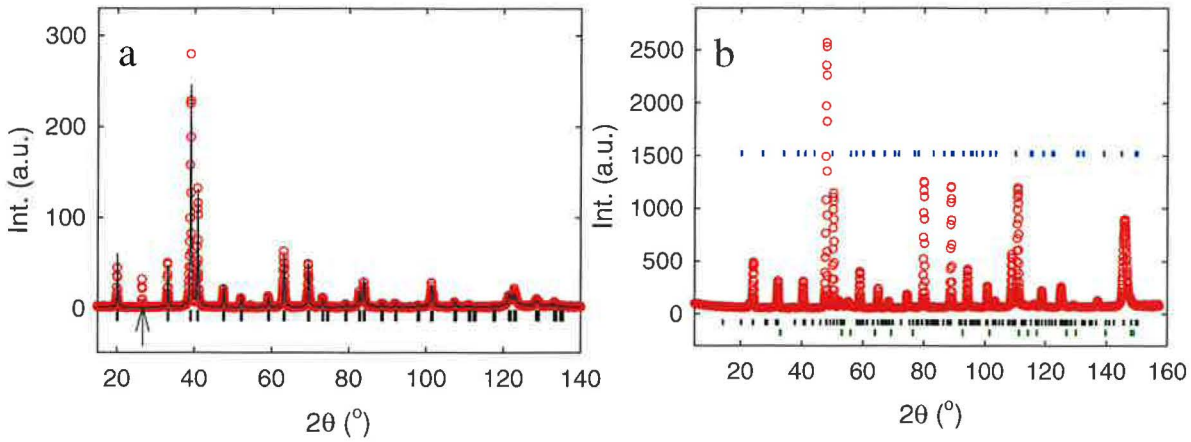

Figure 8.20: Diffraction patterns of the $CePt_3C$ sample.
a - X-ray diffraction; the arrow marks the strongest diffraction line of the excess carbon, b - neutron diffraction (D1a diffractometer, ILL).

Specific heat and entropy

The C_p(T) curve (Figure 8.21.a) exhibits a broad anomaly with a moderate maximum at ~ 1.5 K. Below 1 K the C_p vs T dependence is almost linear down to 0.4 K whereas above 2 K the C_p/T(T) curve (not presented) is logarithmic up to approximately 10 K. The anomaly becomes incessantly suppressed by the magnetic field as shown in the Figure 8.21.c. It does not occur due to magnetic ordering as suggested by the neutron diffraction experiments. However, magnetic correlations in a non-ordered Kondo lattice/heavy fermion state cannot be excluded due to limit of observation of magnetic scattering (~0.2 μ_B) in the performed neutron diffraction experiment.

	Θ_D (K)	Θ_{E1} (K)	n1	Θ_{E2} (K)	n2
$LaPt_3C$	92	110	6	270	6
$CePt_3C$	96	135	6	280	6

Table 8.8: Parameters of the phonon specific heat of $LaPt_3Al$ and $CePt_3Al$.

The γ coefficient is estimated by a huge value of 1.15 $Jmol^{-1}K^{-2}$ corroborating the picture of heavy quasi-particles (fermions) formation due to electron mass renormalization. After subtracting the phonon contribution obtained from the specific heat data of the nonmagnetic analogue $LaPt_3C$, the magnetic specific heat C_{mag} was obtained (Figure 8.21.b) and the magnetic entropy S_{mag} was calculated (Figure 8.21.d).

The results of the fit of the phonon part of the specific heat are summarized in the Table 8.8.

Besides the C_p anomaly at 1K, an additional wide-ranging contribution of unknown origin extends around 20 K. It may arise from the crystal field acting on the Ce^{3+} ion ground state, however, no satisfactory fit of the Schottky-type contribution was obtained. This may be caused by disorder in the alloy and an altered distribution of the CF splitting. The magnetic entropy reaches $R \ln 2$ only at $\sim$ 20 K signalizing that the potential magnetic ordering occurs in the presence of Kondo-type interaction yielding reduction of the Ce magnetic moment.

Electrical resistivity and magnetotransport

The temperature dependence of the electrical resistivity of the sample 2 is shown in the Figure 8.22.a. It's almost identical for all investigated samples. The low-temperature maximum extends around $\sim$ 3 K, indicating onset of a coherence state, proceed into logarithmic trend up to 80 K. The resistivity moderately increases above 80 K up to the room temperature.

Contrary, the magnetoresistance shows significant differences, depending on the sample consistency. The MR curves of the sample 1 are depicted in the Figure 8.22.b. The MR measured at 1 K exhibits a maximum around 3 T reflecting possible disruption of coherence (and hence a gap at the density of states) but it remains positive up to 9 T; higher field should be applied to suppress the proposed gap. Relics of its concave character are seen still at 30 K.

As already shown, the specific-heat data reveal a large electronic contribution at low T contrary to the decrease of the density of states at the Fermi level expected for a gap-forming system; strong anisotropy of the Fermi surface may be the reason for the observed phenomena. The gap formation in $CePt_3C$ is not straightforward due to lack of sign of valence fluctuations as reflected by the specific heat and susceptibility measurements (as shown further).

Because the Kondo temperature is very sensitive to local disorder of ligands around the f ion, they can be random in the neighborhood of defects and dislocations. The plot of the magnetoresistance against magnetization (Figure 8.22.d) suggests strong influence of imperfections in the Kondo lattice leading to distribution of the Kondo temperatures [549]. The shape of the curve corresponds to the dominant effect of disordered ligands around the

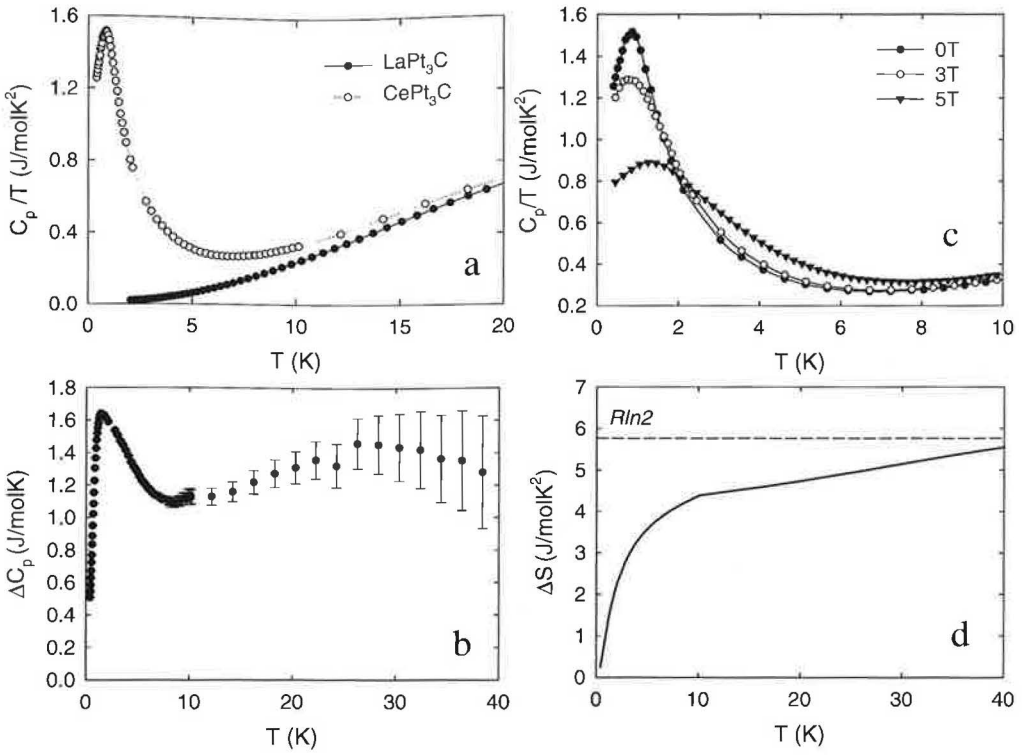

Figure 8.21: Specific heat and magnetic entropy of $CePt_3C$.
a - C_p of $CePt_3$ and $LaPt_3C$. b - magnetic contribution to the specific heat, C_{mag}. c - evolution of C_p in magnetic fields. d - magnetic entropy, S_{mag}.

$4f$ impurity rather then Kondo holes in the Kondo lattice.

The pulsed-field MR at 1.6 K of the sample 6 (with the carbon excess) is shown in the Figure 8.22.c. It is positive in the whole magnetic field range, however, yielding only 1.5 % MR at 45 T. The observed behavior cannot be described using the above mentioned scenario of collective effects of imperfections in the Kondo lattice. Amazingly, the magnetoresistance curve resembles that of the highly-ordered graphite fibres [548]. We may speculate, that the excess graphite is dispersed in the way forming regular arrangement, e.g. very thin fibers (not observable by the SEM method), which dominates in the transport phenomena in the material.

Magnetization and magnetic susceptibility

The high-field magnetization data together with the magnetic susceptibility are depicted in Figure 8.23. No metamagnetism was observed, the magnetic moment reaches $\sim$ 1.1 μ_B at $\sim$ 50 T (2 K) as expected for a non-magnetic Kondo lattice Ce-based compound. The analysis of the susceptibility data by means of the modified Curie-Weiss law yielded the effective magnetic moment 2.44 μ_B, θ_P = -46 and the $\chi_0 = 1.1\times10^{-10}$.

Discussion in the frame of the Kondo disorder model [542] or Griffiths phase model [543] seems to be relevant, similarly as in case of the splat-cooled $CePt_3Al$ sample.

The obtained temperature dependence of the Wilson ratio in $CePt_3C$ is in fact unphysical.

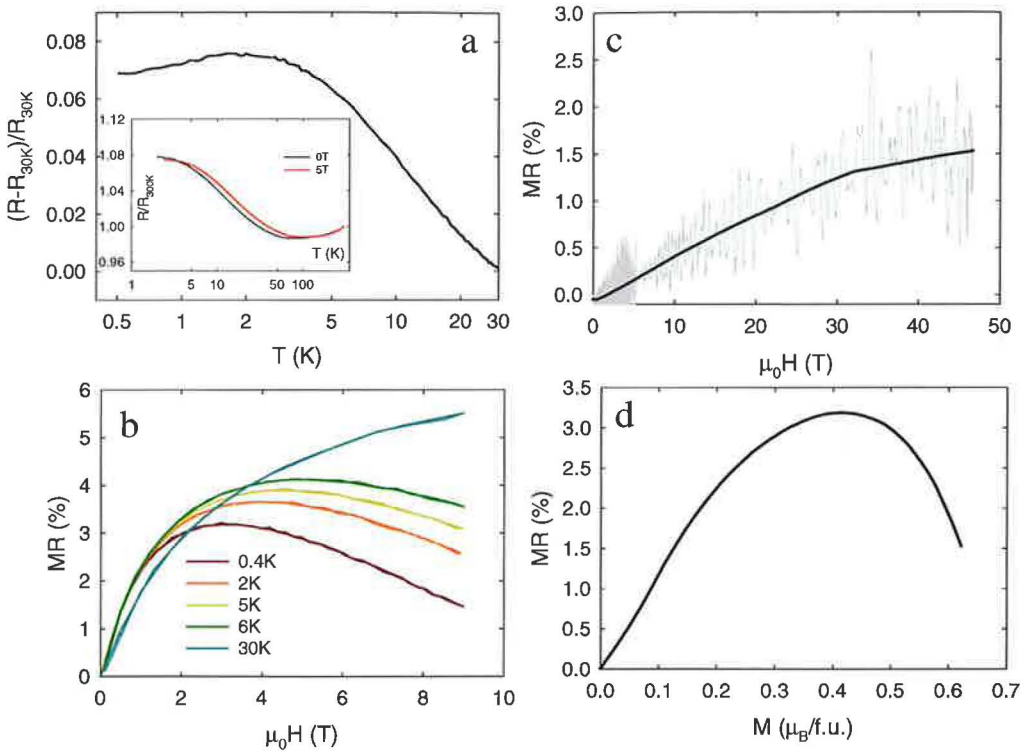

Figure 8.22: Electrical resistivity and magnetotransport of $CePt_3C$.
a - Relative electrical resistivity at low temperatures, the inset show the full temperature scale. b - magnetoresistance of the sample 1. c - high-field magnetoresistance of the sample 5. d - plot of the MR vs. magnetization at 2 K.

It shows a pronounced maximum at around 6 K (with R = 1.9 and 4 in B = 8 T and 0.01 T, respectively). The data do not definitely correspond to the behavior of a FL system (universal value R = 2 in a Kondo system) in the examined temperature range. The linear decrease of the R vs T dependence below $\sim$ 4 K seems to be consistent with the results of the Kondo disorder model [542].

We speculate, that magnetic ordering is suppressed due to disorder-induced inter-electron correlations leading to the local spin instability, similarly as in the splat-cooled $CePt_3Al$ compound. Nevertheless, the Kondo disorder model can not be used straightforwardly for explanation of the observed behavior.

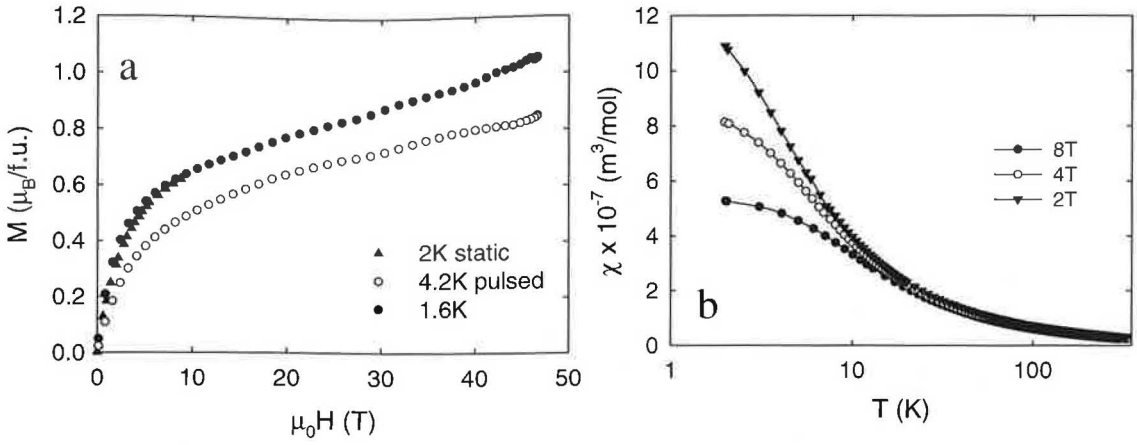

Figure 8.23: High-field magnetization (a) and magnetic susceptibility (b) of $CePt_3C$.

8.1.4 $CePt_3Ge$

The preparation of this novel compound was motivated by the investigation of Ge doping in $CePt_3Si$ [303]. The goal was to explore the novel phase and its properties.

We have prepared and investigated a series of samples as summarized in the Table 8.9, the details concerning the preparation procedures are presented in the Chapter 3.

We have not observed any difference when melting the components with the commercial or SSE treated Ce metal. In contrast, the crystal growth led to successful stabilization of the grown ingot in case of the SSE purified Ce only. The crystal growth of the compound was impossible in the tri-arc furnace (more then 10 trials were performed). Finally, one highly-oriented crystalline sample (D/2) was grown in the tetra-arc furnace using the pre-reacted components containing the SSE-treated Ce metal.

SEM analysis and diffraction experiments

The powder X-ray diffraction pattern and the SEM micrographs are shown in the Figure 8.24.

The composition and microstructure of the all samples does not vary significantly with respect to their preparation. The Ce : Pt : Ge ratio was found to be close to the 1 : 3 : 1 composition. As an example the micrograph of the grown and splat-cooled sample, respectively, is depicted in Figures 8.24.b,c. Although the composition observed by the SEM analysis suggested formation of the novel 1 : 3 : 1 phase, we calculated the theoretical pattern of several ternary Ce - Pt - Ge based compounds and compared them to our XRD data. Obviously, our XRD pattern could not be satisfactorily described using the known structures and/or their superposition.

The observed diffraction pattern cannot be indexed by the tetragonal $CePt_3B$-type structure, instead at least four possible structural arrangements reproduce the diffraction data. The space group and lattice parameters of the proposed structures are summarized in Table 8.10. In fact, only the model structure no. 3 is worth considering. It would roughly correspond to doubling of the original $CePt_3B$-type unit cell.

Label	preparation	annealing	cooling
1	arc melted	N	-
2	arc melted	Y	S
3	arc melted	Y	Q
4	arc melted	Y	S
5	arc melted	Y	Q
6	arc melted	Y	S
7	arc melted	Y	Q
8	arc melted	N	-
9	arc melted	N	-
A/1	grown	N	-
B/1	grown	Y	S
C/1	grown	N	-
D/2	grown	N	-
1	splat-cooled	N	-
2	splat-cooled	N	-
3	splat-cooled	Y	S
4	splat-cooled	Y	Q

Table 8.9: Summary of the investigated $CePt_3Ge$ samples. Y/N - yes/no; S/Q - slow/quenched.

	space group	a (Å)	b (Å)	c (Å)
1	$P4/mmm$	7.743	-	26.358
2	$Pmmm$	13.440	8.034	2.592
3	$P4/mmm$	11.342	-	14.470
4	$Pmmm$	20.340	5.541	2.877

Table 8.10: Crystal structures proposed for the $CePt_3Ge$ compound.

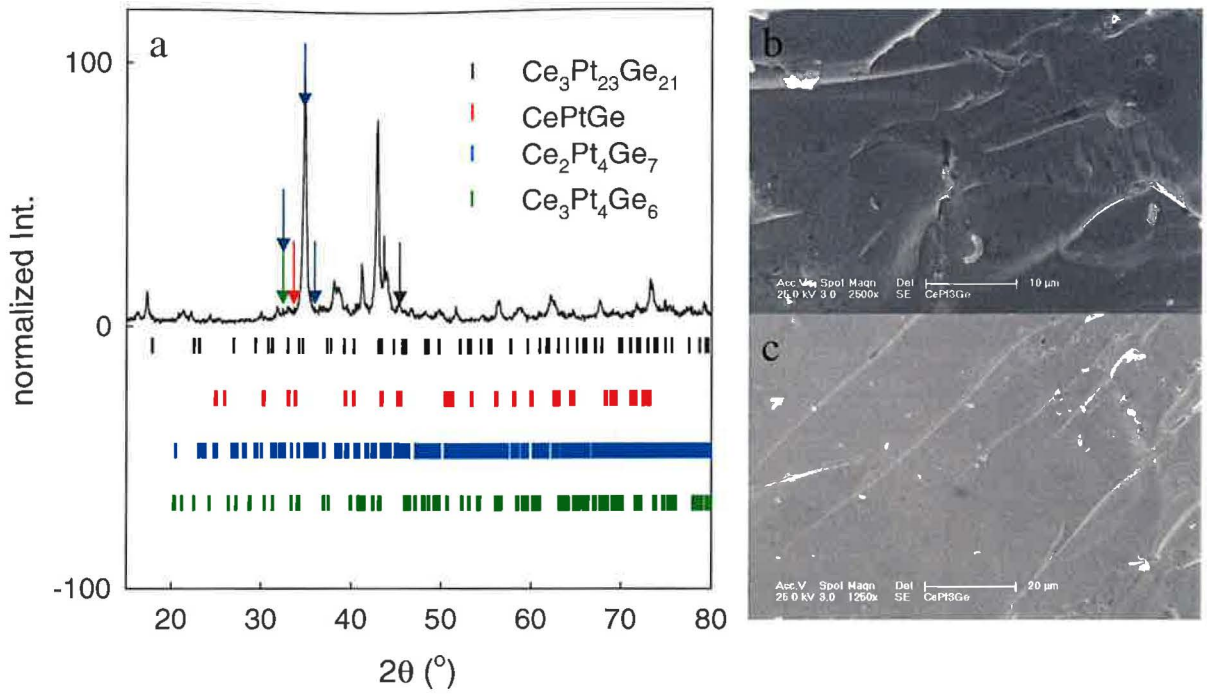

Figure 8.24: XRD pattern and SEM images of $CePt_3Ge$ (melted sample 4). a - XRD data, the vertical lines correspond to the Bragg positions of the related ternary Ce - Pt - Ge based phases. b - SEM micrograph of the D/2 sample. c - SEM micrograph of the splat-cooled sample 1. The arrows correspond to the Bragg position(s) of the most intensive reflection(s) in the related compounds.

Let's discuss the influence of the synthesis procedure on microstructural arrangement of the $CePt_3Ge$ samples, investigated by the XRD measurements. The four representative diffraction patterns are depicted in Figure 8.25. Figures 8.25.a and 8.25.b correspond to the melted and grown samples, while the 8.25.c and 8.25.d to those obtained by the splat-cooling method. The materials obtained by the melting techniques, involving in fact slow cooling rate show almost identical patterns. Only the reflections exhibit some broadening in the as-cast materials, which is commonly observed in many intermetallic phases.

The splat-cooled samples revealed either a broad bump in the diffraction data (Figure 8.25.c), suggesting dominance of an amorphous fraction, or strongly enhanced intensities and diffraction peak widths (Figure 8.25.d) due to significant texture and strain in the material induced by rapid cooling. Because the crystal structure is not unambiguously determined, further analysis of the data using a relevant texture and/or strain model was not performed.[7]

[7]In addition, powder XRD measurements under pressure were performed in ITU Karlsruhe. The motivation was to inspect a change of the crystal structure to the tetragonal $CePt_3B$-type. If the $CePt_3Ge$ exhibited USC in analogy to the $CePt_3Si$, we would further investigate the role of the non-centrosymmetry in formation of the HFSC state in these compounds. However, it was observed, that the crystal structure is rigid up to the highest applied pressure of 50 GPa.

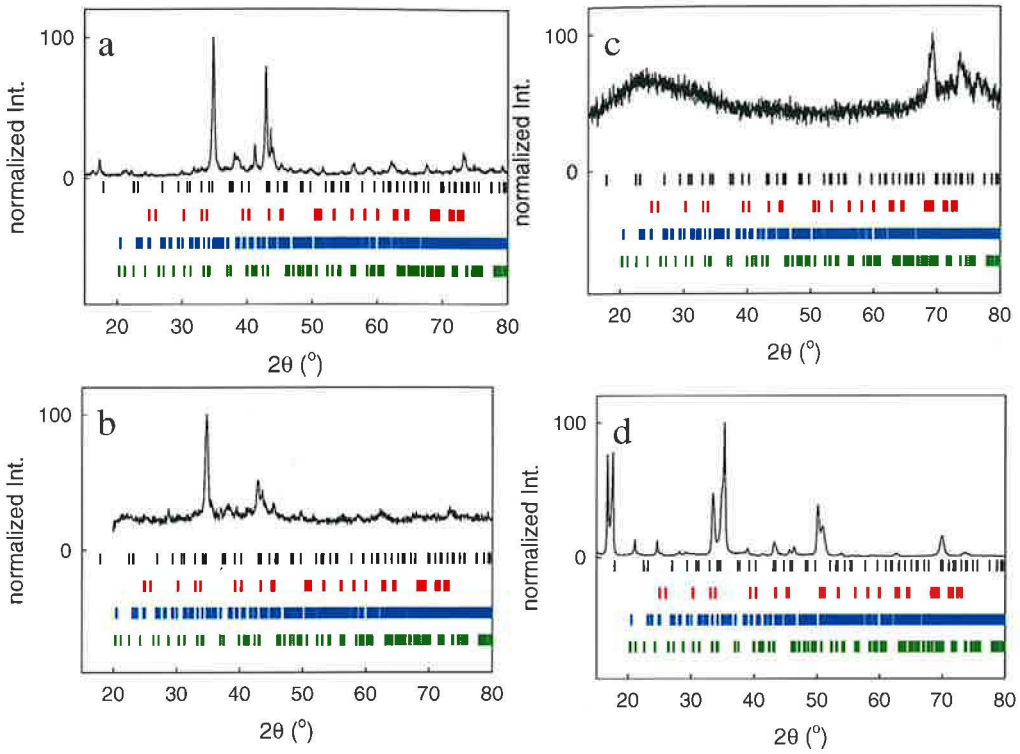

Figure 8.25: XRD patterns of several $CePt_3Ge$ samples
a - arc melted sample 2, b - grown sample D/2, c - splat-cooled sample 1, d - splat-cooled sample 3. The colors of the vertical lines (Bragg positions of the related phases) are identical with those in the Figure 8.24.a.

Specific heat and magnetic entropy

The $CePt_3Ge$ was investigated in detail by the measurements of the specific heat down to 0.3 K and magnetic fields up to 9 T. We performed the measurements on the arc-melted, grown and splat-cooled samples, respectively, for comparison as shown in the Figure 8.26.a. Except an additional anomalies at around 1.8 K and 3 K due to small amount of an unknown impurity phase in the arc-melted compounds (sample 1, 2), the specific heat shows a distinct peak at $T \sim 0.6$ K in all investigated samples.

The C_p of the grown sample D/2 is depicted in the Figure 8.26.b. When applying magnetic field, the anomaly broadens and shifts to higher temperatures. The measure of redistributed entropy (isothermal entropy change, ΔS) and adiabatic temperature change (ΔT) due to the applied magnetic field is shown in the Figures 8.26.c and 8.26.d. The values are not exceptional, the are in the range of those presented for other Kondo-lattice Ce compounds.

The specific heat and caloric effects are not much affected by the splat-cooling procedure as shown in Figure 8.27.a and 8.27.b, respectively.

To estimate the strength of the Kondo-type interaction in the $CePt_3Ge$ system, the magnetic entropy was calculated from the magnetic contribution to the specific heat, C_{mag}. The procedure was analogue to that applied in case of the previously discussed compounds. The

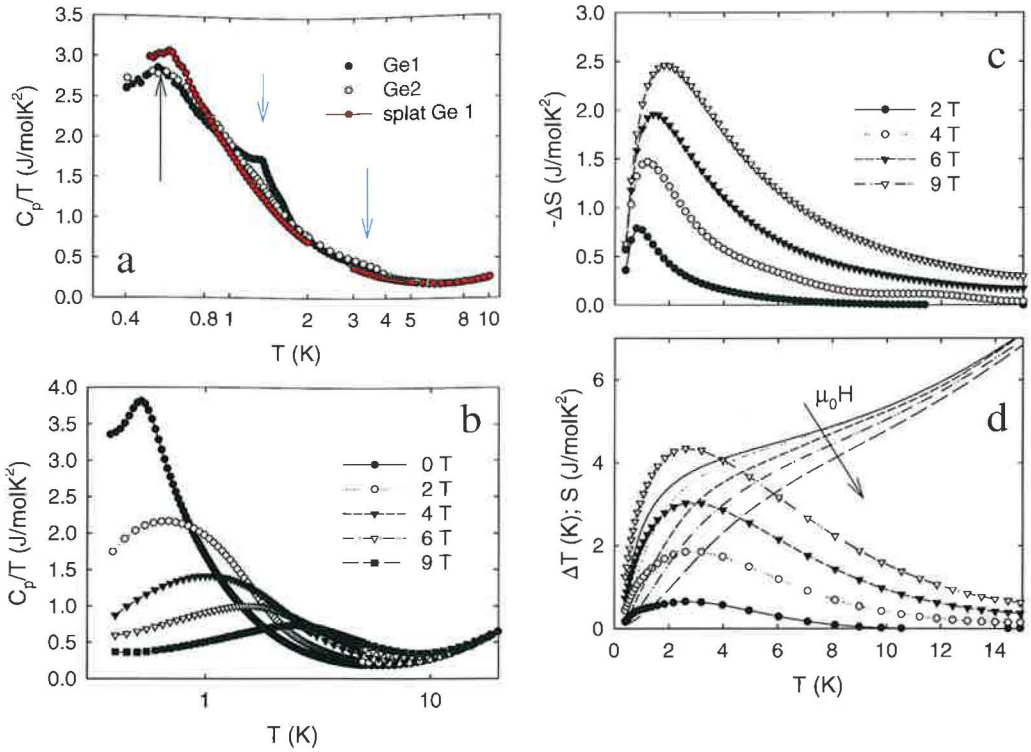

Figure 8.26: Specific heat and caloric effects of $CePt_3Ge$.
a - comparison of the low-temperature part of the specific heat of the arc-melted samples 1 and 2, and the splat-cooled sample 1, respectively. b - low-temperature part of the specific heat of the grown sample D/2 in magnetic fields. c - isothermal entropy change in several magnetic fields (sample D/2). d - adiabatic temperature change together with the total entropy in magnetic fields (sample D/2).

parameters describing the phonon and electron contribution, respectively, are summarized in the Table 8.11.

The low-temperature part of the magnetic entropy, S_{mag} is shown in the Figure 8.27.c. together with the C_{mag}. S_{mag} reaches the doublet-related $R\ln 2$ value at around 25 K pointing to a considerable Kondo-type interaction in the system. The Ce^{3+}-related $R\ln 6$ value is reached at $\sim$ 140 K. The Kondo temperature was roughly estimated from the single-ion Kondo model.[8] We obtain the value of $T_{\mathrm{K}} \sim 2.5$ K. The corresponding plot of the C_{mag} vs. the reduced temperature, T/T_{K} is shown in the Figure 8.27.d.

The specific heat data were further submitted to the analysis in the frame of the anisotropic Kondo model [550]. The procedure was motivated by the study of the non-magnetic Kondo lattice compound $CePt_3Al$ and its La-substituted derivative [551]. In a system with Ising-like crystal field ground state and strongly anisotropic exchange interaction in one crystallographic direction (e.g. the mentioned $CePt_3Al$ case), the specific heat can collaps onto a universal scaling curve $C_{\mathrm{p}}/\gamma T$ vs T/T_{m} and the shift of the temperature of the peak on the

[8]The model was already discussed in the Chapter 2, we used the relation: $\gamma_{T=0K} T_{\mathrm{K}} = 0.68R$, where $\gamma_{T=0K}$ is the γ value extrapolated from the low temperature data to 0 K.

	γ (J/molK^2)	Θ_D (K)	Θ_{E1} (K)	n1	Θ_{E2} (K)	n2
$LaPt_3Ge$	7.0	108	150	8	280	4
$CePt_3Ge$	7.0	104	150	8	295	4

Table 8.11: Parameters of the electronic and phonon specific heat of $LaPt_3Ge$ and $CePt_3Ge$.

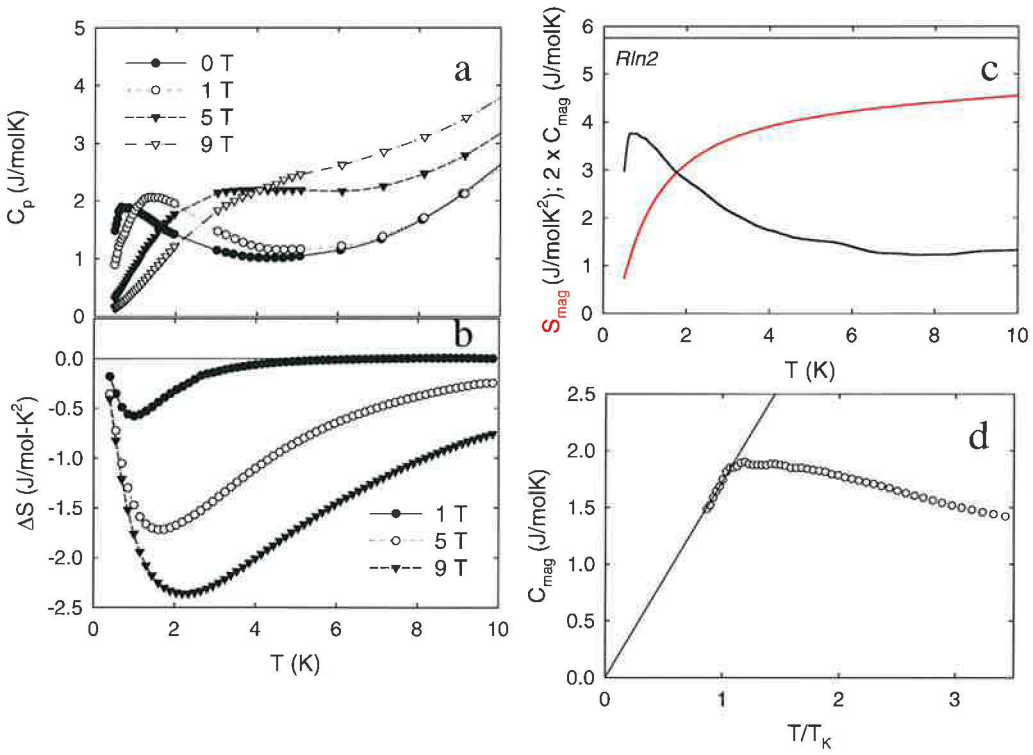

Figure 8.27: Specific heat and entropy of splat-cooled $CePt_3Ge$ (splat-cooled sample 2). a - evolution of the specific heat in magnetic fields. b - magnetic contribution to the specific heat and the magnetic entropy. c - calculated isothermal entropy change at several magnetic fields. d - plot of the magnetic contribution to the specific heat against T_K-reduced temperature. The solid line represents the fit of the single-ion Kondo model in the $T \rightarrow 0$ limit.

C_p/T is given by $T_m = \alpha^* R/\gamma$, where α^* is a function of the uniaxial exchange parameter and the conduction-band density of states.

The shift of the T_m and the γ-coefficient, is shown in the Figure 8.28.a and 8.28.b, respectively. The calculated parameter α^* with respect to the magnetic field is depicted in the Figure 8.28.c. The numerical data according to the reference [551] are shown for comparison (Figure 8.28.d). In contrast to the trend observed in the La-doped $CePt_3Al$ case, the specific heat of the $CePt_3Ge$ reflects the main trends of the anisotropic Kondo model: the C_p-anomaly shifts to higher temperatures, the anomaly becomes broader and lower, and the parameter α^* roughly decreases with increasing the magnetic field.

In fact the presented numerical data can be strictly applied to the single-crystal with

the magnetic field applied along the uniaxial direction, nevertheless, our results can be satisfactorily described with the proposed model.

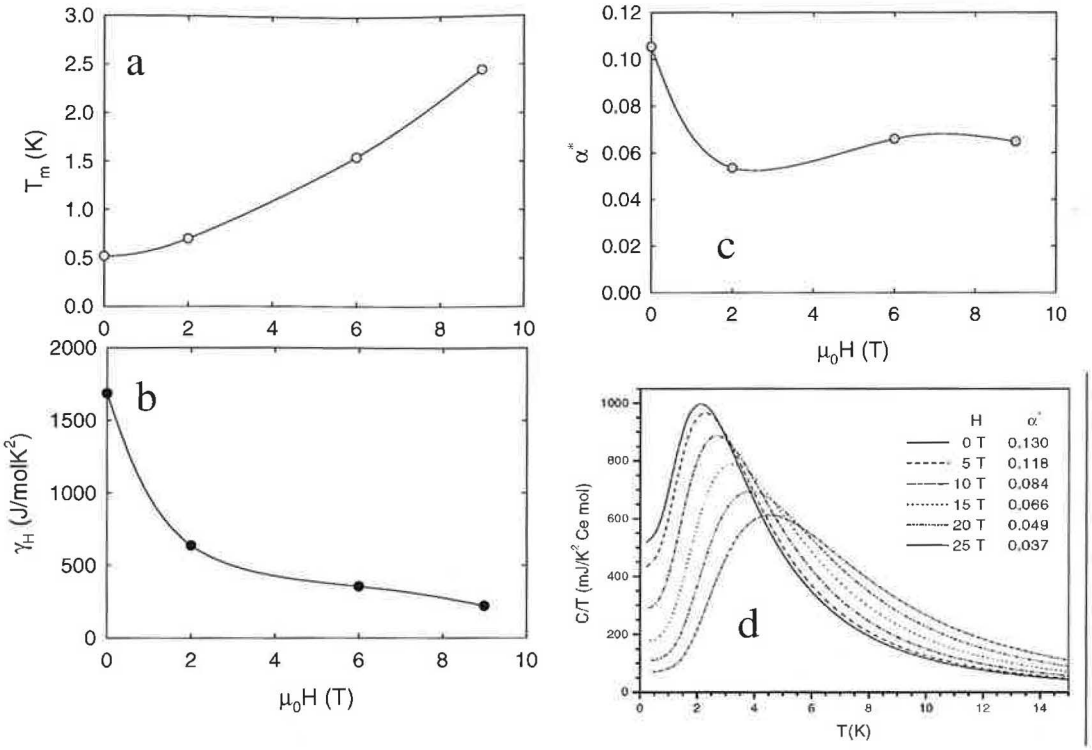

Figure 8.28: Test of the anisotropic Kondo model.
a - evolution of the position of the maximum on the specific heat (T_m) in magnetic fields. b - evolution of the Sommerfeld coefficient(γ_H) in magnetic fields. c - calculated parameter α^* in magnetic fields. d - specific heat according to the anisotropic Kondo model, from [551].

Electrical resistivity and magnetoresistance

The temperature dependence of the relative electrical resistivity ($R_{300K,260K}$) of $CePt_3Ge$ is shown in Figure 8.29. The Figure 8.29.a presents the comparison of the resistivity of the grown and splat-cooled samples, respectively. The relative decrease of resistivity on cooling is about 40 % in the grown material in contrast to the almost constant value in the splat-cooled sample.

The resistivity of the grown sample D/2 shows a broad anomaly with a maximum at around 60 K. The $R_{300K,260K}$ vs T curve further decays linearly down to 20 K.

The detail of the $R_{300K,260K}$ vs T curve of the splat-cooled material (sample 2) is demonstrated in the Figure 8.29.b. The resistivity shows a maximum at $T_{max} \sim 4$ K and a logarithmic temperature dependence with a positive slope below T_{max} and with a negative slope above T_{max} up to ~ 20 K, respectively.

The low-temperature behavior of the electrical resistivity in magnetic fields is shown in the Figure 8.29.c. The magnetic field causes an accrue of the low-temperature $R_{300K,260K}$ vs

T dependence up to 3 T. Further increasing of the applied magnetic field up to 9 T suppresses the resistivity.

The resistivity of the splat-cooled sample 1 is presented in the Figure 8.29.d. The zero-field curve does not exhibit the pronounced maximum characteristic for the sample 2 - related one, only a smooth decay can be detected below 6 K. The magnetic field causes a continuous enhancement of the low-temperature resistivity. At 3 T the $R_{300K,260K}$ vs T curve corresponds to almost exponential dependence as generally observed in gap-forming systems.

We further employed several models for description of this phenomenon according to [7]. However, the low-temperature increase of the resistivity was not satisfactory to treat the system in terms of e.g. hopping conductivity. Finally, the naive fit of the simple activation model revealed the size of the proposed gap $\Delta/k_B = 3.02\times10^{-8}$.

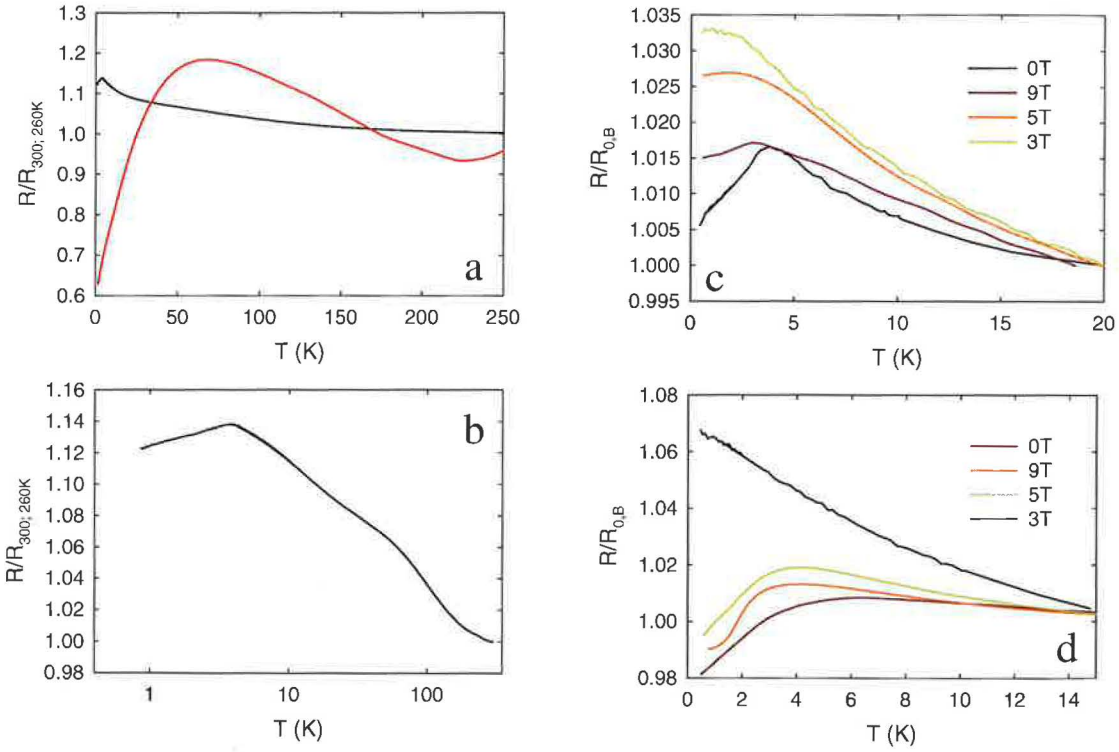

Figure 8.29: Electrical resistivity of $CePt_3Ge$ samples.
a - relative electrical resistivity, $R/R_{300K,260K}$ of the splat-cooled (black line) and grown samples (red line), b - detail of the $R/R_{300K,260K}$ vs T of the splat-cooled sample, c - evolution of the relative electrical resistivity, $R/R_{0,B}$ in magnetic fields (splat-cooled sample 1), d - evolution of the relative electrical resistivity, $R/R_{0,B}$ in magnetic fields (splat-cooled sample 2).

The electrical resistivity of the arc-melted sample in comparison to the grown material is finally depicted in Figure 8.30. The relative resistivity (Figure 8.30.a) is characterized by a pronounced maximum around 4 K followed by a step-like decrease down to 0.35 K (the detail of the low-temperature part is shown in inset of the Figure 8.30.b). In addition, a broad anomaly rounds above 80 K. In fact, the 80 K-related feature corresponds to that

observed in the $R_{300K,260K}$ vs T curve of the grown sample (Figure 8.29.a). In contrast, the low-temperature step-like anomaly in the arc-melted material lacks in the grown-sample data. The possible reason is an influence of an impurity phase, modifying also the specific heat data (Figure 8.26.a).

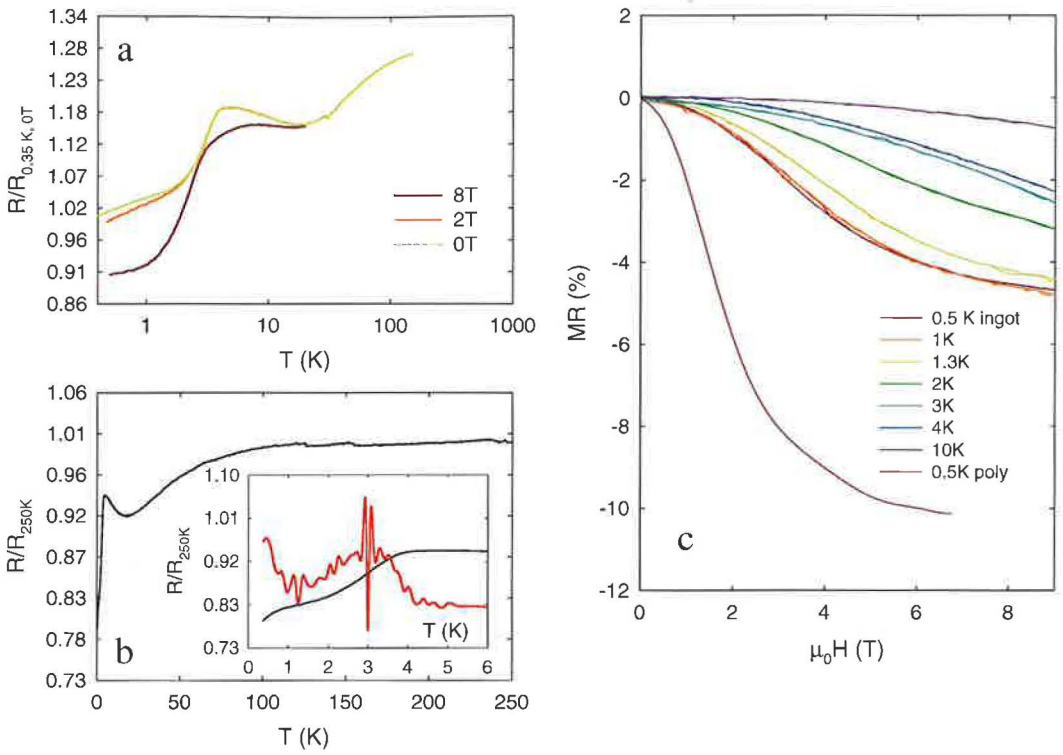

Figure 8.30: Electrical resistivity of $CePt_3Ge$.
a - relative electrical resistivity, $R_{0.35K,0T}$ in magnetic fields of the arc-melted sample 1, b - zero-field $R_{0.35K,0T}$ vs T curve, the inset represents the low-temperature detail, the red line corresponds to the 1^{st} derivative of the curve of the arc-melted sample 1, c - magnetoresistance (MR) at several temperatures of the grown sample D/2, the MR curve of a arc-melted sample is also shown.

Finally, let's discuss the results of magnetoresistance (MR) measurements. The MR curves of the grown and arc-melted sample, respectively, are depicted in the Figure 8.30.c. Except the absolute value, the trend of the MR dependencies is in fact identical in all arc-melted and grown samples, respectively. In contrast the splat-cooled samples show much different character by means of the absolute values (approximately 10-times lower) and the slope of the MR curves.

To explore the role of sample microstructure on the MR behavior, the results were discussed in the frame of the Kondo lattice model (bulk-ordered samples) and the localization model of metallic glasses (splat-cooled materials). The plot of the characteristic parameter $R - R_0/R$ vs $\sqrt{H}$ of the splat-cooled sample 1 is shown in Figure 8.31.a, the detail of the 0.4 K-curve in the Figure 8.31.b, respectively. The low-field region is characterized by a maximum of the $R - R_0/R$, which turns into negative linear decay at higher magnetic fields.

The observed behavior can be well attributed to moderate-strength spin-orbit scattering yielding to the localization effects. In contrast the ordered samples cannot be treated by this approach as demonstrated in Figure 8.31.d for the grown D/2 sample.

Instead, the plot of the MR vs magnetization is presented in the Figure 8.31.c. The character of the plotted dependence reveals a dominant role of the Kondo holes as impurities in the MR of the $CePt_3Ge$ Kondo lattice [549].

The presented MR results demonstrate an enormous role of the sample preparation leading to e.g. different grain-order on electronic properties of $CePt_3Ge$.

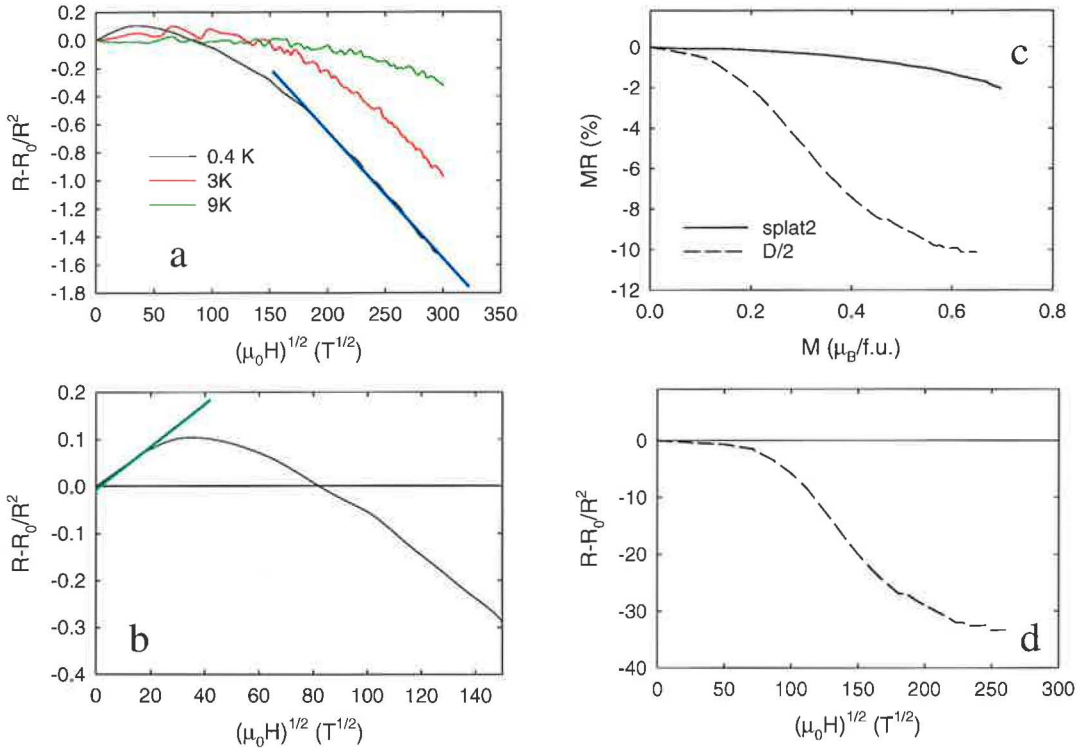

Figure 8.31: Magnetoresistance of the $CePt_3Ge$ in terms of the Kondo lattice model and localization effects.
a - plot of the parameter, $R - R_0/R$ vs $\sqrt{H}$ at several temperatures, the blue line represents the fit according to the model of moderate spin-orbit scattering, b - detail of the $R - R_0/R$ vs $\sqrt{H}$ curve at 0.4 K in low fields, the green line represents the fit according to the model of moderate spin-orbit scattering in low magnetic fields, c - magnetoresistance (MR) vs magnetization (M) of the two $CePt_3Ge$ samples, d - $R - R_0/R$ vs $\sqrt{H}$ curve at 0.4 K of the grown sample D/2.

Magnetization and magnetic susceptibility

The results of the magnetization and susceptibility investigations of $CePt_3Ge$ are depicted in Figure 8.32. They are in fact rather similar to those of the $CePt_3X$ with Al or C. The magnetization curves do not show any sign of metamagnetism up to 50 T (Figure 8.32.a)

in consistency with the monotonous temperature dependence of the magnetic susceptibility (Figure 8.2.b). No anomaly, which could be attributed to magnetic ordering was observed down to 2 K.

For comparison, the magnetization curves of the grown sample D/2 and the arc-melted polycrystalline sample 1 are presented in Figures 8.32.c, d. The more pronounced curvature of M vs H curve the arc-melted sample suggests presence of Ce^{3+}-impurities in the material as suggested already by the specific heat and electrical resistivity measurements.

The analysis of the susceptibility data by means of the modified Curie-Weiss law yielded the effective magnetic moment 2.42 μ_B, θ_P = -40 and the $\chi_0 = 4.0\times10^{-9}$.

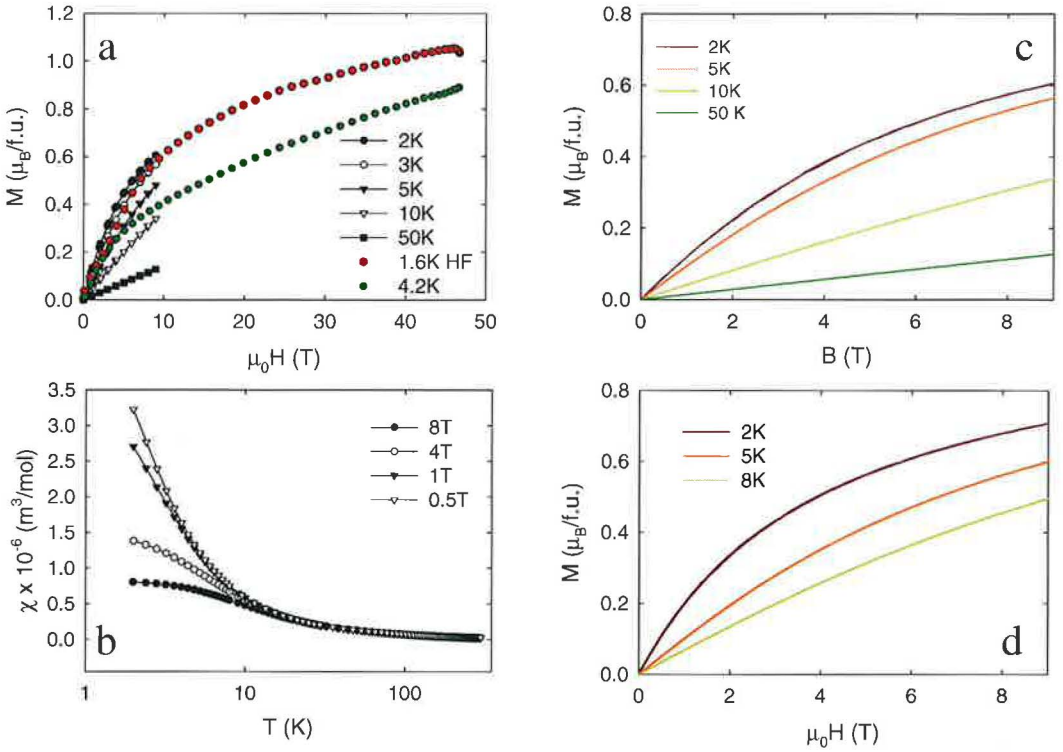

Figure 8.32: Magnetization and magnetic susceptibility of $CePt_3Ge$.
a - high-field magnetization data of the grown sample D/2, magnetic field was applied along the cylinder axis, the data obtained on the PPMS device are shown for comparison, b - static magnetic susceptibility, c - magnetization curves of the grown sample D/2, magnetic field was applied along the cylinder axis, d - magnetization curves of the arc-melted sample 3.

Neutron diffraction experiment in the mK temperature region

The macroscopic investigations of the $CePt_3Ge$ compound did not unambiguously excluded magnetic ordering below 2 K. To inspect the possibility of long-range magnetic ordering or al least static magnetic correlations in the compound, a powder neutron diffraction experiment down to 70 mK was performed.

The results are shown in Figure 8.33. We observe no Bragg peaks due to magnetic scattering indicating, that the long-range magnetic order lacks down to 70 K. The Figure

8.33.b demonstrates the differential magnetic intensity suggesting presence of short-range correlations of magnetic origin at the low temperatures. Because the crystal structure is not unambiguously determined, additional interpretation characteristic by means of correlation length was not performed.

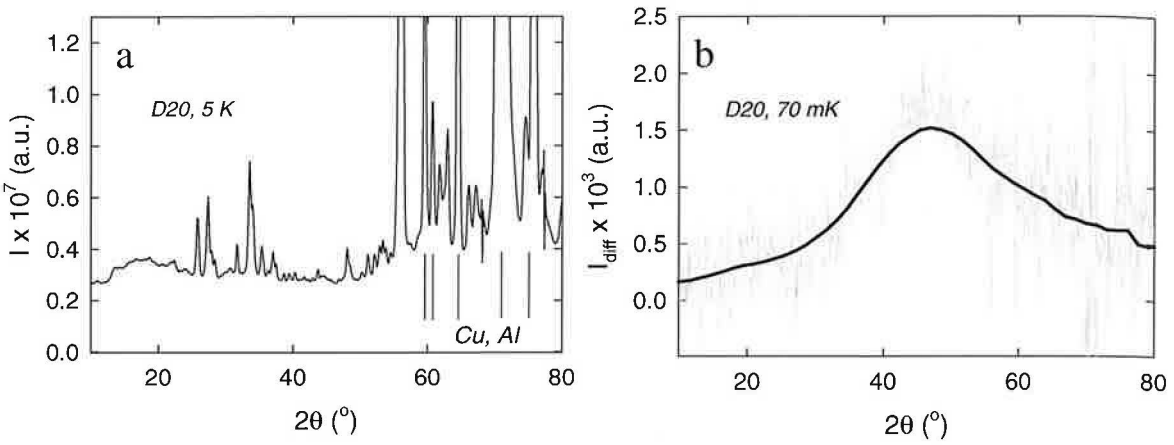

Figure 8.33: Neutron diffraction pattern of the $CePt_3Ge$.
a - original 5 K data, the vertical lines marks the Bragg positions of the Cu and Al (material of the sample holder). b - differential neutron diffraction intensity obtained by subtraction of the 5K and 70 mK data.

8.1.5 $CePt_3Si$

The $CePt_3Si$ compound has been intensively studied by many groups as already presented in the Chapter 5. Here we include remarks on preparation of this material and several so far unpublished results.

Sample preparation and characterization

We have prepared and investigated a series of $CePt_3Si$ samples as summarized in the Table 8.12, the details concerning the preparation procedures are presented in the Chapter 3. We obtained arc-melted, grown and splat-cooled materials, respectively.

We have not observed any difference when melting the components with the commercial or SSE treated Ce metal. In contrast, the crystal growth led to successful stabilization of the grown ingot in case of the SSE purified Ce only.

The growth of the single-crystal was, however, in fact unsuccessful. Finally we have obtained a good highly-crystalline piece of material, but never a macroscopic single-crystal at all. The reason is the peculiar phase diagram of the Ce - Pt - Si constituents (included in Appendix), which contain many ternary phases with very similar values of melting point. Therefore, at least two phases become enough stable during the solidification above the ingot-melt interface. This leads to formation of very thin crystalline needles of equal orientation, which are separated by a different phase.

Label	preparation	annealing	cooling
1	arc melted	N	-
2	arc melted	Y	S
3	arc melted	Y	Q
4	arc melted	Y	S
5	arc melted	N	-
A/1	grown	N	-
B/1	grown	N	-
C/1	grown	N	-
D/1	grown	Y	S
E/2	grown	N	-
F/2	grown	N	-
G/2	grown	Y	S
1	splat-cooled	N	-
2	splat-cooled	Y	S

Table 8.12: Summary of the investigated $CePt_3Ge$ samples.
Y/N - yes/no; S/Q - slow/quenched.

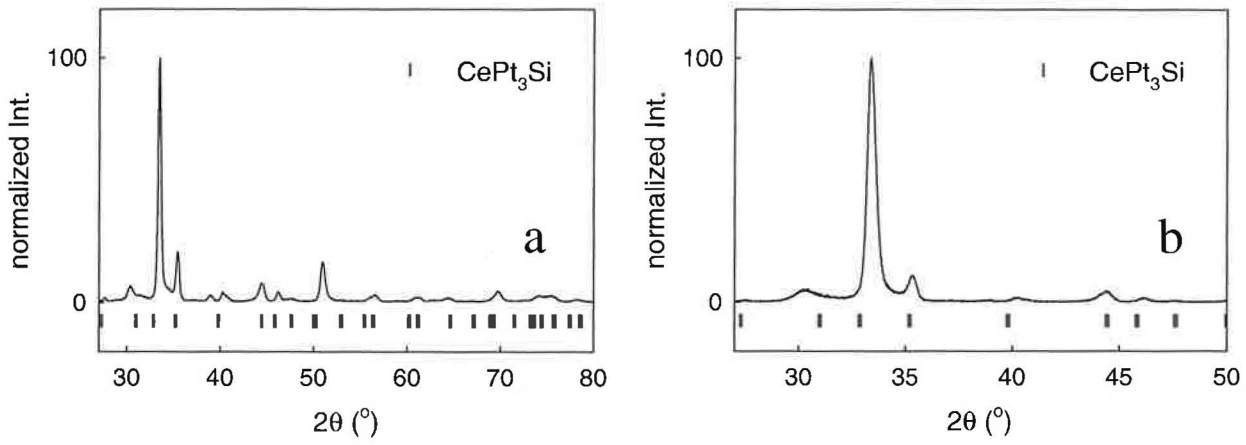

Figure 8.34: XRD pattern of $CePt_3Si$.
a - arc-melted material, b - splat-cooled sample. The vertical lines correspond to the Bragg positions of the tetragonal $CePt_3B$-type structure.

The prepared samples were characterized using the SEM analysis and XRD. The SEM micrographs confirmed good homogeneity of the samples and the element analysis confirmed the stoichiometry to be close to the expected $1 : 3 : 1$.

The results of the XRD measurements are shown in Figure 8.34. The XRD patterns of samples obtained by arc-melting or grown in the furnace revealed the expected $CePt_3B$

	γ (J/molK^2)	Θ_D (K)	Θ_{E1} (K)	n1	Θ_{E2} (K)	n2		
$LaPt_3Si$	9.5	151	124	4	438	4	166	4
$CePt_3Si$	9.5	151	130	8	438	4	190	4
Δ_i (K)	11±1	80(2)±3	160(2)±8					

Table 8.13: Parameters of the electronic and phonon specific heat of $LaPt_3Si$ and $CePt_3Si$. CF splitting, Δ_i in $CePt_3Si$, the (2)-affix symbolizes a doublet.

structure with the lattice parameters in a good agreement with literature (varying up to 1.5 % only). Surprisingly, analysis of the XRD data of the splat-cooled samples suggested formation of a new structure type: orthorhombic with the lattice parameters a = 3.108 Å, b = 17.703 Å, c = 6.542 Å. Additional long-term annealing caused transformation of the orthorhombic crystal structure to the tetragonal $CePt_3B$-type.

Analysis of the specific heat

The low-temperature specific heat of $CePt_3Si$ in context of HFSC was discussed by several authors (Figure 8.35.a). Our new contribution to the field are the measurements up to 9 T yielding intact character of the T_N-related anomaly. An additional new result is the low-temperature specific heat of the splat-cooled $CePt_3Si$. The C_p/T vs T curve shows an increasing tail down to 0.35 K masking the expected T_c-related anomaly. The T_N-connected anomaly is much broader then that of the 'ordered' material and its maximum shifts to $\sim$ 3.5 K.

Further, we present the analysis of the specific heat data in temperatures up to 300 K using the analogue procedure to that previously described. The experimental C_p/T vs T together with the fit of the electron and phonon contributions are shown in the Figure 8.35.b. Due to clear proof of crystal field excitations in the $CePt_3Si$ [285], we analyzed the remaining contribution to the specific heat data using the Schottky-type formula for the $j = 5/2$.

The energy scheme obtained by this procedure is summarized in Table 8.13. The applied approach is somewhat simplified, because it does not take into account the mixing of the Kondo interaction and CF effects. Notwithstanding,, it rather satisfactorily described the data in the paramagnetic region, where the Kondo-type screening can be neglected. The reliability of the performed procedure is corroborated by the nice agreement of the calculated Schottky entropy and magnetic entropy obtained from the experimental data as shown in the Figure 8.35.d. The fit of the Schottky-type contribution is depicted in the Figures 8.35.e and 8.35.f, respectively.

Pilot high-field investigations

So far, no results of high-field investigations of $CePt_3Si$ were not published. Recently, high-field measurements of magnetization and magnetoresistance of the $CePt_3Si$ sample E/2 were performed by us; the results are shown in Figure 8.36.

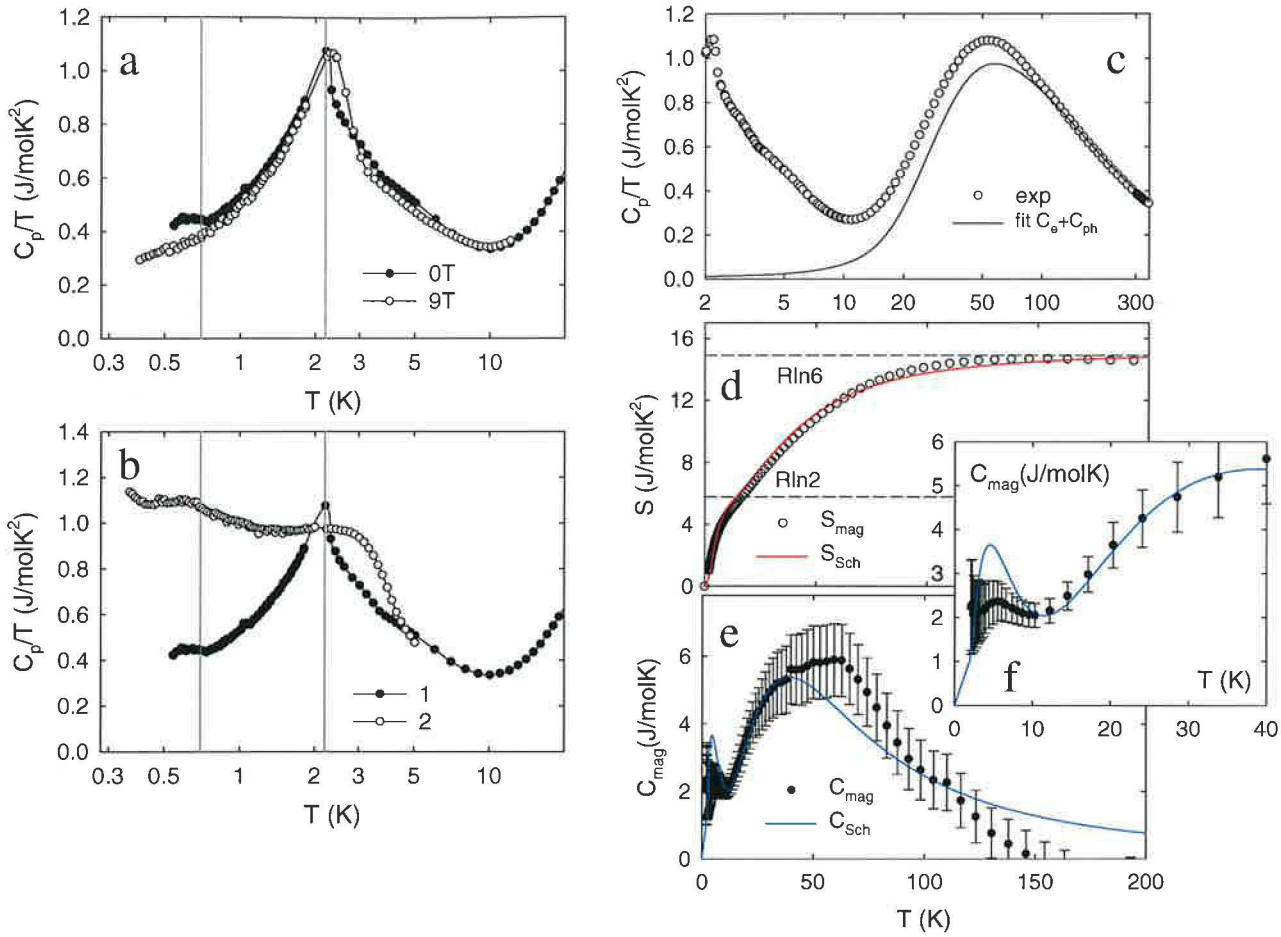

Figure 8.35: Specific heat of $CePt_3Si$.
a - comparison of the zero-field and 9 T-C_p data, b - comparison of the C_p of the grown (sample 1) and splat-cooled (sample 2) material, c - C_p (open circles) in comparison to the fit of the electron and phonon contribution (C_e+C_{ph}), d - magnetic and Schottky entropy, e - fit of the Schottky contribution to the C_p (solid line) in comparison to the magnetic part of the specific heat (C_{mag}), f - low temperature detail of (e).

The high-field magnetization curves for the pulsed field applied parallel and perpendicular, respectively, to the ingot axis are depicted in Figure 8.36.a,b. The data obtained in the PPMS apparatus up to 9 T are shown as well. For field applied along the a-axis, the magnetization shows a wide-spread step-like anomaly at around 20 T at 1.6 K, which can be attributed to the field-induced metamagnetic transition from the ground-state antiferromagnetic structure to probably field-induce ferromagnetic state. An analogues behavior was not observed for the complementary investigated direction. Comparison of the magnetization curves recorder in the two investigated orientations of the sample with respect to the pulsed-field is shown in the Figure 8.36.c. Above 35 T, both curves coalesce each other.

MR curve, presented in the Figure 8.36.c shows a maximum at around 17 T (at 2.2 K),

which appears to coincide with the magnetization results. The value of MR reaches almost 50 %, than decreases down to negative value of $\sim$ 30 % at 38 T and remains constant up to 50 T.

So far, the observed phenomena may be interpreted in terms of change of the ground-state magnetic structure, but further high-field investigations of $CePt_3Si$ using different samples (polycrystalline, oriented powder etc.) are in progress to improve the insight into the high-field behavior of $CePt_3Si$.

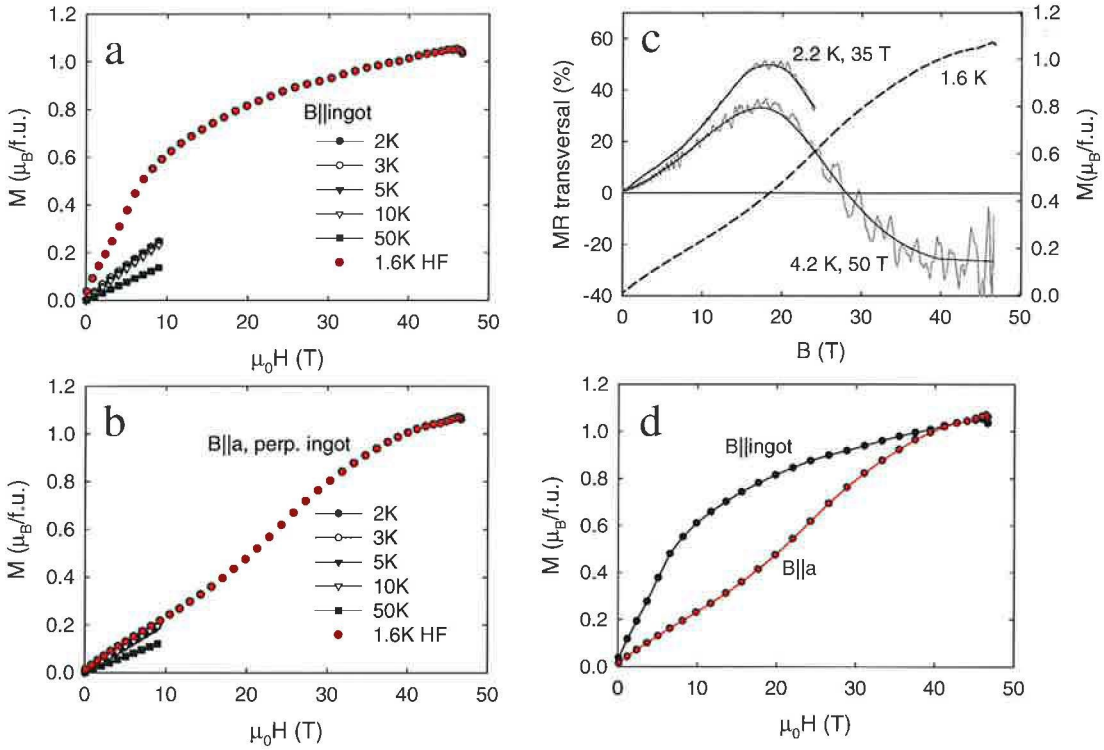

Figure 8.36: High-field magnetization (M) and magnetoresistance, MR of $CePt_3Si$. a - magnetization curves of $CePt_3Si$ ingot (E/2) for magnetic field applied parallel to the ingot axis; HF - high-field data, the remaining curves were recorded in the PPMS apparatus, b - magnetization curves of $CePt_3Si$ ingot (E/2) applied perpendicularly to the ingot axis $\sim$ a-axis, c - M and MR vs H curves for field applied perpendicular to the ingot axis ($\sim$ a-axis), d - comparison of the two high-field magnetization curves at 1.6 K.

Electrical resistivity of the splat-cooled $CePt_3Si$

Various investigations of the electrical resistivity of the $CePt_3Si$ were already performed. Here we present the results of the measurements obtained on the splat-cooled sample (Figure 8.37). In agreement with our expectations[9], the electrical resistivity lacks the onset of

[9]We assumed, that at least the observed change of the crystal structure and induced disorder suppresses the HFSC.

superconductivity down to 0.35 K. Instead, the relative electrical resistivity, $R/R_{20K,B}$ (Figure 8.37.a) reproduce the character observed in other splat-cooled samples. The zero-field curve shows a cusp below 2 K, which becomes suppressed under magnetic field up to 9 T.

Finally, the plot of the relative electrical resistivity of the arc-melted and splat-cooled sample is shown in the Figure 8.37.b to demonstrate the important role of disorder induced by the splat-cooling treatment. The resistivity of the 'ordered' sample exhibits almost 80 % decrease down to the SC transition, while the resistivity of the splat-cooled material varies up to 8 % only.

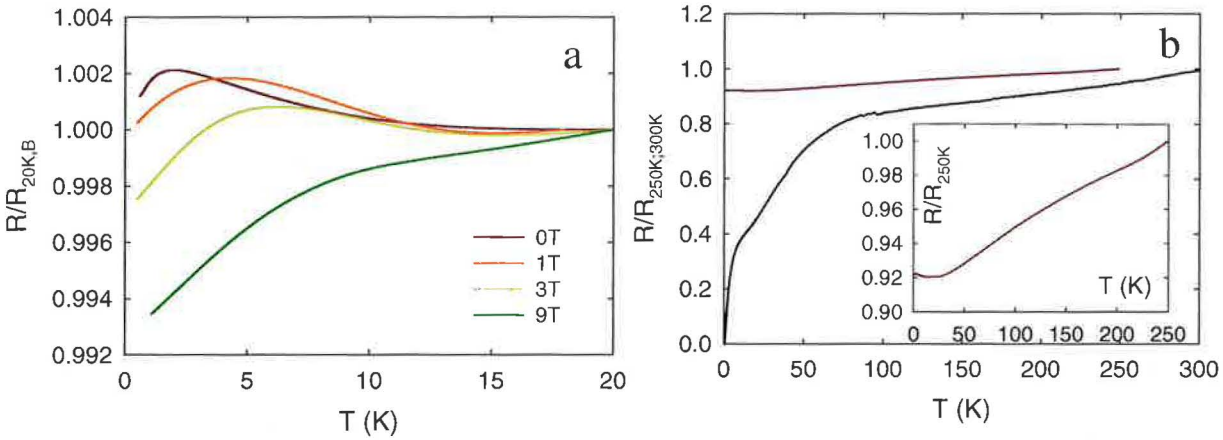

Figure 8.37: Electrical resistivity of splat-cooled $CePt_3Si$.
a - low-temperature relative electrical resistivity, $R/R_{20K,B}$ in magnetic fields up to 9 T, b - comparison of the zero-field relative resistivity, $R/R_{250K;300K}$ of the splat-cooled and grown sample B/1; the inset shows the splat-cooled sample-related curve.

Magneto-electric effect

At present there is an active search for materials displaying coupled electric and magnetic properties, so-called *magnetoelectric* materials. Of particular interest are those materials in which ferromagnetic and ferroelectric behaviors coexist. The most famous are $BiFeO_3$ and $BiMnO_3$ [558]-[560]. Recently magneto-electric effect has been observed in a metastable polymorph of iron tri-oxide (ϵ-phase)[561]. Recently, observation of the magnetoelectric effect was proposed in heavy fermion systems [313]. Because the coupling of electric and magnetic dipole is conditioned by the lack of inversion center, $CePt_3Si$ was assumed to be a good candidate to prove the hypothesis.

We investigated the temperature dependence of the capacitance in zero magnetic field and at 14 T, respectively. The zero-field results are shown in Figure 8.38. The relative capacitance (C/C_{220K}) decays rapidly in the interval 220 K to 150 K, and subsequently saturates to 80 % of its initial value. Similar behavior was observed on the capacitance loss. In addition, a broad peak at 15 K was detected on the loss vs T curve. So far, no results on capacitance measurements of heavy fermion, or even intermetallic compounds are available. Therefore, the interpretation of the observed anomaly is not clear. If we correlate it with

a kind of dissipation process, the anomaly may occur e.g. due to population of the Kondo doublet (the specific heat analysis revealed the first excited level at $\sim$ 11 K) or onset of strong electron correlations (electron *condensation*) in the system.

The 14 T data show no dramatic difference with repeat to the zero-field curve. The relative change of capacitance at 14 T is 0.2 %, which is comparable to the value observed in the ϵ-Fe_2O_3. The same result was obtained during two different experiments on two different samples, but to say finite 'yes' to the magneto-electric effect in $CePt_3Si$, further experiments are in progress.

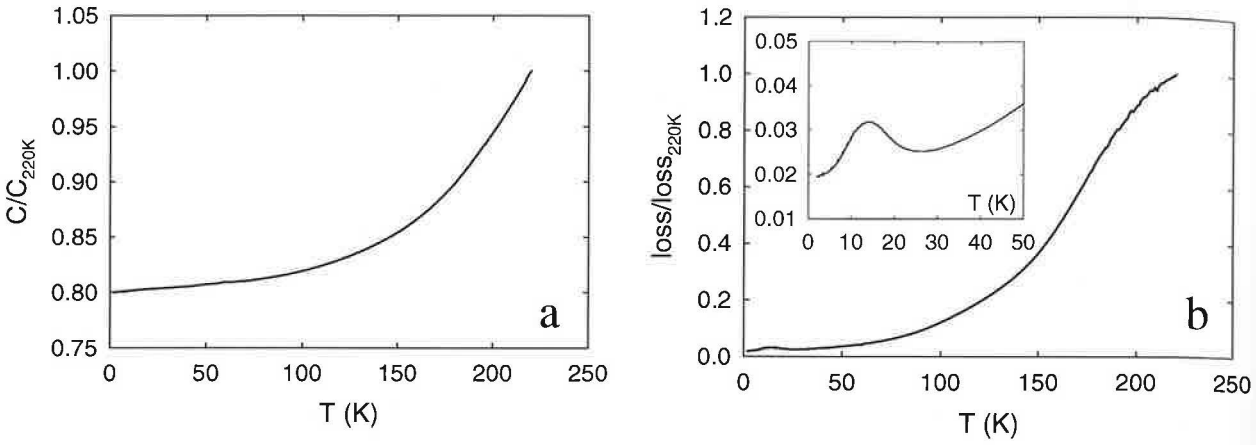

Figure 8.38: Capacitance of $CePt_3Si$.
a - temperature dependence of the relative capacitance, C/C_{220K}, b - temperature dependence of the relative loss; the inset depicts the low-temperature anomaly.

8.2 $Ce(Pt,T)_3Si/CePt_3(Si,X)$derivatives

In the following section, comprehensive results of investigations of the $CePt_3Si$ samples substituted on the Pt and Si sites, respectively, are presented.

8.2.1 T = Pd, Ru, Rh, Ir, Au, Cu

Sample preparation and characterization

The Pt element in $CePt_3Si$ was substituted by Pd, Ru, Rh, Ir, Au and Cu, respectively. The samples were gradually doped with the transition metal up to x = 0.02. Higher level of doping caused inhomogeneities in composition and formation of impurity phases as revealed by subsequent SEM investigations (Figure 8.39) and XRD measurements. The samples with the maximum obtained substitution were further investigated, their level of substitution (x) and lattice parameters are summarized in Table 8.14. Examples of the XRD patterns in comparison to results of the Rietveld analysis are depicted in Figure 8.40.

Because of different x (level of substitution), the lattice parameters of the obtained compounds were extrapolated to the maximum x = 3 and related to those of $CePt_3Si$. The results are plotted in Figure 8.41.

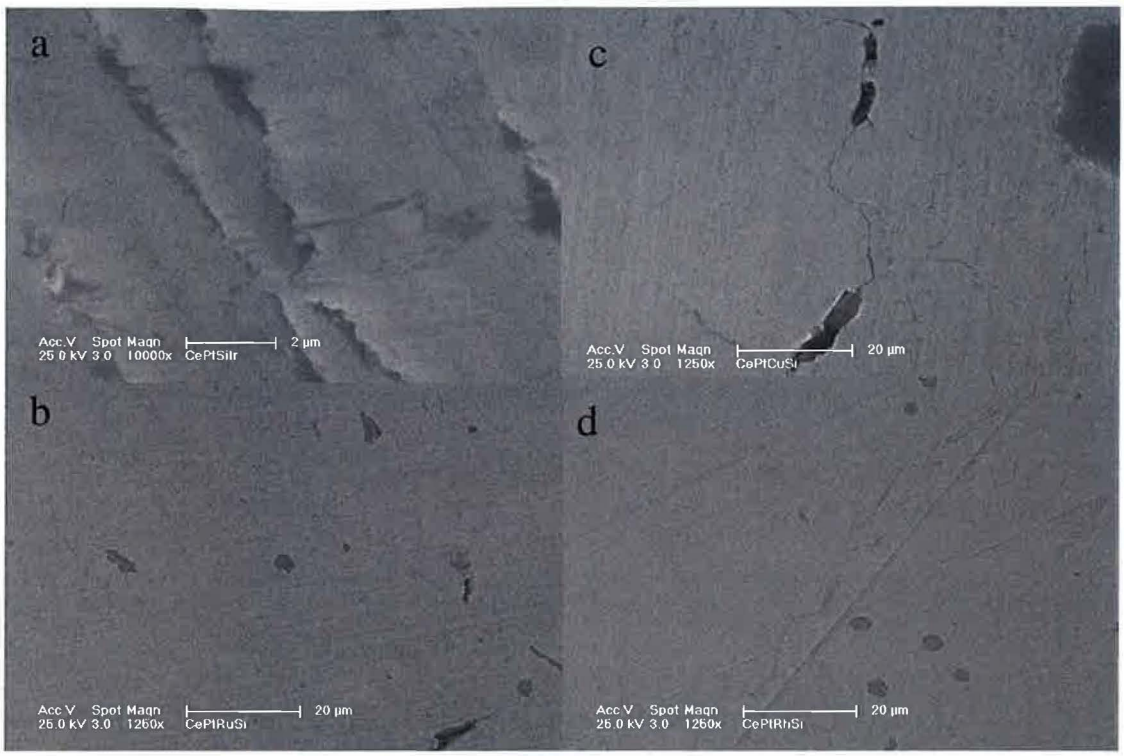

Figure 8.39: SEM micrographs of $CePt_{1-x}T_xSi$.
a - Ir, b - Ru, c - Cu, d - Rh.

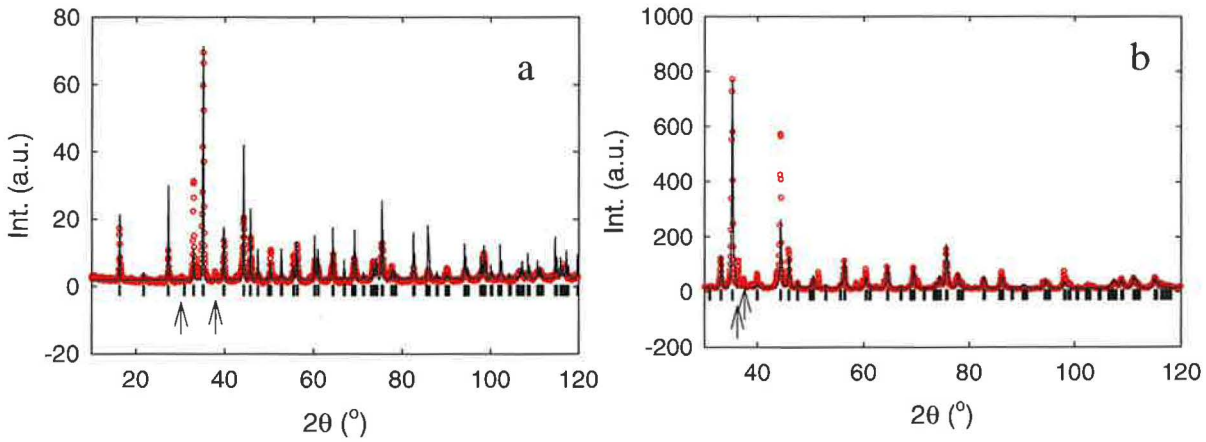

Figure 8.40: XRD patterns of the $CePt_{1-x}T_xSi$ samples.
a - Cu, b - Pd. The vertical lines correspond to the Bragg positions of the $CePt_3Si$ structure, the arrows correspond to the Bragg positions of the unknown impurity reflections.

The relative lattice parameters were compared in the context of the van der Waals radii reduced by the number of *d*-electrons (Figure 8.41.a,b)[10]. Except Au (134 pm), all elements

[10]We used the van der Waals radii rather then the metallic radii, which are tabulated for the coordination

	a (Å)	c (Å)	c/a	V (Å^3)	x in $Ce(Pt_{1-x}T_x)_3Si$
Cu	4.092	5.432	1.33	90.95	0.2
Ru	4.096	5.380	1.31	90.27	0.1
Rh	4.083	5.416	1.33	90.29	0.2
Pd	4.081	5.425	1.33	90.35	0.15
Ir	4.089	5.425	1.33	90.69	0.2
Au	4.070	5.443	1.34	90.18	0.05
Pt	4.072	5.442	1.34	90.24	-

Table 8.14: Level of substitution (x), lattice parameters (a, c) and unit cell volume of $CePt_{1-x}T_xSi$ samples.

have the van der Waals radii smaller then Pt (below 130 pm). The relative lattice parameter a is slightly enhanced and the lattice parameter c reduced in most of the compounds, the Au-substituted sample shows an opposite trend.

Inspecting the trend with respect to the standard redox potential of the elements, we observe the same behavior (Figure 8.41.c). Finally, to demonstrate the difference between the van der Waals radii and the metallic radii (both for the coordination number 12) reduced to the number of d electrons, the plot 8.41.d is included. The value of the metallic radius is not tabulated for Pd element, therefore we included the covalent radius instead.

Specific heat

In this section, we present the results of specific heat investigations performed on the samples with the maximum achieved substitution (according to the Table 8.14). We must stress out, that in spite of presence of low-temperature anomalies in the vicinity of the expected SC transition, formation of the HFSC state is not unambiguously confirmed by this measurements. Further presented electrical resistivity data suggested SC in the Au-doped sample only.

The results of the low-temperature specific heat of all investigated samples, including the $CePt_3Si$ for comparison are depicted in Figure 8.42.a. There are at least four important features, which can be observed in contrast to the heat capacity of the $CePt_3Si$:

- modification/lack of the T_N-related anomaly
- modification/lack of the T_c-related anomaly
- low-temperature upturn
- appearance of a new anomaly.

number 12. Moreover, the bond in the intermetallic compounds is not strictly of metallic character like in pure metals with fcc or hcp structures.

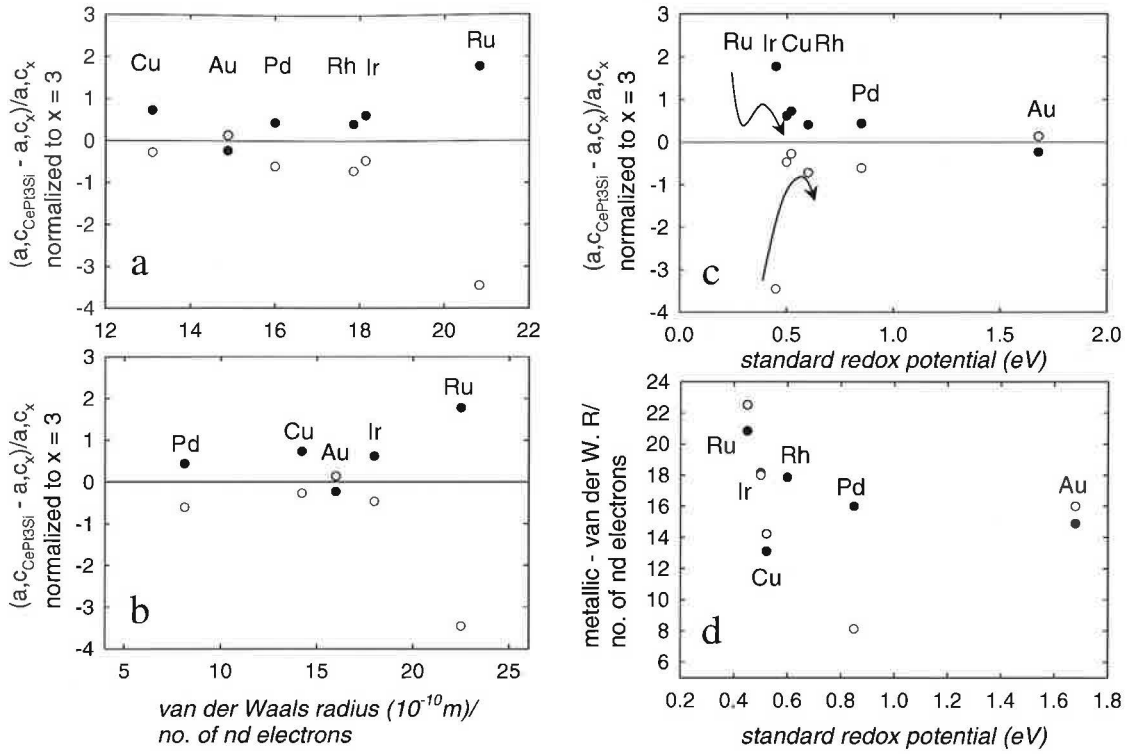

Figure 8.41: Reduced lattice parameters of $CePt_3Si$ samples substituted on the Pt site. a, b - reduced lattice parameters vs the van der Waals radii per number of d electrons, c - reduced lattice parameters vs the standard redox potential, d - metallic (black circles)/van der Waals (open circles) radii vs standard redox potential, covalent radius is used for Pd (metallic is not available).

The substituted samples can be divided into several groups according to the above-listed features.

- The C_p/T vs T data of the Ir-doped sample lack the T_c-related anomaly, the curve shows a large low-temperature upturn. The T_N-related anomaly is visible as a broad shoulder on the low-T upturn.
- The C_p/T vs T data of the Ru-doped sample lack the T_c-related anomaly, the curve shows a large low-temperature upturn resulting in a symmetric cusp at around 0.8 K. The T_N-related anomaly is visible as a broad shoulder on the low-T upturn.
- The C_p/T vs T data of the Pd and Cu-doped samples show both anomalies and no low-T upturn.
- The C_p/T vs T data of the Au-doped sample show the T_N-related anomaly accompanied by a huge low-T upturn of the C_p/T vs T data.
- The specific heat of the Rh-doped sample was measured down to 2 K only and seems to copy the behavior of the Ru or Ir-doped samples, respectively.

Evolution of the specific heat in magnetic fields is shown in the Figure 8.42 for three representatives. The Figure 8.42.b depicts the suppressio of the low-T cusp in the Ru-doped sample. A moderate influence of the 9 T-field on the low-temperature specific heat was observed in the Cu-doped sample (Figure 8.42.c). Contrary, a huge suppression of the low-T tail on the C_p/T vs T dependence of the Ir-doped sample was observed. In fact, the T_N-related anomaly appears more clearly in the 9 T-field.

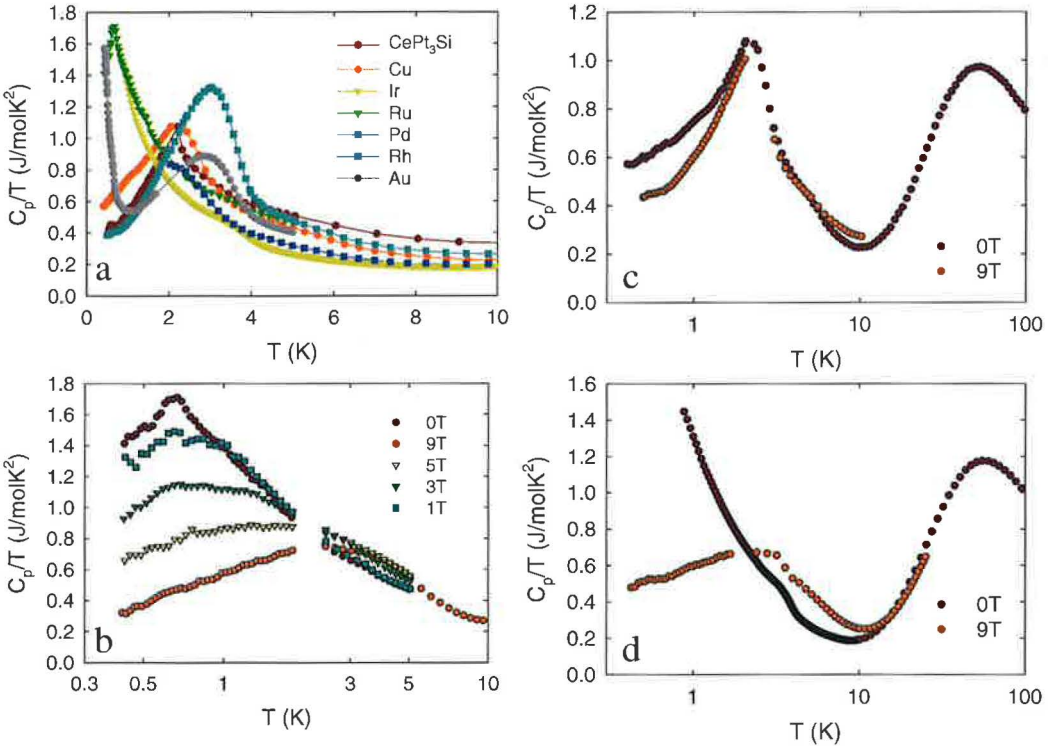

Figure 8.42: Specific heat of $CePt_{1-x}T_xSi$ samples.
a - all substitutions, b - $CePt_{2.9}Ru_{0.1}Si$, b - $CePt_{2.9}Ru_{0.1}Si$, c - $CePt_{2.8}Cu_{0.2}Si$, d - $CePt_{2.8}Ir_{0.2}Si$.

The C_p/T vs T data of the Au-doped sample are depicted in Figure 8.43. The detail of the low-temperature behavior of the specific heat in magnetic fields up to 9 T is depicted in the Figure 8.43.b. A huge logarithmic tail grows below $\sim$ 1 K in zero magnetic field, and becomes significantly suppressed at 9 T-field. The observed upturn serves as a sign of the NFL behavior. Our observations have a nice analogy to numerous studies of doped HFSC, like UPt_3 [562] or $CeCoIn_5$ [563].

The T_N-related anomaly is only moderately modified in the 9 T-field; its maximum shifts to lower temperatures and becomes slightly broaden.

The C_p/T vs T data of the Pd-doped sample together with the a.c. susceptibility data are depicted in Figure 8.44. The data show both anomalies like the $CePt_3Si$, which are just shifted to higher temperatures in case of the T_N and to lower temperatures in case of the T_c, respectively. The T_c-connected cusp is gradually suppressed in magnetic field, while the large T_N-corresponding anomaly becomes slightly narrower in the 9 T-field. In addition, a

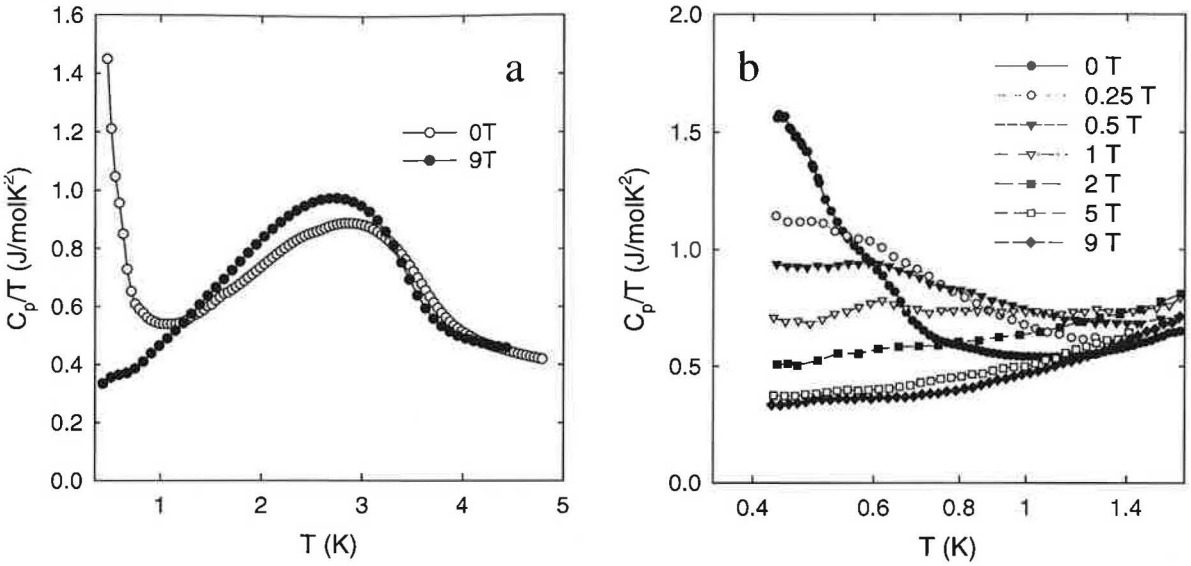

Figure 8.43: Specific heat of $CePt_{2.95}Au_{0.05}Si$.
a - specific heat in zero field and 9 T, b - evolution of the low-temperature specific heat in magnetic fields up to 9 T.

logarithmic tail appears just above the T_N up to $\sim$ 10 K suggesting presence of strong spin fluctuations.

When comparing the obtained C_p results to the measurements of the a.c. susceptibility, analogue features can be found (Figure 8.44.c,d). Besides the clear T_N-related anomaly, a broad bump above T_N was observed. It shows a substantial dependence with respect to the frequency of the applied a.c. magnetic field (not shown). We may speculate, that either the spin fluctuations show considerable dynamics or the process of magnetic ordering succeeds to an inhomogeneous magnetic state like short-range ordering or percolation of magnetic islands/clusters, similarly as in the CeNi-CeCu system [102].

Magnetization and magnetic susceptibility

The results of magnetization and susceptibility investigations of the substituted samples are depicted in Figure 8.45. They differ negligibly comparing to those of the $CePt_3Si$ compound. The magnetization curves do not show any sign of metamagnetism up to 9 T as expected from the results of the specific heat measurements. The curvature of M vs H curve of the Ir, Ru and Rh-doped samples is much pronounced then that in the Pd and Cu-substituted samples. It may be intrinsic or more probably occurs to presence of Ce^{3+}-impurities in the materials.

The results of the analysis of the susceptibility data by means of the modified Curie-Weiss law are summarized in Table 8.15. The values of the effective magnetic moment correspond well to the theoretical free-ion value. The paramagnetic Curie temperature is considerably large and negative in all investigated samples and the obtained values do not significantly deviates from the value obtained for the $CePt_3Si$. The χ_0 term does not significantly contribute to the susceptibility in the all presented cases.

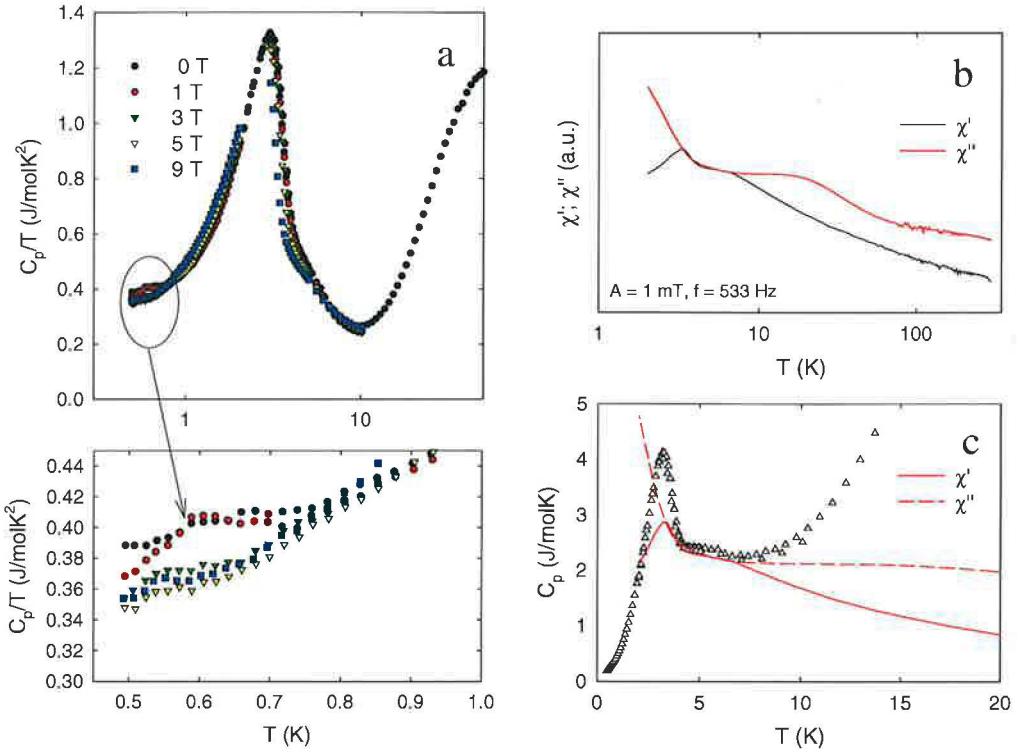

Figure 8.44: Specific heat and a.c. susceptibility of $CePt_{2.85}Pd_{0.15}Si$.
a - specific heat in zero field and 9 T, b - real (χ' and imaginary (χ") parts of the a.c. susceptibility, c - sign of spin fluctuations in the specific heat and a.c. susceptibility above T_N.

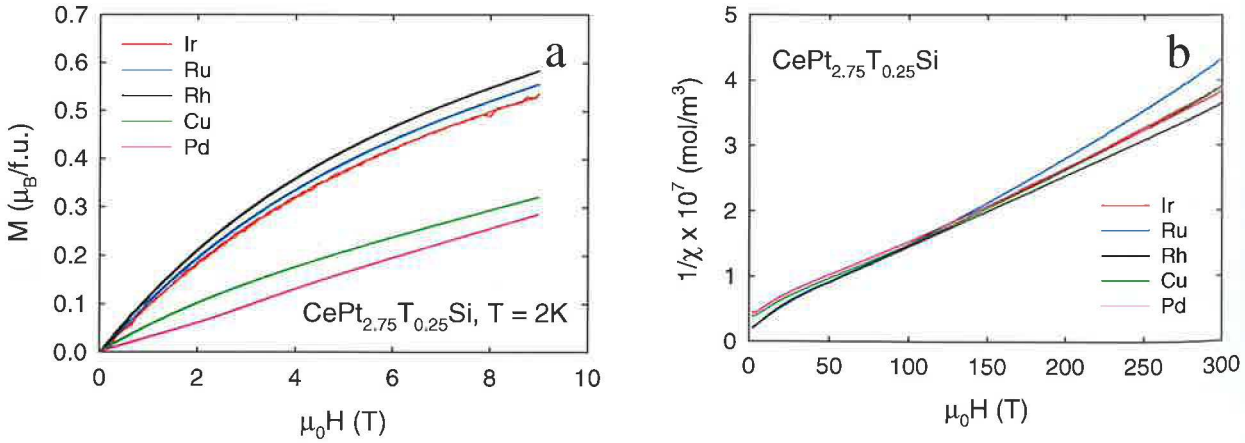

Figure 8.45: Magnetization curves at 2 K (a) and inverse magnetic susceptibility (b) of $CePt_{1-x}T_xSi$ samples.

Electrical resistivity

Measurements of the electrical resistivity served as the proof of superconductivity in the doped materials. The results are shown in Figure 8.46. It was found, that except the Au-

	μ_{eff} (μ_B)	θ_P (K)	χ_0 (m^3/mol)
Cu	2.6(3)	-50	5.6×10^{-9}
Ir	2.4(8)	-35	3.3×10^{-9}
Pd	2.5(3)	-48	3.1×10^{-9}
Rh	2.4(7)	-37	0.9×10^{-9}
Ru	2.5(1)	-34	4.5×10^{-9}

Table 8.15: Parameters obtained by the analysis of magnetic susceptibility using the modified Curie-Weiss law.
μ_{eff} - effective magnetic moment, θ_P - paramagnetic Curie temperature (the error of its determination is about 5 K), χ_0 - constant term.

doped sample, superconductivity lacks down to 0.35 K in the other cases. Unfortunately, the only sample - Pd-substituted, which revealed a clear T_c-related anomaly on the specific heat data, could not be investigated due to its degradation.

The samples can be categorized into three different groups according to their zero-field temperature dependencies of the relative electrical resistivity (Figure 8.46.a):

- superconducting samples: Au-doped,
- more then 50 % decrease of the resistivity: Cu-doped,
- up to 15 % decrease of the resistivity: Rh, Ru, Ir-doped (Figure 8.46.b).

The resistivity of the Au-substituted sample is in fact analogue to the resistivity of $CePt_3Si$. Beside the expected shift of the critical temperature, minor deviations can be found in the vicinity of the T_N and at around 100 K, where the crystal-field effects are expected.

Let's briefly discuss the effect of magnetic field on the SC state in the Au-doped material. As expected, the SC state is immediately suppressed by the external magnetic field in contrast to the critical field of $\sim$ 3 T at 0.4 K observed in the $CePt_3Si$ (Figure 8.46.d). Turning our attention to the normal-state magnetoresistance, no anomalies appears up to 9 T. We observe a moderate positive value of 4 % at 9 T-field at 3 K (Figure 8.46.c).

Similar deviations were found in the resistivity curve of the Cu-doped sample, which shows no superconductivity. The low-temperature resistivity decreases smoothly down to 0.35 K without showing any pronounced minimum.

The R/R_{300K} vs T curves of the Ru, Ir and Rh-based materials show a suppressed CF-connected feature at around 100 K. Moreover, the curvature of the low-temperature part of the resistivity (below $\sim$ 20 K) differs significantly as demonstrated in Figure 8.47 for the Ru (a) and Rh (b) substituted samples. The Ru and Rh-related zero-field R/R_{300K} vs T dependencies reveal a minimum at around 15 K. In contrast to the $CePt_3Si$, or the Cu and Au-doped sample (Figure 8.47.d), the resistivity below 20 K is considerable modified when applying external magnetic field.

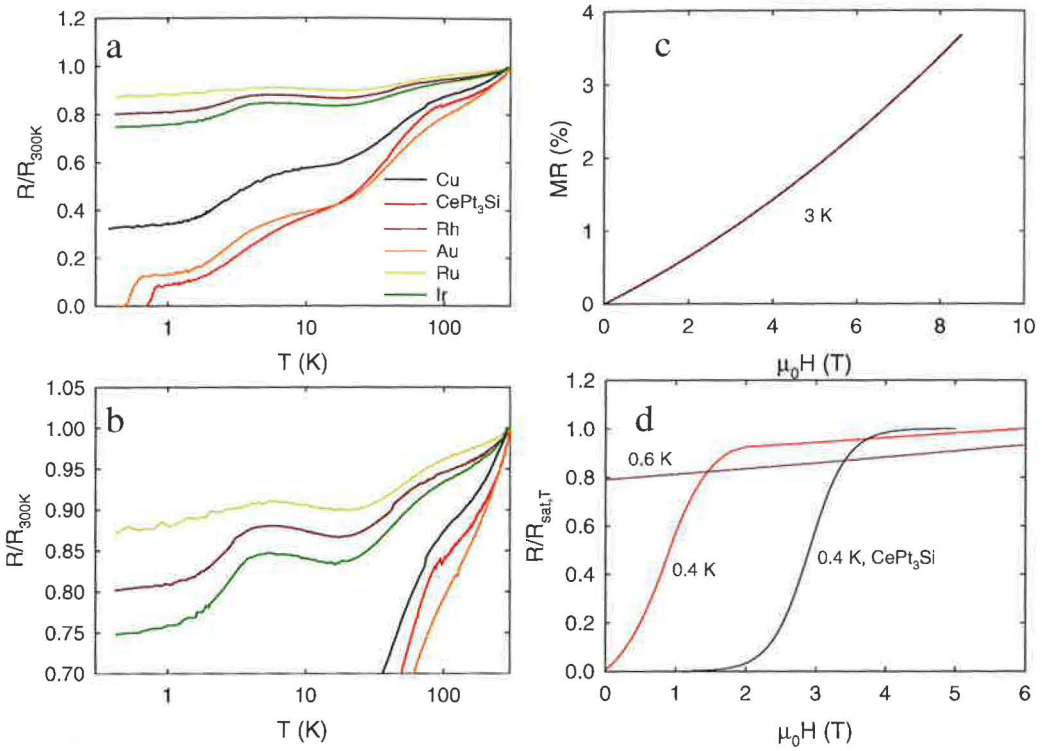

Figure 8.46: Relative electrical resistivity (R/R_{300K}) and magnetoresistance (MR) of $CePt_{1-x}T_xSi$ samples.
a - R/R_{300K} vs T of substituted samples in comparison to the $CePt_3Si$, b - detail of a, c - MR of the Au-substituted sample recorded at 3 K, d - relative change of the electrical resistivity in magnetic field in the SC region - comparison of the Au-doped sample and the $CePt_3Si$.

The reason for these observations may be the enhanced magnetic (spin-disorder scattering) contribution, which is expected to be 'more field-dependent' in contrast to the Kondo scattering mechanism. However, considering the broad character of the specific heat anomalies related to the onset of magnetic ordering, more complex mechanism involving for example percolation of the magnetically-correlated areas in the sample are more probable. Investigations by means of frequency-dependent a.c. susceptibility would be helpful to clarify the proposed mechanism.

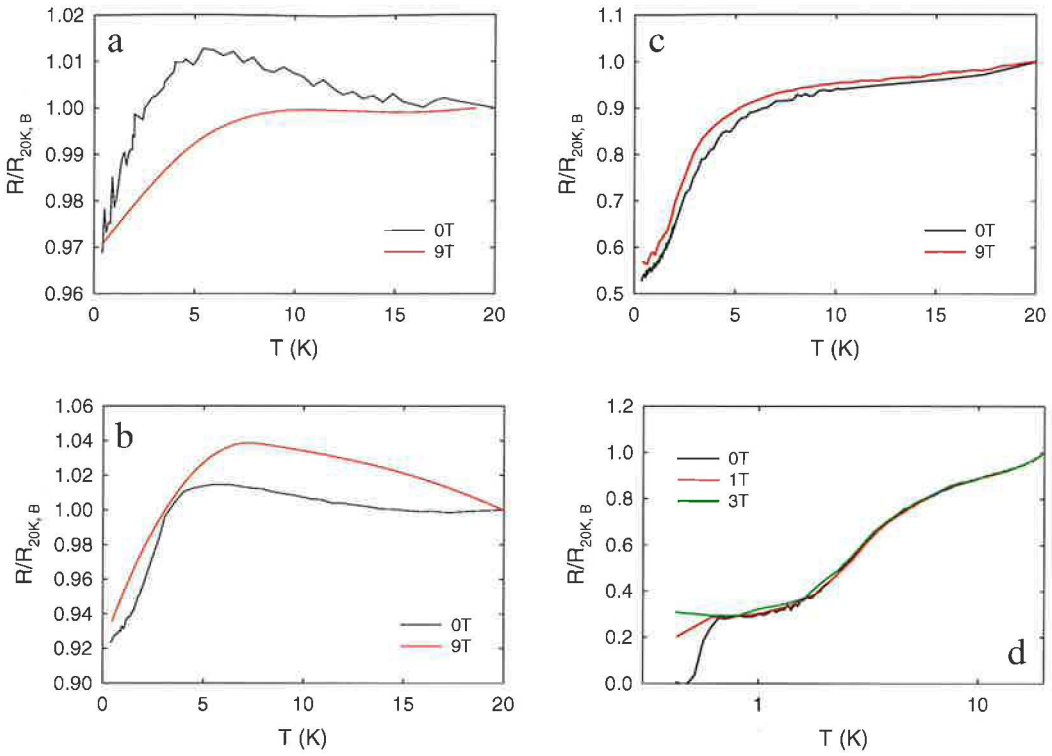

Figure 8.47: Low-temperature relative electrical resistivity ($R/R_{20K,B}$) of $CePt_{1-x}T_xSi$ samples.
a - Ru, b - Rh, c - Cu, d - Au.

8.2.2 X = C

The substitution of Si by C was already discussed in the section related to the $CePt_3C$ compound. Here we briefly discuss the most important results of the investigations of the $CePt_3Si_{1-x}C_x$ compounds, focusing mostly on the sample with x = 0.2.

Sample preparation and characterization

We have prepared a series of samples: $CePt_3Si_{1-x}X_x$ with x = 0; 0.1; 0.2; ...; 1, and investigated them by SEM and XRD. All samples appeared to be homogeneous as demonstrated by the SEM images in Figure 8.48.

The results of analysis of the XRD patterns are schematically depicted in Figure 8.49. For $x \leq 0.3$, the samples formed the $CePt_3B$-type structure with the lattice parameters decreasing with the increasing C content. For $x > 0.4$, the samples formed the structure analogues to the $CePt_3C$, where the Si atoms occupy the C positions randomly. In the intermediate region, a mixture of crystal structures was observed. However, we cannot conclude if in fact two phases of similar composition and unique structures form in the material or the composition close to x = 0.35 may exist in both structure types.

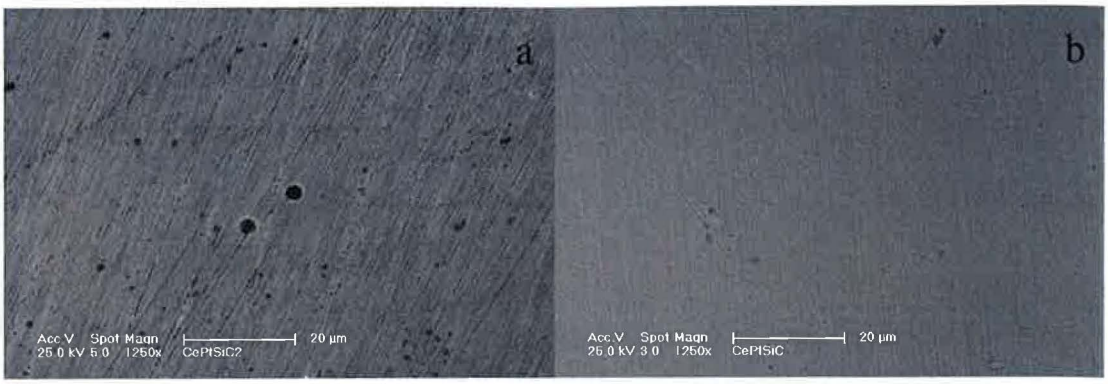

Figure 8.48: SEM micrographs of $CePt_3Si_{1-x}C_x$.
a - x = 0.2 of C, b - x = 0.5.

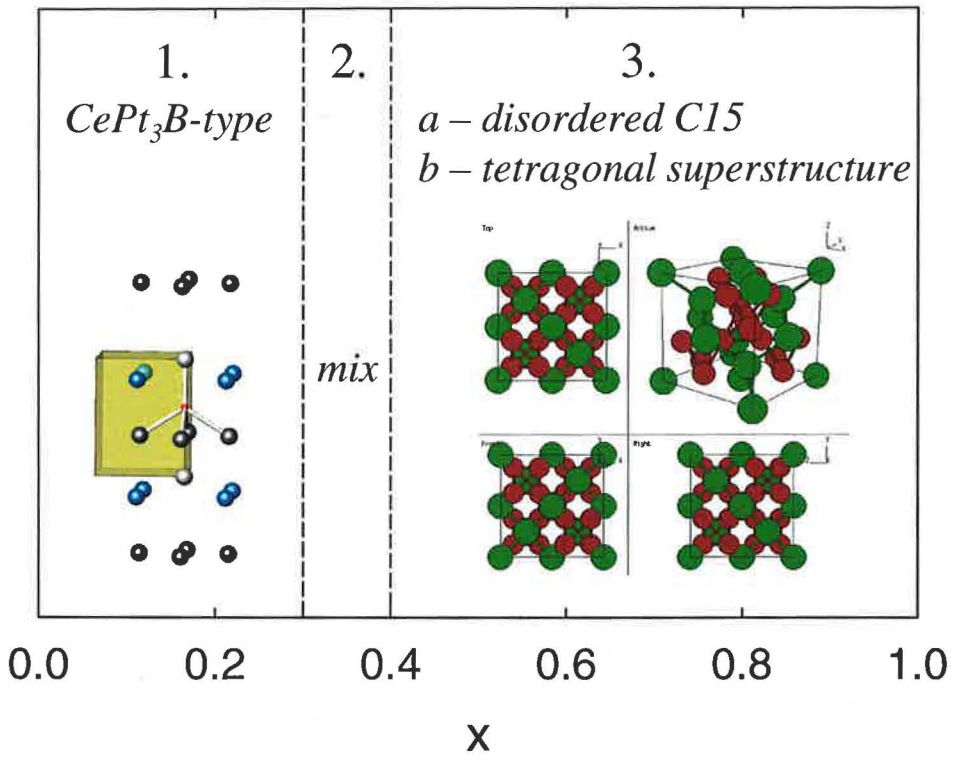

Figure 8.49: Crystal structures in the $CePt_3(Si_{1-x}C_x)$ system for x = 0 - 1.

Specific heat

Results of the specific heat measurements are shown in Figure 8.50. The low-temperature C_p/T vs T curve of the sample with x = 0.1 shows a steep upturn below $\sim$ 10 K with a sign of the T_N-related anomaly. Similarly, the C_p/T vs T dependence of the x = 0.2 sample increases below 10 K resulting in a kink around T_N. Then further grows on cooling up to 0.7 K, where a net symmetric cusp appears. The low-temperature tail is continuously suppressed by magnetic field, similarly as in the case of the $CePt_3Si$ samples doped with the transition

	γ (J/molK^2)	Θ_D (K)	Θ_{E1} (K)	n1	Θ_{E2} (K)	n2		
$CePt_3Si$	9.5	156	115	8	400	4	185	4
Δ_i (K)	5.5±1	45±3	130(2)±8	190±10				

Table 8.16: Parameters of the electronic and phonon specific heat of $CePt_3Si_{0.8}C_{0.2}$ together with the CF splitting, Δ_i, the (2)-affix symbolizes a doublet.

elements (e.g. Au) suggesting analogues interpretation of the observed phenomena.

The specific heat data were analyzed using the procedure employed in case of $CePt_3Si$, we used the parameters of $CePt_3Si$ as the input. The results of the fit of the electronic, phonon and Schottky-type contributions to the specific heat are summarized in Table 8.16 and the fitting curve in comparison to the experimental data is depicted in the Figure 8.50.c.

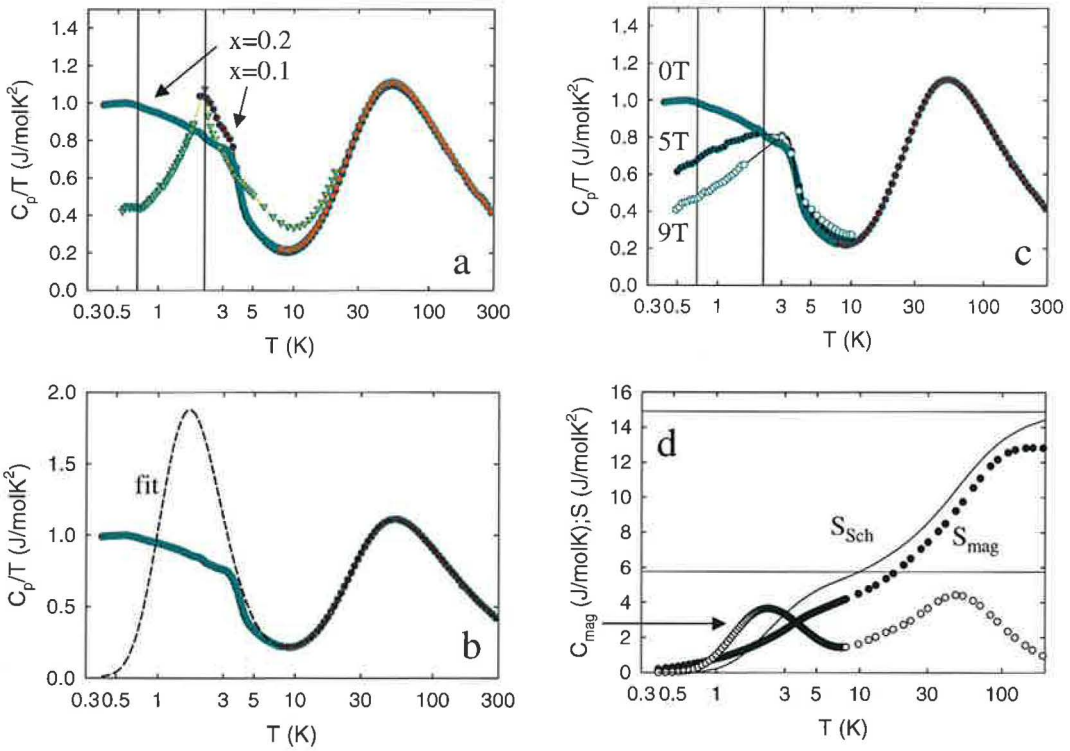

Figure 8.50: Specific heat and magnetic entropy of $CePt_3Si_{2.8}C_{0.2}$.
a - comparison of the low-temperature specific heat for x = 0.1 and 0.2, respectively, b - fit of the specific heat data, the vertical solid lines in (a) and (b) sub-figures mark the position of the T_N and T_c, respectively, c - evolution of the specific heat in magnetic fields, d - comparison of the calculated Schottky entropy (S_{Sch}) and the magnetic entropy (S_{mag}), the magnetic contribution to the specific heat is also shown, the solid horizontal lines correspond to the $R\ln 2$ and $R\ln 6$ value, respectively.

Electrical resistivity and magnetic susceptibility

Comparison of the relative electrical resistivity in the temperature range 0.35 - 300 K of $CePt_3Si_{2.8}C_{0.2}$ and $CePt_3Si$, respectively, is shown in Figure 8.51.a. Similarly as in the case of transition element-doped samples, the main features are more or less conserved, but suppressed. The T_c-related step-like transition is much smaller in comparison to the $CePt_3Si$ and shifted to lower temperatures as expected.

Influence of magnetic field on the SC state also reproduces the expected trend, described in the previous section. Superconductivity is rapidly suppressed in the external magnetic field as shown in the Figure 8.51.b - d, respectively.

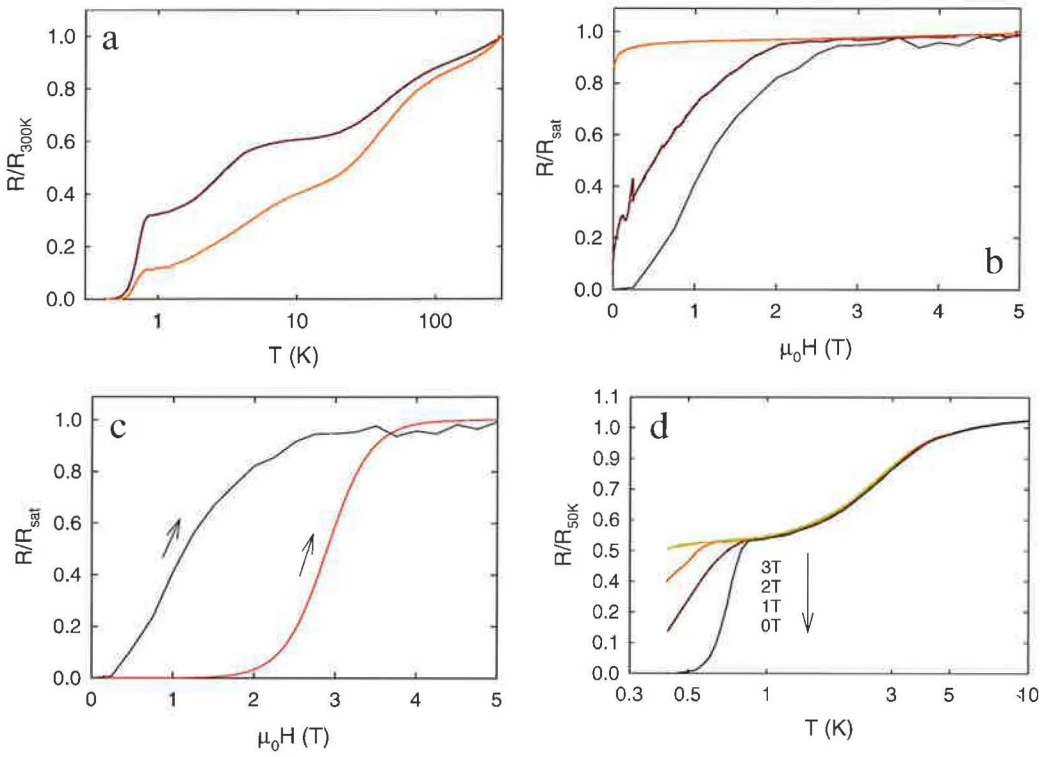

Figure 8.51: Relative electrical resistivity and magnetoresistance of $CePt_3(Si_{2.8}C_{0.2}$. a - comparison of the relative electrical resistivity of $CePt_3Si_{2.8}C_{0.2}$ to that of $CePt_3Si$, b - relative electrical resistivity in magnetic fields at 0.4 K, 0.6 K and 1 K, c - comparison of the electrical resistivity in magnetic field at 0.4 K (reduced to the 5 T value) of $CePt_3Si_{2.8}C_{0.2}$ to that of $CePt_3Si$, d - evolution of the low-temperature relative electrical resistivity in magnetic fields.

The analysis of the susceptibility data by means of the modified Curie-Weiss law yielded the effective magnetic moment of 2.38 μ_B/f.u., θ_P = -35 K and the $\chi_0 = 0.4\times10^{-9}$.

8.2.3 Comments on substitution effect in $CePt_3Si$.

The presented results demonstrated, that any substitution cause significant modification of the structure and physical behavior of the $CePt_3Si$. When introducing a p or d element into

the system, substitutions above $\sim$ x = 0.2 in $CePt_{1-x}T_xSi$ and x = 0.3 in $CePt_3Si_{1-x}C_x$, respectively, yield change of the crystal structure. The change of the crystal structure generally converts the characteristic properties of the $CePt_3Si$ to behavior of a non-magnetic Kondo ground state with possibility of magnetic correlations.

The HFSC state is suppressed in almost all $CePt_{1-x}T_xSi$ samples with x $\sim$ 0.2. When we were able to introduce a higher concentration of the d or p element (Cu, Rh, Ir, Ru, C), the SC state was suppressed and the ordering temperature (T_N) was shifted to higher temperatures.

However, we cannot simply say, that the long-range AF magnetic ordering was supported with the substitution: in almost all cases, the T_N-related anomaly becomes broader. The reason may be simply metallurgical - there are inhomogeneities in the material, or more fundamental - formation of short-range order, enhancement of the spin-fluctuations or percolative magnetic states may form above T_N. The most probable is the cooperative role of metallurgical disorder implying the disorder-induced physical phenomena.

Chapter 9

Results and discussion - $CeRu_2$ related compounds

The $CePt_3Si$ is not only exceptional because of its unconventional SC state; in addition its crystal structure (tetragonal $CePt_3B$ - type) exhibits interesting crystallo-chemical aspects as already mentioned in the Chapter 5. Because of the close values of metallic radii of Pt and Ru, a possibility of formation of the $CeRu_3Si$ phase, in analogy with the $CePt_3Si$ was investigated. The interaction of components under different synthesis conditions starting from the desired $Ce_{20}Pt_{60}Si_{20}$ composition was therefore studied. The observed phases were subsequently characterized by means of metallography, scanning electron microscopy (SEM), powder X-ray diffraction (XRD), specific heat, electrical resistivity and a.c. susceptibility measurements.

9.1 Observed Ce - Ru - Si phases - preparation and characterization

As deduced from XRD and SEM analysis, the interaction between Ce, Ru and Si in 20: 60: 20 composition leads to formation of at least two phases depending on the synthesis conditions . Summary of the observed phases is depicted in the Table 9.1. The appearance of the corresponding microstructure is presented in Figure 9.1.

The samples are heterogeneous, consisting of small crystallites ($\sim$ 1 mm) of the $CeRu_2Si_2$ off-stoichiometric variants, typically with moderate access of Ru (up to 8 atomic %). The crystallites are embedded in matrix of the majority phase (phase 1.), which can be described with the summary formula: $Ce_{35}Pt_{58}Si_7$. In addition, the annealed samples contain a minority fraction of precipitated Ru (phase 3.).

In general the tendency to form three phases due to Ru segregation increases with increasing annealing time and becomes suppressed with quenching. The homogeneity range of precipitated Ru does not extend much to the ternary area, only less then 2 at. % of both the Ce and Si were detected in the Ru-phase, which may arise from the signal of neighboring Ce and Si containing phases.

The long-term melted sample contained 2 phases, described in summary as: $Ce_{23}Ru_{69}Si_{10}$ and $Ce_{17}Ru_{78}Si_5$. The former can be treated as $CeRu_3$ with a negligible excess of Si, while

Sample	Si:Ru:Ce	Conditions	No. of phases
S1	20 : 60 : 20	ann./slow/21 d./1225 K	3
S2	20 : 60 : 20	ann./slow/10 d./1125 K	3
S3	20 : 60 : 20	ann./quench/21 d./1225 K	3
S4	20 : 60 : 20	ann./quench/10 d./1125 K	2
S5	20 : 60 : 20	as cast	2
S6	9 : 57 : 34	as cast	2
S7	9 : 57 : 34	ann./slow/10 d./1125 K	2
S8	9 : 57 : 34	ann./quench/10 d./1125 K	2

Table 9.1: Initial composition of the samples (in at. %), synthesis conditions and number of the observed phases.

Sample	1. Si : Ru : Ce	2. Si : Ru : Ce	3. Si : Ru : Ce	relative content 1:2:3 (%)
S1	9 : 57 : 34	36 : 46 : 18	2 : 97 : 1	40 : 55 : 5
S2	10 : 56 : 34	35 : 46 : 19	1 : 99 : 0	50 : 48 : 2
S3	6 : 55 : 39	37 : 46 : 17	1 : 98 : 1	60 : 38 : 2
S4	7 : 54 : 39	38 : 42 : 20	-	70 : 30
S5	11 : 56 : 33	35 : 49 : 16	-	75 : 25
S6	7 : 58 : 35	0 : 41 : 59	-	97 : 3
S7	7 : 57 : 36	0 : 41 : 59	-	99 : 1
S8	8 : 55 : 37	0 : 40 : 60	-	99 : 1

Table 9.2: Composition of the observed phases in at. %.

Space group	$Fd\bar{3}m$
Cell parameter (Å)	$a = 7.5097(6)$
Volume (Å^3)	423.52(4)
Fraction coordinates (x y z)	
Si, Ru: (0.625 0.625 0.625)	Ce: (0 0 0)
Number of reflections	52
Number of refined parameters	15
Zero point, 2θ	0.023
Asymmetry parameters	-0.019; 0.056
Half-width parameters	
U	0.0421
V	-0.0903
W	0.2560
Rietveld reliability factors (%)	
R_P	10.1
R_WP	11.6
χ^2	2.5
R_B	7.68
R_F	5.97

Table 9.3: Parameters of structural refinements of the $Ce_{35}Pt_{58}Si_7$ sample (S6).

the latter can be described as $CeRu_{5-x}Si_x$ with x = 0.3, respectively, as corroborated by XRD pattern.

Against conjecture no phase of 20 : 60 : 20 composition was finally observed. This result may be still a bit unexpected when taking into account the analogy with the Ce - Pt - Si phase diagram. The noncentrosymmetric crystal structure of $CePt_3B$-type is formed both in the Si and B case, although the ratio between their atomic radii, R is considerably large $R_B/R_{Si} \sim 0.74$. On the other hand, the atomic radii of Ru and Pt are very close ($R_{Ru}/R_{Pt} \sim 0.96$) and there are many examples in the literature of isostructural compounds formation [553]-[555]. On the other hand, the notoriously known 20: 40: 40 composition does not exist in the identical crystal structure for the Ce - T - Si (T = Ru, Pt), respectively [556].

The analysis of the powder XRD data confirmed the SEM observations. The novel $Ce_{35}Ru_{58}Si_7$ phase can be described by the cubic structure of the $Fd\bar{3}m$ space group. The results of the Rietveld analysis of the sample S6 is shown in the Table 9.3. The lattice parameter a refined from the XRD data varies up to 2% only within the S1 - S8 series.

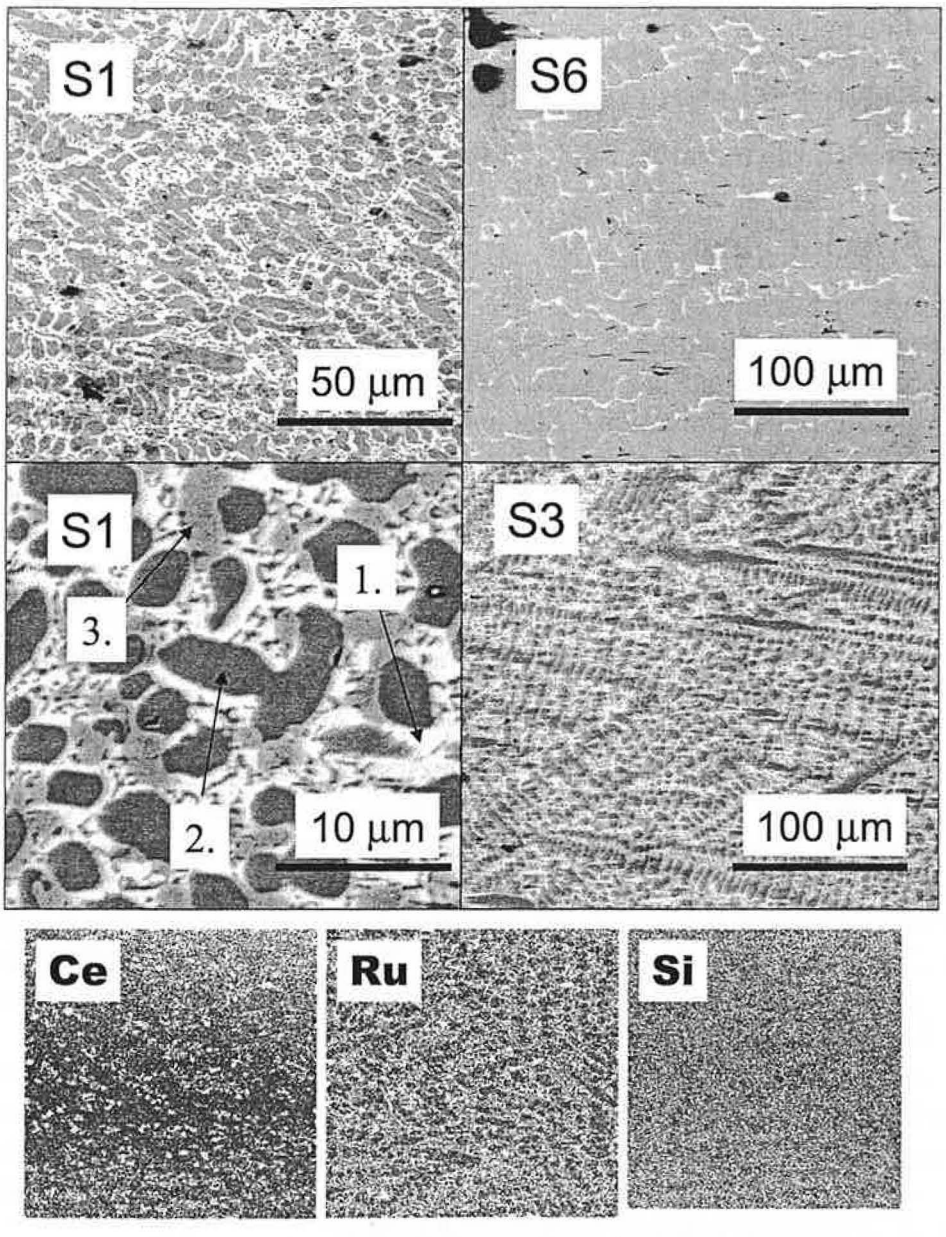

Figure 9.1: SEM micrographs and density maps of the Ce - Ru - Si samples.
As examples, the micrographs of the samples S1, S6 and S3 are shown. The composition of the phases labelled as 1., 2. and 3., respectively, is defined in the text. The bottom figures correspond to the element-density maps of Ce, Ru and Si in the sample S1.

9.2 Macroscopic investigations

Physical behavior of the investigated samples is mainly influenced by their microstructure and the ratio of the present phases. To keep the discussion comprehensible, two groups of the studied compounds will be presented separately:

- Si-derivatives of $CeRu_2$,
- phases with the initial 20 : 60 : 20 composition.

9.2.1 Specific heat

Si-derivatives of $CeRu_2$

The temperature dependence of the specific heat shows a single anomaly of λ-type at around 3 K as depicted in Figure 9.2.a. With respect to other results, it is attributed to the superconducting phase transition. The anomaly is continuously suppressed when applying the magnetic field (Figure 9.2.c), consistently with electrical resistivity and a.c. susceptibility observations as shown further.

Phases with the initial 20 : 60 : 20 composition

The low-temperature specific heat of the samples containing at least two phases with characteristic properties is shown in the Figure 9.2.b. The 3 K-anomaly occurs due to the superconducting $CeRu_2$-related phase, as corroborated by the electrical resistivity measurements (Figure 9.2.d).

The huge peak at $\sim$ 6 K has rather speculative origin. A simple interpretation is a presence of Ce-oxide in the sample. Because of its huge effect due to antiferromagnetic ordering at 6 K, even a small amount of the oxide considerably influences the specific heat data. In order to confirm the hypothesis, the contribution of the Ce-oxide was subtracted from the original data using the values presented in the reference [564].

After the performed subtracting procedure, an additional broad effect remains left on the C_p/T vs T curve as shown in the Figure 9.2.b. It might be present either due to inaccuracy in the subtraction or due to intrinsic phenomena. The idea to attribute the 6 K-anomaly to the Ce-oxide seems to be not satisfying for the explanation.

A second possible interpretation arises from the intrinsic behavior of the slightly off-stoichiometric $CeRu_2Si_2$ phase. We take into account its sensitivity to substitutions, the role of the observed off-stoichiometry, and in addition the almost nano-size of the grains in the samples. All the mentioned factors may drive the system into e.g. antiferromagnetic state, however, these speculations will be discussed further.

Influence of external magnetic field and caloric effects in the SC state

The character of the superconducting state in the investigated samples considering the specific heat measurements will be discussed. Detailed measurements up to 9 T-magnetic field are depicted in Figure 9.3.a. A pronounced decrease in the C_p/T under applied field suggests either structure in the electron density of states near the Fermi level or structure in the low-phonon density of state. Similar behavior was observed in the $CeRu_2$.

The fit of the γ coefficient in the SC state yielded $\gamma = 9$ mJ/molK^2 in comparison to the normal-state value of 20.3 mJ/molK^2. Both presented values are considerably reduced in comparison to the $CeRu_2$. The magnitude of C_p jump at the T_c does not correspond to

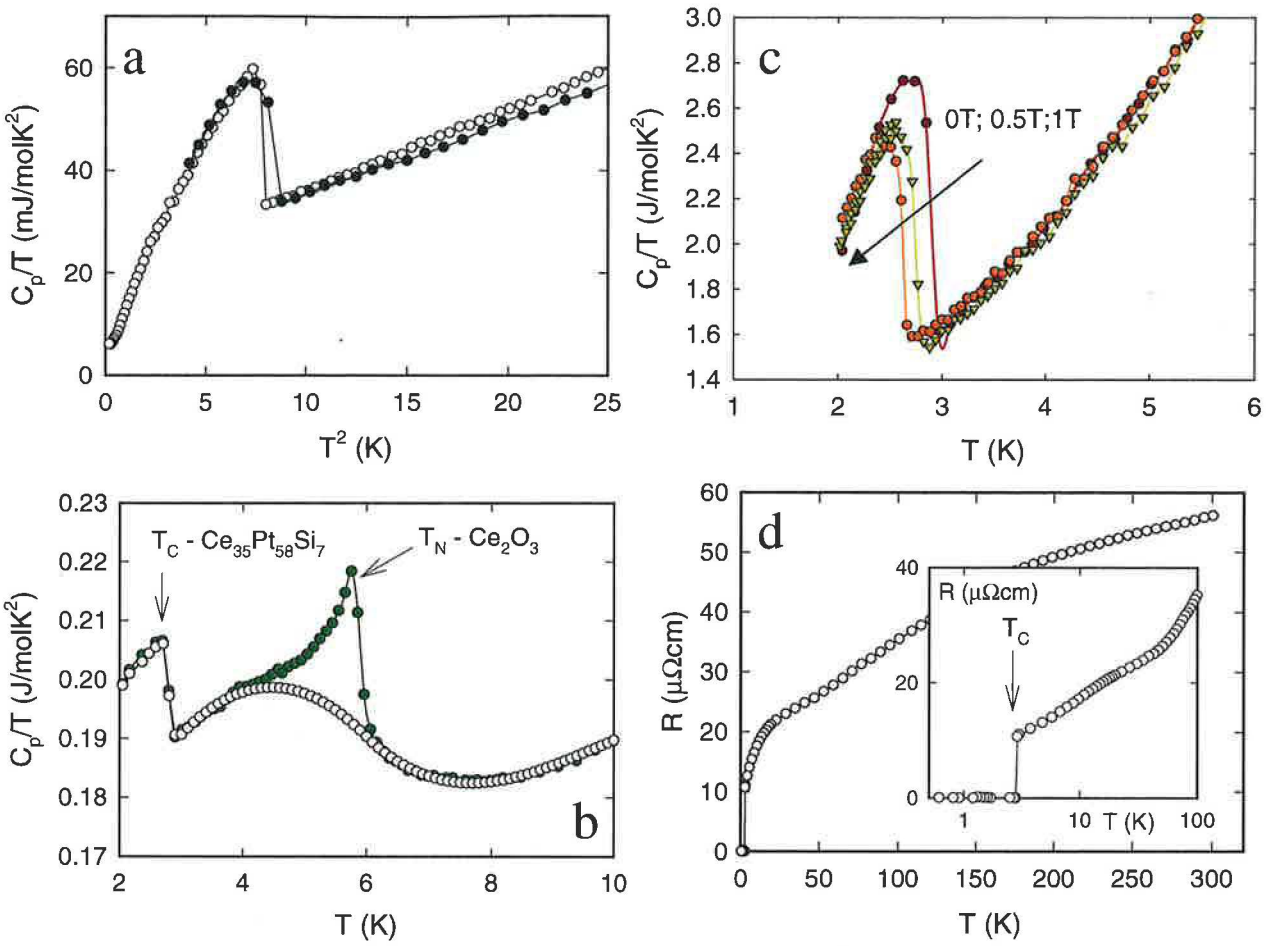

Figure 9.2: Specific heat, C_p of the Ce - Ru - Si phases.
a - sample S6 (black circles) and S8 (open circles), b - sample S6, c - C_p in magnetic fields up to 1 T of the sample S6, d - electrical resistivity of the sample S1, the inset depicts the onset of SC below $\sim$ 3 K.

the value expected from the BCS theory, similarly as in the $CeRu_2$. The evolution of ΔC_p at the T_c in magnetic field is shown in Figure 9.3.b. The d decrease of T_c under magnetic field is depicted in Figure 9.3.c suggesting the $H_{C2,0}$ value of about 8.35 T.

Comparison of the temperature dependence of the entropy in zero-field and in 9 T-field, respectively, is shown in the Figure 9.3.d. In contrast to the $CeRu_2$, which revealed both dependencies to be identical, we observe a decrease of the entropy in the superconducting state. The estimated magneto-caloric effects by means of the isothermal entropy change and the adiabatic temperature change are shown in Figure 9.3.e and 9.3.f, respectively.

The low-temperature specific heat was further analyzed using the procedure described in [553] including the fit of the sum of a linear and an exponential dependence to the specific heat data. We have obtained: $C_p = A\exp(-B/T)$, $A = 145\gamma T_C$, $B = 0.16T_C$. Considering the slightly enhanced parameter f defined as $\Delta C_p/\gamma T_C$ ($f = 2.46$ in our compound vs $f = 2$ in $CeRu_2$), we may expect moderate enhancement of the strong coupling in the Si-modified

$CeRu_2$.

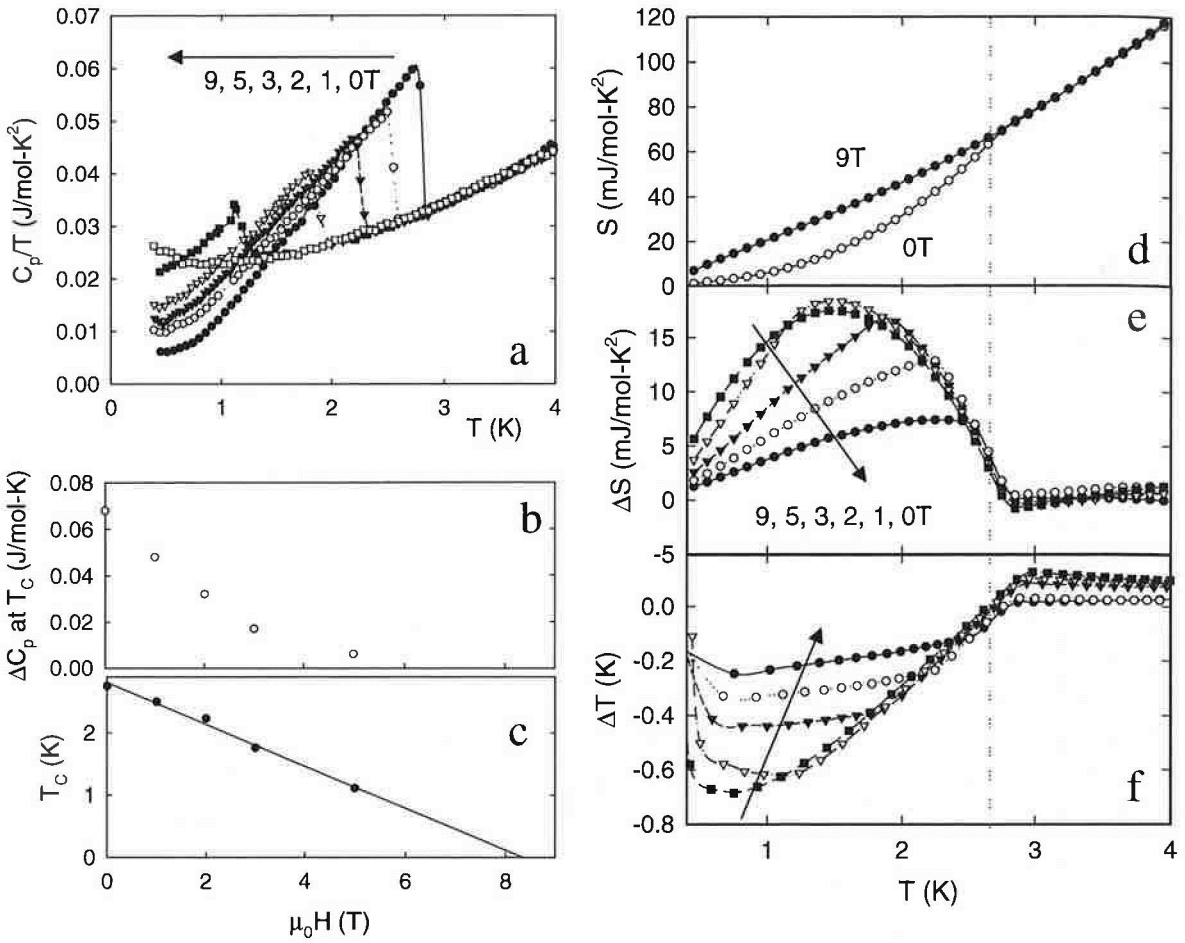

Figure 9.3: Specific heat, C_p and caloric effects in the sample S7.
a - C_p in magnetic fields, b - evolution of the jump on the C_p (ΔC_p) in magnetic field, c - evolution of the critical temperature T_c in magnetic field, d - entropy, S at zero field and 9 T, e - isothermal entropy change, ΔS up to 9 T, adiabatic temperature change, ΔT up to 9 T.

9.2.2 Magnetization and a.c. susceptibility

The most controversial feature reported in $CeRu_2$ is its coexistence of static magnetic state of ferromagnetic nature and superconductivity below $\sim$ 6 K. In addition, a cross-over in the reversible and irreversible behavior accompanied by a peak effect at $\sim$ 1.5 T is reported. In our Si-containing samples, both manifestations of the $CeRu_2$ exoticism vanish.

The magnetization isotherms near T_c are presented in Figure 9.4.a. First, the peak effect-related feature undoubtedly lacks. Second, the expected cross-over from the irreversible to the reversible region was not observed, the irreversibility persists up to the T_c as manifested by a hysteresis loop recorded just below the T_c, depicted in Figure 9.4.b. The net remnant

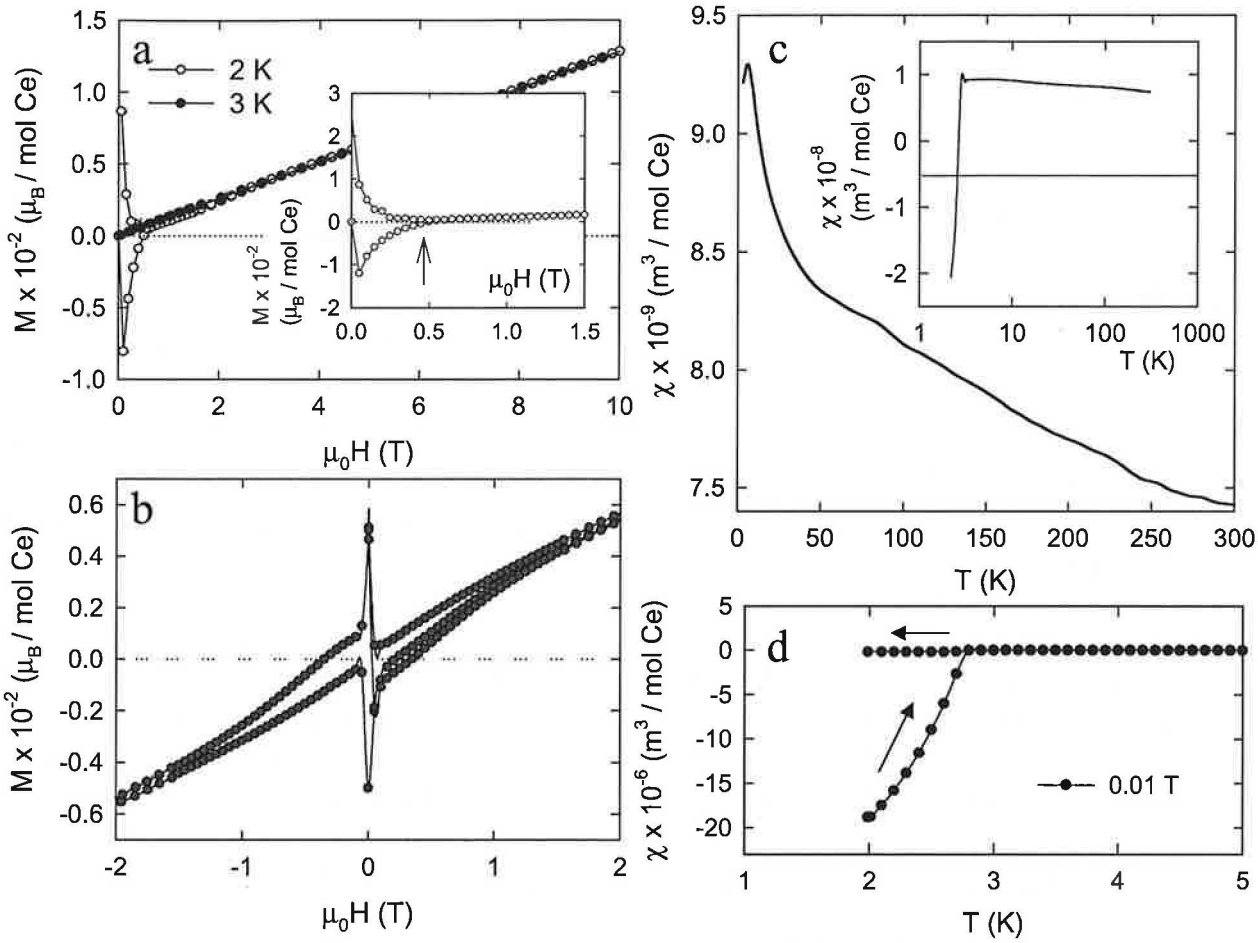

Figure 9.4: Magnetization and a.c. susceptibility of the Ce - Ru - Si samples.
a - S6: magnetization isotherm at 2 K and 3 K, respectively, the inset shows the low-field detail of the 2.5 K curve, the arrow marks the H_{c2} value, b - magnetization hysteresis curve at 2 K, c - temperature dependence of the static magnetic susceptibility at 4 T, the inset shows the 0.01 T curve, d - ZFC and FC dependencies of the static magnetic susceptibility, the arrows correspond to the increasing (ZFC) /decreasing (FC) temperature, respectively, during the measurement.

magnetization is more disputable rather than serving a proof of the small-moment ferromagnetism coexisting with the SC state. Moreover, it vanishes just above the T_c. As the ferromagnetic state in $CeRu_2$ should nucleate far above the SC region, our results suggest rather lack of ferromagnetism in the Si-modified compounds.

The static magnetic susceptibility measured at 4 T of the sample with the 20 : 60 : 20 composition is shown in Figure 9.4.c. It shows a pronounced increase on cooling resulting in a sharp maximum just before an abrupt decay due to the transition into the SC state (inset of the Figure 9.4.c). The origin of the maximum is unclear. It may be connected with the speculative AF ordering of the $CeRu_2Si_2$ phase or represent an intrinsic property

of the $CeRu_2$-related Si-modified phase. It is worth mentioning that the maximum is much enhanced with the increasing magnetic field, which would rather support the a conclusion about onset of antiferromagnetism in the mixed Ce - Ru - Si system.

The SC state was in addition evidenced by the a.c. susceptibility measurements (not shown) and investigations of the thermal hysteresis as depicted in Figure 9.4.d. The temperature dependence of the zero-field cooled and field cooled magnetization, respectively, corroborates the irreversible character of the SC revealed by the hysteresis loops measurements up to the upper critical field (H_{c2}).

Occurrence of ferromagnetism in $Ce(Ru,Si)_2$ phases and namely $CeRu_2$ itself seems to be almost fictive. The muon spectroscopy investigations suggested condensation of a static magnetic state below $\sim$ 40 K in $CeRu_2$ and the authors correlated those observations to the results of the a.c. susceptibility measurements. However, we observed no clear sign of ferromagnetism in our samples in spite of analogue behavior of the magnetic susceptibility reported for $CeRu_2$. Moreover, the a.c. magnetic susceptibility of all annealed samples (prepared from the SSE-purified Ce metal) shows much suppressed or even none enhancement of susceptibility at the critical region around 40 K.

It is really worth mentioning, that the influence of the annealing is independent of their initial composition, it means the same effect was observed in the single- or multiple-phase materials. It implies, that the relevant synthesis procedure including annealing ensures much better homogeneity and purity of the samples resulting in common behavior of the magnetic susceptibility at low temperatures. Nevertheless, the phenomenon of ferromagnetism in $CeRu_2$ can not be strictly controverted considering our speculations.

9.2.3 Electrical resistivity

Phases with the initial 20 : 60 : 20 composition

The characteristic behavior of the electrical resistivity with respect to temperature is almost identical for the S1 - S3 samples; only the absolute values vary within 20 %. The temperature dependence of the electrical resistivity, $R(T)$ shows almost a linear slope starting at the room temperature down to 20 K with a moderate change of slope at around 150 K. At the low temperature region, the $R(T)$ curve exhibits a broad knee at 20 K followed by an abrupt jump of resistivity to zero value due to entering the superconducting state at $T_c \sim 3$ K.

When plotting the $R(T)$ curve against logarithm of T, we observe linear behavior of resistivity from above the T_c up to 20 K suggesting non-Fermi-liquid (NFL) type correlations or spin fluctuations appear in the system. The effect probably originats the $CeRu_2Si_2$-type phase, which exhibits strong AF spin fluctuations below 10 K resulting in a NFL behavior.

Under applied magnetic field, the superconducting state is obviously suppressed in fields above 6 T at ultralow temperatures ($T = 0.4$ K) and 0.6 T at $T = T_c$, respectively, in all three samples. The superposition of the phase 1(SC $CeRu_2$-related variant) and phase 2 ($CeRu_2Si_2$-type) contributions to the entire electrical transport (neglecting the minority phase 3 (Ru-precipitates) effect) can be estimated considering the phase layout in the bulk sample. The low-T superconducting phase 1 forms a 3D-network guaranteeing percolation of the electrical current when passing through the sample. The phase 2 accommodates spherical/ellipsoidal cavities within the phase 1 arrangement. The unique net-like micro-

assembly suggests dominant contribution of the phase 1 to the electrical resistivity yielding almost intact traits of superconductivity below T_c. The temperature dependencies show almost no influence of the coexisting phases on the superconducting behavior in contrast to the a.c. susceptibility data as shown previously.

Superconducting $CeRu_2$-related phases

The temperature dependence of the electrical resistivity of the as cast and annealed samples, S6 and S7, respectively, shows no unexpected feature. It is almost linear in the range 50 - 100 K and the low-temperature T^3 dependence turns into a rapid drop-off at the $T_c \sim 3$ K.

Contrary, the sample S8 (quenched after annealing procedure) exhibits diametrically different behavior. The temperature dependence of the relative electrical resistivity is shown in Figure 9.5.a. It shows a $T^{1/2}$-dependence above 125 K and a negative linear trend in the range 6 - 125 K. The observed behavior corresponds to that of the metallic glasses [557] and can be interpreted as an increase in the strength of electron-phonon interaction under increasing disorder and mass density due to rapid quenching. The negative linear term, ($\sim T < \theta_D$) and the -$T^{1/2}$ behavior ($\sim T > \theta_D$), respectively, occurs due to weak localization effects. Simultaneously, a minimum should be observed in the resistivity curve. Because the data were recorded up to 200 K only that is in the range of θ_D in this compound, the expected resistivity minimum was not observed.

The low-temperature part (0.4 - 6 K) exhibits a characteristic downturn (Figure 9.5.b), probably it is a manifestation of the SC state shielded by the dominant transport pathway in the material.

The R/R_{200K} vs. T dependence in the magnetic field is shown in the Figure 9.5.c. The resistivity above $\sim$ 10 K is not much influenced by the magnetic field. The low-temperature data reflect considerable suppression of the proposed SC state. The observed phenomena corroborate the interplay between the weak-localization mechanism above $\sim$ 10 K and the 'shielded' superconductivity at low temperatures.

The magnetoresistance recorded at 2 K is shown in the Figure 9.5.d. It positive and shows a cubic dependence in H up to 5 T.

9.2.4 Evidence of antiferromagnetic ordering in nano-sized $CeRu_2Si_2$ - a controversy

Our investigations of the samples with nominal Ce : Ru : Si composition of 20 : 60 : 20 revealed a challenging result - possibility of antiferromagnetism induced in the $CeRu_2Si_2$ phase coexisting with the superconducting $Ce(Ru,Si)_2$ phase. The a.c. susceptibility together with the specific heat is presented in Figure 9.6. Besides the anomaly at 3 K related to the SC phase, additional feature appears at around 6 K. As already mentioned in the discussion of our specific heat results, interpretation by means of a contribution of the Ce-oxide is not satisfactory.

We further considered the role of the grain-size and inhomogeneity in $CeRu_2Si_2$ composition. It is generally known that the $CeRu_2Si_2$ phase is archetypal heavy fermion compound, which can be driven to the antiferromagnetic ordering by various substitutions (as mentioned in the Chapter 6). The substitutions causes change of the electronic structure but

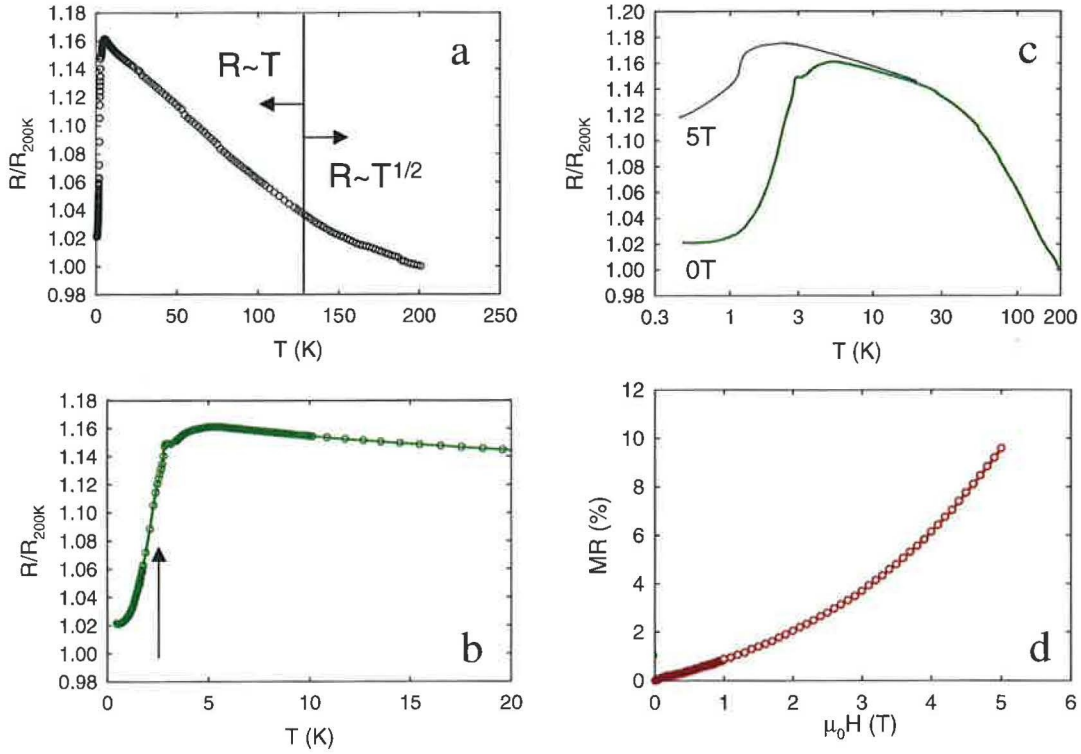

Figure 9.5: Electrical resistivity, R and magnetoresistance, MR of the sample S8. a - relative resistivity R/R_{200K}, b - low-temperature part of the R/R_{200K} dependence, the arrow marks the T_c determined from the a.c. susceptibility, c - comparison of the R/R_{200K} dependence at 0 T and 5 T, respectively, d - magnetoresistance, MR at 2 K.

also induce disorder in the system. Up to date it is not straightforward, what is the pivotal mechanism pushing the Ce ion into the magnetically-ordered state. It is therefore possible, that the reduction of dimensions by means of the submicron grain size induces analogical phenomena, or at least serve as a cooperative factor beside the disorder introduced by the off-stoichiometry.

However, our speculations must be certainly probed on microscopic scale and using nano-scale samples prepared by different experimental techniques.

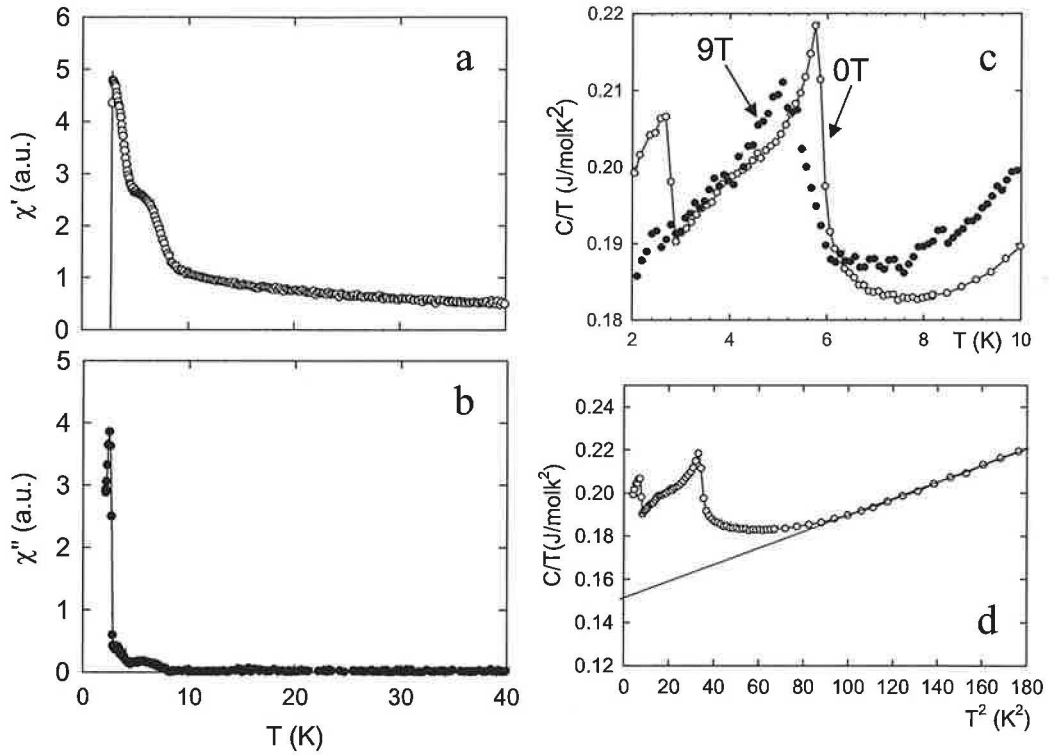

Figure 9.6: A.c. susceptibility and specific heat of sample S1.
a - real part of the a.c. susceptibility, χ', b - imaginary part of the a.c. susceptibility, χ" c - comparison of the specific heat at 0 T and 9 T, respectively, d - fit of the electronic contribution to the specific heat yielding $\gamma \sim 150$ mJ/molK^2.

Sample	T_C(K)/AC	T_C(K)/C_p	T_C(K)/R	additional anomalies
S1	2.85	2.80	2.83	5.80
S2	2.70	2.78	-	6.00
S3	2.68	2.65	-	5.72
S4	2.72	2.76	-	5.90
S5	2.73	2.75	2.73	2.90
S6	2.25	2.52	-	2.90
S7	2.78	2.88	-	2.90
S8	2.83	2.91	2.90	2.90

Table 9.4: Values of the critical temperature, T_c for all Ce - Ru - Si samples.

Chapter 10

Summary and conclusions

We have studied the general impurity and disorder phenomena in the context of the the physics of rare-earth metallic systems. It has been treated by means of the following perspectives:

- Super-purification of rare-earth elements
- Role of the Ce^{3+} ion as the Kondo impurity
- Perturbed coexistence of magnetism and unconventional superconductivity in heavy fermion Ce-based superconductors
- Electronic properties of systems with reduced dimensions and/or induced disorder

The problem of the commercial level of purity in rare earths used for sample preparation was solved using the unique solid-state electrotransport (SSE) procedure. The prototype of the SSE apparatus was designed, constructed and tested. Three rare earth elements: Ce, Tb and Er, respectively, were purified by the SSE method. The influence of the SSE purification on their structure and physical properties was investigated in detail by various experimental techniques. The most significant was the dramatic decrease of the residual resistivity ratio in the super-purified samples. The Ce metal purified by the SSE method was further used in synthesis of the samples studied in the scope of the thesis.

Numerous samples of Ce-based intermetallic compounds were prepared, additionally thermally-treated and studied thoroughly. In fact the two groups of materials were studied, those derived from the $CePt_3Si$ and $CeRu_2$, respectively.

The former group of materials was related to the unique noncentrosymmetric heavy fermion superconductor (HFSC) with co-existence of a long-range antiferromagnetic (AF) ordering: $CePt_3Si$. We investigated the effect of p and d metal substitution on the electronic properties. Concretely, the Pt metal was substituted by Au, Cu, Ru Rh, Pd, Ir, and the Si element by B, Al, Ge, C, respectively. It was observed, that in any case the HFSC state is rapidly suppressed by any trace substitution in the Pt or Si sites. In contrast, the magnetic ordering is in general favored by substitution as demonstrated with the significant increase of the Nèel temperature, T_N in comparison to the $CePt_3Si$. In addition, the off-stoichiometry from the 1 : 3 : 1 composition influences the coexistence of the HFSC and AF ordering similarly.

The $CePt_3X$, X = B, Al, Ge, C compounds were prepared and studied by various techniques. Except the B compound, their crystal structure is different from the $CePt_3Si$. The Ge, Al and C containing compounds are not superconducting and lack long-range magnetic ordering down to 50 mK as confirmed by the neutron diffraction experiment. The $CePt_3B$ orders antiferromagnetically below 8 K and undergoes an additional order-to-order magnetic phase transition at $\sim$ 5 K. Moreover, the anisotropic Kondo model was successfully applied in the $CePt_3Ge$ compound.

The investigations of the $CePt_3X$ compounds ($CePt_3X$, X = B, Al, Ge, Si) prepared by the splat-cooling technique revealed various interesting results. The crystal structure of the $CePt_3Si$ was found to be different to that of the conventionally-fabricated material and both the AF ordering and SC lacks in the splat-cooled sample. Formation of amorphous or submicron-grain phases was observed in the other $CePt_3X$ compounds. The thermodynamic, and namely the transport properties of the splat-cooled systems suggested interplay between the Kondo-impurity physics due to Ce and weak to medium localization effects of the perturbed electron-phonon scattering in analogy with metallic glasses.

The studies of the $CePt_3Si$ doped with a p or d metal demonstrated, that any substitution cause significant modification of the structure and physical behavior of the $CePt_3Si$. The change of the crystal structure generally converts the characteristic properties of the $CePt_3Si$ to behavior of a non-magnetic Kondo ground state with possibility of magnetic correlations. The HFSC state is suppressed in $CePt_{1-x}T_xSi$ compounds samples with x $\sim$ 0.2, and the ordering temperature (T_N) is in general shifted to higher temperatures. The investigations further suggested 'coexistence' of two kinds of inhomogeneities in the substituted materials: the metallurgical and as their consequence, the fundamental. They cooperation leads to formation of inhomogeneous magnetic states in the vicinity of the T_N.

The study of the later group of materials based on the Ce - Ru - Si revealed the two crucial results: occurrence of superconductivity with the critical temperature T_c of about 3 K in all compounds (due to the $CeRu_2$-related Si-doped phase: $Ce_{35}Pt_{58}Si_7$), and possibility of AF ordering in the nanoscaled heavy fermion compound $CeRu_2Si_2$. The investigations further suggested lack of ferromagnetism in the $Ce_{35}Pt_{58}Si_7$ samples; in fact in the $CeRu_2$ itself. The fast cooling rates of the $Ce_{35}Pt_{58}Si_7$ material turns its properties to those of non-magnetic metallic glasses.

The pilot studies of the nanoscaled Tb, splat-cooled materials and submicron-grain $CeRu_2Si_2$ are enormously inspirative. They prompted attractive trend of the future research in the field of rare-earths and strongly correlated electron systems (SCES) - modification of the $4f$/SCES's states in submicron dimensions, and its consequences.

In nanosized systems the electronic states are no more continuous like in macroscopic metals, but discreet due to space restriction of the electron wave functions. Therefore quantum effects in various physical properties of nanosystems can be observed as a consequence of the electron state separation.

It lies ready to hand that the effect of dimensionality on mechanisms of physical phenomena in strongly-correlated, heavy-fermion compounds and unconventional superconductors must be really prodigious and worth research work. The stagnancy in the SCES-related research in recent years will be therefore prevented and connection between the hot topics in nanoscience and the exotic SCES-physics will be undoubtedly fruitful.

Appendix A

Periodic table of elements

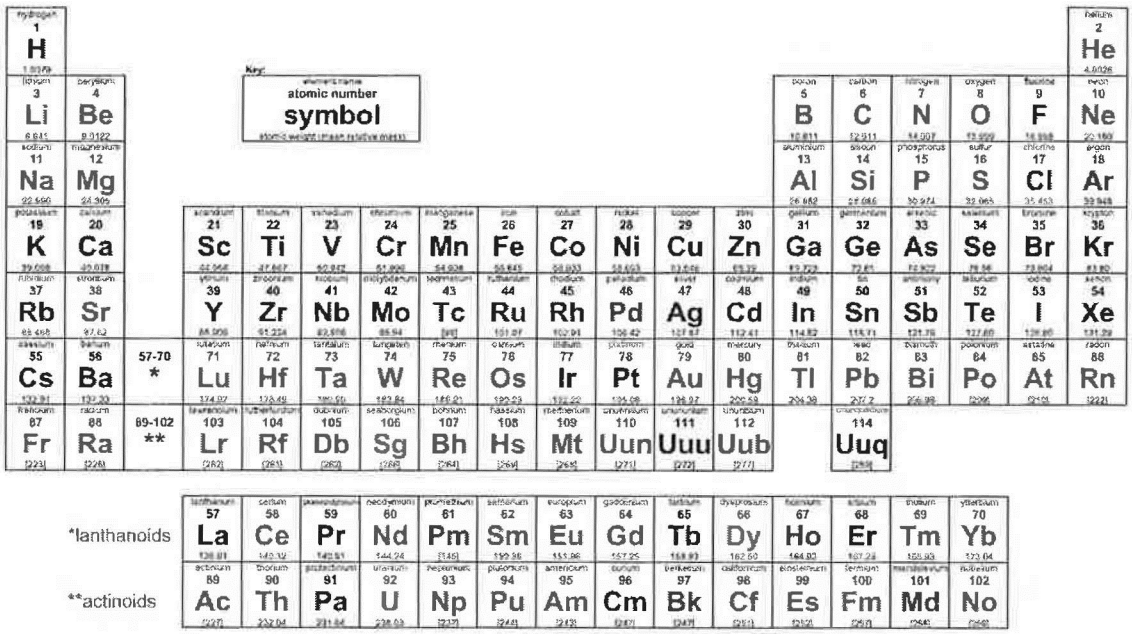

Figure A.1: Periodic table of elements, the essence.

Appendix B

Ternary phase diagrams

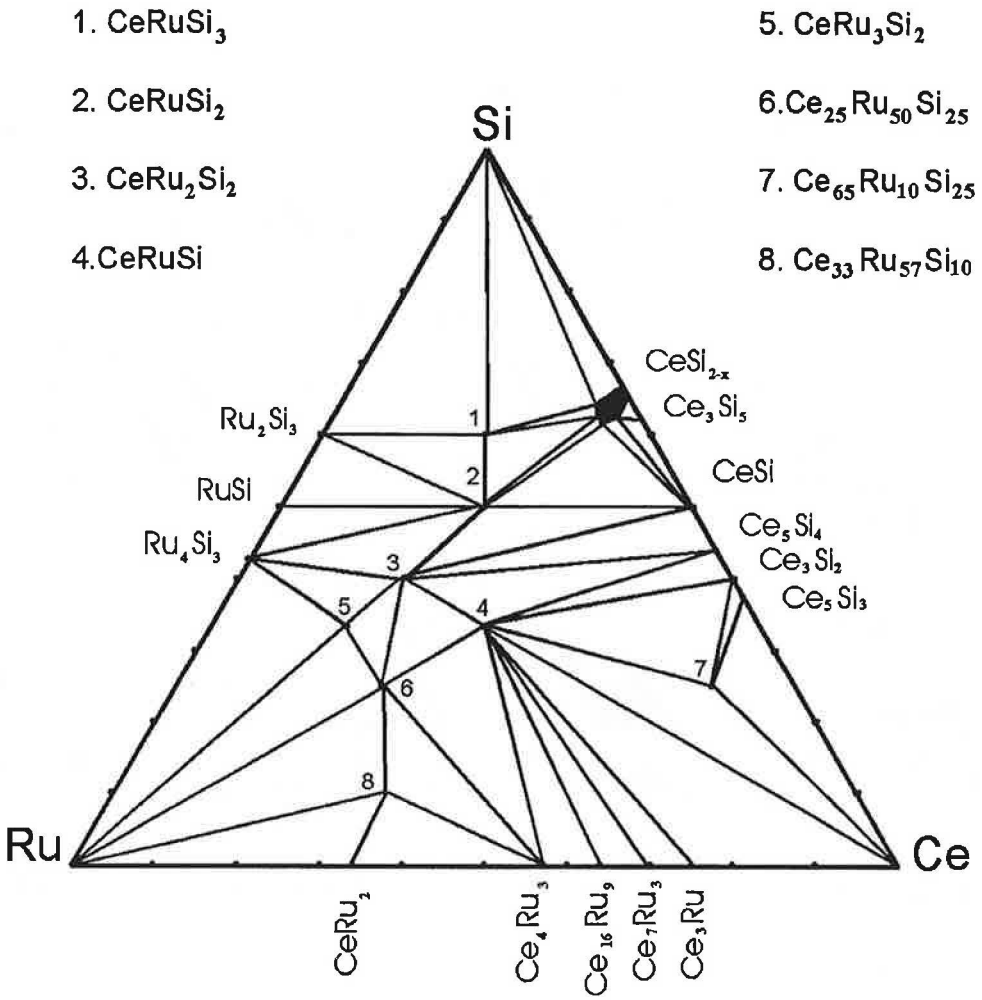

Figure B.1: Isothermal cross-section of the Ce-Ru-Si phase diagram at 600 ° according to [565].

1 - $CePtSi_3$ 2 - $CePtSi_2$ 3 - $Ce(Pt,Si)_2$ 4 - $CePt_2Si_2$ 5 - $Ce_{43}Pt_{14}Si_{43}$
6 - CePtSi 7 - $Ce_3Pt_{23}Si_{11}$ 8 - $CePt_2Si$ 9 - $CePt_3Si$

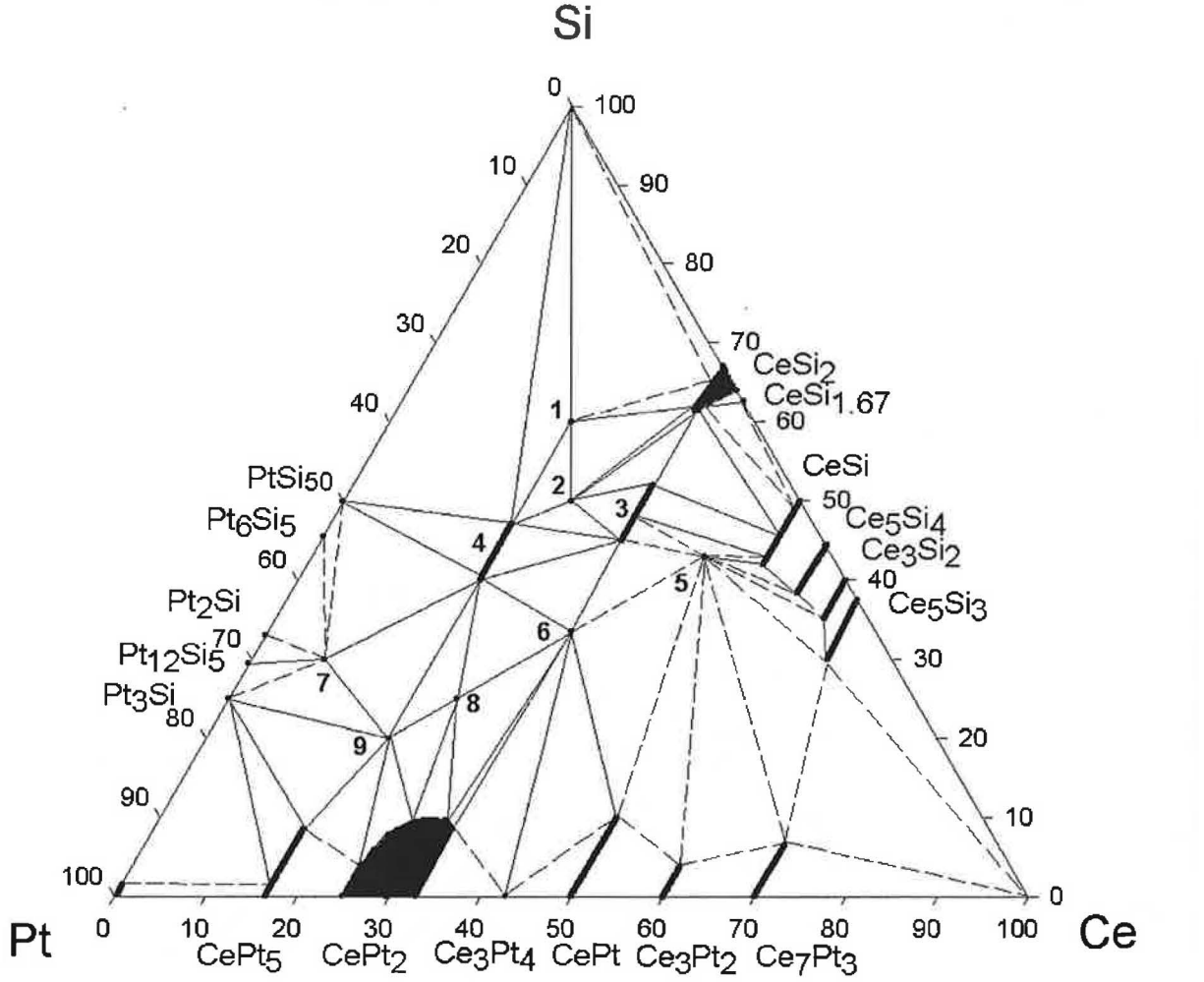

Figure B.2: Isothermal cross-section of the Ce - Pt - Si phase diagram at 600 ° according to [566].

Appendix C

Rietveld analysis

A powder diffraction pattern is recorded in numerical form for a discrete set of scattering angles (times of flight or energies). We will refer to this scattering variable as $\mathcal{T}$. Then, the experimental powder diffraction pattern is usually given as two arrays $\{\mathcal{T}_i, y_i\}_{i=1...n}$. In the case of data that have been manipulated or normalized in some way the three arrays $\{\mathcal{T}_i, y_i, \sigma_i\}_{i=1...n}$, where σ_i is the standard deviation of the profile intensity y_i, are needed in order to properly weight the residuals in the least squares procedure. The profile can be modelled using the calculated counts y_{ci} at the ith step by summing the contribution from neighboring Bragg reflections plus the background:

$$y_{ci} = \sum_{\psi} S_{\psi} \sum_{h} I_{\psi,\mathbf{h}} \Omega(T_i - T_{\psi,\mathbf{h}}) + b_i \tag{C.1}$$

The vector $\mathbf{h}$ labels the Bragg reflections, the subscript ψ labels the phase and vary from 1 up to the number of phases existing in the model. In FullProf the term phase is synonymous of a same procedure for calculating the integrated intensities, $I_{\psi,\mathbf{h}}$. This includes the usual meaning of a phase and also the case of the magnetic contribution to scattering (treated usually as a different phase) coming from a single crystallographic phase in the sample. The general expression of the integrated intensity is:

$$I_{\psi,\mathbf{h}} = \{\mathcal{LAPCF}\}_{\psi,\mathbf{h}} \tag{C.2}$$

The meaning of the different terms is the following:

- S_{ψ} is the scale factor of the phase
- $\mathcal{L}_h$ contains the Lorentz, polarization and multiplicity factors
- $\mathcal{F}_h$ is the structure factor
- $\mathcal{A}_h$ is the absorption correction
- $\mathcal{P}_h$ is the preferred orientation function
- Ω is the reflection profile function that models both instrumental and sample effects[1]

[1]The profile can be described using one of the following functions: Gaussian, Lorentzian, modified Lorentzian, intermediate Lorentzian, Pearson VII, Pseudo-Voight; for definition see e.g. [88].

- $\mathcal{C}_h$ is the instrumental and sample effects and includes special corrections (non linearity, efficiencies, special absorption corrections, extinction, etc)
- b_i is the background intensity.

The Rietveld method consist of refining a crystal (and/or magnetic) structure by minimizing the weighted squared difference between the observed and the calculated pattern against the parameter vector α. The function minimized in the Rietveld Method is:

$$\chi^2 = \sum_{i=1}^{n} w_i \{y_i - y_{ci}(\alpha)\}^2 \tag{C.3}$$

with $w_i = 1/\sigma_i^2$, σ_i^2 being the variance of the observation y_i.

The quality of the agreement between observed and calculated profiles is measured by a set of nowadays-conventional factors:

- profile factor
$$R_{\mathrm{P}} = \frac{100 \sum_{i=1\ldots n} |y_i - y_{ci}|}{\sum_{i=1\ldots n} y_i} \tag{C.4}$$
- weighted profile factor
$$R_{wp} = 100[\frac{\sum_{i=1\ldots n} w_i |y_i - y_{ci}|^2}{\sum_{i=1\ldots n} w_i y_i^2}]^{1/2} \tag{C.5}$$
- expected weighted profile factor
$$R_{exp} = 100[\frac{n-p}{\sum_{i=1\ldots n} w_i y_i^2}]^{1/2} \tag{C.6}$$
- goodness of fit indicator
$$S = \frac{R_{wp}}{R_{exp}} \tag{C.7}$$
- reduced χ-square
$$\chi_v^2 = S^2 \tag{C.8}$$
- Bragg factor
$$R_{\mathrm{B}} = 100 \frac{I_{obs,h} - I_{calc,h}}{I_{obs,h}} \tag{C.9}$$
- crystallographic R_{F}-factor
$$R_{\mathrm{F}} = 100 \frac{F_{obs,k} - F_{calc,h}}{F_{obs,h}} \tag{C.10}$$

The observed integrated intensity $I_{obs,h}$ is in fact calculated from the Rietveld formula:

$$I_{obs,h} = I_{calc,h} \sum_i \frac{\Omega(\mathcal{T}_i - \mathcal{T}_h)(y_i - b_i)}{y_{ci} - b_i}. \tag{C.11}$$

This formula is equivalent to a proportional sharing of the integrated intensity of a cluster between its components according to the actual model.

variable	U	V	W
value	0.00169	0.00108	0.00362

Table C.1: Instrumental function parameters determined for the Seifert diffractometer.

instrument	λ (nm)	U	V	W
D1a	191	0.12	-0.21	0.17
D20	240	3.00844	-1.81197	0.49958

Table C.2: Instrumental function parameters determined for the D1a and D20 diffractometers.

Peak-shape parameters - instrumental function

The dependence of the peak-shape parameters on the scattering variable (2θ for constant wavelength diffractometers) is parameterized by the pseudo-Voight function.[2]

The influence of the instrumental resolution function was kept fixed during the refinement. The corresponding half-width parameters U, V, W are summarized in the Table C.1.

Line broadening

Because of the preparation procedure, remnant strains or grain size may be present. The mentioned effects cause additional peak broadening coming from several sources besides the above screened instrumental effects:

- Finite crystallite (not particle) size (< 100-500 nm)
- Strain (atoms deformed from ideal positions in a nonuniform manner)
- Extended defects

The careful analysis of the powder diffraction data may serve as a tool for their estimation.

In general, there are the following methods of extracting size and strain information[3].:

[2]The variables are defined by the relations:

$$FHWM_G^2 = (U + D_{st}^2)\tan^2\theta + V\tan\theta + W + \frac{I_G}{\cos^2\theta} \tag{C.12}$$

$$FHWM_L^2 = X\tan\theta + \frac{Y + F(S_z)}{\cos\theta} \tag{C.13}$$

where $FHWM_G$ is the Gaussian and $FHWM_L$ is the Lorentzian component, respectively. U, W, V are the half-width parameters (normally characterizing the instrumental resolution function), X and Y are the Lorentzian isotropic strain and size parameters, respectively. D_{st} is the anisotropic Gaussian contribution of microstrain, I_G is the isotropic size parameter of gaussian character and $F(S_z)$ is the anisotropic Lorentzian contribution of particle size. For more details, see [88].

[3]Macrostrain effect causing shift of the position of the diffraction maxima is expected in the splat samples only and is not discussed, however, was not observed. For details, see please e.g. [91]

- Scherrer formula (average size, neglects strain):

$$D_V = K\lambda/(\beta\cos\theta) \tag{C.14}$$

D_V - Volume Weighted crystallite size, K - Scherrer constant (0.87-1.0), λ - the wavelength of the radiation, *beta* - the integral breadth of a reflection (in radians) located at 2θ.

- Integral breadth methods (provide average values of size and strain)
- Peak shape methods (provide size and strain distributions)

Strain is a term used more often in engineering than in chemistry. Strain is defined as the deformation of an object divided by it.s ideal length. In crystals there we can observe two types of strain: uniform and non-uniform strain. Uniform strain causes the unit cell to expand/contract in an isotropic way. This simply leads to a change in the unit cell parameters and shift of the peaks. There is no broadening associated with this type of strain. Non-uniform strain leads to systematic shifts of atoms from their ideal positions and to peak broadening. This type of strain arises from the following sources: point defects (vacancies, site-disorder), plastic deformation (cold worked metals, thin films) and poor crystallinity.

While the size and strain effects broadening show a different 2θ dependence, it provides a way to separate them. The method for decoupling size and strain broadening by looking at the peak width as a function of 2θ is the so-called Williamson-Hall plot. It is constructed as follows:

- plot $(\beta_{obs} - \beta_{instr}\cos\theta)$ on the y-axis (in radians 2θ)
- plot $4\sin\theta$ on the x-axis.

If the data appears to be linear, the crystallite size from the y-intercept of the linear fit, and the strain from the slope of the linear fit can be obtained, respectively.

The microstructural effects within FullProf are treated using the Voigt approximation: both instrumental and sample intrinsic profile are supposed to be described approximately by a convolution of Lorentzian and Gaussian components. The TCH pseudo-Voigt profile function [92] is used to mimic the exact Voigt function and it includes the Fingers treatment of the axial divergence [93]. The integral breadth method to obtain volume averages of sizes and strains is used to output a microstructural file where an analysis of the size and strain contribution to each reflection is written. However, no physical interpretation is given by the program, only a phenomenological treatment of line broadening in terms of coherent domain size and strains due to structural defects is performed.

Texture

Additionally, preferred orientation of the crystallites in the sample may be estimated. Two functions are available in the Fullprof software:

- Exponential function

$$P_h = G_2 + (1 - G_2)\exp(G_1\alpha_h^2), \tag{C.15}$$

where and G_1, G_2 are refinable parameters and α_h is the acute angle between the scattering vector and the normal to the crystallites (platy habit).

- Modified March's function

$$P_h = G_2 + (1 - G_2)\{[(G1\cos\alpha_h)^2 + \frac{\sin^2\alpha_h}{G_1}]\}^{-3/2} \quad \text{(C.16)}$$

Where and G_1, G_2 are refinable parameters. This expression is adapted to both fibber and platy habits:

- $G_1 > 0$ platy habit
- $G_1 = 0$ no preferred orientation
- $G_1 < 0$ needle-like habit

Appendix D

Additional results

To keep the consistency of the main part of the thesis, some results were finally not included. They are briefly presented in the following chapter. Some of the results were already published, some of them are just used for preparation of future publications.

D.1 Disordered alloys - electrical resistivity in CeNi-CeCu system

The most important results are so far published in the following paper:

- Marcano et al, *Cluster-glass transitions in $CeNi_{1-x}Cu_x$ as studied by magnetocaloric effect*, Physica B-Condensed Matter 378-80 (2006)762.

The results are depicted in the Figures D.1 - D.3.

D.2 Disordered alloys - $LaFe_2Si_2$ doped with Mn

The most important results are published in the following papers:

- Vejpravova et al, *Influence of Mn substitution on magnetic behavior of $La(Fe_{1-x}Mn_x)_2Si_2$ alloys*, J. Magn. Magn. Mater. 290-291 (2005) 621.

- Turek et al, *Local moments, exchange interactions, and magnetic order in Mn-doped $LaFe_2Si_2$ alloys*, J. Magn. Magn. Mater. 316 (2007) e403.

D.3 Isostructural $CePt_3Si$-related compounds with La and Pr

Some results will be soon published in the following paper:

- Divis et al, *The electronic structure and crystal field of RPt_3Si (R = Pr, Nd, Sm) compounds*, accepted in Physica B.

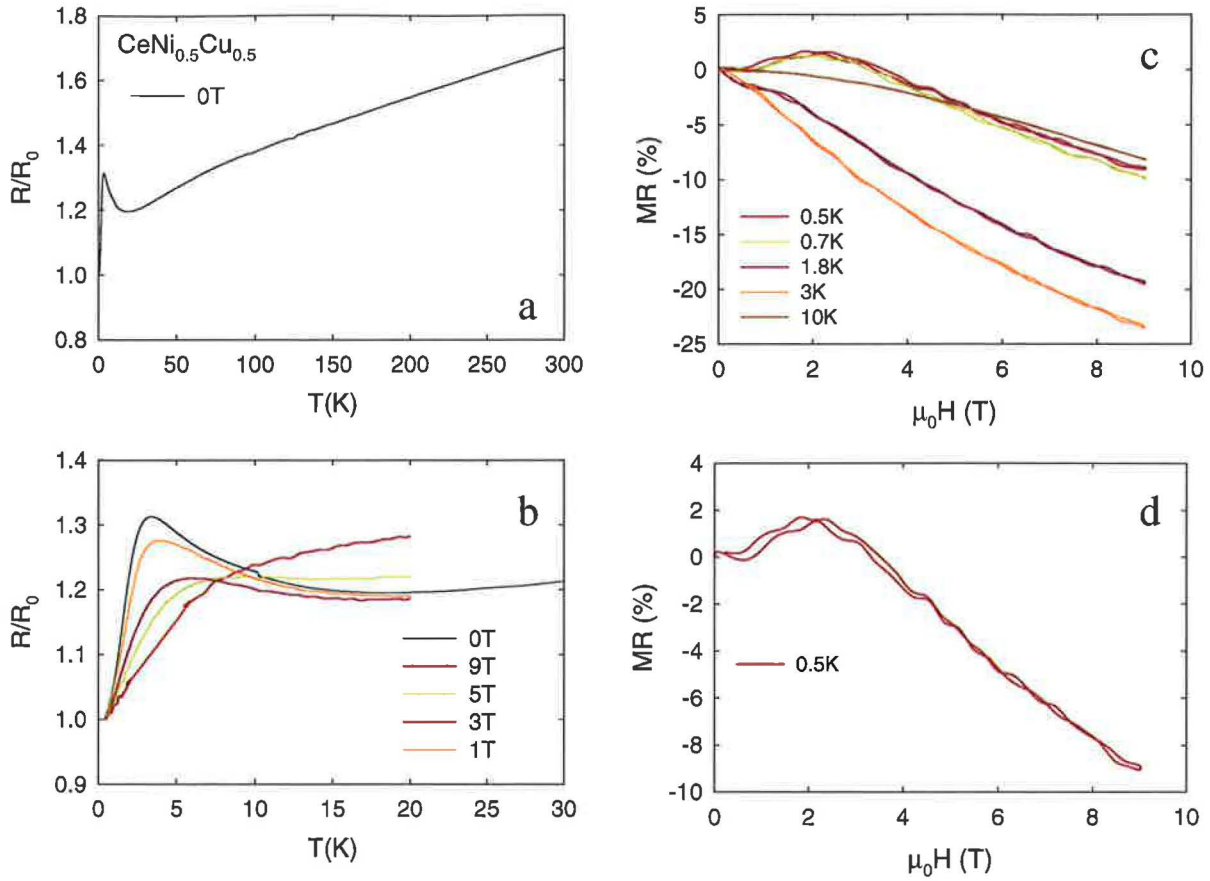

Figure D.1: Electrical resistivity and magnetoresistance of the $CeNi_{0.5}Cu_{0.5}$ compound. a - zero-field temperature dependence. b - low-temperature dependence of the resistivity at several magnetic fields. c - magnetoresistance curves at low temperatures. d - magnetoresistance at 0.5 K.

D.3.1 Electronic structure of RPt_3Si, R = La, Ce, Pr

The first-principle calculations were performed for the RPt_3Si, R = La, Ce, Pr compounds and are depicted in the Figures D.4 - D.5.

D.3.2 $PrPt_3Si$

Beside the specific heat and magnetic susceptibility investigations presented in the above mention publication (Divis et al, Physica B), detailed measurements of the specific heat under magnetic field below 2 K were performed. We speculate, that the 1 K - related anomaly may be originated by an unusual phenomena involving coupling of the electron and nuclear spins.

It can be described as follows: when a system consists of magnetic atoms with the electronic singlet ground state and with nuclear spin and interacting with each other by the exchange interaction, a remarkable change in magnetic properties takes place around a certain ratio between the exchange interaction and the zero-field electronic level splitting.

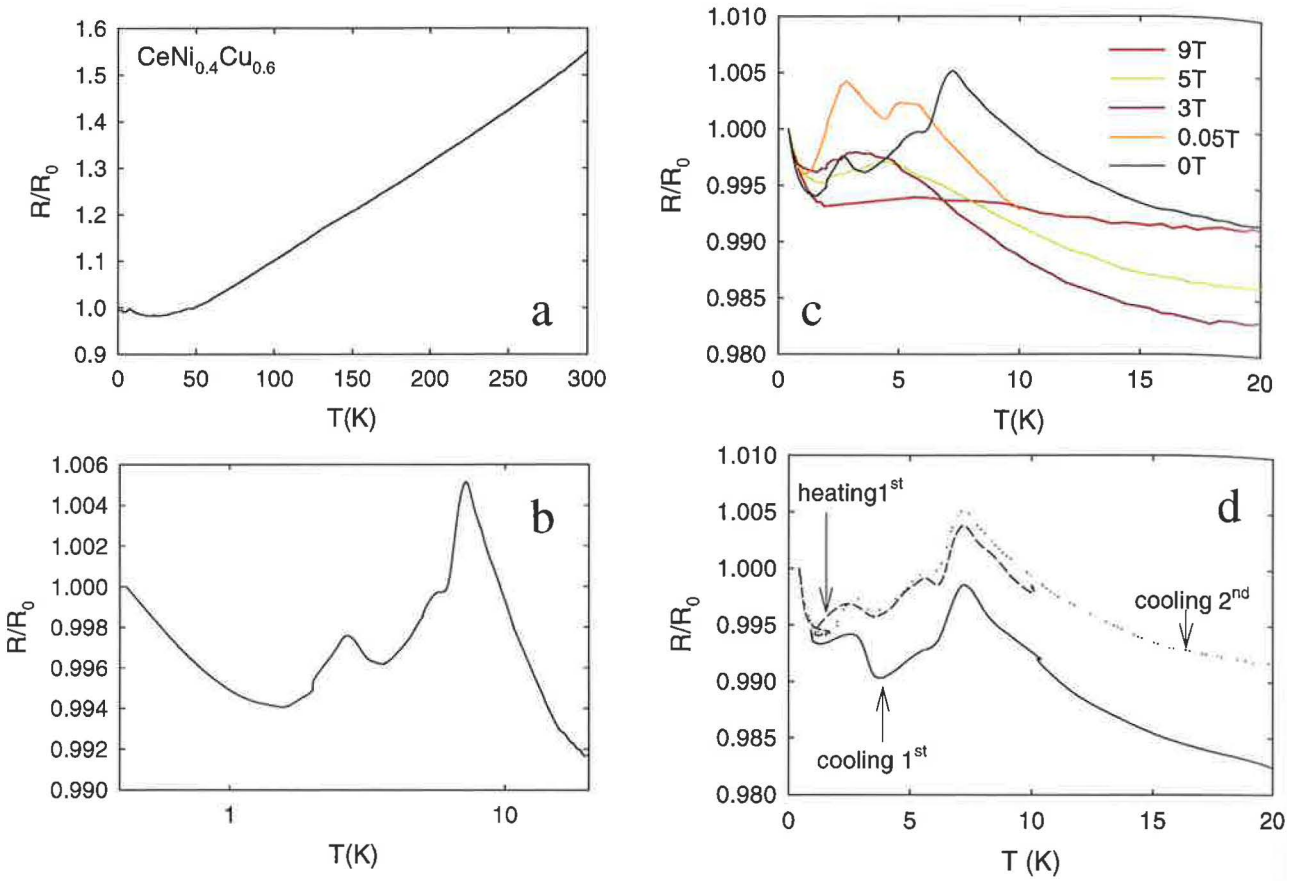

Figure D.2: Electrical resistivity of the $CeNi_{0.4}Cu_{0.6}$ compound.
a - zero-field temperature dependence. b - low-temperature dependence of the resistivity at zero magnetic field. c - low-temperature dependence of the resistivity at several magnetic fields. d - low-temperature dependence of the resistivity at zero magnetic field in two cooling-heating cycles.

The two regimes divided by this ratio are called the electronic and the nuclear regimes. However, the proposed mechanism must be probed by proper theoretical calculations, which are in progress.

The so far obtained results are depicted in the Figures D.6 - D.7.

D.3.3 $PrPt_3B$

In contrast to the previous reports [309], we have not observed any sign of ferromagnetism down to 0.3 K. Instead, the scenario seems to resemble that of in the $PrPt_3Si$ system. The results are shown in the Figures D.8 - D.9.

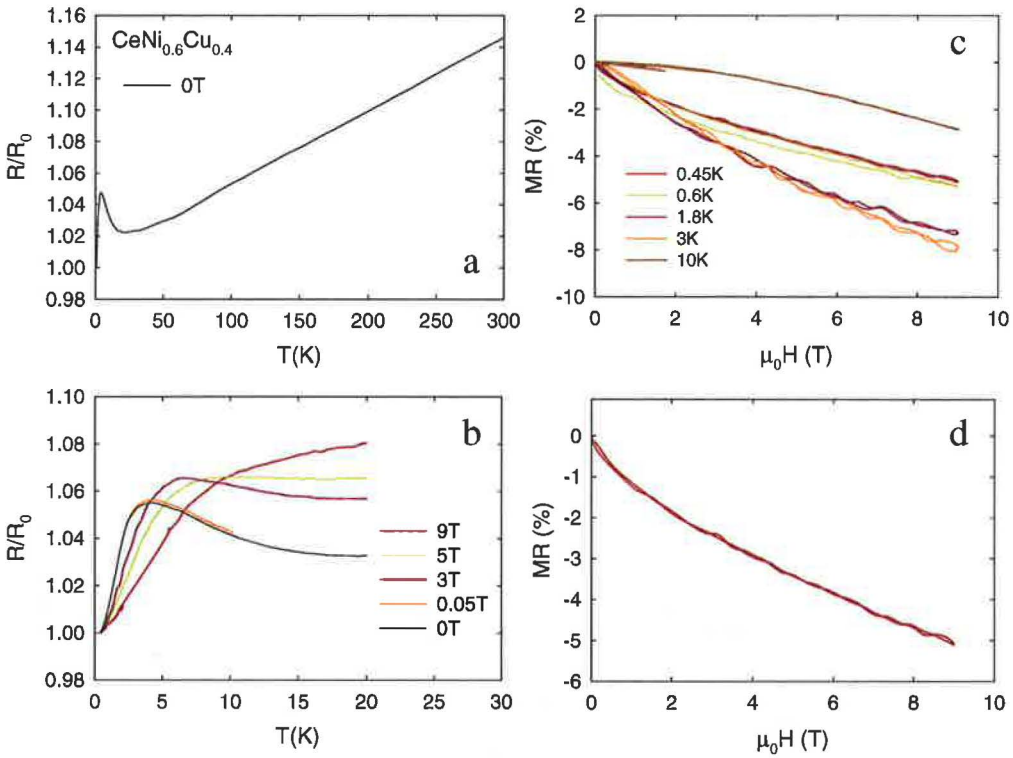

Figure D.3: Electrical resistivity and magnetoresistance of the $CeNi_{0.6}Cu_{0.4}$ compound. a - zero-field temperature dependence. b - low-temperature dependence of the resistivity at several magnetic fields. c - magnetoresistance curves at low temperatures. d - magnetoresistance at 0.5 K.

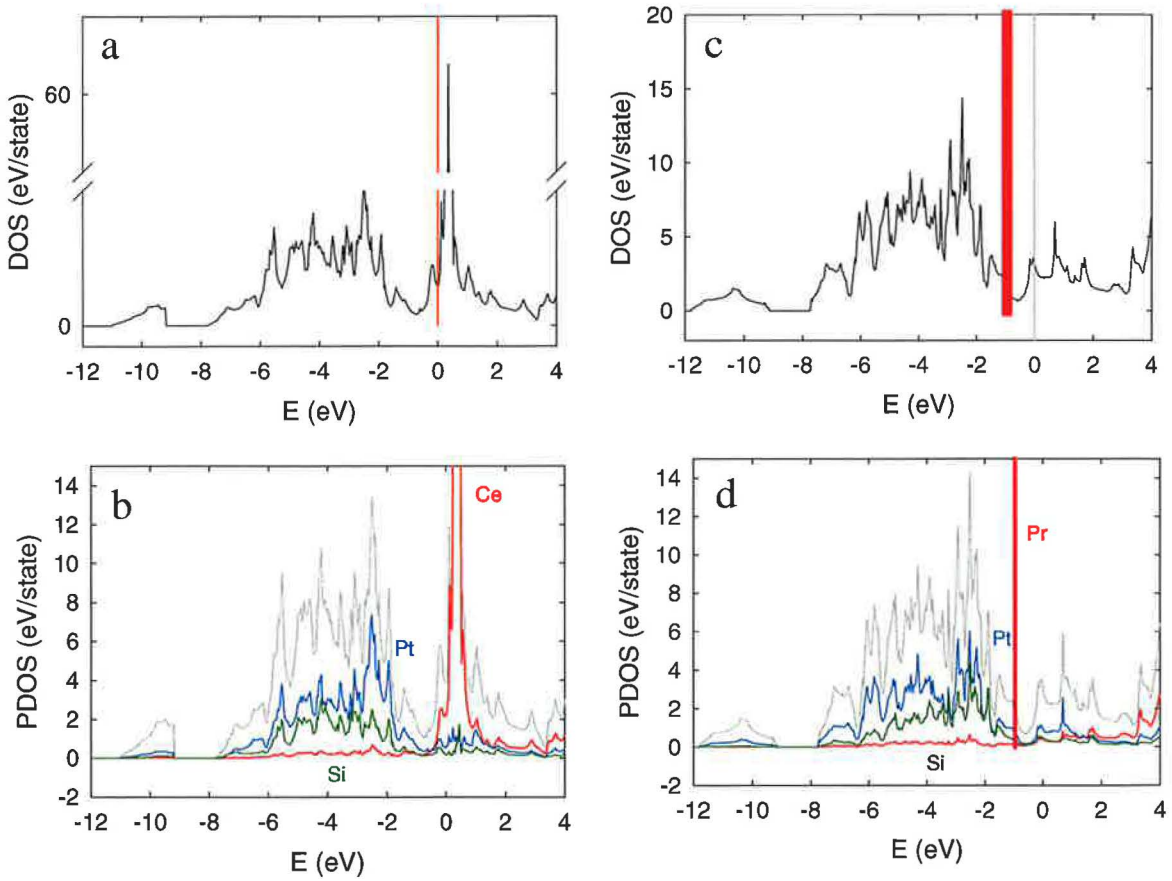

Figure D.4: Calculated density of states of the $CePt_3Si$ and $PrPt_3Si$ compounds. a - total DOS of the $CePt_3Si$. b - projected DOS of the $CePt_3Si$. c - total DOS of the $PrPt_3Si$, the red line corresponds to the $4f$ level. d - projected DOS of the $PrPt_3Si$, the red line corresponds to the $4f$ level.

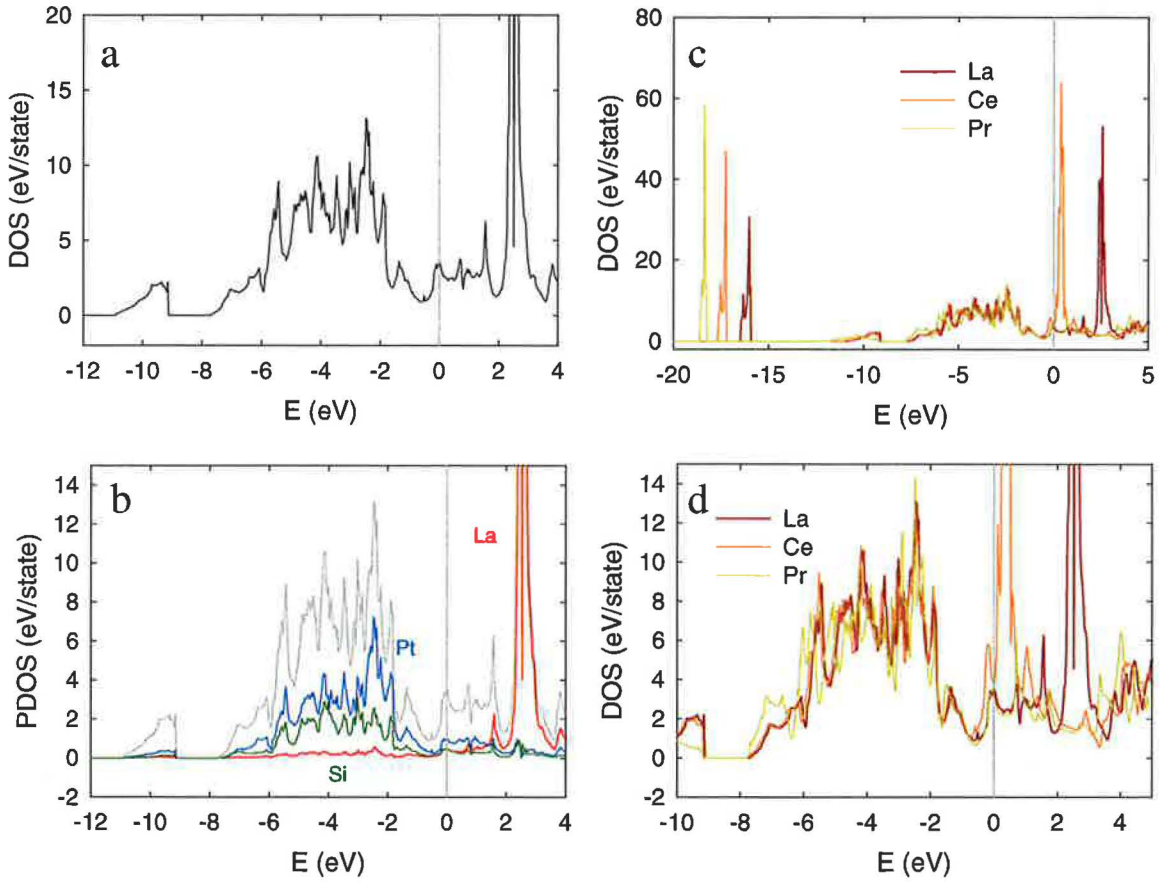

Figure D.5: Calculated density of states of the $LaPt_3Si$ in comparison to other isostructural compounds with Ce and Pr.
a - total DOS of the $LaPt_3Si$. b - projected DOS of the $LaPt_3Si$. c - comparison of the total DOS of the RPt_3Si, R = La, Ce, Pr. d - detail of DOS in the vicinity of the Fermi level.

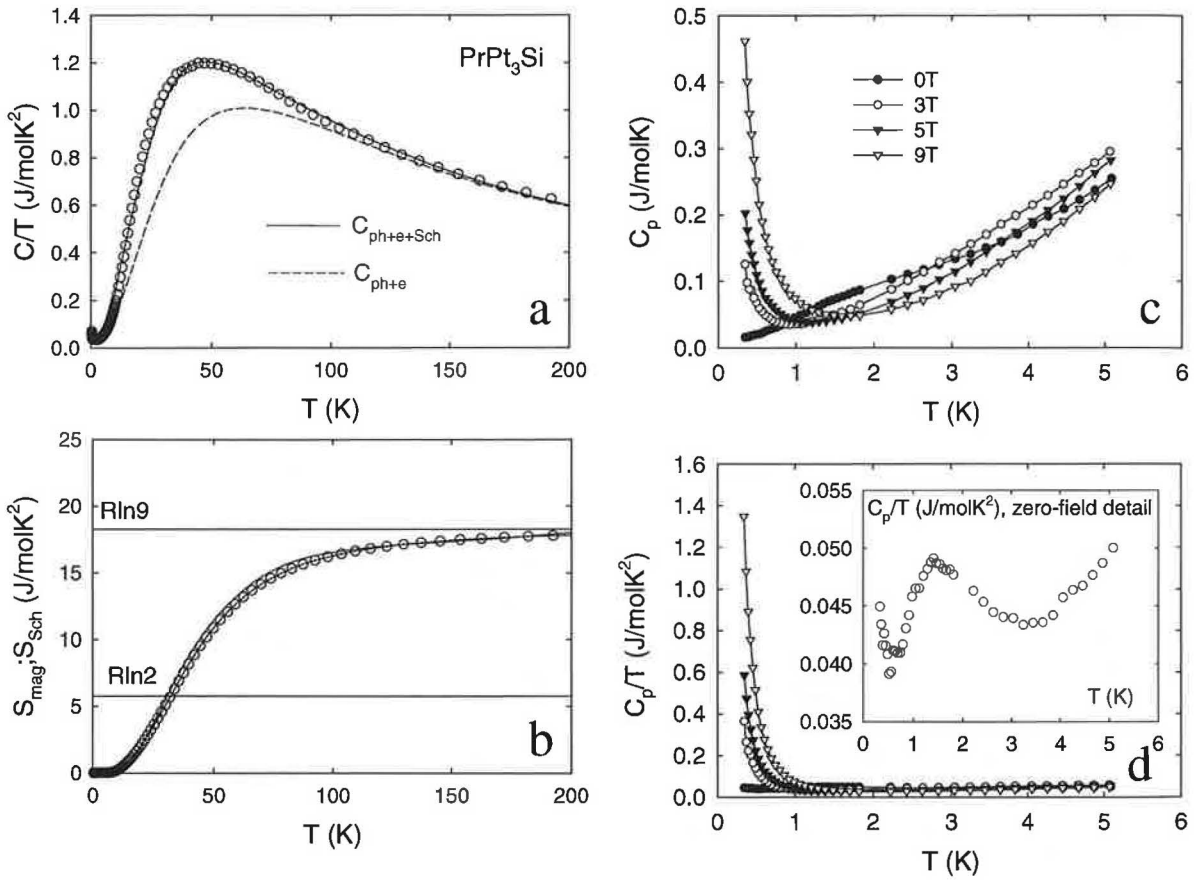

Figure D.6: Specific heat and magnetic entropy of the $PrPt_3Si$ compound. a - Experimental specific heat in comparison to the fit of the electron and phonon parts. b - calculated magnetic entropy in comparison to the calculated Schottky entropy. c - low-temperature specific heat under magnetic field. d - detail of the zero-field curve.

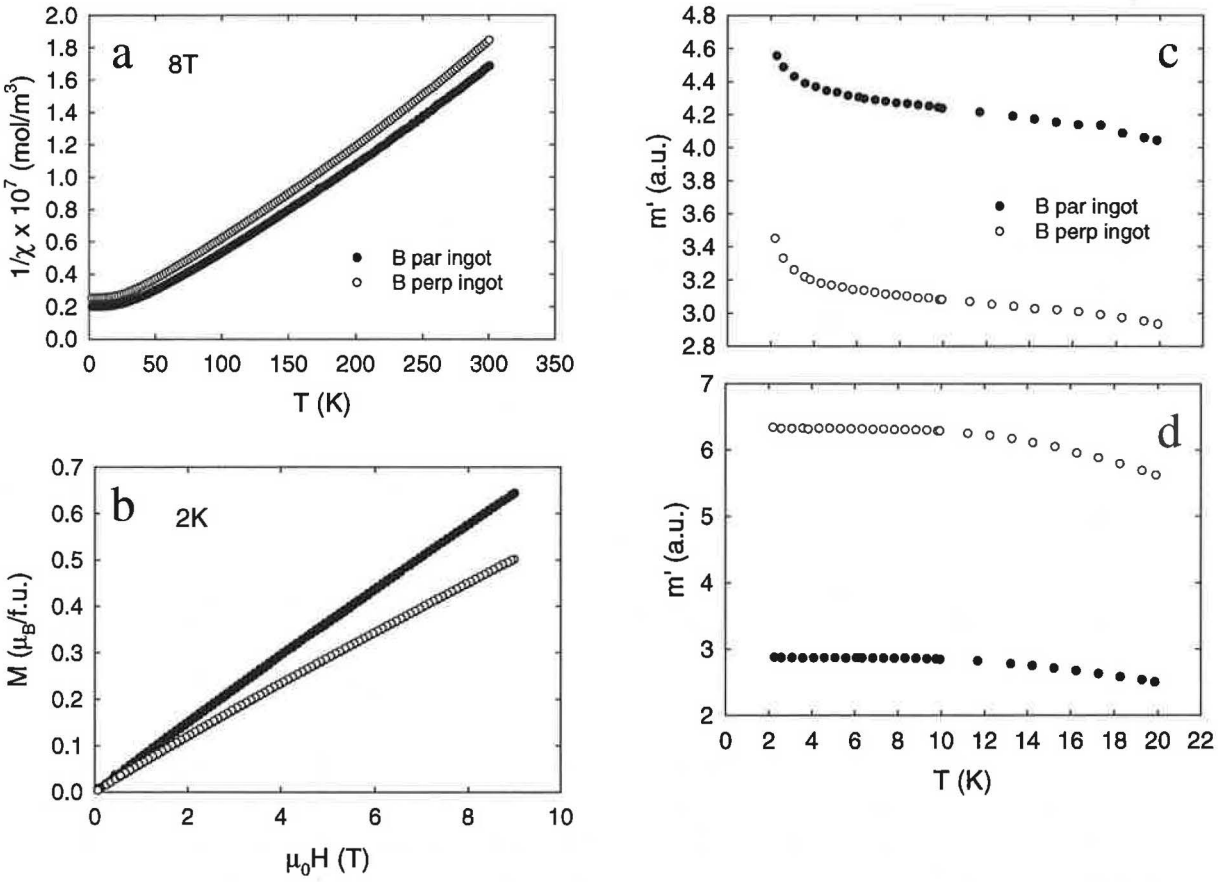

Figure D.7: Magnetization and magnetic susceptibility of the $PrPt_3Si$ ingot.
a - inverse magnetic susceptibility for the magnetic field applied parallel and perpendicularly to the ingot growth direction. b - magnetization curves at 2 K for both mentioned geometries. c - real part of the a.c. magnetic susceptibility, d - imaginary part of the a.c. susceptibility.

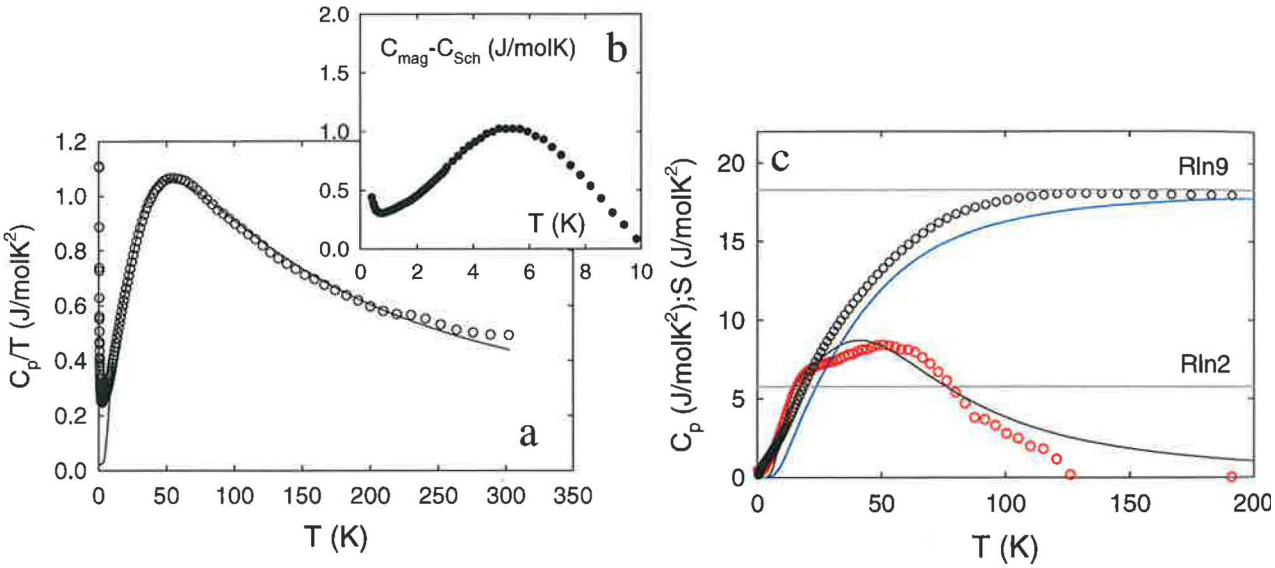

Figure D.8: Specific heat and magnetic entropy of the $PrPt_3B$ compound.
a - Experimental specific heat in comparison to the fit of the electron and phonon parts (black line). b - remanent broad effect in the specific heat after subtracting the Schottky type contribution from the magnetic specific heat c - magnetic entropy (open circles) in comparison with the calculated Schottky entropy (blue line). The fit of the magnetic specific heat (red circles) by the Schottky-type term (black line) is also shown.

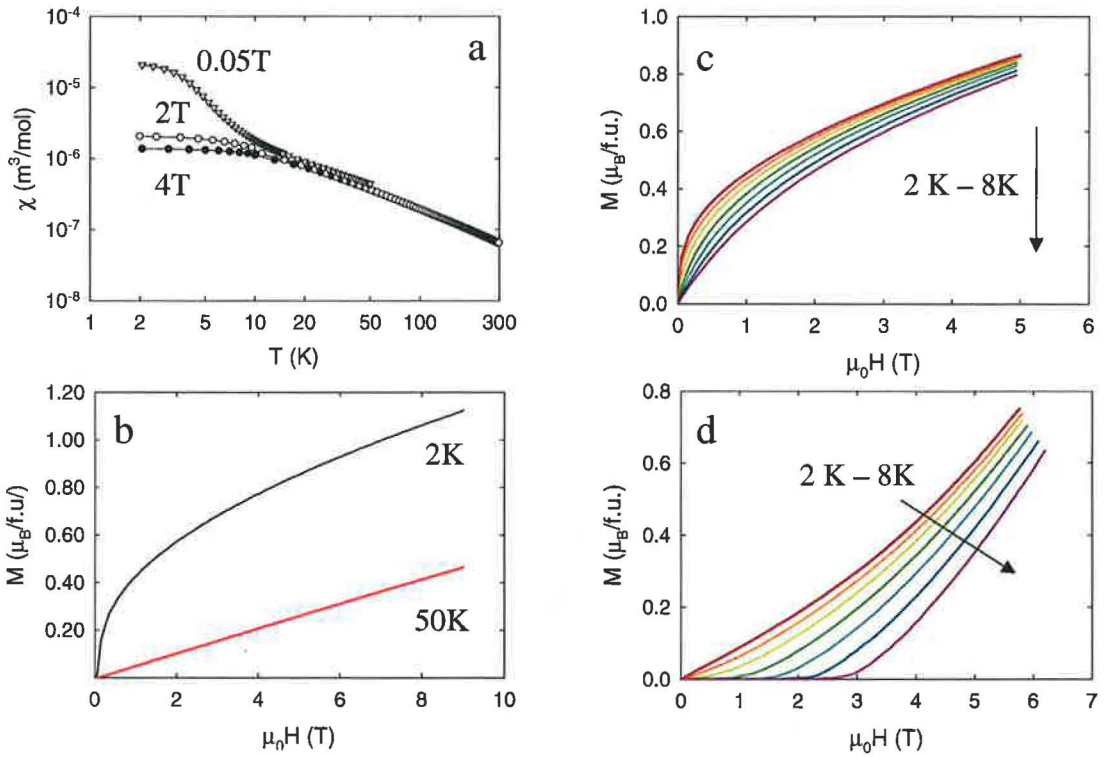

Figure D.9: Magnetization and magnetic susceptibility of $PrPt_3B$.
a - magnetic susceptibility at the low temperature region. b - magnetization curves at 2 K and 50 K, respectively. c - magnetization curves at 2 - 8 K, d - Arrot's plots at 2 - 8 K.

Bibliography

[1] Ch. Kittel, Introduction to Solid State Physics, John Wiley&Sons, 1976.

[2] J.M. Ziman, Electrons and phonons, Oxford, 1960.

[3] K. Yoshida, Theory of Magnetism, Springer-Verlag, Berlin Heidelberg, 1996.

[4] E. Bauer, Highly Correlated Electron Systems The Kondo Problem to Heavy Fermions, TU Wien, A script for a lecture given at the Vienna University of Technology summer semester, 2000.

[5] D.C. Mattis, The Theory of Magnetism, Springer-Verlag Berlin Heidelberg, 1981.

[6] A. Gonis, N. Kioussis, M. Ciftan, Electron Correlations and Materials Properties 2, Kluwer Academic, 2001.

[7] V.F. Ganthmakher, Electrons and Disorder in Solids, Oxford Univeristy Press, 2005.

[8] T. Hicks, Magnetism in Disorder, Oxford Univeristy Press, 1995.

[9] L.P. Levy, Magnetism and Superconductivity, Springer-Verlag Berlin Heidelberg, 2000.

[10] P. Svoboda P, V. Sechovsky V, A.A. Menovsky, Physica B 339 (2003) 177.

[11] A. Krimmel, A. Severing, A. Murani et al, Physica B 180 (1999) 191.

[12] V.T. Rajan, Phys. Rev. Lett. 51 (1983) 308.

[13] P. Schlottmann, P.D. Sacramento, Adv. Phys. 42(1993) 641.

[14] A. Okiji, N. Kawakami, J. Magn. Mag. Mater. 54-7 Part 1 (1986) 327.

[15] P.W. Anderson, Phys. Rev. 124 (1961) 41.

[16] H.R. Krishnamurthy, J.W. Wilkins, K.G. Wilson, Phys. Rev. B 21 (1980) 1003.

[17] R. Shankar, Rev. Modern Phys. 66 (1994) 129.

[18] J. Maldacena, C. Nunez, Phys. Rev. Lett. 86 (2001) 588.

[19] D.L. Cox, A. ZawadowskiAdv. Phys. 47 (1998) 599.

[20] S. Egegrt, I. Affleck, M. Takahashi, Phys. Rev. Lett. 73(1994) 332.

[21] I. Affleck, A.W.W. Ludwig, Nuclear Phys. B, 360 (1991) 641.

[22] P.W. Anderson Phys. Rev. Lett. 65 (1990) 2306.

[23] M. ogata, H. Shiba, Phys. Rev. B 41 (1990) 2326.

[24] J.Q. Xiao, J.S. Jiang, C.L. Chien et al, Phys. Rev. Lett. 68 (1992) 3749.

[25] K.I. Kobayashi, T. Kimura, Y. Tomioka et al, Phys. Rev. B 59 (1999) 11159.

[26] J.E. Gordon, C.W. Dempesy, T. Soller , Phys. Rev. 124 (1961) 724.

[27] C.A. Martin. J. Phys.: Condens. Matter 3 (1991) 5967.

[28] H. v. Lhneysen, T. Pietrus, G. Portisch et al, Phys. Rev. Lett. 72 (1994) 3262.

[29] J. Kondo, Prog. Theor. Phys. 32 (1964) 37.

[30] R. Schrieffer, P.A. Wolff, Phys. Rev. 185 (1969) 847.

[31] S. Doniach, Physica B & C 91 (1977) 231.

[32] B. Coqblin, J.R. Schrieffer, Phys. Rev. 149 (1966) 491.

[33] A. Georges, G. Kotliar, W. Krauth et al., Rev. Modern Phys. 68 (1986) 13.

[34] P.W. Anderson, Phys. Rev. B 1 (1970) 4464.

[35] T.C. Wu, S.H. Leu, S.T. Tu, Appl. Math. Comput. 105 (1999) 1.

[36] F. Steglich, J. Aarts, C.D. Bredl et al, Phys. Rev. Lett. 43 (1979) 1892.

[37] G.R. Stewart, Z. Fisk, J.O. Willis et al, Phys. Rev. Lett. 52 (1984) 679.

[38] C. Petrovic, P.G. Pagliuso, M.F. Hundley et al, J. Phys. Condens. Matter. 13 (2001) L337.

[39] C. Geibel, C. Schank, S. Thies et al, Z. Physik B-Condens. Matter. 84 (1991) 1.

[40] E. Bauer, G. Hilscher, H. Michor et al, Phys. Rev. Lett. 92 (2004) 027003.

[41] N. Kimura, K. Ito, K. Saitoh et al, Phys. Rev. Lett. 95 (2005) 247004.

[42] P.A. Frigeri, D.F. Agterberg, A. Koga et al, Phys. Rev. Lett. 93, (2004).

[43] K.V. Samokhin, E.S. Zijlstra, S.K. Bose, Phys Rev. B 69 (2004) 094514.

[44] K.V. Samokhin, Phys. Rev. Lett. 94, (2005).

[45] I.A. Sergienko, S.H. Curnoe, Phys. Rev. B 70, (2004).

[46] A. Inoue, Acta Materialia, 48 (2000) 279.

[47] A.S. Argon, Acta Metalurgica, 27 (1979) 47.

[48] H.A. Davies, Phys. Chem. Glasses 17 (1976) 159.

[49] A.L. Greer, Science 267 (1995) 1947.

[50] K. Nahmf, W.H. Kettler, M. Rosenberg et al, J. Phys. F: Met. Phys. 17 (1987) 2085.

[51] S.G. Gumbatov, Kh.M. Pashaev, G.Kh. Panova, A.A. Shukov, Solid State Commun. 58 (1986) 389.

[52] J.J. Lin and L.Y. Kao, J. Phys.: Condens. Matter 13 (2001) L119.

[53] D.G. Rowan, Y.H. Szczech, M.A. Tusch and D.E. Logan, J. Phys.: Condens. Matter. 7 (1995) 68536068.

[54] D.S. Golubev, A.D. Zaikin, Phys. Rev. Lett. 81 (1998) 1074.

[55] Aleiner I L, Altshuler B L and Gershenson M E 1999 Waves Random Media 9 201 Altshuler B L, Gershenson M E and Aleiner I L 1998 Physica E 3 58

[56] A. Zawadowski, J. von Delft, D. Ralph Phys. Rev. Lett. 83 (1999) 2632.

[57] Y. Imry, H. Fukuyama, P. Schwab, Europhys. Lett. 47 (1999) 608.

[58] P. Mohanty, E.M.Q. Jariwala, R.A. Webb, Phys. Rev. Lett. 78 (1997) 3366.

[59] B. Khavin,M. E. Gershenson, A.L. Bogdanov, Phys. Rev. Lett. 81 (1998) 1066.

[60] P.D. Pivin, A. Anderson, J.P. Bird et al, Phys. Rev. Lett. 82 (1999) 4687.

[61] A.G. Huibers, J. Folk, S.R. Patel et al, Phys. Rev. Lett. 83 (1999) 5090.

[62] P. Mohanty, Physica B 280 (2000) 446.

[63] V. E. Kravtsov, B.L. Altshuler, Phys. Rev. Lett. 84 (2000) 3394.

[64] B.L. Altahuler, A.G. Aronov, Phys. Rev. Lett. 44 (1980) 1288.

[65] B.L. Altshuler, A.G. Aronov, and D.E. Khmelnitsky, J. Phys. C 15 (1982) 7367.

[66] E. Efetov, Advances In Phys. 32 (1983)53.

[67] R.G. Jordan, Contemp. Phys. 15 (1974) 375.

[68] Seith and Wever, unpublished, presented in [81].

[69] V.B. Fiks, Fizika Tverdogo Tela 6 (1964) 1589.

[70] V.B. Fiks, Proc. Europhys. Conf. *Atomic Transport in Solids and Liquids* eddited by A. Lodding and T. Lagerwall (1971) 3.

[71] H.B. Hutington, A.R. Grone, J. Phys. Chem. Solids 20 (1961) 76.

[72] H.B. Hutington, and S.-C. Ho, J. Phys. Soc. Jpn. 18 (1962) 202.

[73] H. Jones, Rep. Prog. Phys. 36 (1973) 1425 and references there in.

[74] D.T. Peterson, Proc. Europhys. Conf. *Atomic Transport in Solids and Liquids* eddited by A. Lodding and T. Lagerwall (1971) 104.

[75] O.N. Carlson, F.A. Schmidt, D.T. Peterson, Proc. 10^{th} Rare Earth Research Conf. CONF-730402-P2 II (1973) 701.

[76] D. Fort, J. Less-Common Metals, 134 (1987) 45.

[77] D. Fort, J. Less-Common Metals, 166 (1990) 173.

[78] D. Fort, V.K. Pecharsky,K.A. Gschneider, J. Alloys and Compd. 226 (1995) 190.

[79] V.K. Pecharsky,K.A. Gschneider, D. Fort, Phys. Rev. B, 47 (1993) 5063.

[80] V.K. Pecharsky,K.A. Gschneider, D. Fort, Phys. Rev. Lett., 78 (1997) 4281.

[81] R.G. Jordan, D.W. Jones, M.G. Hall, 'The Growth of Gadolinium Single Crystals During Solid State Electrotransport', *Proc. Int. Conf. on Crystal Growth eddited by N. Kato, K.A. Jackson, J.B. Mullin, Tokyo, Japan*, 4 (1974) 25.

[82] R.G. Jordan, D.W. Jones, J. Less-Common Metals, 31 (1973) 125.

[83] K. Maezawa, Y. Saito, S. Wakabayashi, Jpn. J. of Appl. Phys, 24 (1985) 28.

[84] K. Maezawa, S. Sakane, T. Fukuhura et al, Physica B 259-261 (1999) 1091.

[85] H. Aoki, S. Uji, A.K. Albessard et al, Phys. Rev. Lett. 71 (1993) 2110.

[86] Y. Onuki, I. Umehara, A.K. ALbessard et al, J. Phys. Soc. Jpn. 61 (1992) 960.

[87] Y. Haga, E. Yamamoto, N. Kimura et al, J. Magn. Magn. Mater. 177 (1998) 437.

[88] T. Roisnel, J. Rodrguez-Carvajal, International Union for Crystallography, Newletter No. 20 (1998), *http://www-llb.cea.fr/fullweb/winplotr/winplotr.htm*

[89] H.M. Rietveld, Acta Cryst. 22 (1967) 151; H.M. Rietveld, J. Applied Cryst. 2 (1969) 65.

[90] L.B.McCusker et al., J. Appl. Cryst. 32 (1999) 36.

[91] V. Valvoda, M. Polcarová, P. Lukáč, Základy strukturní analýzy, Karolinum Praha, 1992.

[92] P. Thompson, D.E. Cox,J.B. Hastings, J. Appl. Cryst. 20 (1987) 79.

[93] L.W. Finger, J. Appl. Cryst. 31 (1998) 111.

[94] PPMS Quantum Design, Software and Hardware Manuals, San Diego, 1999.

[95] M. Rotter, H. Muller, E. Gratz E et al, Rev. Sci. Instr. 69 (1998) 2742.

[96] H. Krug, M. Doerr, D. Eckert et al, Physica B 294-295 (2001) 605.

[97] D. Eckert, R. Grssinger, M. Doerr et al, Physica B 294-295 (2001) 705.

[98] P. Kerschl, A. Handstein, K. Khlopkov et al, J. Magn. Magn. Mater. in press

[99] J. Baruchel, J. L. Hodeau, M. S. Lehmann et al, Neutron and synchrotron radiation for condensed matter studies I, Europe media duplication S.A., 1994.

[100] J. Baruchel, J. L. Hodeau, M. S. Lehmann, et al, Neutron and synchrotron radiation for condensed matter studies II, Europe media duplication S.A., 1994.

[101] D. L. Price, K. Skoeld, Methods of experimental physics-Neutron scattering part A, B, C, vol. 23, Academic press, Inc., 1987.

[102] N. Marcano, J. I. Espeso, J. C. Gómez Sal et al, Phys. Rev. B 71 (2005) 134401.

[103] Drulis, H., Drulis, M., in: Landoldt- Brnstein, NS (Wijn, H.P.J., ed.), Berlin, Heidelberg, New York : Springer, Vol.III/19d1 (1991) 1.

[104] Handbook on the Physics and Chemistry of Rare Earths, Elsevier-North Holland, ed. by K.A. Gschneidner, J.-C. Bnzli, V. Pecharsky, vol. 1 - 34, details on volume content: http://www.info.sciencedirect.com/content/books/handbooks/collections/physchem/.

[105] Handbook of magnetic materials, ed. K.H.J Buschow, Elsevier-North Holland, vol. 1, 5, 7, 9, 11, 12, 14, details on volume content: http://www.elsevier.com/wps/find/bookdescription.cws_home/500754/description.

[106] Book Series Landolt-Brnstein - Group III, Condensed Matter, ed. by J.J.M. Franse, R. Gersdorf, W. Suski, H. Troc, Volume 32D, Springer Berlin Heidelberg, 2004.

[107] D.A. Jehan, D.F. McMorrow, R.A. Cowley et al, Phys. Rev. B 48 (1993) 5594.

[108] K. Shimizu, T. Kimura, S. Furomoto et al, Nature 412 (2001) 316.

[109] Handbook of Chemistry and physics, 61st ed., edited by R. Weast and M. Astle (CRC Press. Inc., Boca Raton, Folrida, 1980 - 1981).

[110] D.C. Koskenmaki, K.A. Gschneidner, in Handbook on the physics and chemistry of rare earths: Metals, edited by K. A. Gschneidner, L. Eyring (North- Holland Physics Publishing, Amsterdam, 1981), Vol. 1, Chap. 4.

[111] G. Eliashberg, H. Capellmann, JETP Lett. 67 (1998) 125.

[112] L. Davis, L. H. Adams, J. Phys. Chem. Solids 25 (1964) 379.

[113] S.V. Konovalov, V.V. Singer, I.Z. Radovskij et al, Solid State Phys. 29 (1987) 1768.

[114] Y. Aoki, H. Sato, Y. Komaba et al, Phys. Rev. B 54 (1996) 12172.

[115] V.G. Orlov, I.V. Kurchatov, Solid State Commun. 67 (1988) 689.

[116] M.R. MacPherson, G.E. Everett, D. Wohlleben et al, Phys. Rev. Lett. 26 (1971) 20.

[117] F.H. Spedding, A.H. Daane, K.W. Herrmann, Acta Crystallogr.9 (1956) 559

[118] G.I. Kataev, M.R. Sattarov, A.M. Tishin, Phys. Status Solid. (a) 114 (1989) K79.

[119] T.J. McKenna, S.J. Campbell, Chaplin et al, J. Phys.: Condens. Matter 3 (1991) 1855.

[120] S.Y. Dankov, Yu.I. Spichkin, A.M. Tishin, J. Magn. Magn. Mater. 152 (1996) 208.

[121] C. Rau, C. Jin, M. Robert, J. Appl. Phys. 63 (1988) 3667.

[122] J. Baruchel, J. Sandonis, A. Pearce, Physica B 156-157 (1989) 765.

[123] G.I. Kataev, M.R. Sattarov, A.M. Tishin, Phys. Status Solidi (a) 114 (1989) K79.

[124] S.A. Nikitin, A.M. Tishin, S.E. Bykhover, Phys. Status Solidi (a) 114 (1989) K99.

[125] S.A. Nikitin, A.M. Tishin, R.V. Bezdushnyi et al, J. Magn. Magn. Mater. 92 (1991) 397.

[126] P.M. Gehring, L. Rebelsky, D. Gibbs et al, Phys. Rev. B 45 (1992) 243.

[127] S. Kawano, N. Achiwa, A. Onodera et al, Physica B 180-181 (1992) 46.

[128] T.J. McKenna, S.J. Campbell, D.H. Chaplin et al, J. Magn. Magn. Mater. 124 (1993) 105.

[129] S. Kawano, J.A. Fernandez-Baca, R.M. Nicklow, J. Appl. Phys. 75 (1994) 6060.

[130] E. Arenholz, E. Navas, K. Starke et al, Phys. Rev. B 51 (1995) 8211.

[131] C. Dufour, K. Dumesnil, M. Vergnat et al, J. Magn. Magn. Mater. 140-144 (1995) 771.

[132] S.Y. Dan'kov, Yu.I. Spichkin, A.M. Tishin, J. Magn. Magn. Mater. 152 (1996) 208.

[133] K.Ya. Mulyukov, G.F. Korznikova, I.Z. Sharipov, Phys. Status Solidi (a) 161 (1997) 493.

[134] S.Y. Dankov, Yu.I. Spichkin, A.M. Tishin, J. Magn. Magn. Mater. 152 (1996) 208.

[135] B. Watson, N. Ali, J. Phys.: Condens. Matter 8 (1996) 1797.

[136] J.W. Cable , E.O. Wollan , W.C. Koehler et al, Phys. Rev. B 140 (1965) 1896.

[137] D. Gibbs, J. Bohr, J.D. Axe et al, Phys. Rev. B 34 (1986) 8182.

[138] S. Kawano, B. Lebech, N. Achiwa, J. Phys.: Condens. Matter 5 (1993) 1535.

[139] D.A. Jehan, D.F. McMorrow, J.A. Simpson et al, Phys. Rev. B 50 (1994) 3085.

[140] B. Watson, N. Ali, J. Phys.: Condens. Matter 7 (1995) 4713.

[141] K.A. Gschneidner, V.K. Pecharsky, D. Fort, Phys. Rev. Lett., 78 (1997) 4281.

[142] B. Watson, N. Ali, J. Alloys Compounds 250 (1997) 662.

[143] V.K. Pecharsky, K.A. Gschneidner, D. Fort, D.: Phys. Rev. B 47 (1993) 5063.

[144] R.A. Cowen, B. Stolzman, R.S. Averback et al, J. Appl. Phys. 61 (1987) 3317.

[145] J.A. Borchers, M.B. Salamon, R. Du et al, J. Appl. Phys. 63 (1988) 3458.

[146] J.J. Rhyne, R.W. Erwin, J. Borchers et al, Physica B 159 (1989) 111.

[147] J.J. Rhyne, R.W. Erwin, J. Borchers et al, Phys. Scr. T 29 (1989) 31.

[148] H.U. Astrom, G. Benediktsson, J. Phys. Condens. Matter 1 (1989) 4381.

[149] J. Bohr, J. Magn. Magn. Mater. 83 (1990) 530.

[150] J.A. Borchers, M.B. Salamon, R.W. Erwin et al, Phys. Rev. B 43 (1991) 3123.

[151] S.K. Godovikov, S.A. Nikitin, A.M. Tishin, Phys. Lett. A 158 (1991) 265.

[152] R.S. Eccleston, S.B. Palmer, J. Phys.: Condens. Matter 4 (1992) 10037.

[153] H. Lin, M.F. Collins, T.M. Holden et al, Phys. Rev. B 45 (1992) 12873.

[154] O.V. Snigirev, A.M. Tishin, A.V. Volkozub, J. Magn. Magn. Mater. 111 (1992) 149.

[155] A.S. Bulatov, V.F. Dolzhenko, A.V. Korniets, J. Magn. Magn. Mater. 147 (1995) 403.

[156] S. Kawano, B. Lebech, N. Achiwa et al, J. Magn. Magn. Mater. 140-144 (1995) 763.

[157] K. Tajima, Y. Shinoda, M. Tadakuma, J. Magn. Magn. Mater. 140-144 (1995) 765.

[158] M.J. Conover, A. Kaldowsky, C.P. Flynn, Phys. Rev. B 53 (1996) R2938.

[159] G. Helgsen, Y. Tanaka, J.P. Hill et al, Phys. Rev. B 56 (1997) 2635.

[160] A. del Moral, M. Ciria, J.I. Arnaudas et al, J. Appl. Phys. 81 (1997) 5311.

[161] H. Tang, D. Weller, T.G. Walker et al, Phys. Rev. Lett. 71 (1993) 444.

[162] E. Vescovo, C. Carbone, O. Rader, Phys. Rev. B 48 (1993) 7731.

[163] C. Rau, S. Eichner, Phys. Rev. B 34 (1986) 6347.

[164] J.J. Rhyne, R.W. Erwin, J. Borchers et al, Physica B 159(1989) 111.

[165] M. Farle, K. Baberschke, Phys. Rev. Lett. 58 (1987) 511.

[166] P. Grnburg, R. Schreiber, Y. Pang et al, Phys. Rev. Lett. 57 (1986)2442.

[167] M.B. Salamon, S. Sinha, J.J. Rhyne et al, Phys. Rev. Lett. 56 (1986) 259.

[168] S. Sinha, J. Cunningham, R. Du, J. Magn. Magn. Mater, 54 (1986) 773.

[169] C. F. Majkrzak, J.W. Cable, J. Kwo et al, Phys. Rev. Lett 56 (1986) 2700.

[170] J. Unguris, R.J. Celotta, D.T., Pierce, Phys. Rev. Lett. 67 (1991) 140.

[171] Rührig, M., Schäfer, R., Hubertet al, Phys. Status Solidi (a) 125 (1991) 635.

[172] C.F. Majkrzak, J. Kwo, M. Hong et al, Adv. Phys. 40(1991) 99.

[173] G. Helgsen, Y. Tanaka, J.P. Hill et al, Phys.Rev. B 56 (1997) 2635.

[174] J.A. Borchers, M.B. Salamon, R.W. Erwin et al, Phys. Rev. B43 (1991) 3123.

[175] J.P. Bucher, D.C. Douglass, L.A. Bloomfield, Phys. Rev. Lett. 66 (1991) 3052.

[176] H. Drulis, M. Drulis, in: Landoldt- Brnstein, NS (Wijn, H.P.J., ed.), Berlin, Heidelberg, NewYork : Springer, Vol.III/19d1 (1991), p.1.

[177] Wu Ruqian, A.J. Freeman, J. Magn. Magn. Mater. 99 (1991) 81.

[178] D.A. Jehan, D.F. McMorrow, R.A. Cowley et al, Phys. Rev. B 48 (1993) 5594.

[179] D.A. Jehan, D.F. McMorrow, J.A. Simpson et al, Phys. Rev. B 50 (1994) 3085.

[180] C. Dufour, K. Dumesnil, M. Vergnat et al, J. Magn. Magn. Mater. 140-144 (1995) 771.

[181] R.S. Beach, J.A. Borchers, R.W. Erwin et al, J. Appl. Phys. 69 (1991) 4335.

[182] I. Aruna, B.R. Mehta, L.K. Malhotra et al, Adv. Functional Mater. 15 (2005) 131.

[183] M.O. Oyewumi, R.A. Yokel, M. Jay et al, J. Control. Release 95 (2004) 613.

[184] M.O. Oyewumi, S.Q. Liu, J.A. Moscow et al, Bioconjugate Chem. 14 (2003) 404.

[185] J.A. Nelson, L.H Bennett, M.J. Wagner, J. Amer. Chem. Soc. 124 (2002) 2979.

[186] J.A. Ascencio, A.C. Rincon, G. Canizal, J. Phys. Chem. B 109 (2005) 8806.

[187] J.Q. Wang, Q.H. Yu, X.R. Gao et al, J. Rare Earth. 21 (2003) 127.

[188] V.D. Kosynkin, S.D. Moiseev, C.H. Peterson et al, J. Alloys Compd. 192 (1993) 192 118.

[189] J. Spooner, K.A. Grace, N. Robjohns, Cim Bull. 84 (1991) 125.

[190] D.Z. Wang, Q. Wan, Y.C. Yang, J. Rare Earths 14 (1996) 223.

[191] D.X. Zhang, L.D. Sun, D.L. Niu, J. Rare Earth. 13 (1995) 290.

[192] J. Yan, J. Xiong, China's rare earth industry: Past, present and future, 1999.

[193] D.A. Bertuol, A.M. Bernardes, J.A.S. Tenorio, J. Power Source. 160 (2006) 1465.

[194] A. Facchini, A. Teatini, G. Verganti, Chimica & Industria 51 (1969) 970.

[195] H.G. Fu,D.N. Zou, J. Rare Earth. 22 (2004) 68.

[196] J.B. Hedrick, S.P. Sinha, V.D. Kosynkin, J. Alloys Compd. 250 (1997) 467.

[197] H.F. Li, F.Q. Guo, Z.F. Zhang et al, J. Alloys Compd. 408 (2006) 995.

[198] G. Morteani, European Journal of Mineralogy 3 (1991) 641.

[199] P.F. Nogueira, F.B. Neto, Adv. Powder Tech. 299 (1999) 200.

[200] M. Owen,R. Tipman, Cim Bull. 92 (1999) 65.

[201] C.A. Pereira, A.E.C. Peres, Mineral. Eng. 10 (1997) 1291.

[202] L. Shang,X.Y. Lui, Worlds Poultry Sci. J. 53 (1997) 369.

[203] D. Sheng, M.D. Li, C.L. Yuan, J. Rare Earth. 23 (2005) 369.

[204] W.P. Song, P. Chen, H.G. Wan et al, J. Rare Earth. 23 (2005) 508.

[205] N.V. Thakur, D.V. Jayawant, N.S. Iyer et al, Hydrometallurgy 34 (1993) 99.

[206] T. Uda, Mater. Trans. 43 (2002) 55.

[207] J.A. Van Orman, T.L. Grove, N. Shimizu, Earth and Planetary Sci. Lett. 198 (2002) 93.

[208] E. Baumgartner, E. Treibacher, Mater. Chem. Phys. 31 (1992) 89.

[209] J.M. Grau, L. Data, X.L. Seoane et al, Catalysis Lett. 53 (1998) 161.

[210] J.S. Javorniczky, P.J. Newman, D.R. Macfarlane et al, J. Non-Crystalline Solids 184 (1995) 249.

[211] Y. Liu, X.Y. Wang, X. Bai, J. Rare Earth. 23 (2005) 41.

[212] Y. Shodai, M. Inaba, K. Onoda et al, J. Rare Earth. 24 (2006) 1.

[213] K. Wakui, K. Satoh, G. Sawada et al., J. Jpn. Petroleum Inst. 42 (1999) 307.

[214] S.H. Zeng, X. Bai, X.Y. Wang et al, J. Rare Earth. 24 (2006) 177.

[215] J.R. Gao, X.P. Song, X. Wang, J. Rare Earth. 16 (1998) 105.

[216] J.P. Liu, H.J. Li, H.S. Xue, J. Rare Earth. 22 (2004) 117.

[217] O. Mao, Z. Altounian, J.O. Strom-Olsen et al, J. Mater. Research 14 (1999) 750.

[218] L.P. Wang, E.J. Guo, H.B. Chen et al, J. Rare Earth. 24 (2006) 103.

[219] YS Wang ,QD Wang , CJ Ma et al, Mater. Sci. Eng. A 342 (2003) 178.

[220] Y.C. Yang, Rare Met. Mater. Eng. 29 (2000) 78.

[221] R.A. Barrea, E.V. Bonzi, Radiation Phys. Chem. 59 (2000) 347.

[222] O.G. de Lucio, J. Miranda, Revista Mexicana de Fisica 50 (2004) 319.

[223] O.G. de Lucio, J. Miranda, Nuclear Instruments & Methods in Phys. Research Section B-Beam Interactions with Materials and Atoms 248 (2006) 47.

[224] Denker A, Opitz-Coutureau J. Proton-induced x-ray emission using 68 MeV protons. X-Ray Spectrometry 2004; 33: 61-66.

[225] G. Pepper, T.J. Gray, J.L. Duggan et al., Bulletin Amer. Phys. Soc. 19 (1974) 569.

[226] G. Pepper, R.D. Lear, T.J. Gray et al, Bulletin Amer. Phys. Soc. 19 (1974) 88.

[227] H. Adachi, H. Ino, H. Miwa, Phys. Rev. B 56 (1997) 349.

[228] R. Ahuja, S.Auluck, B. Johansson et al, Phys. Rev. B 50 (1994) 5147.

[229] L.T. Baczewski, D. Givord, J.M. Alameda et al. Acta Physica Polonica A 83 (1993) 629.

[230] M.S.S. Brooks ,O. Eriksson, B. Johansson, J. Alloys Compd. 223 (1995) 204.

[231] C. De Nadai, A. Mirone, S.S. Dhesi et al. Phys. Rev. B (2004) 69.

[232] O. Eriksson, M.S.S. Brooks, B. Johansson et al, J. Appl. Phys. 69 (1991) 5897.

[233] S.K. Godovikov, Izvestiya Akademii Nauk Sssr Seriya Fizicheskaya 50 (1986) 2315.

[234] H. Ishii, J. Low Temp. Phys. 135 (2004) 579.

[235] B. Johansson, L. Nordstrom, O. Eriksson et al Phys. Scripta T39 (1991) 100.

[236] J. Kanamori, J. Alloys Compd. 408 (2006) 2.

[237] A.R. Mackintosh, J. Jensen, Physica B 180 (1992) 1.

[238] K. Maiti, M.C. Malagoli, A. Dallmeyer et al, Pramana-Journal of Phys. 58 (2002) 725.

[239] K. Maiti, M.C. Malagoli, A. Dallmeyer et al, Phys. Rev. Lett. (2002) 88.

[240] H.R. Ott, Acta Physica Polonica A 85 (1994) 7.

[241] A.Y. Perlov, S.V. Halilov, H. Eschrig, Phys. Rev. B 61 (2000) 4070.

[242] F. Pourarian, Physica B 321 (2002) 18.

[243] S.M. Saini, N. Singh, T. Nautiyal et al, Solid State Commun. 140 (2006) 125.

[244] H.L. Skriver, N.M. Rosengaard, Phys. Rev. B 46 (1992) 7157.

[245] K. Starke, E. Navas, E. Arenholz et al, Ieee Transactions on Magnetics 31 (1995) 3313.

[246] A. Stunault, N. Bernhoeft, C. Vettier et al, J. Magn. Magn. Mater 226 (2001) 1116.

[247] T. Trappmann, M. Gajdzik, C. Surgers et al, EuroPhys. Lett. 39 (1997) 159.

[248] I. Turek, J. Rusz, M. Divis, J. Magn. Magn. Mater 290 (2005) 357.

[249] P. Vajda, Physica B 289 (2000) 435.

[250] P. Vajda, J. Alloys Compd. 404 (2005) 131.

[251] J. Voigt, U. Rucker, S. Nerger et al ., J. Magn. Magn. Mater 240 (2002) 559.

[252] R. Wiesendanger, M. Bode, Solid State Commun. 119 (2001) 341.

[253] W. Dai, B.G. Shen, D.X. Li et al, Sci. China Series E-Technological Sciences 39 (1996) 284.

[254] K.A. Gschneidner, V.K. Pecharsky, J. Rare Earth. 24 (2006) 641.

[255] K. Latka, L. Tomkowicz, J. Solid State Chem. 168 (2002) 331.

[256] Y. Long, Y.P. Chen, J. Rare Earth. 21 (2003) 447.

[257] A.M. Tishin, J. Appl. Phys. 68 (1990) 6480.

[258] W. Wu, D.W. Lu, J. Rare Earth. 22 (2004) 654.

[259] W. Wu, Z. Feng, L.J. Guo, Journal of Materials Science & Technology 22 (2006) 839.

[260] J.F. Deng, T. Sinks, L. Elliott et al, Brit. J. Industrial Med. 48 (1991) 609.

[261] Z.Y. Hu, H. Richter, G. Sparovek et al, J. Plant Nutrition 27 (2004) 183.

[262] M. Kamijo, T. Suzuki, K. Kawai et al, J. Biosci. Bioeng. 87 (1999) 340.

[263] C.F. Liu, L.H. Jin, C.Q. Liu, J. Rare Earth. 22 (2004) 691.

[264] H.F. Wu , X.J. Li, P.Q. Liao et al, J. Rare Earth. 23 (2005) 245.

[265] H.F. Wu , X.J. Li, J.H. Feng et al, J. Rare Earth. 24 (2006) 108.

[266] L.N. Yu, D.F. Wang, H.Y. Li et al, J. Rare Earth. 24 (2006) 125.

[267] S. Buckingham, J. Maheswaran, B. Meehan et al, Rare Earths '98 315-3 (1999) 339.

[268] T.Y. Chai, H. Yang, J. Rare Earth. 22 (2004) 752.

[269] A. Corgne, B.J. Wood, Contributions to Mineralogy and Petrology 149 (2005) 85.

[270] M. Croker, Powder Metal. Int. 24 (1992) 24 106.

[271] X.L. Cui, Q.H. Yang, X.X. Fu, J. Rare Earth. 21 (2003) 124.

[272] P.G. Eriksson, K.C. Condie, H. Tirsgaard et al, Sediment. Geo. 120 (1998) 5.

[273] R.E. Gayoso, S.J. Nassiff, J. Radioanal. Nucl. Chem. 230 (1998) 161.

[274] G.S. Guo, G.T. Wang, Z.T. Sui, J. Rare Earth. 21 (2003) 132.

[275] C.K. Gupta, N. Krishnamurthy, Int. Mater. Rev.37 (1992) 197.

[276] M. Hecht, E. Nonon, Int. J. Cast Met. Res. 16 (2003) 307.

[277] E. Kaschnitz, P. Reiter, G. Pottlacher, Int. J. ThermoPhys. 26 (2005) 1229.

[278] T. Kurobori, T. Matsuki, K. Somaiah et al, J. Appl. Phys. 37 (1998) 1907.

[279] M. Peisach, C.A. Pineda, Nuclear Instruments & Methods in Physics Research Section B 49 (1990) 10.

[280] C.A. Pineda , M.Peisach, J. Radioanal. Nucl. Chem. 151 (1991) 387.

[281] A.Y. Stankovsky, V.V. Artisyuk, M. Saito, Nucl. Tech. 142 (2003) 306.

[282] S.S. Saxena, P. Monthoux, NATURE 427 (2004) 799.

[283] S. Sullow, G.J. Niewuwenhuys, A.A. Menovsky et al, Physica B 199 (1994) 644.

[284] H. Sato, Y. Abe, H. Okada et al, Phys. Rev. B 62 (2000) 15125.

[285] N. Metoki, K. Kaneko, T.D. Matsuda et al, J. Phys. Condens. Mater. 16 (2004) L207.

[286] E.A. Goremychkin, R. Osbourne, Phys. Rev. B 47 14280 (1993).

[287] E.A. Goremychkin, R. Osbourne, Phys. Rev. B 47 14580(1993).

[288] S. Horn, E. Hollandmoritz, M. Loewenhaupt et al, Phys. Rev. B 23 3171(1981).

[289] L. Regnault, WAC Erkelens, J. Rossatmignod et al, Phys. Rev. B 38 4481 (1988).

[290] K. Kuwahara, K. Iwasa, M. Kohgi et al, Physica B 385, 82-84,(2006).

[291] Kohgi M, Iwasa K, Nakajima M et al, J. Phys. Soc. Japan 72 1002 (2003).

[292] M. Yogi, Y. Kitaoka, S. Hashimoto et al, Phys. Rev. Lett. 93, (2004).

[293] M. Yogi, Y. Kitaoka, S. Hashimoto et al, Physica B 359, 389-391 (2005).

[294] K. Ueda, K. Hamamoto, T. Kohara et al, Physica B 359, 374-376 (2005).

[295] K. Izawa, Y. Kasahara, Y. Matsuda et al, Phys. Rev. Lett. 94, (2005).

[296] I. Bonalde, W. Bramer-Escamilla, E. Bauer, Phys. Rev. Lett. 94, (2005).

[297] R.P. Kaur, D.F. Agterberg, M. Sigrist, Phys. Rev. Lett. 94, (2005).

[298] M. Ishikawa, N. Takeda, Solid State Commun. 133, 249-251 (2005).

[299] G. Motoyama, S. Yamamoto, Y. Oda et al, Physica B 359, 187-189 (2005).

[300] E. W. Scheidt, F. Mayr, G. Eickerling et al," Journal of Phys.-Condensed Matter 17, L121-L124 (2005).

[301] J.S. Kim, D.J. Mixson, D.J. Burnette et al, Phys. Rev. B 71 (2005) 212505.

[302] D. P. Young, M. Moldovan, X. S. Wu et al, Phys. Rev. Lett. 94, (2005).

[303] E. Bauer, G. Hilscher, H. Michor et al, Physica B 359, 360-367 (2005).

[304] E. Bauer, R. Lackner, G. Hischer et al, J. Phys. Condens. Mater. 17, 1877-1888 (2005).

[305] E. Bauer, G. Hilscher, H. Michor, Czech. J. Phys. 54, D401-D406 (2004).

[306] J. Vejpravova, J. Prokleska, V. Sechovsky, Czech. J. Phys. 54, D407-D410 (2004).

[307] J. Vejpravova, J. Prokleska, V. Sechovsky, Physica B 359, 377-379 (2005).

[308] R. Lackner, M. Sieberer, H. Michor et al, J. Phys. Condens. Mater. 17 (2005) S905.

[309] O.L. Sologub, K. Hiebl, P.S. Salamakha et al, J. Alloys Compd. 360 (2003) 54.

[310] A.I. Tursina, A.V. Gribanov, H. Noel et al, J. Alloys Compd. 395, 93 (2005).

[311] A.I. Tursina, A. Gribanov, H. Noel et al, Acta Crystallogr. 60, i8 (2004).

[312] E. Bauer, R. Lackner, G. Hilscher, et al, Phys. Rev. B (2006) 73 104405.

[313] S. Fujimoto, J. Phys. Soc. Jpn., 75 (2006) 0031.

[314] K. Nakatsuji A. Sumiyama, Y. Oda et al, J. Phys. Soc. Jpn., 75 (2006) 0031.

[315] K. Borkje, A. Sudbo, Phys. Rev. B, 74 (2006) 1098-0121.

[316] T. Yasuda, H. Shishido, T. Ueda et al, J. Phys. Soc. Jpn. 73, 1657-1660 (2004).

[317] A.I. Tursina, A.V. Gribanov, H. Noel et al, J. Alloys Compd. 383, 239-241 (2004).

[318] T. Takimoto, Physica B 359, 747-749 (2005).

[319] T. Takeuchi, M. Shiimoto, H. Kohara et al, Physica B 359, 380-382 (2005).

[320] T. Takeuchi, S. Hashimoto, T. Yasuda et al, J. Phys. Condens. Mater. 16, L333-L342 (2004).

[321] H. Shimahara, J. Phys. Soc. Jpn. 73, 2635-2638 (2004).

[322] K.V. Samokhin, Phys. Rev. B 70, (2004).

[323] Y. Onuki, T. Yasuda, H. Shishido et al, Physica B 359, 368-370 (2005).

[324] M. Nicklas, G. Sparn, R. Lackner et al, Physica B 359, 386-388 (2005).

[325] N. Metoki, K. Kaneko, T. D. Matsuda et al, Physica B 359, 383-385 (2005).

[326] S.Hashimoto, T. Yasuda, T. Kubo et al, J. Phys. Condens. Mater. 16, L287-L296 (2004).

[327] P.A. Frigeri, D.F. Agterberg, M. Sigrist, New J. Phys. 6, (2004).

[328] P.A. Frigeri, D.F. Agterberg, A. Koga et al, Physica B 359, 371-373 (2005).

[329] A. Amato, E. Bauer, C. Baines, Phys. Rev. B 71, (2005).

[330] M. Yoshizawa, M. Tamura, M. Ozawa et al, J. Phys. Soc. Jpn. 66, 2355-2366 (1997).

[331] M. Yoshizawa, H. Kitaichi, M. Nakamura et al, J. Magn. Magn. Mater 177, 305-306 (1998).

[332] S.H. Yang, H. Kumigashira, T. Yokoya et al, Phys. Rev. B 53, 11946-11948 (1996).

[333] A. Yamashita, K. Ishii, T. Yokoo et al, Phys. Rev. Lett. 79, 3771-3774 (1997).

[334] K. Yagasaki, M. Hedo, T. Nakama, J. Phys. Soc. Jpn. 62, 3825-3828 (1993).

[335] K. Yagasaki, M. Hedo, T. Nakama et al, Physica B 194, 2089-2090 (1994).

[336] E. Wuilloud, Y. Baer, M.B. Maple, Helvetica Physica Acta 55, 563 (1982).

[337] E. Wuilloud, Y. Baer, M.B. Maple, Phys. Lett. A 97, 65-69 (1983).

[338] B. Wolf, C. Hinkel, S. Holtmeier et al, J. Low Temp. Phys. 107, 421-441 (1997).

[339] A. A. Tulapurkar, D. Heidarian, S. Sarkar et al, Physica C 355, 59-64 (2001).

[340] V. Tsvyashchenko, L.N. Fomicheva, A.A. Sorokin et al, Phys. Rev. B 65, (2002).

[341] G.X. Tessema, J. Peyrard, A. Nemoz et al, Zeitschrift fur Physikalische Chemie-Wiesbaden 116, 209-214 (1979).

[342] K. Tenya, S. Yasunami, T. Tayama et al, J. Phys. Soc. Jpn. 68, 224-231 (1999).

[343] K. Tenya, S. Yasunami, T. Tayama et al, Physica B 261, 692-693 (1999).

[344] T. Suzuki, H. Goshima, S. Sakita et al, J. Phys. Soc. Jpn. 65, 2753-2756 (1996).

[345] T. Suzuki, H. Goshima, S. Sakita et al, Physica B 230, 176-178 (1997).

[346] T. Suzuki, N. Okuda, H. Goshima et al, J. Magn. Magn. Mater 177, 415-416 (1998).

[347] J. Suzuki, N. Metoki, Y. Haga et al, Physica B 241, 871-873 (1997).

[348] H. Sugawara, H. Sato, T. Yamazaki et al, J. Phys. Soc. Jpn. 64, 4849-4855 (1995).

[349] N.E. Sluchanko, V. V. Glushkov, S. V. Demishev et al, Jetp Lett. 69, 798-803 (1999).

[350] H. Sato, Y. Kobayashi, H. Sugawara et al, J. Phys. Soc. Jpn. 65, 1536-1539 (1996).

[351] H. Sakata, N. Nishida, M. Hedo et al, J. Phys. Soc. Jpn. 69, 1970-1973 (2000).

[352] N.L. Saini, S. Agrestini, D. Di Castro et al, J. Alloys Compd. 317, 542-545 (2001).

[353] N.L. Saini, S. Agrestini, E. Amato et al, Phys. Rev. B 70, (2004).

[354] S.B. Roy, A. K. Pradhan, P. Chaddah, Superconductor Science & Technology 7, 602-605 (1994).

[355] S.B. Roy, B.R. Coles, J. Phys. Condens. Mater. 6, L663-L665 (1994).

[356] S.B. Roy, A.K. Pradhan, P. Chaddah, Phys. Rev. B 52, R9847-R9850 (1995).

[357] S.B. Roy, A.K. Pradhan, P. Chaddah, Physica C 271, 181-186 (1996).

[358] S.B. Roy, P. Chaddah, Phys. Rev. B 55, 11100-11102 (1997).

[359] S.B. Roy, P. Chaddah, L.E. Delong, Physica C-Superconductivity and Its Applications 304, 43-50 (1998).

[360] S.B. Roy, P. Chaddah, S. Chaudhary, J. Phys. Condens. Mater. 10, 8327-8340 (1998).

[361] S.B. Roy, P. Chaddah, S. Chaudhary, J. Phys. Condens. Mater. 10, 4885-4900 (1998).

[362] S.B. Roy, P. Chaddah, L.E. Delong, Physica C 308, 312 (1998).

[363] S.B. Roy, P. Chaddah, Pramana-J. Phys. 53, 659-684 (1999).

[364] S.B. Roy, S. Chaudhary, P. Chaddah et al, Physica C 322, 115-122 (1999).

[365] S.B. Roy, P. Chaddah, Physica B 262, 20-30 (1999).

[366] S.B. Roy, P. Chaddah, S. Chaudhary, Solid State Commun. 109, 427-432 (1999).

[367] S.B. Roy, P. Chaddah, S. Chaudhary, Phys. Rev. B 62, 9191-9199 (2000).

[368] G. Ravikumar, T.V.C. Rao, P.K. Mishra et al, Physica C 276, 9-17 (1997).

[369] N.G. Patil, S.S. Banerjee, S. Saha et al, Physica C 282, 2043-2044 (1997).

[370] J. Osterwalder, T. Riesterer, L. Schlapbach et al, Phys. Rev. B 31, 8311-8313 (1985).

[371] Y.G. Naidyuk, A.V. Moskalenko, I.K. Yanson et al, Low Temperature Phys. 24, 374-376 (1998).

[372] A.P. Murani, R.S. Eccleston, Physica B 241, 850-852 (1997).

[373] H. Mukuda, K. Ishida, Y. Kitaoka et al, J. Phys. Chem. Solid. 59, 2163-2165 (1998).

[374] A.V. Moskalenko, Y.G. Naidyuk, I.K. Yanson et al, Physica B 261, 690-691 (1999).

[375] A.V. Moskalenko, Y.G. Naidyuk, I.K. Yanson et al, Low Temp. Phys. 27, 613-615 (2001).

[376] T. Miyahara, T. Hanyu, H. Ishii et al, J. Phys. Soc. Jpn. 62, 4129-4136 (1993).

[377] S. Miraglia, M. Anne, H. Vincent et al, J. Less-Common Met. 153, 51-56 (1989).

[378] H. Matsui, T. Yasuda, M. Hedo et al, J. Phys. Soc. Jpn. 67, 3580-3584 (1998).

[379] K. Matsuda, Y. Kohori, T. Kohara, J. Phys. Soc. Jpn. 64, 2750-2753 (1995).

[380] K. Matsuda, Y. Kohori, T. Kohara, Physica B 224, 166-168 (1996).

[381] K. Matsuda, A. Sekiyama, S. Suga et al, Physica B 281, 729-730 (2000).

[382] Y.G. Kim, J. Y. Lee, Scripta Metallurg. Mater. 24, 2123-2128 (1990).

[383] J.S. Kang, C. G. Olson, M. Hedo et al, Phys. Rev. B 60, 5348-5353 (1999).

[384] T. Kagayama, R. Kitakoga, G. Oomi et al, Physica B 261, 694-695 (1999).

[385] K. Kadowaki, H. Takeya, K. Hirata, Phys. Rev. B 54, 462-468 (1996).

[386] R. Kadono, W. Higemoto, A. Koda et al, Phys. Rev. B 6322, (2001).

[387] K. Ishida, H. Mukuda, Y. Kitaoka et al, Zeitschrift fur Naturforschung Section A-A Journal of Physical Sciences 51, 793-796 (1996).

[388] Y. Inada, M. Hedo, T. Ishida et al, Physica B 230, 387-390 (1997).

[389] Y. Inada, M. Hedo, K. Sakurai et al, J. Magn. Magn. Mater 177, 389-390 (1998).

[390] A.D. Huxley, C. Paulsen, O. Laborde et al, J. Phys. Condens. Mater. 5, 7709-7718 (1993).

[391] D. Huxley, P.D. deReotier, A. Yaouanc et al, Phys. Rev. B 54, R9666-R9669 (1996).

[392] D. Huxley, R. Cubitt, D. McPaul et al, Physica B 224, 169-171 (1996).

[393] D. Huxley, J.X. Boucherle, M. Bonnet et al, J. Phys. Condens. Mater. 9, 4185-4195 (1997).

[394] D. Huxley, N.H. van Dijk, D.M. Paul et al, Physica B 261, 696-698 (1999).

[395] J. Herrmann, N. R. Dilley, S.H. Han et al Czech. J. Phys. 46, 785-786 (1996).

[396] M. Hedo, Y. Inada, T. Ishida, E. Yamamoto et al, J. Phys. Soc. Jpn. 64, 4535-4539 (1995).

[397] M. Hedo, Y. Inada, T. Ishida, E. Yamamoto et al, Physica B 237, 215-217 (1997).

[398] M. Hedo, Y. Inada, E. Yamamoto et al, J. Phys. Soc. Jpn. 67, 272-279 (1998).

[399] M. Hedo, Y. Inada, K. Sakuraiwa et al, Phil. Mag. B77, 975-1000 (1998).

[400] M. Hedo, Y. Kobayashi, Y. Inada et al, Physica B 261, 688-689 (1999).

[401] M. Hedo, T. Nakama, A.T. Burkov et al, Physica B 281, 88-89 (2000).

[402] D. Groten, S. Ramakrishnan, B. Becker et al, Physica B 230, 377-379 (1997).

[403] H. Goshima, T. Suzuki, T. Fujita et al, Physica B 224, 172-174 (1996).

[404] T. Ekino, H. Fujii, T. Nakama et al, Czech. J. Phys. 46, 783-784 (1996).

[405] N.R. Dilley, J. Herrmann, S.H. Han, et al, Physica C 265, 150-158 (1996).

[406] N.R. Dilley, J. Herrmann, S.H. Han et al, Physica B 230 , 332-334 (1997).

[407] N.R. Dilley, J. Herrmann, S.H. Han et al, Phys. Rev. B 56, 2379-2382 (1997).

[408] N.R. Dilley, M. B. Maple, Physica C 278, 207-212 (1997).

[409] S. Chaudhary, S.B. Roy, P. Chaddah et al, Superconductor Science & Technology 12, 308-314 (1999).

[410] S. Chaudhary, K. J. Singh, S.B. Roy et al, Physica C 377, 130-134 (2002).

[411] S. Takahashi, M. Tachiki, R. Modler et al, Physica C 263, 30-34 (1996).

[412] M. Tachiki, S. Takahashi, P. Gegenwart et al, Zeitschrift fur Physik B 100, 369-380 (1996).

[413] M. Tachiki, T. Koyama, S. Takahashi, Physica C 263, 1-11 (1996).

[414] S. Suga, A. Sekiyama, J. Electron Spect. Related Phenomena 124, 81-97 (2002).

[415] F. Steglich, R. Modler, P. Gegenwart et al, Physica C 263, 498-504 (1996).

[416] A. Sekiyama, T. Iwasaki, K. Matsuda et al, Nature 403, 396-398 (2000).

[417] A. Sekiyama, S. Suga, Physica B 312, 634-639 (2002).

[418] A. Sekiyama, S. Suga, S. Ueda et al, Solid State Commun. 121 , 561-564 (2002).

[419] R. Schleser, P.J.E.M. van der Linden, P. Wyder et al, Phys. Rev. B 67, (2003).

[420] H. Sato, Y. Aoki, Y. Kobayashi et al, Physica B 230, 402-405 (1997).

[421] G. Ravikumar, T. V. R. Rao, P. K. Mishra et al, Physica C 298, 122-132 (1998).

[422] G. Ravikumar, K. V. Bhagwat, V. C. Sahni et al, Phys. Rev. B 61, R6479-R6482 (2000).

[423] A. Palenzona, J. Alloys Compd. 176, 241-246 (1991).

[424] T. Nakama, M. Hedo, T. Maekawa et al, J. Phys. Soc. Jpn. 64, 1471-1475 (1995).

[425] S. Matsuo, S. Higashitani, Y. Nagato et al, J. Phys. Soc. Jpn. 67, 280-289 (1998).

[426] M. Matsumoto, J. Phys. Soc. Jpn. 70, 2505-2508 (2001).

[427] M. B. Maple, Y. Dalichaouch, M. C. deAndrade et al, J. Phys. Chem. Solid. 56, 1963-1968 (1995).

[428] M. B. Maple, M.C. deAndrade, J. Herrmann et al, J. Alloys Compd. 250, 585-595 (1997).

[429] Y. Kohori, K. Matsuda, T. Kohara, Hyperfine Interact. 121, 503-506 (1999).

[430] T. Kiss, F. Kanetaka, T. Yokoya et al, Phys. Rev. Lett. 94, (2005).

[431] Y. Kishimoto, Y. Kawasaki, T. Ohno, Phys. Lett. A 317, 308-314 (2003).

[432] Y. Kishimoto, Y. Kawasaki, T. Ohno et al, J. Magn. Magn. Mater 272-76, 509-510 (2004).

[433] R. Kadono, J. Phys. Condens. Mater. 16, S4421-S4438 (2004).

[434] Y. Homma, K. Sumiyama, H. Yamauchi et al, J. Phys. Soc. Jpn. 66, 1457-1464 (1997).

[435] P. Gegenwart, M. Deppe, M. Koppen et al, Annalen der Physik 5, 307-319 (1996).

[436] D. . Agterberg, V. Barzykin, L.P. Gorkov, Europhys. Lett. 48, 449-454 (1999).

[437] P. Walker, T. Rayment, R. M. Lambert, J. Catal. 117, 102-120 (1989).

[438] A. Sorokin, G.K. Ryasniy, B.A. Komissarova et al, Solid State Commun. 126, 181-184 (2003).

[439] N. Selhaoui, O. J. Kleppa, Zeitschrift fur Metallkunde 84, 744-747 (1993).

[440] S. B. Roy, Phil. Mag. B 65, 1435-1444 (1992).

[441] G. Ravikumar, V.C. Sahni, P.K. Mishra, et al Phys. Rev. B 57, R11069-R11072 (1998).

[442] D.J. Peterman, J. H. Weaver, M. Croft et al, Phys. Rev. B 27, 808-818 (1983).

[443] J.G. Park, M. Ellerby, K.A. McEwen et al, J. Magn. Magn. Mater 140, 2057-2058 (1995).

[444] Y. Onuki, R. Settai, H. Aoki, Physica B 224, 141-148 (1996).

[445] Y. Onuki, Y. Inada, M. Hedo et al, Physica B 261, 1060-1065 (1999).

[446] T. Miyahara, T. Yamazaki, A. Kota et al, J. Phys. Soc. Jpn. 59, 3660-3668 (1990).

[447] Y. Kucherenko, S. L. Molodtsov, A. N. Yaresko et al, Phys. Rev. B 70, (2004).

[448] J.S. Kang, Y. Onuki, C.G. Olson et al, Physica B 281, 731-733 (2000).

[449] Y. Inada, Y. Onuki,Low Temp. Phys. 25, 573-591 (1999).

[450] M. Higuchi, Y. Onuki, A. Hasegawa, Physica B 230, 486-489 (1997).

[451] M. Hakimi, J. G. Huber, Physica B & C 135, 434-437 (1985).

[452] J. Garcia, J. Bartolome, M.S. Delrio et al, Zeitschrift fur Physikalische Chemie Neue Folge 163, 277-282 (1989).

[453] J. Garcia, A. Marcelli, M. S. Delrioral et al, Physica B 158, 521-522 (1989).

[454] G.W. Crabtree, M.B. Maple, W. K. Kwok et al, Phys. Essays 9, 628-646 (1996).

[455] S. Chaudhary, A.K. Rajarajan, K.J. Singh et al, Solid State Commun. 114, 5-8 (2000).

[456] P. Chaddah, S.B. Roy, Bulletin of Materials Science 22, 275-278 (1999).

[457] J. Chaboy, J. Garcia, A. Marcelli, J. Magn. Magn. Mater 104, 661-662 (1992).

[458] J. Chaboy, J. Garcia, A. Marcelli, J. Magn. Magn. Mater 166, 149-164 (1997).

[459] G.E. Barberis, D. Davidov, J.P. Donoso et al, J. Phys. F-Metal Phys. 11, 1249-1260 (1981).

[460] S.S. Banerjee, N.G. Patil, S. Saha et al, Phys. Rev. B 58, 995-999 (1998).

[461] Y. Aoki, T. Nishigaki, H. Sugawara et al, Phys. Rev. B 55, 2768-2771 (1997).

[462] M. Angst, R. Puzniak, A. Wisniewski et al, Phys. Rev. B 67, (2003).

[463] J.W. Allen, S.J. Oh, I. Lindau et al, Phys. Rev. B 26, 445-448 (1982).

[464] J.W. Allen, S.J. Oh, M. B. Maple et al, Phys. Rev. B 28, 5347-5349 (1983).

[465] J. Chaboy, J. Garcia, A. Marcelli, J. Magn. Magn. Mater. 166 (1997) 149.

[466] M. Battisti, A. Marcelli, S. Chudinov et al, J. Magn. Magn. Mater 197, 888-890 (1999).

[467] M.K. Chattopadhyay, S.B. Roy, P. Chaddah, Phys. Rev. B 71, 024523 (2005).

[468] S. Chaudhary, S.B. Roy, P. Chaddah, Solid State Commun. 111, 263-268 (1999).

[469] S. Chudinov, M. Brando, A. Marcelli et al, Physica B 244, 154-158 (1998).

[470] D. Groten, E. Ardonne, S. Ramakrishnan et al, Physica C 306, 271-276 (1998).

[471] M. Hedo, Y. Kobayashi, Y. Inada et al, J. Phys. Soc. Jpn. 67, 3561-3569 (1998).

[472] Y. Homma, K. Sumiyama, H. Yamauchi et al, J. Phys. Soc. Jpn. 66, 1457-1464 (1997).

[473] Y.G. Kim, U.I. Chung, J. Y. Lee, J. Alloys Compd. 202, 203-209 (1993).

[474] Y.G. Kim, J. Y. Lee, J. Alloys Compd. 191, 243-249 (1993).

[475] H. Mukuda, K. Ishida, Y. Kitaoka et al, J. Phys. Soc. Jpn. 67, 2101-2106 (1998).

[476] T. Nakama, Y. Uwatoko, T. Kohama et al, J. Magn. Magn. Mater 177, 425-426 (1998).

[477] S.B. Roy, B. R. Coles, Physica B 163, 424-426 (1990).

[478] S.B. Roy, P. Chaddah, Physica C 273, 120-126 (1996).

[479] S.B. Roy, P. Chaddah, Physica C 279, 70-78 (1997).

[480] S.B. Roy, P. Chaddah, J. Phys. Condens. Mater. 9, L625-L632 (1997).

[481] N.L. Saini, S. Agrestini, D. Di Castro et al, J. Alloys Compd. 317, 542-545 (2001).

[482] N.L. Saini, S. Agrestini, E. Amato et al, Phys. Rev. B 70, 094509 (2004).

[483] Z.Y. Wu, N.L. Saini, S. Agrestini et al, J. Phys. Condens. Mater. 12, 6971-6978 (2000).

[484] P. Haen, J. Flouquet, F. Lappiere et al, J. Low Temp. Phys. 67(1987) 391.

[485] H. Wilhelm, K. Alami-Yadri, B. Revaz et al, Phys. Rev. B 59, 3651-3660 (1999).

[486] F. Weickert, P. Gegenwart, J.A. Mydosh et al, Physica B 359, 68-70 (2005).

[487] H. Walf, D. Mienert, W. Wagener et al, Hyperfine Inter. 121, 629-632 (1999).

[488] C. Tien, S.W. Feng, J.S. Hwang, J. Phys. Condens. Mater. 10, 10269-10282 (1998).

[489] C. Tien, L.Y. Jang, C.Y. Kuor et al, J. Phys. Condens. Mater. 12, 8983-8994 (2000).

[490] S. Sullow, M.C. Aronson, B. D. Rainford et al, Physica B 261, 54-55 (1999).

[491] S. Sullow, M.C. Aronson, B. D. Rainford et al, Phys. Rev. Lett. 82, 2963-2966 (1999).

[492] S. Sullow, G.J. McIntyre, P. Haen et al, J. Magn. Magn. Mater 226, 179-181 (2001).

[493] R. Rawat, V. G. Sathe, J. Phys. Condens. Mater. 17, 313-322 (2005).

[494] B.D. Rainford, A.J. Neville, D.T. Adroja et al, Physica B 359, 166-168 (2005).

[495] H. Okura, K. Ishida, Y. Kawasaki et al, Physica B 281, 61-63 (2000).

[496] J.M. Mignot, L.P. Regnault, J.L. Jacoud et al, Physica B 171, 357-361 (1991).

[497] H. Wilhelm, D. Jaccard, Physica B 261, 79-80 (1999).

[498] P. Haen, H. Bioud, T. Fukuhara, Physica B 261, 85-86 (1999).

[499] P. Haen, H. Bioud, T. Fukuhara, Physica B 281, 59-60 (2000).

[500] P. Haen, T. Fukuhara, Physica B 312, 437-439 (2002).

[501] M.J. Besnus, P. Haen, F. Mallmann et al, Physica B 224, 322-324 (1996).

[502] H. Aoki, M. Takashita, N. Kimura et al, J. Phys. Soc. Jpn. 70, 774-783 (2001).

[503] R. Daou, C. Bergemann, S. R. Julian, Physica B 378-80, 807 (2006).

[504] R. Daou, C. Bergemann, S. R. Julian, Phys. Rev. Lett. 96 (2006) 026401.

[505] G. P. Kopitsa et al., Jetp Lett. 81, 556 (2005).

[506] M. Sato et al., J. Phys. Soc. Jpn. 73, 3418 (2004).

[507] H. Kadowaki, M. Sato, S. Kawarazaki, Phys. Rev. Lett. 92, (2004).

[508] T. Honma et al., J. Phys. Condens. Mater. 15, S2171-S2174 (2003).

[509] D. Takahashi et al., Physica B 329, 489 (2003).

[510] D. Takahashi et al., Phys. Rev. B 67, (2003).

[511] S. R. Saha et al., Phys. Rev. B 65, (2002).

[512] J. Flouquet et al., Physica B 319, 251 (2002).

[513] S. R. Saha et al., J. Phys. Chem. Solid. 63, 1171 (2002).

[514] T. Yanagisawa, Y. Nemoto, T. Goto, and Y. Onuki, Physica B 312, 271 (2002).

[515] H. Kumigashira et al., Physica B 312, 658 (2002).

[516] J. D. Denlinger, G. H. Gweon, J. W. Allen et al, Physica B 312, 670 (2002).

[517] R. Welter, G. Venturini, B. Malaman et al, J. Alloys Compd. 202, 165 (1993).

[518] L. Rebelsky et al., J. Appl. Phys. 63, 3405 (1988).

[519] R. Welter, G. Venturini, and B. Malaman, J. Alloys Compd. 185, 235 (1992).

[520] A. A. Velikhovski et al., Ieee Transactions on Magnetics 30, 1208 (1994).

[521] Y. D. Seropegin, B. I. Shapiev, A. V. Gribanov et al, J. Alloys Compd. 288, 147 (1999).

[522] V. N. Nikiforov et al., Physica B 188, 514 (1993).

[523] V. N. Nikiforov et al., Fizika Tverdogo Tela 35, 648 (1993).

[524] F. Lapierre et al., Physica B 230, 120 (1997).

[525] I. A. Krivosheev et al., Hyperfine Inter. 104, 187 (1997).

[526] V. N. Duginov et al., Phys. Rev. B 55, 12343 (1997).

[527] S. Yomo, P. H. Hor, R. L. Meng et al, J. Magn. Magn. Mater 54-7, 477 (1986).

[528] U. Rauchschwalbe et al., Phys. Rev. B 30, 444 (1984).

[529] R. L. Meng, P. H. Hor, S. Yomo, and C. W. Chu, Physica B & C 135, 394 (1985).

[530] Y. Kishimoto et al., Physica B 336, 398 (2003).

[531] Y. Kishimoto, Y. Kawasaki, T. Ohno, Phys. Lett. A 317, 308 (2003).

[532] Y. Kishimoto et al., J. Phys. Soc. Jpn. 73, 190 (2004).

[533] Y. Kishimoto et al., J. Magn. Magn. Mater 272-76, 509 (2004).

[534] Y. Kishimoto et al., J. Magn. Magn. Mater 272-76, 507 (2004).

[535] R. B. King, Journal of Solid State Chemistry 131, 394 (1997).

[536] M. Gulacsi, Z. Gulacsi, Solid State Commun. 90, 51 (1994).

[537] S. Sullow, B. Ludoph, G.J. Nieuwenhuys et al, Physica B 223&224(1996) 347.

[538] M.A. Continentino, S.N. de Medeiros, M.T.D. Orlando et al, Phys. Rev. B 64 (2001) 012404.

[539] Z. Blazina, S.M. Westwood, J. Alloy. Compd. 201 (1993) 151.

[540] H. Kitazawa, S. Nimori, J. Tang et al, Physica B 237 (1997) 212.

[541] B.-L. Young, D.E. MacLaughin, M.S. Rose et al, Phys. Rev. B, 70 (204) 024401

[542] O.O. Bernal, D.E. MacLaughlin, H.G. Lukerfahr et al, Phys. Rev. Let. 75 (1995) 2023.

[543] A.H. Castro Neto, G. Castilla, B.A. Jones, Phys. rev. Lett. 81 (1998) 3531.

[544] T. Chui, P. Lindenfeld, W.L. McLean et al, Phys. Rev. Let. 47 (1981) 1617.

[545] A. Kawabata, Solid State Commun. 34 (1980) 431.

[546] J. B. Bieri, A. Fert, G. Creuzet et al, J. Phys. Met. Phys. 16 (1986) 2099.

[547] J.M. Lawrence, Y.-C. CHen, G.H. Kwei et al, Phys. Rev. B, 56 (1997) 5.

[548] T.C. Chieu, G. Timp, M.S. Dresselhaus et al, Phys. Rev. B, 27 (1983) 3686.

[549] F. Ohkawa, Phys. Rev. Lett. 64 (1990) 2300.

[550] T.A. Costi, C. Kieffer, Phys. Rev. Lett. 76 (1996) 1683., T.A. Costi, C. Kieffer, Phys. Rev. Lett. 80 (1998) 1038.

[551] R. Pietri, K. Ingersent, B. Andraka, Phys. Rev. Lett. 86 (2001) 1090.

[552] E.A. Goremychkin, R. Osborn, B.D. Rainford et al, Phys. Rev. Lett. 89 (2002) 147201.

[553] A.D. Huxley, C. Paulsen, O. Laborde, J.L. Tholence, D. Sanchez, A. Junod, R. Calemczuk, J. Phys. Condens. Mater., 5 (1993) 7709.

[554] L. Rebelski, K. Reilly, S. Horn, H. Borges, J.D. Thomson, J.O. Willis, R. Aikin, R. Caspari, C.D. Bredl, J. Appl. Phys, 63 (1988) 3405

[555] A.B. Andrews, J.J. Joyce, A.J. Arko, J.D. Thompson, J. Tang, J.M. Lawrence, J.C. Hemminger, Phys. Rev. B, 51 (1995) 3277

[556] D. Gignoux, D. Schmidt, M. Zerguine, C. Ayache, E. Bonjour, Phys. Lett. A, 117 (1986) 145.

[557] R. Gupta, A. Gupta, A.K. Nigam et al, J. Alloy. Compd. 326 (2001) 275.

[558] J. Wang et al, Science 299 (2003) 1719.

[559] J. Li et al, Appl. Phys. Lett. 84 (2003) 5261.

[560] A. Sharan et al, Appl. Phys. Lett. 83 (2003) 5169.

[561] M. Gich et al, Nanotechnology 17 (2006) 687.

[562] W. Trinkl, U. Weilnhammer, S. Corsepius et al, Phys. Rev. B 54 (1996) 1163.

[563] J. S. Kim, J. Alwood, G. R. Stewart et al, Phys. Rev. B 54 (2001) 134524.

[564] M.E. Huntelaar, A.S. Booij, E.H.P. Cordfunke et al, J. Chem. Thermodynamics 32 (2000) 465.

[565] Yu.D. Seropegin, B.I. Shapieva, A.V. Gribanovaet al, J. Alloy Compd. 288 (1999) 147.

[566] A.V. Gribanov, Y.D. Seropegin, A.I. Tursinaet al, J. Alloy Compd. 383 (2004) 286.